Optimization and Exploration of Catalysts for Hydrodeoxygenation Upgrading of Bio-oil through Experiments and DFT Calculations

Zur Erlangung des akademischen Grades eines
DOKTORS DER INGENIEURWISSENSCHAFTEN (DR.-ING.)

von der KIT-Fakultät für Chemieingenieurwesen und Verfahrenstechnik des Karlsruher Instituts für Technologie (KIT)

genehmigte

DISSERTATION

von
M. Sc. Yanjun Wen
aus Weifang

Tag der mündlichen Prüfung: 17. März 2026
Erstgutachter: Prof. Dr. rer. nat. Nicolaus Dahmen
Zweitgutachter: Prof. Dr. Reinhard Rauch

Acknowledgements

I would first like to express my deepest gratitude to my main supervisor, Prof. Dr. Nicolaus Dahmen, whose extensive knowledge, insightful guidance, and inspiring passion have profoundly influenced my growth as a researcher. His unwavering support has greatly enriched both my academic skills and personal character throughout my doctoral journey.

I am especially grateful to my mentor, Dr. Klaus Raffelt, for his meticulous experimental guidance and detailed feedback, which significantly strengthened the quality of my research. Additionally, I deeply appreciate his support in applying for scholarships and his highly effective scientific advice, which greatly facilitated my research progress. His continuous encouragement and patience were instrumental in overcoming experimental challenges and achieving successful outcomes.

I also extend my sincere appreciation to my second supervisor, Prof. Dr. Felix Studt, whose comprehensive instruction in DFT calculations greatly enhanced my technical skills and understanding in computational research methodologies.

My heartfelt thanks go to Dr. Dmitry I. Sharapa for his patient and detailed guidance on DFT calculations, which provided me with critical insights and significantly contributed to my computational analyses.

Special thanks to Yannik Träutlein and Birgit Rolli for their dedicated product analysis and testing. I would also like to express my gratitude to Thomas Zevaco, Michael Zimmermann, Armin Lautenbach, and Dieter Schild for their valuable testing support. Additionally, I am very thankful to Thomas Tietz for his technical assistance with experimental equipment. A special acknowledgment goes to Mariana Myriam Campos Fraga for introducing me to bio-oil experiments. Furthermore, I deeply appreciate the help and support provided by my colleagues Wenxuan Li, Jiachen Chen, Naiara da Costa Telis, Bing Wang, Amir Jalalinejad, and others.

Finally, my deepest thanks go to my wife, Huaning Li, whose companionship and emotional support have been invaluable throughout this journey. I am also deeply grateful to my family for their constant encouragement and unwavering support.

Thank you all very much!

This monograph thesis contains these 2 Peer-reviewed original publications:

1. *Yanjun Wen, Foteini Zormpa, Dmitry I. Sharapa, Felix Studt, Klaus Raffelt, Nicolaus Dahmen*, Exploring the hydrodeoxygenation of lignin β-O-4 dimer model compound and bio-oil by DFT and experimental studies, Molecular Catalysis, Volume 580, 2025, 115134, https://doi.org/10.1016/j.mcat.2025.115134.

2. *Yanjun Wen, Wenxuan Li, Dmitry Sharapa, Thomas A. Zevaco, Dieter Schild, Felix Studt1, , Klaus Raffelt, Nicolaus Dahmen,* Engineering Ni(0)/Ni(II) interfaces in LDH-Derived Ni–Al catalysts for mild lignin depolymerization, Bioresource Technology, Volume 442, 2026, 133697, https://doi.org/10.1016/j.biortech.2025.133697.

Declaration on Reuse of Peer-reviewed original publications:

In this monograph, all figures, tables, and textual materials related to the two peer-reviewed publications mentioned above are explicitly cited each time they are reused.

Statement

A generative AI tool (ChatGPT) was used solely for language and grammar editing of this thesis. All research design, data, analyses, and conclusions are my own and remain my responsibility; the tool was not used to generate content, data, or references.

Acronyms

Ar	Argon
BET	Brunauer–Emmett–Teller
CINEB	Climbing Image Nudged Elastic Band
CTAB	Cetyltrimethylammonium bromide
DDO	Direct deoxygenation
DFT	Density Functional Theory
EDX	Elemental mapping via energy Dispersive X-ray spectroscopy
GC	Gas Chromatography
GC-FID	Gas Chromatography - Flame Ionization Detector
GC-MS	Gas Chromatography - Mass Spectrometry
GGA	Generalized Gradient Approximation
HDO	Hydrodeoxygenation
HHV	Higher Heating Value
HYD	Hydrogenation-Dehydration
ICP-OES	Inductively Coupled Plasma – Optical Emission Spectroscopy
LDA	Local Density Approximation
LDH	Layered Double Hydroxides
LDO	Layered Double Oxides
LHSV	Liquid Hourly Space Velocity
PBE	Perdew Burke Ernzerhof
PPE	2-Phenylethyl phenyl ether
SAF	Sustainable Aviation Fuels
SDS	Sodium Dodecyl Sulfate
SEM	Scanning Electron Microscopy
TCD	Thermal Conductivity Detector
TEM	Transmission Electron Microscopy
TPD	Temperature-Programmed Desorption

VASP	Vienna Ab-initio Simulation Package
XAS	X-ray Absorption Spectroscopy
XANES	X-ray absorption near edge spectra
XPS	X-ray Photoelectron Spectroscopy
XRD	X-Ray Diffraction

Summary

This thesis investigates the catalytic upgrading of bio-oil to optimize its composition for fuel applications, with a focus on improving the stability and selectivity of bio-based hydrocarbons. Catalytic upgrading plays a crucial role in converting bio-oil into high-quality liquid fuels, ensuring improved stability and performance in energy applications. This research also explores the reaction pathways of oxygen-containing compounds during catalytic bio-oil upgrading, aiming to enhance selectivity and fuel quality. This research also explores the reaction pathways of oxygen-containing compounds during catalytic bio-oil upgrading, aiming to enhance selectivity and fuel quality.

Bio-oil, derived from lignocellulosic biomass, contains high levels of oxygenated compounds, which hinder its direct use as transportation fuel. These oxygenated compounds contribute to instability and low heating value, necessitating effective catalytic upgrading strategies. Catalytic upgrading provides a viable pathway to selectively remove oxygen while preserving the hydrocarbon framework, improving fuel properties. However, the high oxygen content in bio-oil (~35-50 %) poses a significant challenge for refining, leading to poor thermal stability and high acidity. Oxygenated species lead to undesired side reactions, catalyst deactivation, and increased coke formation during upgrading processes. Currently, hydrodeoxygenation (HDO) is the most widely applied catalytic upgrading technique to improve bio-oil quality. However, oxygen removal often leads to excessive hydrogen consumption and undesired cracking reactions, reducing carbon efficiency. This thesis investigates novel catalytic strategies to selectively remove oxygen while maximizing hydrocarbon retention, enabling efficient bio-oil upgrading.

Chapter 1 and Chapter 2 provides a comprehensive overview of the background on catalytic upgrading of bio-oil to improve its quality for fuel applications. The chapter introduces the key challenges associated with bio-oil, including its high oxygen content, poor stability, and incompatibility with conventional petroleum-based fuels. Various catalytic processes for bio-oil upgrading are discussed, highlighting their advantages and limitations. Furthermore, the fundamental reaction pathways of catalytic HDO and its impact on the removal of oxygen-containing species are explored. In addition, the chapter introduces the role of different catalyst types (e.g., metal-supported catalysts, bifunctional catalysts) and their performance in deoxygenation reactions. The influence of reaction conditions such as temperature, pressure, and hydrogen supply is also reviewed. Finally, the existing research gaps in catalytic bio-oil upgrading are identified, and the key objectives of this thesis are outlined.

In the Results and Discussion (Chapter 4), Part I (Section 4.2) investigates the critical role of HDO in the efficient utilization of biomass, with a particular focus on ruthenium

(Ru) catalysts. Since oligomeric species play a significant role in bio-oil upgrading, this chapter employs a dimer model compound to elucidate the reaction mechanism, providing insights for the rational design of catalysts in subsequent studies. Initially, the adsorption behavior of 2-Phenylethyl phenyl ether (PPE) on the Ru (0001) surface was examined using density functional theory (DFT) calculations, leading to the determination of its optimized adsorption configuration. Subsequently, the reaction pathways for HDO on the Ru catalyst were computationally analyzed, offering mechanistic insights into the transformation of dimeric lignin-derived compounds. Building upon these theoretical findings, the catalytic performance of Ru/Nb_2O_5 was evaluated in the HDO of PPE, demonstrating high efficiency in oxygen removal. To further assess its practical applicability, the catalyst was tested in the HDO of real bio-oil, allowing for a more comprehensive evaluation of its effectiveness under complex reaction conditions. This study systematically investigates the HDO of PPE over a Ru-based catalyst, illustrating the potential of employing dimer model compounds in mechanistic studies and highlighting the promising capabilities of Ru-based catalysts for bio-oil upgrading.

Building on the findings of Part I (Section 4.2), which identified C-O bond cleavage in β-O-4 linkages as the key step, a series of catalysts were designed for β-O-4 hydrogenolysis. Part II (Section 4.3) investigates the catalytic depolymerization of biomass oligomers, a crucial step in biomass valorization. Due to the stringent conditions required for their conversion into high-value monomers, Ni-based catalysts derived from layered double hydroxides (LDH) were developed to enhance depolymerization efficiency under mild conditions. The catalytic performance of these Ni/Al-LDH-derived catalysts was evaluated using a biomass dimer model compound, achieving complete conversion at 125 °C and 25 bar. Characterization techniques, including TEM and XPS, confirmed the coexistence of Ni(0) and Ni(II) species on the catalyst surface. DFT calculations revealed that Ni(II) modifies the d-band center of Ni(0), influencing its adsorption behavior and catalytic activity. The Ni/NiO interface also displayed superior thermodynamic and kinetic properties compared to Ni (111). This chapter highlights the synergistic role of Ni(0) and Ni(II) in lignin depolymerization, providing insights for the rational design of efficient Ni-based catalysts under mild conditions.

The designed catalysts exhibited high C-O bond cleavage activity In Section 4.3, yielding primarily oxygenated monomers. However, their limited deoxygenation capability indicated the need for further optimization to achieve efficient oxygen removal. Part III (Section 4.4) builds upon these findings by incorporating oxophilic metal dopants into the Ni-based catalysts to enhance their deoxygenation performance. A series of Ni/Al_2O_3 catalysts doped with Mo, Ce, Nb, and W was synthesized using an interlayer doping strategy based on layered double hydroxide (LDH) structures. These modifications significantly improved the catalysts' ability to remove oxygen-containing

functional groups. Guaiacol, a widely used model compound for lignin-derived bio-oil, was employed to assess catalytic performance, achieving complete conversion and 99% selectivity toward cyclohexane under optimized conditions. Notably, the doped catalysts also demonstrated superior efficiency in deoxygenating crude bio-oil, outperforming commercial noble metal-based Ru/C catalysts. Mechanistic investigations integrating DFT calculations and experimental characterization revealed that MoOx clusters on Ni surfaces reduce the C-O bond cleavage energy barrier to 0.40 eV, significantly lower than that of conventional Ni catalysts. This enhancement underscores the synergistic effect of oxophilic metal dopants, which facilitates oxygen removal while maintaining catalytic stability. This chapter provides an advanced catalyst design strategy for bio-oil upgrading, offering a cost-effective alternative to noble metal catalysts and deepening the fundamental understanding of HDO mechanisms in biomass valorization.

In Section 4.4, the catalytic upgrading strategies effectively achieved oxygen removal, yet predominantly produced oxygen-containing monomeric compounds with limited carbon chain lengths. Such upgraded bio-oils typically cannot satisfy the requirements for high-value transportation fuels such as sustainable aviation fuel (SAF) or biodiesel. To overcome this limitation, Part IV (Section 4.5) explores the utilization of biomass-derived syngas (CO/H_2) as an external carbon source to enhance the carbon chain length of upgraded bio-oil hydrocarbons through catalytic C–C coupling. A series of Ru/β-zeolite catalysts were developed and evaluated for their capability to promote carbon-chain elongation using guaiacol as a representative phenolic compound. Among the tested catalysts, Ru/β-zeolite demonstrated exceptional catalytic activity, achieving effective C–C coupling and chain elongation under moderate reaction conditions. Furthermore, application of this catalyst to real bio-oil confirmed its high catalytic efficiency, successfully extending the carbon chain length and significantly improving fuel properties. Characterization techniques, including X-ray diffraction (XRD) and scanning electron microscopy coupled with energy-dispersive X-ray spectroscopy (SEM-EDX), revealed that the zeolite support maintained its crystalline structure, while Ru nanoparticles were uniformly dispersed, providing abundant active sites. This study demonstrates the potential of employing syngas-assisted catalytic upgrading strategies to produce high-quality renewable fuels, offering valuable insights for sustainable biomass valorization and the development of advanced catalytic processes for biofuel production.

Chapter 5 summarizes the primary findings and key contributions of this thesis, highlighting the advancements made in catalytic HDO for biomass-derived feedstocks. The thesis provides a deeper understanding of catalytic mechanisms and illustrates effective strategies for optimizing catalyst performance to enhance bio-oil upgrading efficiency. The chapter also identifies directions for future research, emphasizing the need to further investigate catalyst stability, recyclability, and industrial scalability. It

suggests exploring catalyst performance in continuous-flow systems and conducting more in-depth mechanistic studies on catalyst-substrate interactions. These efforts could significantly contribute to the development of practical, sustainable, and economically feasible biofuel production processes.

Zusammenfassung

Diese Dissertation untersucht das katalytische Upgrading von Bioöl zur Optimierung seiner Zusammensetzung für Kraftstoffanwendungen, mit einem Fokus auf die Verbesserung der Stabilität und Selektivität von biobasierten Kohlenwasserstoffen. Das katalytische Upgrading spielt eine entscheidende Rolle bei der Umwandlung von Bioöl in hochwertige flüssige Kraftstoffe und gewährleistet verbesserte Stabilität und Leistung in Energieanwendungen. Diese Forschung untersucht auch die Reaktionswege sauerstoffhaltiger Verbindungen während des katalytischen Bioöl-Upgradings mit dem Ziel, Selektivität und Kraftstoffqualität zu verbessern.

Bioöl, das aus lignozellulosischer Biomasse gewonnen wird, enthält hohe Anteile an oxygenierten Verbindungen, die seine direkte Verwendung als Transportkraftstoff verhindern. Diese oxygenierten Verbindungen tragen zur Instabilität und zum niedrigen Heizwert bei, was effektive katalytische Upgrading Strategien erforderlich macht. Das katalytische Upgrading bietet einen praktikablen Weg, um Sauerstoff selektiv zu entfernen und gleichzeitig die Kohlenwasserstoffstruktur zu erhalten, wodurch die Kraftstoffeigenschaften verbessert werden. Der hohe Sauerstoffgehalt im Bioöl (~35-50 %) stellt jedoch eine erhebliche Herausforderung für die Raffinierung dar und führt zu geringer thermischer Stabilität und hoher Azidität. Oxygenierte Spezies führen zu unerwünschten Nebenreaktionen, Katalysatordeaktivierung und erhöhter Koksbildung während der Upgradingprozesse. Derzeit ist die Hydrodeoxygenierung (HDO) die am häufigsten angewandte katalytische Aufwertungstechnik zur Verbesserung der Bioölqualität. Die Sauerstoffentfernung führt jedoch oft zu erhöhtem Wasserstoffverbrauch und unerwünschten Crackreaktionen, was die Kohlenstoffeffizienz verringert. Diese Dissertation untersucht neuartige katalytische Strategien zur selektiven Entfernung von Sauerstoff bei maximaler Ausbeute von Kohlenwasserstoff, um ein effizientes Bioöl-Upgrading zu ermöglichen.

Kapitel 1 und 2 bieten einen umfassenden Überblick über den Hintergrund des katalytischen Upgradings von Bioöl zur Verbesserung seiner Qualität für Kraftstoffanwendungen. Das Kapitel stellt die wichtigsten Herausforderungen im Zusammenhang mit Bioöl vor, einschließlich seines hohen Sauerstoffgehalts, seiner geringen Stabilität und seiner Unverträglichkeit mit konventionellen erdölbasierten Kraftstoffen. Verschiedene katalytische Prozesse zum Bioöl-Upgrading werden diskutiert, wobei ihre Vorteile und Einschränkungen hervorgehoben werden. Darüber hinaus werden die grundlegenden Reaktionswege der katalytischen HDO und ihre Auswirkungen auf die Entfernung sauerstoffhaltiger Spezies untersucht. Zusätzlich stellt das Kapitel die Rolle verschiedener Katalysatortypen (z.B. metallgestützte Katalysatoren, bifunktionale Katalysatoren) und ihre Leistung bei Desoxygenierungsreaktionen vor. Der Einfluss von Reaktionsbedingungen wie

Temperatur, Druck und Wasserstoffversorgung wird ebenfalls beschrieben. Schließlich werden die bestehenden Forschungslücken im katalytischen Bioöl-Upgrading identifiziert und die Hauptziele dieser Dissertation umrissen.

Teil I (Abschnitt 4.2.2) untersucht die entscheidende Rolle der HDO bei der effizienten Nutzung von Biomasse, mit besonderem Fokus auf Ruthenium (Ru)-Katalysatoren. Da oligomere Spezies eine bedeutende Rolle beim Bioöl-Upgrading spielen, verwendet dieses Kapitel eine Dimer-Modellverbindung, um den Reaktionsmechanismus aufzuklären und Erkenntnisse für das rationale Design von Katalysatoren in nachfolgenden Studien zu liefern. Zunächst wurde das Adsorptionsverhalten von 2-Phenylethylphenylether (PPE) auf der Ru (0001)-Oberfläche mittels Dichtefunktionaltheorie (DFT)-Berechnungen untersucht, was zur Bestimmung seiner optimierten Adsorptionskonfiguration führte. Anschließend wurden die Reaktionswege für HDO am Ru-Katalysator rechnerisch analysiert, was mechanistische Einblicke in die Transformation von dimeren, aus Lignin abgeleiteten Verbindungen bot. Aufbauend auf diesen theoretischen Erkenntnissen wurde die katalytische Leistung von Ru/Nb_2O_5 bei der HDO von PPE bewertet, was eine hohe Effizienz bei der Sauerstoffentfernung zeigte. Um seine praktische Anwendbarkeit weiter zu bewerten, wurde der Katalysator in der HDO von echtem Bioöl getestet, was eine umfassendere Bewertung seiner Wirksamkeit unter komplexen Reaktionsbedingungen ermöglichte. Diese Studie untersucht systematisch die HDO von PPE über einen Ru-basierten Katalysator und veranschaulicht das Potenzial der Verwendung von Dimer-Modellverbindungen in mechanistischen Studien sowie die vielversprechenden Fähigkeiten von Ru-basierten Katalysatoren für das Bioöl-Upgrading.

Aufbauend auf den Erkenntnissen aus Teil I (Abschnitt 4.2), die die C-O-Bindungsspaltung in β-O-4-Verknüpfungen als Schlüsselschritt identifizierten, haben wir eine Reihe von Katalysatoren für die β-O-4-Hydrogenolyse entwickelt. Teil II (Abschnitt 4.3) untersucht die katalytische Depolymerisation von Biomasse-Oligomeren, einen entscheidenden Schritt in der Biomasseverwertung. Aufgrund der strengen Bedingungen, die für ihre Umwandlung in hochwertige Monomere erforderlich sind, wurden Ni-basierte Katalysatoren, die aus Doppelschichthydroxiden (LDH) abgeleitet wurden, entwickelt, um die Depolymerisationseffizienz unter milden Bedingungen zu verbessern. Die katalytische Leistung dieser von Ni/Al-LDH abgeleiteten Katalysatoren wurde unter Verwendung einer Biomasse-Dimer-Modellverbindung bewertet, wobei eine vollständige Umwandlung bei 125 °C und 25 bar erreicht wurde. Charakterisierungstechniken, einschließlich TEM und XPS, bestätigten die Koexistenz von Ni(0)- und Ni(II)-Spezies auf der Katalysatoroberfläche. DFT-Berechnungen zeigten, dass Ni(II) das d-Band-Zentrum von Ni(0) modifiziert, was sein Adsorptionsverhalten und seine katalytische Aktivität beeinflusst. Die Ni/NiO-Schnittstelle zeigte auch überlegene thermodynamische und kinetische Eigenschaften im Vergleich zu Ni (111). Dieses Kapitel hebt die synergetische Rolle

von Ni(0) und Ni(II) bei der Lignindepolymerisation hervor und bietet Erkenntnisse für das rationale Design effizienter Ni-basierter Katalysatoren unter milden Bedingungen.

Die in Abschnitt 4.3 entwickelten Katalysatoren zeigten eine hohe C-O-Bindungsspaltungsaktivität, die hauptsächlich oxygenierte Monomere lieferte. Ihre begrenzte Desoxygenierungsfähigkeit deutete jedoch auf die Notwendigkeit weiterer Optimierungen hin, um eine effiziente Sauerstoffentfernung zu erreichen. Teil III (Abschnitt 4.4) baut auf diesen Erkenntnissen auf, indem oxophile Metalldotierungen in die Ni-basierten Katalysatoren eingebaut werden, um ihre Desoxygenierungsleistung zu verbessern. Eine Reihe von Ni/Al_2O_3-Katalysatoren, die mit Mo, Ce, Nb und W dotiert sind, wurde unter Verwendung einer Zwischenschichtdotierungsstrategie basierend auf Doppelschichthydroxid (LDH)-Strukturen synthetisiert. Diese Modifikationen verbesserten signifikant die Fähigkeit der Katalysatoren, sauerstoffhaltige funktionelle Gruppen zu entfernen. Guajacol, eine weit verbreitete Modellverbindung für aus Lignin abgeleitetes Bioöl, wurde verwendet, um die katalytische Leistung zu bewerten, wobei unter optimierten Bedingungen eine vollständige Umwandlung und 99% Selektivität zu Cyclohexan erreicht wurden. Bemerkenswert ist, dass die dotierten Katalysatoren auch eine gute Effizienz bei der Desoxygenierung von Rohbioöl zeigten und kommerziellen Edelmetall-basierten Ru/C-Katalysatoren überlegen waren. Mechanistische Untersuchungen mit integrierten DFT-Berechnungen und experimentellem Nachweis zeigten, dass MoOx-Cluster auf Ni-Oberflächen die Energiebarriere der C-O-Bindungsspaltung auf 0,40 eV reduzieren, was deutlich niedriger ist als bei herkömmlichen Ni-Katalysatoren. Diese Verbesserung unterstreicht den synergetischen Effekt oxophiler Metalldotierungen, der die Sauerstoffentfernung erleichtert und gleichzeitig die katalytische Stabilität aufrechterhält. Dieses Kapitel bietet eine fortschrittliche Katalysatordesignstrategie für das Bioöl-Upgrading, die eine kostengünstige Alternative zu Edelmetallkatalysatoren darstellt und das grundlegende Verständnis von HDO-Mechanismen in der Biomasseverwertung vertieft.

In Abschnitt 4.4 erreichten die katalytischen Upgradingsstrategien effektiv die Sauerstoffentfernung, produzierten jedoch überwiegend sauerstoffhaltige monomere Verbindungen mit begrenzten Kohlenstoffkettenlängen. Solche Bioöl Upgrades können typischerweise die Anforderungen für hochwertige Transportkraftstoffe wie nachhaltigen Flugkraftstoff (SAF) oder Biodiesel nicht erfüllen. Um diese zu erreichen, untersucht Teil IV (Abschnitt 4.5) die Verwendung von aus Biomasse gewonnenem Synthesegas (CO/H_2) als externe Kohlenstoffquelle, um die Kettenlänge von in den upgegradeten Bioöl-Fraktionen durch katalytische C-C-Kopplung zu erhöhen. Eine Reihe von Ru/β-Zeolith-Katalysatoren wurde entwickelt und auf ihre Fähigkeit hin bewertet, die Kohlenstoffkettenverlängerung unter Verwendung von Guajacol als Modell eines phenolischen Monomers von Lignin zu fördern. Unter den getesteten Katalysatoren zeigte Ru/β-Zeolith eine außergewöhnliche katalytische Aktivität und

erreichte eine effektive C-C-Kopplung und Kettenverlängerung unter moderaten Reaktionsbedingungen. Darüber hinaus bestätigte die Anwendung dieses Katalysators auf echtes Bioöl seine hohe katalytische Effizienz, verlängerte erfolgreich die Kohlenstoffkettenlänge und verbesserte die Kraftstoffeigenschaften erheblich. Die chemische Analytik, einschließlich Röntgenbeugung (XRD) und Rasterelektronenmikroskopie gekoppelt mit energiedispersiver Röntgenspektroskopie (SEM-EDX), zeigten, dass der Zeolith-Träger seine kristalline Struktur beibehielt, während Ru-Nanopartikel gleichmäßig verteilt blieben, was zahlreiche aktive Stellen bot. Diese Studie demonstriert das Potenzial der Verwendung von synthesegasunterstützten katalytischen Upgradingsstrategien zur Herstellung hochwertiger erneuerbarer Kraftstoffe und bietet wertvolle Einblicke für die nachhaltige Biomasseverwertung und die Entwicklung fortschrittlicher katalytischer Prozesse für die Biokraftstoffproduktion.

Kapitel 5 fasst die wichtigsten Ergebnisse und Beiträge dieser Dissertation zusammen und hebt die Fortschritte hervor, die in der katalytischen HDO für Biomasse-basierte Pyrolyseöle erzielt wurden. Die Dissertation bietet ein tieferes Verständnis katalytischer Mechanismen und zeigt effektive Strategien zur Optimierung der Katalysatorleistung, um die Effizienz des Bioöl-Upgradings zu verbessern. Das Kapitel identifiziert auch Richtungen für zukünftige Forschungen und betont die Notwendigkeit, die Katalysatorstabilität, Recyclingfähigkeit und industrielle Skalierbarkeit weiter zu untersuchen. Es schlägt vor, die Katalysatorleistung in kontinuierlichen Durchflusssystemen zu erforschen und tiefergehende mechanistische Studien zu Katalysator-Substrat-Wechselwirkungen durchzuführen. Diese Bemühungen könnten wesentlich zur Entwicklung praktischer, nachhaltiger und wirtschaftlich machbarer Biokraftstoffproduktionsprozesse beitragen.

Table of Contents

Acknowledgements II
List of publications ..... 错误!未定义书签。
Acronyms V
Summary VII
Zusammenfassung XI
Chapter 1 Introduction 1
1.1 Motivation 1
1.2 Scope of this work 2
Chapter 2 Literature Review 5
2.1 Bio-oil upgrading 5
2.2.1 Background and significance of bio-oil 5
2.2.2 Existing bio-oil upgrading techniques 6
2.2 Bio-oil hydrodeoxygenation (HDO) 11
2.2.1 Background and significance of HDO 11
2.2.2 Current Status of HDO Technology 14
2.2.3 Challenges in HDO process 16
2.3 Application of Density Functional Theory (DFT) in HDO research 17
2.3.1 Fundamental principles of DFT methods 17
2.3.2 Current applications of DFT in HDO reaction mechanism research 18
Chapter 3 Materials and Methods 21
3.1 Catalyst preparation 21
3.1.1 Ru based catalyst 21
3.1.2 Ni-Al LDH catalyst 21
3.1.3 Mo doped Ni-Al LDH catalyst 23
3.1.4 zeolite catalyst 24
3.2 Characterization 24
3.3 Catalytic performance test 27
3.3.1 model compound 27
3.3.2 Bio-oil HDO 28
3.3.4 Upgrading in syngas 28

3.4 DFT calculation 29
Chapter 4 Results and Discussions 31
4.1 Introduction 31
4.2 Exploring the hydrodeoxygenation of lignin β-O-4 dimer model compound and bio-oil by DFT and experimental studies 31
4.2.1 DFT calculation 31
4.2.2 Catalyst characterization 36
4.2.3 HDO catalytic performence 38
4.2 Mild catalytic hydrogenolysis of β-O-4 lignin linkage over a synergistic catalyst of Ni (0) and Ni (II) 41
4.2.1 Catalyst characterization 41
4.2.2 Hydrogenolysis of PPE 46
4.3.3 DFT calculation 48
4.3 Interlayer doping of Mo in Ni/Al_2O_3 catalysts for enhanced hydrodeoxygenation performance of bio-oil 52
4.3.1 Catalyst characterization 52
4.3.2 HDO of guaiacol 56
4.3.3 HDO of bio-oil 58
4.3.4 DFT calculation 60
4.4 Syngas-promoted catalytic C–C coupling of bio-oil toward longer-chain products 64
4.4.1 Catalyst characterization 64
4.4.2 C-C coupling of guaiacol 68
4.4.3 C-C coupling of bio-oil 70
Chapter 5 Final conclusion and outlook 73
Reference 76
Supporting Information 105
List of Figures 157
List of Tables 161

Chapter 1 Introduction

1.1 Motivation

The interconnected challenges of achieving carbon neutrality, addressing the global energy crisis, and mitigating environmental pollution have become central to international policy discourse.[1,2] These challenges arise from a complex interplay of factors, including supply chain disruptions as, e.g., due to the COVID-19 pandemic, market instability resulting from geopolitical tensions, and the consequences of climate change.[3] Collectively, these factors have led to substantial volatility in energy prices and considerable disruptions to the global economic system. Unlike previous energy crises, the current scenario uniquely integrates energy security concerns with climate change mitigation and environmental sustainability, forming a multifaceted and interdependent set of challenges.[4]

The imperative for an energy transition has become a core priority for governments globally. A prominent illustration of this shift is the European Green Deal, one of the most ambitious legislative frameworks enacted to date, which aims to achieve climate neutrality by 2050 through comprehensive policies designed to expedite the adoption of renewable energy sources.[5,6] The effectiveness of this approach was notably demonstrated in 2020, when renewable energy generation surpassed fossil fuel generation within the European Union for the first time, marking a significant milestone in the transition towards a sustainable energy system. Nonetheless, specific sectors, particularly transportation, pose considerable challenges to achieving comprehensive defossilization. As one of the primary sources of greenhouse gas emissions, transportation faces substantial technological and infrastructural barriers to full electrification. Consequently, diversified energy solutions such as green hydrogen production, advanced battery technologies, and the development of a comprehensive zero-carbon technological ecosystem have garnered increased attention. A successful transition necessitates coordinated advancement across technological innovation, supportive policy frameworks, and infrastructure improvements to facilitate deep decarbonization effectively. Given the global energy crisis and the pressing agenda of carbon neutrality, biomass has garnered significant interest as the most prevalent renewable carbon resource on Earth. The feedstocks for biomass, including agricultural and forestry residues, dedicated energy crops, and municipal organic solid waste, are widely available. The efficient utilization of these resources presents a viable pathway toward achieving a carbon-neutral cycle, positioning biomass as a highly promising renewable energy source.The inherent challenges of biomass—a diffuse, bulky, and heterogeneous solid—complicate its logistics and continuous processing. Transforming it into a dense, pumpable liquid intermediate addresses these issues by streamlining storage, transport, and upgrading efficiency. Thermochemical liquefaction is the key

process that enables this transformation from raw feedstock to a workable liquid. Bio-oil, derived from biomass liquefaction processes through fast pyrolysis or hydrothermal liquefaction, represents a promising renewable liquid fuel alternative due to its higher energy density and improved handling characteristics compared to solid biomass.[7,8] It holds significant potential to replace or supplement fossil fuels, particularly in sectors where electrification remains challenging, such as aviation and maritime transport. Nevertheless, raw bio-oil typically exhibits high oxygen content (35-50 %) and some other unfavorable properties, including high acidity, corrosiveness, low energy density, and instability.[9–12] To address these limitations and enhance bio-oil's compatibility with existing fuel standards, catalytic hydrodeoxygenation (HDO) is essential.[13–15] HDO can effectively reduce the oxygen content of bio-oil to below 1%, substantially improving its fuel properties and facilitating its integration into the existing fuel infrastructure and standards.

1.2 Scope of this work

Fast pyrolysis bio-oil is a highly complex mixture of oligomeric and monomeric oxygenates derived from lignin and carbohydrates. Its direct use as a fuel is hampered by high oxygen content, chemical instability, and a broad molecular-weight distribution. In particular, the oligomeric fraction, which still retains multiple aromatic units connected by linkages such as β-O-4, is significantly more recalcitrant toward hydrotreating than isolated monomeric oxygenates, and thus represents a key bottleneck for efficient bio-oil HDO and upgrading. Catalytic hydrotreatment is a promising route to stabilize and upgrade bio-oil, but rational process design is impeded by an incomplete mechanistic understanding of (i) how key lignin-derived linkages such as β-O-4 are cleaved, (ii) how the resulting oxygenated monomers can be selectively hydrodeoxygenated, and (iii) how these intermediates can be further transformed into higher-value, fuel-range products. In particular, a consistent picture that connects elementary reaction steps, catalyst structure, and process-level upgrading strategies is still lacking.

To address these gaps, this thesis follows a three-stage upgrading concept:

1. Depolymerization of bio-oil oligomers via selective cleavage of β-O-4 linkages to generate oxygenated monomers.
2. HDO of these monomers to yield deoxygenated molecules with improved stability.
3. C–C coupling of components in the light phase of bio-oil to construct longer-chain products with higher fuel value.

Within this framework, the overall aim of the thesis is to establish structure–activity relationships that guide the design of efficient catalysts for each stage, by combining experimental catalysis with DFT calculations.

Research objectives and storyline

The work is structured around four interconnected research objectives, which build on each other from fundamental mechanistic insight to catalyst design and process-relevant upgrading strategies:

1. Elucidate the mechanism of β-O-4 C–O bond cleavage in bio-oil oligomers over a representative Ru catalytic system (Section 4.2).
    - *Approach:* Experimental hydrotreatment of oligomeric model feeds combined with DFT calculations of elementary steps on Ru-based surfaces.
    - *Role in storyline:* Provides a mechanistic basis for how β-O-4 linkages are activated and cleaved, defining key intermediates and active motifs that later guide catalyst selection.
2. Design high-activity catalysts for β-O-4 linkage cleavage, guided by the above mechanistic insights (Section 4.3).
    - *Approach:* Experimental screening and kinetic evaluation of Ni/Al_2O_3-based catalysts, supported by DFT modeling of C–O bond activation on Ni surfaces.
    - *Role in storyline:* Translates the Ru-based mechanistic understanding to a more earth-abundant Ni system, establishing how catalyst composition and active-site structure govern β-O-4 hydrogenolysis.
3. Investigate HDO of the oxygenated monomers obtained after depolymerization (Section 4.4).
    - *Approach:* Experimental HDO of guaiacol and related monomers over Ni/Al_2O_3 and Mo-promoted Ni/Al_2O_3, complemented by DFT studies on the effect of Mo on the electronic structure of Ni and on key HDO steps.
    - *Role in storyline:* Bridges depolymerization and final fuel upgrading by optimizing the selective removal of oxygen while preserving carbon efficiency, and clarifies how Mo promotion tunes Ni sites for improved HDO performance.
4. Upgrade light-phase bio-oil components via C–C coupling to transform them into longer-chain, higher-value products (Section 4.5).
    - *Approach:* Experimental evaluation of Ru/β-zeolite catalysts for C–C coupling of *oxygenated* and partially deoxygenated species present in the light phase of technical bio-oil.
    - *Role in storyline:* Demonstrates how molecular-level insight can be leveraged to design catalytic systems that not only stabilize but also molecular-weight–upgrade components of the light phase of technical bio-oil into fuel-range products.

Methodological approaches and analytical framework

Across these objectives, the thesis employs a unified experimental–computational framework:

1. Experimental catalytic evaluations of Ru-, Ni-, Mo–Ni-, and Ru/β-zeolite-based catalysts under conditions relevant to bio-oil upgrading, including activity, selectivity, and stability assessments.

2. DFT modeling of adsorption, activation barriers, and reaction pathways for key elementary steps (β-O-4 cleavage and deoxygenation) on the corresponding catalytic surfaces, to rationalize observed trends and predict active motifs.
3. Comprehensive catalyst characterization to correlate metal–support interactions, promoter effects, and active-site structure with catalytic performance.

Within this scope, the subsequent chapters address the following specific questions:

Section 4.2: How do metal–support interactions in Ru/Nb_2O_5 systems influence β-O-4 bond cleavage and HDO selectivity of oligomeric feeds? (*Experiment + DFT*)

Section 4.3: How are β-O-4 lignin model compounds hydrogenolyzed over Ni/Al_2O_3, and which Ni surface features control C–O bond activation? (*Experiment + DFT*)

Section 4.4: How does Mo promotion modify Ni/Al_2O_3 for guaiacol HDO in terms of electronic structure and active-site functionality, and how does this translate into improved activity/selectivity? (*Experiment + DFT*)

Section 4.5: How can Ru/β-zeolite catalysts be designed to promote C–C coupling and molecular-weight growth of components of the light phase of technical bio-oil, thereby enhancing product stability and fuel value? (*Experiment*)

Together, these chapters establish a consistent mechanistic and catalytic picture that spans from β-O-4 depolymerization to monomer HDO and finally C–C coupling–driven upgrading, providing a coherent guideline for the rational design of catalysts for bio-oil valorization.

Chapter 2 Literature Review

2.1 Bio-oil upgrading

2.2.1 Background and significance of bio-oil

Among various biomass conversion technologies, fast pyrolysis has gained prominence for biomass liquefaction due to its high bio-oil yield (60–75 wt% for dry wood).[16–19] Typically conducted at temperatures of 450–550 °C and very short gas residence times (less than 2 seconds), fast pyrolysis transforms biomass into vapours, liquid bio-oil and solid products. This efficient liquefaction process notably reduces the volume of biomass, facilitating storage and transportation, while retaining most of its inherent energy content.

Compared with conventional petroleum-based fuels, bio-oil exhibits markedly different physicochemical characteristics. It has a high oxygen content (35–50 wt%), existing primarily in the form of carbonyl, hydroxyl, and carboxyl groups.[20–23] Furthermore, bio-oil contains a significant amount of water (15–30 wt%), with some portion present as chemically bound water.[24–26] Physically, bio-oil's density (1.1–1.3 g/cm³) is relatively high.[27,28] Due to its elevated oxygen content, its heating value (16–19 MJ/kg) is only 40–50% that of petroleum.[29–32] More importantly, bio-oil is strongly acidic (pH 2–3), which imposes challenges on its storage and application.[33–35]

In addition, oxygen-containing functional groups in bio-oil readily undergo condensation reactions, causing an increase in viscosity and a shift toward higher molecular weight species during storage. These changes are exacerbated by acid-catalyzed esterification and etherification, free-radical-initiated polymerization, and acetalization of aldehydes and ketones, further compromising bio-oil's stability.[26,36–40]

Despite these limitations, bio-oil holds tremendous application potential. In the energy sector, it it used today in boilers and kilns as heating oil substitute. Research on high technical readiness level is dedicated to co-process bio-oils in oil refineries. Also, they may be upgraded into drop-in transportation fuels blended to fossil fuels. From a chemical industry standpoint, bio-oil components can serve as a feedstock for resins, plasticizers, furans, and other platform chemicals. Environmentally, its utilization aids in lowering greenhouse gas emissions, reducing dependence on fossil fuels, and contributing to carbon neutrality objectives.

While nearly all commercial processes use wood as the primary feedstock, our research is dedicated to exploiting other types of lignocellulosic biomass, preferably agricultural and forestry residues.Their prudent exploitation not only generates economic benefits but also lessens environmental pollution associated with conventional disposal methods

(e.g., open-air burning). This synergy of economic and environmental advantages endows bio-oil technology with a unique edge in tackling climate change and advancing energy transition.

In conclusion, in-depth studies of bio-oil production and conversion technologies are of considerable practical value. Such efforts not only expand the avenues for renewable energy utilization but also promote the biomass energy industry's development and the optimization of the overall energy structure, thereby bolstering carbon neutrality and sustainable growth.

2.2.2 Existing bio-oil upgrading techniques

To address the challenges posed by high oxygen content, pronounced acidity, low stability, and limited heating value, a variety of upgrading methods to enhance its quality is researched.[41–48] The choice of upgrading technique depends on the intended application; in this work the focus is fuels production, for which deoxygenation-oriented catalytic routes are prioritized. In general, upgrading techniques can be categorized into physical, chemical, and catalytic upgrading.

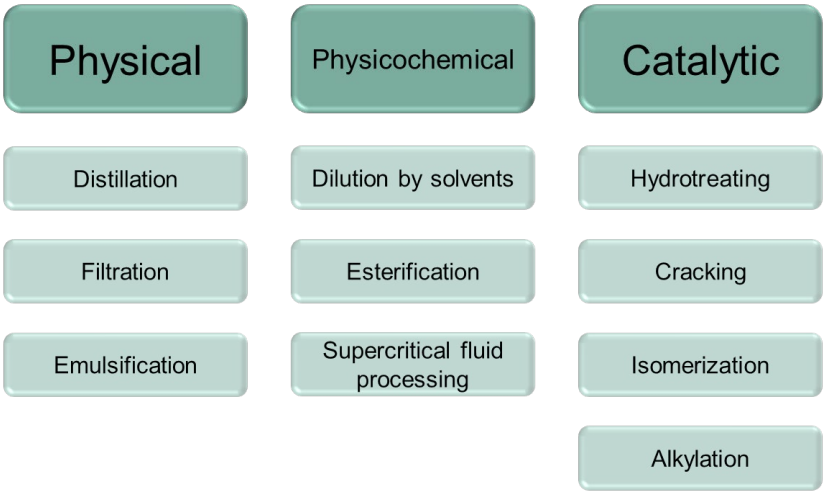

Figure 1-1: Classification of bio-oil upgrading techniques

Physical upgrading primarily focuses on improving physical properties to facilitate its application performance, eg. by distilling different fractions or reducing viscosity through emulsification. Chemical upgrading modifies the structure of oxygen-containing compounds in bio-oil via specific reactions, such as esterification to reduce acidity. Catalytic upgrading, which remains the most extensively studied approach, mainly encompasses catalytic cracking and catalytic hydrogenation. These methods selectively target the oxygen-containing functional groups within bio-oil, thereby significantly improving its overall properties. Moreover, emerging techniques such as

supercritical fluid treatment and electrochemical hydrogenation have recently garnered increasing attention.

Each of these upgrading methods differs considerably in terms of treatment conditions, process efforts and costs. Selecting an appropriate upgrading technology requires comprehensive consideration of the bio-oil's characteristics, the desired product specifications related to its specific application, and the economical feasibility of the process. In recent years, the integrated application of multiple upgrading methods has become a key research direction, aiming to further enhance bio-oil quality efficiency through the development of integrated process schemes.[49–51]

2.2.2.1 Distillation

Distillation is a physical upgrading technique that leverages the boiling point differences of bio-oil components for separation.[52–55] By controlling temperature and pressure during distillation, bio-oil can be fractionated into light, medium, and heavy cuts. The light fraction primarily consists of low-boiling-point compounds such as methanol and acetic acid (below 100 °C).[55,56] The medium fraction, which generally boils between 100–250 °C, includes aldehydes, ketones, and sugars. The non-volatile heavy fraction, meanwhile, comprises higher-molecular-weight oligomers and lignin-derived degradation products.

Owing to the large number of oxygen-containing functional groups in bio-oil, strong intermolecular interactions frequently hamper ideal separations. More critically, by the reactive carbonyl components, bio-oil exhibits marked thermal instability upon heating, triggering polymerization and condensation reactions that increase molecular weight and, in severe cases, cause coking that fouls and blocks distillation equipment. Advanced distillation approaches have been developed to mitigate these challenges. For instance, vacuum distillation lowers the system pressure to reduce the boiling points of components, allowing separation at lower temperatures and thereby suppressing thermal polymerization.[57–59] Molecular distillation exploits variations in mean free path to achieve separation under mild conditions with relatively high efficiency.[60–63] Reactive distillation couples chemical reactions with the distillation process, enabling partial conversion of selected compounds in situ and enhancing overall product quality.[64–67]

In bio-oil upgrading, distillation is primarily used as a pretreatment step to remove moisture, low-boiling organic acids, and improve stability. It can also be integrated with other upgrading technologies, such as catalytic hydrogenation, by first separating distinct fractions and then performing targeted conversions, thereby enhancing overall upgrading efficiency. Nevertheless, due to thermal instability and chemical complexity of bio-oil, distillation alone is insufficient for producing fuel-grade products; it generally must be combined with other upgrading methods.

2.2.2.2 Emulsification

Emulsification refers to creating a stable multiphase-system in which droplets of one immiscible liquid are uniformly dispersed in another continuous phase under the action of emulsifiers.[68–71] The underlying principle relies on the addition of surfactants adsorbing onto the interface, thus reducing interfacial tension and forming an interfacial film of sufficient strength to prevent droplet from coalescence. In the context of bio-oil, emulsification primarily aims to lower viscosity, improve fluidity, reduce coking tendencies, and enhance compatibility with conventional fuels.

Common emulsification methods for bio-oil include mechanical approaches (e.g., high-shear mixing or high-pressure homogenization), ultrasonic emulsification, microfluidic emulsification, and the use of chemical emulsifiers.[72–78] Nonionic surfactants such as sorbitan esters (Span series) and polyoxyethylene fatty acid esters (Tween series) are frequently preferred for their good compatibility and low-temperature stability.[79–81] Ionic surfactants like sodium dodecyl sulfate (SDS) or cetyltrimethylammonium bromide (CTAB) offer strong emulsifying capacity but may lose stability under high-electrolyte conditions.[82,83] Amphoteric surfactants, including lecithin and betaine derivatives, provide excellent pH tolerance and biocompatibility.[84,85]

Although emulsification can significantly enhance short-term performance, maintaining long-term stability remains a challenge. Ostwald ripening causes smaller droplets to merge into larger ones, increasing droplet size and decreasing overall stability.[86,87] Organic acids present in bio-oil may catalyze the hydrolysis of emulsifiers, weakening their stabilizing effect. The aqueous phase of emulsified bio-oil also offers a potential growth medium for microorganisms, potentially leading to product spoilage. In addition, reactive components within bio-oil may undergo polymerization, oxidation, or other reactions that alter emulsion characteristics. Proposed solutions include adding antioxidants and biocides or optimizing surfactant formulations, but further research is needed to ensure the long-term stability of emulsified bio-oil. When integrated with other upgrading techniques, emulsification shows promise as a key step in the bioenergy value chain, fostering cleaner and more efficient biofuel production.

2.2.2.3 Esterification

Esterification is a mild bio-oil upgrading method that primarily converts carboxylic acids into esters.[88–92] It‘s commonly employed as a pretreatment step to reduce the acid value, thereby creating favorable conditions for subsequent deep upgrading. This approach not only reduces the corrosiveness of bio-oil but also enhances its stability and increases heating value. The esterification process consists of two main pathways: direct esterification and transesterification. Direct esterification involves the reaction of carboxylic acids with alcohols to form esters and water, while transesterification entails

the exchange of alkoxy groups between an existing ester and an alcohol to produce new ester compounds.

Several key factors influence the reaction process. First, the molar ratio of alcohol to acid plays a crucial role as an excess of alcohol drives the equilibrium toward ester formation but also increases separation costs.[89,93] Second, the presence of water in the reaction system can hinder equilibrium conversion, necessitating the use of molecular sieves or other water-removal strategies.[94,95]

The advantages of esterification technology are its mild reaction conditions, simple process, and relatively low cost. Unlike other upgrading methods, esterification does not require high-temperature and high-pressure equipment, leading to lower energy consumption, and its catalysts are generally inexpensive. However, it is limited to targeting only acidic components in bio-oil, leaving other oxygenated compounds such as aldehydes and ketones unaffected. Moreover, the water generated during the reaction can suppress conversion efficiency, thereby limiting the overall yield. Additionally, the properties of esterification products still differ significantly from conventional fuels, often necessitating further integration with other upgrading techniques.

2.2.2.4 Supercritical fluid processing

Supercritical fluid processing leverages the distinct physicochemical properties of fluids in their supercritical state to upgrade bio-oil.[10,96–100] Under supercritical conditions, fluids exhibit densities and solvent capabilities similar to those of liquids, alongside diffusion coefficients and viscosities approaching those of gases—an ideal combination for reaction media. Common supercritical fluids include methanol, ethanol, and carbon dioxide, each displaying unique solvent characteristics and reactivity under various temperature and pressure regimes.

The operating conditions for supercritical fluid processing can be demanding. For example, CO_2, with a critical point of 31.1 °C and 7.39 MPa, can act as both a reaction medium and a reactant under these extreme conditions.[101] Bio-oil conversion in supercritical fluids generally involves multiple stages. First, selective dissolution, aided by the fluid's adjustable solvating power. Next, chemical reactions, such as hydrolysis in supercritical water, break down large molecules into smaller compounds while partially converting oxygen-containing functional groups. Finally, various thermochemical processes, including dehydration, decarboxylation, and rearrangements, occur under supercritical conditions.

Supercritical fluid processing offers notable, possible advantages. Its exceptional mass transfer properties can significantly enhance reaction rates, and the fluid's solvating power can be finely adjusted through temperature and pressure control to achieve selective separation. Moreover, this technique integrates reaction and separation steps, simplifying the overall process. From an environmental perspective, using water or CO_2

as the reaction medium avoids organic solvents, making the method more eco-friendly. However, there are also critical challenges. The need for high temperature and pressure equipment increases capital expenditures, and the rigorous reaction conditions lead to elevated energy consumption, affecting economic feasibility. Furthermore, challenges related to heat and mass transfer, as well as maintaining stable, continuous operation, intensify during scale-up. Managing phase behavior when processing high-moisture bio-oil presents another key hurdle that necessitates further investigation.

2.2.2.5 Catalytic Cracking

Catalytic cracking is a key bio-oil upgrading strategy that harnesses the acidic sites of catalysts to facilitate the cleavage and rearrangement of large molecular compounds.[44,102–105] Typically carried out at reaction temperatures of 400–600 °C, this process strikes a balance between achieving sufficient conversion while avoiding excessive cracking.[43,106,107] Taking a zeolite catalyst, like e.g. HZSM-5, its distinctive pore structure and moderate acidity have shown excellent performance in bio-oil catalytic cracking.[108] The microporous channels provide shape-selectivity conducive to forming specific hydrocarbon products, whereas its acidic sites effectively catalyze C–C and C–O bond cleavage.

Despite its promise, catalytic cracking faces several significant challenges. Rapid catalyst deactivation is a primary concern: oxygen-containing compounds in bio-oil tend to form coke deposits that block pores and diminish catalytic activity. In addition, the inherent water content can compromise the hydrothermal stability of the catalyst, accelerating structural collapse. Another critical issue lies in fine-tuning product distribution and boosting selectivity toward target compounds.

To address these challenges, the development of novel catalysts has become a research focal point, as summarized in Table 1-1. Strategies such as adjusting the distribution of acidic sites, introducing specific metal components, and optimizing pore architecture can enhance both catalytic stability and selectivity.[108,109] In parallel, process innovations—ranging from advanced reactor designs and improved regeneration protocols to multistage conversion schemes—offer new avenues for enhancing catalytic cracking efficiency.[110,111] Furthermore, integrating catalytic cracking with other upgrading techniques, for instance, by conducting a preliminary hydrogenation step before catalytic cracking, has demonstrated promising potential for further improving overall product quality.[44,112]

Table 1-1: Catalysts and reaction conditions for catalytic cracking

Catalyst	Feesdstock	Temperature (°C)	Retention time (min)	Reference
HZSM-5	bio-oil model compounds	500	90	[113]
Silica-alumina catalyst	Palm bio-oil	500		[114]
Ni–Co/HZSM-5	bio-oil model compounds	400	30	[115]
HZSM-5	Pine sawdust bio-oil	500-650	-	[115]
Ni/HZSM-5	Pine sawdust bio-oil	400-500	-	[116]
Commerical Ni/zeolite	Pine sawdust bio-oil	550	60	[117]
Y zeolite	Pine sawdust bio-oil	550	7	[118]
Pd/SiO2	bio-oil model compounds	400	-	[119]
bentonite clay	Almond shell bio-oil	400	-	[120]

2.2 Bio-oil hydrodeoxygenation (HDO)

2.2.1 Background and significance of HDO

Catalytic HDO is a selective process carried out under a hydrogen atmosphere to remove hetero-containing functional groups, specifically those with oxygen, from bio-oil.[13,14,44,121–124] During HDO, the C–O bonds in bio-oil molecules are activated on the catalyst surface, then cleaved in the presence of hydrogen, subsequently forming C–H bonds and yielding hydrocarbons along with water. From a mechanistic standpoint, HDO encompasses multiple pathways based on the types of oxygen-containing groups involved.[13,44,121] For instance, carbonyl (C=O) groups can be hydrogenated to alcohol intermediates, which then undergo dehydration to form hydrocarbons; hydroxyl (–OH)

groups can be directly hydrogenated and dehydrated; and ether bonds (C–O–C) can be hydrogenolyzed to smaller alcohols and hydrocarbons.

The key to HDO lies in the bifunctional nature of the catalyst, which must both activate hydrogen and promote C–O bond scission. Typically, the metal phase (e.g., Ni, Co) provides the hydrogenation capacity, whereas acidic sites on the catalyst support facilitate C–O bond cleavage and dehydration reactions.[13,121,122,125–128] Through this synergistic mechanism, HDO can achieve efficient conversion under relatively moderate conditions (commonly 200–400 °C and 2–10 MPa).

HDO is often central among bio-oil upgrading techniques due to its distinctive operational features and superior product quality. Compared to catalytic cracking, HDO removes oxygen while preserving the carbon backbone, thereby enhancing carbon utilization efficiency and yielding a more concentrated product distribution. In contrast, when fuels are the target products, catalytic cracking may generate a larger fraction of small-molecule byproducts, lowering the yield of desirable hydrocarbons.

Compared with milder chemical methods, such as esterification, HDO offers a more comprehensive upgrading effect. Esterification only addresses carboxylic acids and does not target other oxygenated compounds like aldehydes, ketones, and phenolics. By contrast, HDO can simultaneously convert a broad spectrum of oxygen-containing functional groups, significantly reducing the overall oxygen content. Moreover, HDO products exhibit chemical properties more akin to traditional hydrocarbon fuels, thus providing enhanced utility.

When set against supercritical-fluid routes, HDO operates in a different severity regime: it uses elevated H_2 pressures and moderate temperatures in contact with solid catalysts, allowing product selectivity to be tuned via catalyst formulation and reaction parameters. Supercritical-fluid processing, by contrast, relies on maintaining the solvent at or above its critical point, leveraging high solvation and mass-transfer effects. The choice between them is application- and feedstock-dependent.

In terms of energy input and final product quality, HDO also surpasses methods like electrochemical hydrogenation and emulsification.[51,129,130] While electrochemical hydrogenation can proceed under mild conditions, it often suffers from limited energy efficiency and scalability. Emulsification, though simple, does not fundamentally alter bio-oil's chemical composition, limiting the stability and applicability of the products. By contrast, HDO thoroughly transforms the molecular structure of bio-oil, yielding products with superior stability and broader potential applications.

Bio-oil HDO entails a complex reaction network and multiphase catalytic mechanisms, offering valuable insights into selective C–O bond activation and cleavage.[131–133] In particular, investigations into how various oxygenated functional groups compete for adsorption and conversion on the catalyst surface, along with the evolution of surface species in a multicomponent system, are of central importance in catalysis research. A

deeper understanding of these fundamental phenomena not only advances HDO technology but also provides theoretical guidance for other selective catalytic processes.

HDO serves as a crucial method for producing high-grade bio-oil. By substantially improving the physicochemical properties of bio-oil, HDO moves the material toward fuel-range specifications, but the resulting oils typically require further refining. This transformation broadens the scope of bio-based energy applications and offers effective solutions to longstanding challenges such as low stability and low calorific value.

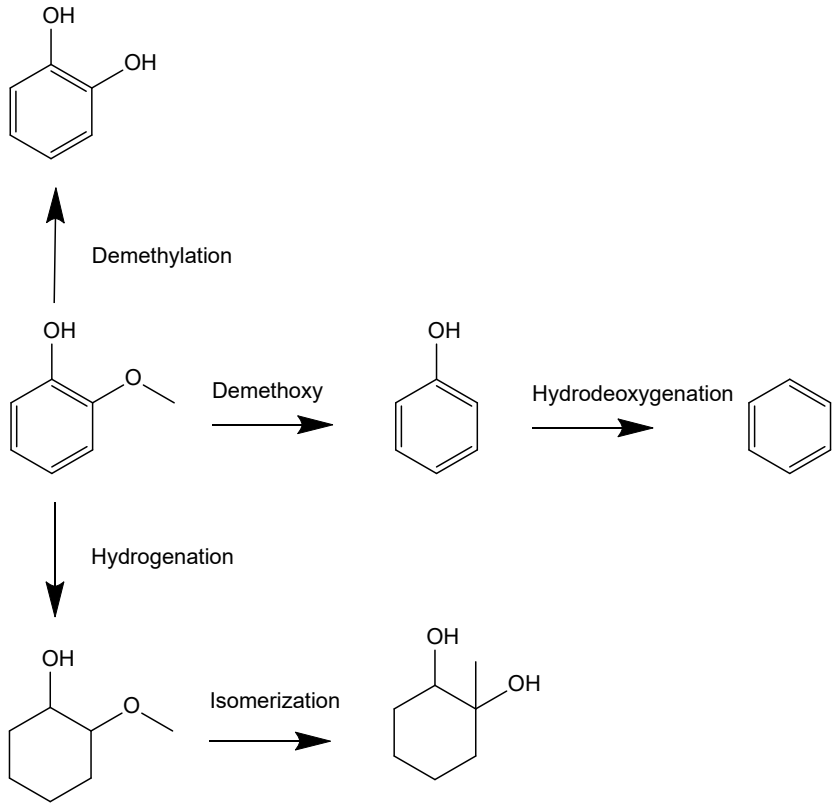

Figure 1-2: Related reactions during the HDO upgrade process, taking guaiacol as an example

Industrial development also stands to benefit significantly from advancements in HDO technology. Beyond producing transportation fuels, HDO can selectively generate valuable chemical feedstocks, such as cyclohexanol, 2-methylfuran, and valerolactone thus opening up new opportunities for the bio-based fine chemicals sector.[134,135] The resulting diversification of conversion pathways enhances the economic viability and market competitiveness of bioenergy. Under the broader context of carbon neutrality, the advancement of highly efficient biomass conversion technologies like HDO holds critical value for realizing the green transformation of industrial production.

2.2.2 Current Status of HDO Technology

Catalysts play a decisive role in HDO, as their performance directly affects reaction activity, selectivity, and stability. Because HDO catalysts must enable both hydrogenation and C–O bond activation, ongoing research encompasses a variety of catalyst systems, including noble metal catalysts, traditional sulfide catalysts, transition-metal catalysts, and newly developed composite catalysts.[13,46,121] Noble metals such as Pt, Pd, and Ru have been extensively investigated for their superior hydrogenation capabilities and high intrinsic activity, achieving efficient conversion under relatively mild conditions.[136–138] These catalysts are effective in removing oxygen from diverse functional groups and exhibit strong resistance to coking. However, their industrial use is constrained by high costs, prompting efforts to reduce precious metal loading, such as alloy formation, to enhance metal utilization efficiency.

Sulfided catalysts (for example, CoMoS and NiMoS) originally developed for hydrodesulfurization in petroleum refining also show promise for C–O bond activation.[139–143] They benefit from mature preparation methods and relatively low cost. However, maintaining their active sulfided phase requires continuous sulfur addition, which introduces sulfur species into liquid product.[144] In addition, the high oxygen content in bio-oil can adversely affect their stability.

Transition metals such as Ni, Co, and Fe have garnered significant attention because of their favorable cost-to-performance ratio.[145–147] Although their intrinsic activity is generally lower than that of noble metals, appropriate modifications can yield substantial catalytic performance. For instance, Ni-based catalysts supported on materials such as zeolites or oxides can develop strong bifunctional properties, providing both hydrogenation and C–O bond cleavage capabilities.[148,149]

New composite catalysts have emerged as a research focal point. Bimetallic or multi-metallic formulations can deliver synergistic improvements in catalytic activity, stability, and selectivity.[146,150–152] For example, introducing small amounts of noble metals into transition-metal catalysts can markedly enhance performance while limiting cost.[126] Meanwhile, tailoring metal–metal interactions refines electronic structures and boosts selectivity.[153] Innovations in support materials, such as hierarchically porous solids and two-dimensional materials, provide promising routes to achieving higher catalytic efficiency.

Support choice is also critical for HDO catalysts. Traditional oxide supports like Al_2O_3, SiO_2, and ZrO_2 are widely used for their stability and high specific surface area, but they can lose activity under hydrothermal conditions.[123,146,148,154] Consequently, research has turned to water-resistant supports, such as carbon materials and phosphides.[14,122,142,155] In addition, optimizing the acidity and pore structure of the support is essential for maximizing mass transfer and catalytic performance.

Optimizing HDO process conditions is vital to achieving efficient bio-oil conversion. Reaction temperature, hydrogen pressure, liquid hourly space velocity (LHSV), and the hydrogen-to-bio-oil ratio must be balanced to ensure both technical and economic viability.[13,156,157] Typically ranging from 200 to 400 °C, the reaction temperature affects reaction rates, product distribution, and catalyst stability. Higher temperatures risk thermal cracking and coking, while lower temperatures hamper conversion. Hydrogen pressure, generally set at 2–10 MPa, influences hydrogen solubility and reactive hydrogen species. Higher pressure extends catalyst life but raises equipment and operational costs. LHSV, usually 0.5–2.0 h^{-1}, reconciles conversion efficiency with catalyst throughput. Heavier feed components may require lower LHSV for sufficient residence time. Typically, stabilization achieves partial deoxygenation (e.g., O/C dropping from 0.8 to 0.4), and two-step hydrotreating yields upgraded oils with about 8–16 wt% oxygen, lower values are reported under more severe conditions.[158–160]

Reactor design and operation also play a pivotal role. Fixed-bed reactors are popular for simplicity, but highly viscous or solids-laden feeds may necessitate slurry-bed or moving-bed setups.[13,161,162] Temperature control, gas–liquid mass transfer, and pressure drop across the catalyst bed all require careful engineering. During HDO scale-up, supporting processes such as feedstock pretreatment, product separation, and hydrogen recycling must also be considered. Feedstock pretreatment can remove solids and moisture, reducing catalyst fouling. Product separation techniques like distillation or extraction should be tailored to product properties, and hydrogen recycling balances fresh hydrogen requirements with the purity of recycled gas.

In recent years, HDO has made significant strides, expanding from laboratory research to pilot and demonstration plants.[163–165] Researchers have conducted in-depth studies of model compounds by combining in situ characterization with theoretical calculations, clarifying how typical oxygenated compounds—phenolics, aldehydes, and ketones—transform on various catalyst surfaces. These findings offer theoretical guidance for catalyst design.

Several new catalyst systems have emerged. Bimetallic catalysts such as PtNi and RuCo exhibit synergistic effects that reduce reliance on precious metals while maintaining high activity.[166,167] Support materials like silicon carbide have enhanced hydrothermal stability, enabling catalysts to operate continuously and stably.[168] Process innovations, including multi-stage HDO combining selective pre-hydrogenation with subsequent deep HDO, address coking issues when bio-oil is upgraded directly.

Coupling HDO with catalytic cracking or performing sequential fractionation and HDO steps has further broadened its application scope. Multiple pilot plants now showcase stable bio-oil conversion to near-commercial fuel standards through optimized catalyst systems and process parameters, although catalyst longevity, energy consumption, and corrosion remain ongoing challenges.[169,170] Beyond fuel production, precisely tuned HDO conditions can selectively retain certain functional groups for high-value bio-

based chemicals, offering a broader range of possibilities for biomass utilization and underscoring the versatility and economic potential of HDO technology.

2.2.3 Challenges in HDO process

From a mechanistic standpoint, several critical scientific questions remain unresolved in HDO. First among these is the impact of molecular interactions in a highly complex system. Bio-oil contains hundreds of oxygenated compounds with varying functional groups, which compete for adsorption and undergo transformation on the catalyst surface in ways far more intricate than single-model compounds.[13] In particular, high concentrations of oxygenated species can lead to hydrogen bonding, acid–base interactions, and steric effects that complicate reaction pathways, making it difficult to establish a thorough understanding of the underlying mechanisms.

Selective control also poses a significant challenge. Disparities in reactivity among different oxygen-bearing functional groups can lead to uneven conversion. For example, aldehydes and ketones are easily hydrogenated, while phenolic compounds often prove more resistant to selective activation.[121,171–174] Achieving high selectivity for target products requires catalyst designs that modulate the relative rates of various pathways, a goal that remains elusive. Moreover, controlling the selective cleavage of C–O bonds over C–C bonds is crucial, demanding catalysts with specialized active sites.

Elucidating structure–activity relationships is equally difficult. Although researchers have developed numerous high-performance catalysts, understanding the intrinsic nature of the active sites remains limited.[175–178] This gap is particularly acute in bifunctional catalysis, where the synergy between metal and acid sites—and the role of supports—remains incompletely understood. Without deeper insight into these cooperative effects, the rational design of superior catalysts remains constrained.

Reaction kinetics and mass transfer effects further complicate the HDO process.[179–181] In multiphase HDO, gas–liquid–solid mass transfer can significantly influence reaction rates. The complexity of bio-oil composition makes it challenging to construct accurate kinetic models. Once heat effects and transport limitations are factored in, the system's mathematical description becomes exceedingly complex. Additionally, the influence of reaction conditions on phase behavior must be investigated more thoroughly.

Finally, tracking the formation and transformation of intermediate species and mapping the full reaction network are formidable tasks. Capturing transient intermediates with in situ characterization is vital to understanding the reaction mechanism; however, current analytical methods still struggle to achieve the requisite temporal and spatial resolution for fast reactions.[137,182–184] Moreover, constructing a comprehensive reaction network that predicts the relative contributions of competing pathways demands new modeling approaches.

2.3 Application of Density Functional Theory (DFT) in HDO research

2.3.1 Fundamental principles of DFT methods

Density Functional Theory (DFT) has emerged as a transformative computational framework in the landscape of quantum mechanical methodologies, offering unprecedented capabilities for investigating electronic structures and reaction mechanisms in catalytic processes.[185–188] The theoretical foundations of DFT are based on groundbreaking Hohenberg-Kohn theorems and the Kohn-Sham equations formulated in the 1960s, which revolutionized computational approaches by establishing that the ground-state electron density, rather than the prohibitively complex many-electron wavefunction, contains all information necessary to determine a system's properties.[189–191]

The epistemological core of DFT rests on a profound conceptual shift: the reformulation of the many-electron problem into a single-electron framework through the introduction of exchange-correlation functionals to account for electron-electron interactions.[192,193] The Hohenberg-Kohn theorems established a one-to-one correspondence between ground-state electron density and ground-state electronic energy, while the Kohn-Sham equations provided a practical computational framework for implementation. This theoretical reconceptualization offers computational advantages, the scaling of computational complexity shifts from exponential with respect to electron number to approximately linear, rendering simulations of complex catalytic systems tractable.

In the domain of catalysis research, the methodological evolution of DFT has traversed a trajectory from early Local Density Approximation (LDA) formulations to Generalized Gradient Approximation (GGA), and subsequently to hybrid and meta-hybrid functionals.[194–196] This progression reflects the increasingly nuanced treatment of electronic correlation effects, establishing progressively more sophisticated frameworks for accurately modeling the electronic structures of catalyst surfaces and the intricate reaction processes occurring thereon.

The selection of appropriate exchange-correlation functionals is paramount for ensuring computational accuracy in catalysis research. The current methodological landscape encompasses several widely employed functionals:

PBE (Perdew-Burke-Ernzerhof) Functional: Representative of the GGA class, PBE exhibits balanced performance in modeling adsorption and catalytic processes on metal surfaces, providing reasonably accurate descriptions of chemical bond formation and cleavage.[197] However, in its standard form without an explicit van der Waals correction,

it systematically underestimates long-range dispersion interactions, which may lead to weaker binding energies for physisorbed or otherwise weakly bound species.

B3LYP Functional: As one of the earliest widely applied hybrid functionals, B3LYP demonstrates excellent performance for organic molecular systems but exhibits systematic deviations in metallic systems.[198,199]

M06 Series Functionals: Particularly the M06-L and M06-2X variants, these functionals employ parameterization approaches to enhance descriptions of dispersion forces and non-covalent interactions, offering advantages in modeling interactions between oxygen-containing organic molecules and catalyst surfaces.[200] However, their strong empirical parametrization and, in the case of M06-2X, the large fraction of exact exchange can reduce their transferability for extended metallic surfaces and make them more computationally demanding than standard GGA functionals.

PBE-D (PBE with dispersion correction) Method: By incorporating dispersion force corrections into the PBE functional, this approach effectively improves the description of adsorption systems and finds widespread application in reaction mechanism research.[201,202]

BEEF-vdW (Bayesian Error Estimation Functional with van der Waals correction) Functional: This emerging class of functionals not only incorporates dispersion force corrections but also provides uncertainty estimates for computational results, offering particular value for reliability assessments of catalytic reaction barriers.[203]

In practical research scenarios, functional selection necessitates judicious consideration based on specific research subjects and computational objectives. For calculations involving metal catalyst surfaces in HDO reactions, PBE+D3(4) and BEEF-vdW functionals are preferentially selected due to their superior descriptive capabilities for transition metal systems.

2.3.2 Current applications of DFT in HDO reaction mechanism research

DFT calculations have played a pivotal role in elucidating the electronic and geometric structural characteristics of HDO catalyst active sites. For active metals (such as Pt, Pd, Ni, etc.), DFT calculations have revealed correlations between d-band center positions and C-O bond activation capabilities, clarifying the intrinsic activity differences among various metals in HDO reactions.[204,205] For support materials (such as MoO_3, TiO_2, etc.), DFT calculations have identified oxygen vacancies as key active centers and quantified the structure-activity relationships between oxygen vacancy formation energies and catalytic activities.[206,207]

Recent DFT research has further expanded to bifunctional catalysts and interfacial catalysis, particularly the synergistic effects at metal-support interfaces.[208,209] Through precise modeling of metal-oxide interfaces, DFT calculations have unveiled synergistic mechanisms between Lewis acidic sites and metal sites, wherein Lewis acidic sites are responsible for polarization activation of carbonyl groups while metal sites provide dissociated hydrogen for hydrogenation reactions. This cooperative action significantly reduces activation barriers for HDO reactions, enhancing catalytic efficiency.

Notably, DFT calculations on bimetallic catalysts (such as NiFe, PtSn, etc.) have revealed how electron transfer between components modulates surface adsorption energies and activation barriers, providing theoretical guidance for designing highly selective HDO catalysts.[210–213] This multi-component analysis represents a significant advance beyond traditional single-site models, acknowledging the complex interplay of electronic and geometric factors in real catalytic systems.

Bio-oil comprises complex components including various oxygen-containing functional groups (such as alcohols, aldehydes, ketones, acids, esters, ethers, etc.). DFT calculations employing model molecules have elucidated the adsorption configurations, adsorption energies, and electronic transfer characteristics of different functional groups on catalyst surfaces.[214–216] DFT-based adsorption studies not only quantitatively describe adsorption energies but also reveal electronic redistribution characteristics during adsorption through charge analysis and density of states calculations, providing microscopic level explanations for catalytic activation mechanisms.[217,218] The integration of energetic and electronic analyses represents a methodological advancement that bridges thermodynamic and electronic structure theories, offering more comprehensive insights than either approach alone.

HDO processes typically involve multiple possible reaction pathways. DFT calculations of activation barriers and reaction energies for different elementary reactions have determined kinetically and thermodynamically favorable pathways.[219,220] For typical ketone compounds in bio-oil, DFT calculations have compared activation barriers between direct deoxygenation (DDO) and hydrogenation-dehydration (HYD) pathways. Results indicate that on most metal catalysts, the HYD pathway (C=O hydrogenation to form alcohols followed by C-OH dehydration) generally has lower activation barriers than the DDO pathway (direct C=O bond cleavage), explaining reaction selectivity observed in experiments. Further transition state analysis reveals that the electrophilic properties of hydrogen atoms in C=O hydrogenation transition states negatively correlate with reaction barriers, providing a theoretical basis for modulating catalyst performance.

Based on DFT calculations, researchers have developed various theoretical descriptors to predict HDO activities and selectivities of catalysts, establishing quantitative correlations between computational results and catalytic performance.[208,221] Among these, d-band center theory has been widely applied to predict activities of metal catalysts. DFT calculations demonstrate that the relationship between the d-band center

position of metals and C-O bond activation barriers exhibits a volcano-type relationship, explaining activity differences among various transition metals in HDO reactions and guiding the design of bimetallic catalysts. Another important descriptor is the adsorption energy scaling relationship; DFT calculations have discovered linear relationships between adsorption energies of different oxygen-containing intermediates, which can be used to construct microkinetic models to predict catalyst performance under actual reaction conditions. For metal oxide catalysts, oxygen vacancy formation energy has been identified as a key theoretical descriptor.[207,222] DFT calculations have established correlations between oxygen vacancy formation energies and C-O bond activation barriers, providing theoretical foundations for designing new reducible oxide catalysts. In the development of theoretical prediction methods, researchers have also recognized the limitations of single descriptors and begun transitioning to multi-descriptor combination models.[217,223] For bimetallic catalysts, factors such as surface undercoordination and alloy formation energy are considered alongside d-band centers, constructing more comprehensive structure-activity relationship models. This multidimensional theoretical analysis framework better reflects the complexity of HDO catalytic systems, improving the accuracy and guidance of predictions.

It is worth emphasizing that DFT-based theoretical predictions increasingly focus on selectivity issues beyond catalytic activity. By comparing barrier differences between different reaction pathways, researchers have established correlations between catalyst electronic structures and product distributions, providing theoretical foundations for designing highly selective HDO catalysts. This shift in research focus from activity to selectivity reflects the trend in HDO catalysis research from pursuing high conversion rates toward precise control of product distributions, acknowledging the increasing importance of selectivity in practical applications.

Chapter 3 Materials and Methods

3.1 Catalyst preparation

3.1.1 Ru based catalyst

Ru/Nb_2O_5 catalyst with a nominal Ru loading of 5 wt% (based on Ru metal) was prepared by a wet impregnation method using $RuCl_3 \cdot xH_2O$ (Sigma-Aldrich, USA) as the Ru precursor and amorphous Nb_2O_5 powder (CBMM, Minas Gerais, Brazil) as the support.[224] In a typical synthesis, a calculated amount of $RuCl_3 \cdot xH_2O$ corresponding to a Ru metal loading of 5 wt% was dissolved in 100 mL of deionized water. The solution was sonicated for 30 min in an ultrasonic water bath to ensure complete dissolution and homogeneous dispersion of the Ru precursor. Subsequently, the amorphous Nb_2O_5 support was gradually added to the Ru precursor solution under continuous stirring to form a slurry. The resulting mixture was magnetically stirred at 600 rpm for 2 h at room temperature to facilitate thorough impregnation of Ru species onto the Nb_2O_5 surface. After impregnation, the solvent was removed by rotary evaporation at 40 °C with a rotation speed of 200 rpm under reduced pressure (45 mbar) until a dry solid was obtained.

The impregnated solid was further dried in an oven at 105 °C overnight to remove residual moisture. The dried sample was then calcined in static air at 350 °C for 2 h with a heating rate of 5 $°C \cdot min^{-1}$ to decompose the Ru precursor and stabilize the Ru species on the Nb_2O_5 support. After calcination, the catalyst was allowed to cool naturally to room temperature.Prior to catalytic reactions, the calcined Ru/Nb_2O_5 catalyst was reduced in a tubular furnace at 350 °C for 2 h under a flowing H_2/N_2 mixture (10 vol% H_2 in N_2, total flow rate of 100 $mL \cdot min^{-1}$). The temperature was increased at a rate of 5 $°C \cdot min^{-1}$. After reduction, the catalyst was cooled to room temperature under N_2 and subsequently used for catalytic testing.

3.1.2 Ni-Al LDH catalyst

Ni-Al LDH Catalysts:

Ni–Al layered double hydroxide (LDH) precursors were synthesized via a homogeneous precipitation method using urea as the precipitating agent.[225] In a typical

synthesis, $Ni(NO_3)_2 \cdot 6H_2O$ and $Al(NO_3)_3 \cdot 9H_2O$ were dissolved in 100 mL of deionized water together with urea, with Ni/Al molar ratios of 0.25:1, 0.5:1, 1:1, 1:2, and 1:4, respectively. The resulting solution was sonicated for 30 min in an ultrasonic water bath to ensure complete dissolution and homogeneous mixing of all components. The solution was then transferred into a three-necked flask and magnetically stirred for 3 h at room temperature to achieve uniform mixing. Subsequently, the flask was placed in an oil bath and heated to 100 °C in air, where the reaction was maintained for 12 h under continuous stirring. During this process, the slow thermal decomposition of urea generated hydroxide ions, inducing homogeneous precipitation of Ni–Al LDH.

After completion of the reaction, the suspension was cooled naturally to room temperature and washed three times with deionized water until the pH of the supernatant reached approximately 7. The precipitate was separated by centrifugation and dried in an oven at 70 °C overnight. The obtained Ni–Al LDH precursors were calcined in air at 500 °C for 3 h with a heating rate of 5 $°C \cdot min^{-1}$ to form Ni–Al layered double oxides (LDOs). Prior to catalytic reactions, the calcined samples were reduced in a tubular furnace at 500 °C for 2 h under a flowing H_2/N_2 atmosphere (10 vol% H_2 in N_2), with a heating rate of 5 $°C \cdot min^{-1}$, yielding the reduced Ni–Al LDH–derived catalysts.

Ni-Al Impregnation catalyst:

For comparison, a Ni–Al impregnation catalyst was prepared by a wet impregnation method.[225] In a typical procedure, an appropriate amount of $Ni(NO_3)_2 \cdot 6H_2O$ (corresponding to a Ni loading of 30 wt% based on Ni metal) and commercial γ-Al_2O_3 were dispersed in deionized water. The suspension was sonicated for 30 min in an ultrasonic water bath to promote homogeneous dispersion of the Ni precursor and the support. The mixture was then transferred into a single-necked flask, and the solvent was removed using a rotary evaporator until a dry solid was obtained. The impregnated sample was subsequently subjected to the same drying, calcination, and reduction procedures as those used for the Ni–Al LDH–derived catalysts, including drying, calcination in air at 500 °C for 3 h (heating rate of 5 $°C \cdot min^{-1}$), and reduction under 10 vol% H_2/N_2 at 500 °C for 2 h (heating rate of 5 $°C \cdot min^{-1}$).

Ni-Al Precipitation catalyst:

A Ni–Al precipitation catalyst was synthesized via a conventional co-precipitation method.[225] In a typical synthesis, $Ni(NO_3)_2 \cdot 6H_2O$ and commercial Al_2O_3 were dispersed in deionized water to form a suspension and sonicated for 30 min to ensure homogeneous mixing. Subsequently, a 1 M NaOH aqueous solution was added dropwise under continuous stirring until the pH of the mixture reached 10. The resulting suspension was aged under stirring at room temperature overnight to allow sufficient growth and stabilization of the precipitated species. After aging, the solid was thoroughly washed with deionized water to completely remove residual Na^+ ions,

followed by drying, calcination, and reduction using the same procedures as those applied to the Ni–Al LDH–derived catalysts.

3.1.3 Mo doped Ni-Al LDH catalyst

All reagents were obtained from Sigma Aldrich (USA). The preparation of the catalysts followed the procedure described below:[226–228] Initially, $Ni(NO_3)_2 \cdot 6H_2O$, $Al(NO_3)_3 \cdot 9H_2O$, urea, and one of the dopant precursors ($C_4H_4NNbO_9 * xH_2O$ for Nb doping, $Ce(NO_3)_3 * 6H_2O$ for Ce doping, $H_{24}Mo_7N_6O_{24} * 4H_2O$ for Mo doping, or WCl_6 for W doping) were dissolved in deionized water and sonicated for 30 minutes. The solution was then transferred into a three-necked flask and stirred with a magnetic stirrer for 3 hours to ensure uniform mixing. The mixture was subsequently heated to 100 °C in an oil bath and reacted for 12 hours. After cooling to room temperature, the solution was washed until the pH reached 7. The precipitate was separated using a centrifuge and dried overnight in an oven at 70 °C. This doped Ni-Al LDH was then calcined at 500 °C for 3 hours with a heating rate of 5 °C/min to form doped Ni-Al LDO. Finally, the doped Ni-Al LDO was reduced in a 10% H_2/N_2 atmosphere under 500 °C for 2 hours at a 5 °C/min heating rate to obtain Nb-, Ce-, Mo-, or W-doped Ni/Al_2O_3 catalysts.

All reagents were obtained from Sigma-Aldrich (USA) and used as received. The doped Ni/Al_2O_3 catalysts were synthesized via a homogeneous precipitation method using urea as the precipitating agent, following procedures reported in the literature. [226–228] In a typical synthesis, $Ni(NO_3)_2 \cdot 6H_2O$, $Al(NO_3)_3 \cdot 9H_2O$, urea, and one selected dopant precursor were dissolved in 100 mL of deionized water. The Ni/Al molar ratio was fixed at 1:2, and the dopant loading was controlled at 2 at.% relative to Ni. The dopant precursors used were $C_4H_4NNbO_9 \cdot xH_2O$ for Nb doping, $Ce(NO_3)_3 \cdot 6H_2O$ for Ce doping, $H_{24}Mo_7N_6O_{24} \cdot 4H_2O$ for Mo doping, and WCl_6 for W doping. The resulting solution was sonicated for 30 min in an ultrasonic water bath to ensure complete dissolution and homogeneous mixing of all components.

Subsequently, the solution was transferred into a three-necked flask and magnetically stirred for 3 h at room temperature to achieve uniform mixing. The flask was then placed in an oil bath and heated to 100 °C in air, where the reaction was maintained for 12 h under continuous stirring. During this process, the gradual thermal decomposition of urea generated hydroxide ions, inducing homogeneous precipitation of doped Ni–Al layered double hydroxide (LDH) precursors. After completion of the reaction, the suspension was cooled naturally to room temperature and washed three times with deionized water until the pH of the supernatant reached approximately 7. The precipitate was separated by centrifugation and dried in an oven at 70 °C overnight.

The obtained doped Ni–Al LDH precursors were calcined in static air at 500 °C for 3 h with a heating rate of 5 °C·min^{-1} to form doped Ni–Al layered double oxides (LDOs). Prior to catalytic reactions, the calcined samples were reduced in a tubular furnace at 500 °C for 2 h under a flowing H_2/N_2 atmosphere (10 vol% H_2 in N_2), with a heating rate of 5 °C·min^{-1}, yielding the reduced doped Ni/Al_2O_3 catalysts. The resulting catalysts are denoted as Ni/Al_2O_3, Nb–Ni/Al_2O_3, Ce–Ni/Al_2O_3, Mo–Ni/Al_2O_3, and W–Ni/Al_2O_3, respectively.

3.1.4 zeolite catalyst

The Ru/β-zeolite catalyst was prepared via an incipient wetness impregnation method. Prior to impregnation, the β-zeolite support (Si/Al molar ratio of 25) was dried in an oven at 70 °C for 12 h to remove physisorbed moisture and ensure accurate pore-volume impregnation. In a typical preparation, a calculated amount of ruthenium (III) chloride hydrate ($RuCl_3 \cdot xH_2O$), corresponding to a Ru loading of 2 wt% based on Ru metal, was dissolved in deionized water. The volume of the aqueous Ru precursor solution was adjusted to match the total pore volume of the dried β-zeolite support. The resulting solution was added dropwise to the β-zeolite under magnetic stirring at 600 rpm to ensure uniform distribution of the Ru precursor throughout the zeolite pore structure.

After impregnation, the mixture was aged at room temperature for 2 h to allow sufficient diffusion and anchoring of Ru species within the β-zeolite framework. The impregnated sample was subsequently dried overnight in an oven at 105 °C to remove residual solvent. The dried precursor was then calcined in air at 350 °C for 4 h with a heating rate of 2 °C·min^{-1} to decompose the Ru precursor and stabilize the Ru species on the β-zeolite. Prior to catalytic reactions, the calcined catalyst was reduced in a tubular furnace under a flowing H_2/N_2 atmosphere (10 vol% H_2 in N_2) at 350 °C for 2 h with a heating rate of 5 °C·min^{-1}. After reduction, the catalyst was cooled to room temperature under a N_2 atmosphere, yielding the reduced Ru/β-zeolite catalyst.

3.2 Characterization

X-ray diffraction (XRD) patterns of the samples were collected on a PANalytical X'Pert Pro X-ray diffractometer operating in Bragg–Brentano geometry, using Cu Kα radiation (λ = 0.154060 nm) and a Ni filter to suppress Cu Kβ radiation. Measurements were carried out at room temperature. The powdered samples were gently ground and loaded onto a flat sample holder for analysis. Diffraction patterns were recorded over a 2θ range of 5–120° at a scan rate of 1°·min^{-1}. Phase identification was performed by

comparison with standard patterns from the ICDD PDF database. No crystallite size analysis (e.g., Scherrer calculation) was performed.

Field-emission scanning electron microscopy (FE-SEM) was performed using a Gemini SEM 500 microscope (Zeiss GmbH) equipped with a Schottky field emission cathode. SEM images were acquired at an accelerating voltage of 10 kV to examine the surface morphology and microstructural features of the samples. Prior to observation, the samples were coated with a thin carbon layer to improve electrical conductivity and minimize charging effects. Dynamic light scattering (DLS) measurements were carried out using a Zetasizer Nano ZS instrument (Malvern Instruments), operating with a laser wavelength of 633 nm and employing non-invasive backscattering (NIBS) detection at a scattering angle of 173°. Before measurement, the samples were dispersed and diluted in dichloromethane. The measurements were conducted in quartz cuvettes with an optical path length of 10 mm (Hellma Analytics, Germany). DLS analysis was used to evaluate the hydrodynamic size distribution of the dispersed nanoparticles.

Transmission electron microscopy (TEM) samples were prepared at room temperature in air by drop-casting a diluted suspension of nanoparticles dispersed in ethanol onto a commercial holey ultrathin amorphous carbon film (approximately 3 nm in thickness) supported on copper grids (400 mesh, Plano 01824). After solvent evaporation, the samples were analyzed by TEM. High-resolution TEM (HRTEM), scanning transmission electron microscopy (STEM), and energy-dispersive X-ray spectroscopy (EDS) mapping were employed to investigate the morphology, crystallinity, and elemental distribution of the nanoparticles.

Raman spectra of the catalysts were recorded using a Renishaw inVia confocal Raman microscope (Renishaw) equipped with a 532 nm excitation laser. Measurements were carried out at room temperature. The catalyst powders were placed on a clean sample holder and analyzed under a confocal optical configuration. Raman spectra were collected in the range of 100–2000 cm^{-1}. The laser power and acquisition parameters were carefully adjusted to obtain an adequate signal-to-noise ratio while avoiding laser-induced heating or structural alteration of the samples.

The Ni content of the catalysts was determined by inductively coupled plasma optical emission spectroscopy (ICP-OES) using an Agilent 725 ICP-OES spectrometer (Agilent). For analysis, approximately 50 mg of catalyst sample was completely digested in aqua regia to dissolve the metal species. The resulting solutions were appropriately diluted prior to measurement. Quantitative analysis was performed based on the measured Ni concentration, and the Ni loading in the catalysts was calculated accordingly.

X-ray photoelectron spectroscopy (XPS) measurements were performed on a PHI 5000 VersaProbe II system (ULVAC-PHI Inc.) equipped with a scanning microprobe X-ray source using monochromatic Al Kα radiation (hν = 1486.7 eV). To minimize surface

oxidation and contamination, samples were prepared inside an anoxic glove box by mounting the catalyst powders onto pieces of silicon wafer. The mounted samples were transferred to the XPS instrument without air exposure using a sealed transfer vessel, enabling air-free handling from sample preparation to analysis. XPS spectra were collected under ultra-high vacuum conditions. Survey spectra and high-resolution core-level spectra were acquired for elemental identification and chemical-state analysis. Binding energies were charge-corrected by referencing the C 1s peak to 284.8 eV. Peak fitting was performed using standard background subtraction and line-shape functions to deconvolute overlapping components and quantify surface chemical states.

H_2 temperature-programmed reduction (H_2-TPR) measurements were carried out using an Altamira AMI-300 Chemisorption Analyzer (Altamira Instruments; German partner: 3P Instruments). Data acquisition and analysis were performed using the proprietary AMI-300 and AMI-Analysis software packages. For each measurement, 100 mg of catalyst sample was loaded into a quartz reactor. Prior to TPR analysis, the sample was degassed under flowing N_2 at 200 °C to remove adsorbed moisture and surface contaminants, and then cooled to 90 °C. Subsequently, the reduction profile was recorded by heating the sample from 90 °C to 650 °C at a linear heating rate of 10 °C·min^{-1} under a flowing 10 vol% H_2/Ar gas mixture. Hydrogen consumption was monitored using a thermal conductivity detector (TCD). The temperature-programmed reduction cycle was repeated five times to evaluate the evolution and stability of the reducibility behavior upon repeated thermal treatment.

The surface acidity of the catalysts was evaluated by NH_3 temperature-programmed desorption (NH_3-TPD) using the same Altamira AMI-300 Chemisorption Analyzer. For each measurement, 100 mg of catalyst was placed in a quartz reactor and pretreated following the same degassing procedure as used for the TPR experiments. After cooling the sample to 90 °C, ammonia was adsorbed onto the catalyst surface. Excess and weakly physisorbed NH_3 was subsequently removed by purging with a carrier gas. NH_3 desorption was then monitored by heating the sample from 90 °C to 650 °C at a rate of 10 °C·min^{-1}, with the desorbed NH_3 detected by a thermal conductivity detector (TCD). The adsorption–desorption procedure was repeated for five cycles to assess the stability and reproducibility of the acidity profiles under repeated thermal treatment.

In situ X-ray absorption spectra (XAS, in terms of XANES and EXAFS) at Ni K absorption edge were recorded at the P65 beamline of PETRA III synchrotron radiation source (DESY, Hamburg) in transmission mode. Higher harmonics were rejected by a pair of Si plane mirrors installed in front of the monochromator. The energy of the X-ray photons was selected by a Si (111) double-crystal monochromator and the beam size was set by means of slits to 0.3 (vertical) x 1.5 (horizontal) mm^2.

X-ray absorption near edge spectra (XANES) were normalized and linear combination analysis was performed on the normalized data using the Athena program from the

IFEFFIT software package.[229] The fits of the EXAFS data were performed using Artemis[230] by a least square method in R-space between 1.0 and 3.0 Å on k^1, k^2, and k^3-weighted data. Coordination numbers (CN), interatomic distances (r), energy shift (δE_0) and mean square deviation of interatomic distances (σ^2) were refined during fitting. The absolute misfit between theory and experiment was expressed by ρ.

3.3 Catalytic performance test

3.3.1 Model compound

Model compound hydrodeoxygenation (HDO) reactions were carried out in a stainless-steel autoclave batch reactor. In a typical experiment, 0.5 g of the model compound phenyl phenyl ether (PPE, 97%, VWR Chemicals), 0.5 g of catalyst, and 50 g of solvent (decalin, 98%, Sigma-Aldrich) were loaded into a 200 mL autoclave. After sealing, the reactor was purged three times with high-purity argon (Ar) to ensure complete removal of air. The reactor was then pressurized with hydrogen to an initial pressure of 50 bar at room temperature. The catalytic reaction was conducted at 250 °C for 2 h under a hydrogen atmosphere. During heating, the temperature was increased at a rate of 3.3 °C·min^{-1}, and the reaction mixture was continuously stirred at 600 rpm to ensure effective mixing.

Upon completion of the reaction, the autoclave was rapidly cooled to room temperature using an ice–water bath to quench the reaction. The solid catalyst was separated from the liquid phase by filtration. The resulting liquid products were subsequently subjected to chromatographic analysis for product identification and quantification. Qualitative identification of reaction products was performed using gas chromatography–mass spectrometry (GC–MS) on an Agilent 6890N gas chromatograph coupled with an Agilent 5973N mass spectrometer. Quantitative analysis was conducted using gas chromatography equipped with a flame ionization detector (GC–FID) on an HP 5890 gas chromatograph fitted with an Rxi®-5Sil MS capillary column (30 m × 0.25 mm × 0.25 μm). The conversion of PPE and the selectivity toward individual products were calculated according to Equation (3) and Equation (4), respectively.

$$\text{Conversion}(\%) = \frac{\text{Mole of substrates consumed}}{\text{Mole of substrates fed}} \times 100\% \quad (3)$$

$$\text{Selectivity}(\%) = \frac{\text{Mole of substrates consumed to form each product}}{\text{Mole of total products}} \times 100\% \quad (4)$$

3.3.2 Bio-oil HDO

Fast pyrolysis bio-oil HDO experiments were conducted in a batch reactor system under conditions identical to those used for the model compound HDO reactions, unless otherwise specified. In a typical experiment, 50 g of bio-oil (light phase of beech wood fast pyrolysis oil, supplied by BTG Biomass Technology Group BV, Enschede, The Netherlands) and 2 g of catalyst were loaded into a 200 mL stainless-steel autoclave reactor. After sealing, the reactor was purged three times with high-purity argon to remove residual air, followed by pressurization with hydrogen at room temperature. The HDO reaction was then carried out using the same temperature, pressure, reaction time, heating rate, and stirring conditions as those applied in the model compound HDO experiments.

After completion of the reaction, the reactor was rapidly cooled to room temperature using an ice–water bath. Due to the complex composition of the reactor effluent, centrifugation was employed to separate the aqueous phase, oil phase, and solid particulates. Specifically, the collected liquid/solid mixture was centrifuged at 13,000 rpm for 40 min, after which the aqueous and oil phases were separated and the solid particulates were isolated. The recovered oil phase was subjected to further compositional analysis. Qualitative identification of compounds in the oil phase was performed using gas chromatography–mass spectrometry (GC–MS). Gaseous products were analyzed using a gas chromatograph (Agilent 6890) equipped with a valve switching system and two columns (Hayesep Q, Restek 57096; and Molsieve 5A, Restek). Elemental analysis of the oil products was conducted to determine the contents of carbon (C), hydrogen (H), and nitrogen (N) using a Leco TrueSpec Macro elemental analyzer (LECO Europe). The oxygen content was calculated by difference, assuming that the samples consisted solely of carbon, hydrogen, nitrogen, and oxygen.

3.3.3 Upgrading in syngas

As a typical model compound for HDO experiments, 0.2 g of the guaiacol (99%, sourced from Sigma Aldrich), 0.1 g of the catalyst, and 20 g of the decalin (98%, sourced from Sigma Aldrich) were placed into batch reactor. The catalyst test under different temperatures was performed under 50 bar (room temperature) bio-syngas (consist of 65 % CO, 30 % H_2, and 5 % CO_2) and 2-hour reaction time at the target temperature. Prior to each reaction, the reactor was purged three times with pure argon (Ar) to ensure complete removal of air. Throughout the reaction, the temperature was increased with a rate of 3.3 °C/min, and the mixture was stirred continuously at 600 rpm. After the reaction, the catalyst was removed through filtration and the liquid product was then analyzed using GC-MS (Agilent 6890N with an Agilent 5973N mass spectrometer) for compound identification and GC-FID (HP 5890 gas chromatograph equipped with an Rxi®5Sil MS capillary column, 0.25 μm × 0.25 μm × 30 m) for

quantification of each compound. For the bio-oil HDO experiments, 3 g of bio-oil (the light phase of beech wood fast pyrolysis oil, supplied by BTG Biomass Technology Group BV, Enschede, Netherlands), 27 g THF (Tetrahydrofuran) and 0.5 g of catalyst were introduced into a 200 ml batch reactor. The subsequent operational procedures were identical to those employed in the model compound HDO experiments. In this case, due to the more complex reactor eluent composition, centrifugation was employed for the separation of the aqueous phase, oil phase, and solid particulates.

Fast pyrolysis bio-oil HDO experiments under bio-syngas atmosphere were carried out following the same operating procedure as that used for the guaiacol HDO experiments, unless otherwise specified. In a typical run, 3 g of bio-oil (light phase of beech wood fast pyrolysis oil, supplied by BTG Biomass Technology Group, Enschede, The Netherlands), 27 g of tetrahydrofuran (THF), and 0.5 g of catalyst were loaded into a 200 mL batch reactor. The reactor was purged three times with argon, charged with bio-syngas to an initial pressure of 50 bar at room temperature, and heated to the target temperature under continuous stirring, using the same heating ramp (3.3 $°C \cdot min^{-1}$), agitation rate (600 rpm), and reaction time (2 h) as in the model compound experiments. After completion of the reaction, the reactor was cooled to room temperature. Owing to the complex composition of the reactor effluent, centrifugation was employed to separate the aqueous phase, oil phase, and solid particulates prior to further analysis.

3.4 DFT calculation

In this study, DFT calculations were performed utilizing the Vienna Ab-initio Simulation Package (VASP) [231,232] with the Atomic Simulation Environment (ASE) software [233]. PBE functional [197] with Grimme's DFT-D3 correction was applied [201]. Inner electrons were modeled using projector augmented wave (PAW) [234,235] pseudopotentials, and a cutoff energy of 400 eV. The Brillouin zone sampling was executed via a Γ-centered k-point mesh, generated employing the Monkhorst-Pack method.

Geometry optimizations proceeded until the force on each atom diminished below the convergence threshold of 0.03 eV/Å, ensuring energy convergence within 10^{-6} eV. For the adsorption energy calculation, it was obtained as the equation 1,

$$E_{ads} = E_{total} - E_{surf} - E_{adsorbate} \quad (1)$$

where E_{total} denotes the total energy of molecule absorbate covered on a surface, E_{surf} denotes the energy of a surface, and $E_{absorbate}$ denotes the energy of molecule in vacuum.

The Climbing Image Nudged Elastic Band (CINEB) [236] and dimer methods were employed to investigate the transition states of elemental reactions. And all of the transition state structures were tested to make sure only one imaginary frequency. The reaction barrier was determined as equation 2，

$$E_{barrier} = E_{TS} - E_{IS} \quad (2)$$

where E_{TS} denotes the energy of transition state, E_{IS} denotes the energy of initial state. The thermochemistry was calculated by the package of VASPKIT [237].

Chapter 4 Results and Discussions

4.1 Introduction

This chapter presents and discusses the results related to all objectives investigated in this study. The discussion opens in Section 4.2 with an integrated DFT–experimental investigation of the hydrodeoxygenation (HDO) of PPE as a representative β-O-4 lignin model compound. This section provides a detailed mechanistic analysis of β-O-4 bond cleavage, identifying the key elementary steps that govern C–O scission and product selectivity. Building on the mechanistic insights obtained, Section 4.3 shifts to catalyst screening and development, focusing on Ni–Al catalysts prepared via an LDH-derived route. Particular emphasis is placed on elucidating the origin of their high catalytic activity, with a detailed discussion of the role of the Ni/NiO interfacial sites in promoting HDO pathways. Subsequently, the Ni–Al catalyst is further optimized through a doping strategy to enhance deoxygenation efficiency; this subsection analyzes how Mo incorporation strengthens deoxygenation performance and rationalizes the underlying structure–activity relationship. Finally, to address the relatively low molecular weight of the HDO-treated products, this chapter explores syngas-driven catalytic upgrading. This concluding part evaluates the experimental feasibility of syngas conversion as a practical route for bio-oil valorization and discusses its potential to broaden the product spectrum toward higher-value chemicals and fuels.

4.2 Exploring the hydrodeoxygenation of lignin β-O-4 dimer model compound and bio-oil by DFT and experimental studies

4.2.1 DFT calculation

Section 3.4 provides the general computational methodology; the key parameters specific to this subsection are summarized here. To elucidate the Ru-catalyzed mechanism, the Ru (0001) surface was modeled using a four-layer slab with a vacuum spacing of 15 Å. The bottom two layers were fixed at bulk positions, while the top two layers were fully relaxed during geometry optimizations. For PPE adsorption on Ru (0001), a 5 × 7 surface supercell and a 2 × 1 × 1 k-point mesh were employed.

Convergence tests with respect to k-point sampling and surface slab size are provided in Figure S1 to Figure S4.

The optimized adsorption configuration of PPE on Ru (0001) is shown in Figure 4-1.[224] PPE binds strongly to Ru (0001) with an adsorption energy of −4.49 eV, reflecting a highly stabilized adsorption geometry at the interface. This stability is primarily attributed to the simultaneous adsorption of the two aromatic rings, which are known to bind strongly on Ru. Indeed, prior PBE calculations for benzene adsorption on Ru (0001) reported adsorption energies of 1.40–1.60 eV.[238–240] In the optimized PPE configuration, the benzene ring occupies the most favorable adsorption site,[241] thus showing that specific strong functional groups direct adsorption geometries and the corresponding energy.[238]

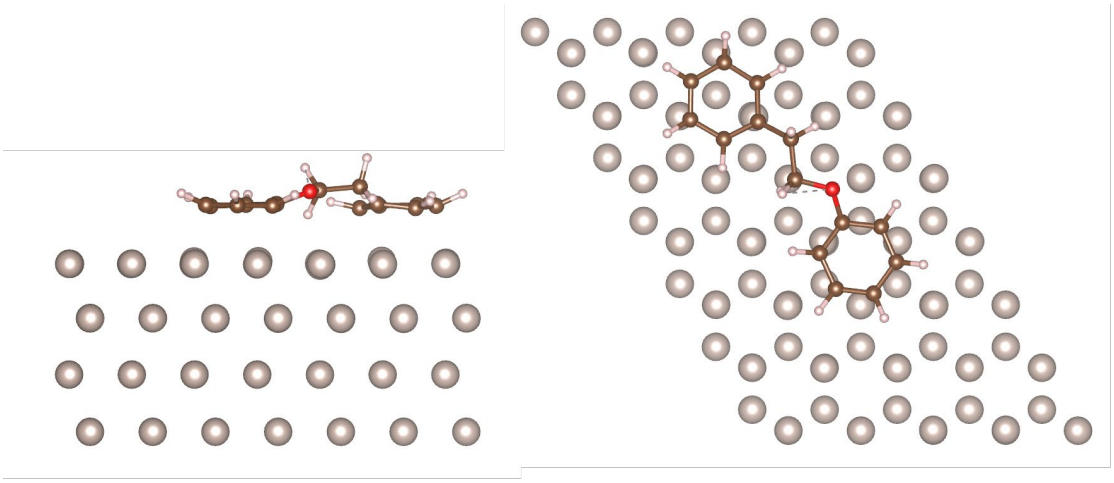

Figure 4-1: The PPE on Ru (0001) adsorption structure. Source: reprinted from ref. [224] in agreement with the terms of use.

Charge-density difference analysis was then performed to visualize interfacial charge redistribution (Figure 4-2).[224] Pronounced charge rearrangement is observed in the vicinity of both benzene rings, indicating strong electronic coupling between the aromatic moieties and the Ru surface. To further support this interpretation, benzene adsorption on Ru (0001) was also evaluated (Figure S4). A single benzene molecule exhibits an adsorption energy of −2.33 eV, corresponding to roughly half of the adsorption strength obtained for PPE. The larger absolute adsorption energies reported here arise from inclusion of the D3 dispersion correction, which was not considered in earlier PBE-only studies. Collectively, these results confirm that PPE adsorption is dominated by the interaction between its aromatic rings and the Ru surface.

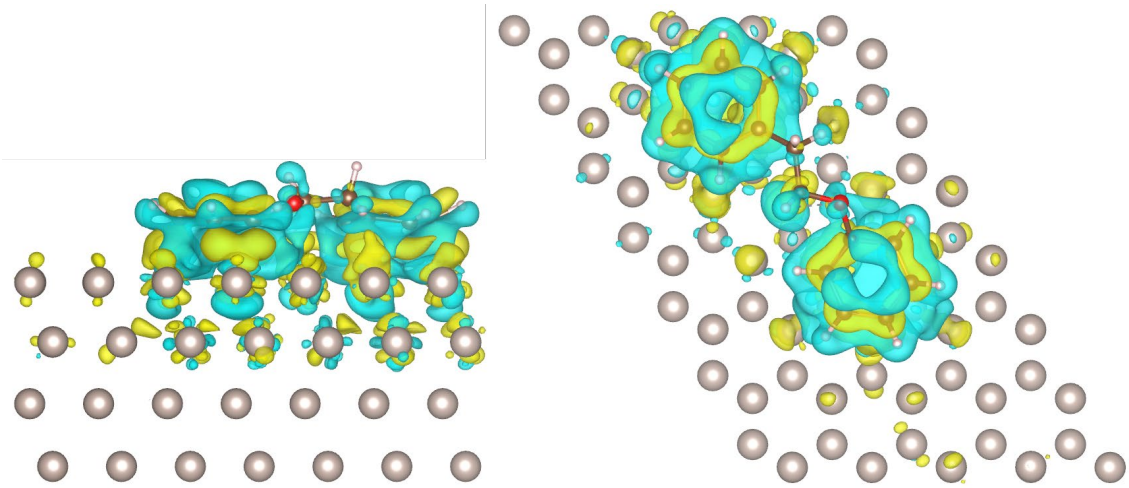

Figure 4-2: The charge difference density plots for PPE adsorption, the blue (yellow) distribution corresponds to charge accumulation (depletion). Source: reprinted from ref. [224] in agreement with the terms of use.

The possible HDO pathways of PPE on Ru (0001) were systematically investigated by transition-state calculations, and the identified reaction network is summarized in Figure 4-3.[224] In these calculations, C–C bond cleavage was neglected because C–C bonds generally exhibit higher bond dissociation energies than C–O bonds, and this assumption is consistent with previous experimental observations.[242,243] For the scission of the C-O bond in the β-O-4 linkage, the results indicate that dehydrogenation followed by cleavage is the most probable reaction pathway. Along this pathway, the highest activation barrier is associated with hydrogenation of the monomer intermediate (0.59 eV). To evaluate the energetics under the experimental conditions (250 °C and 8 MPa) as opposed to ideal conditions, thermal corrections were applied according to the experimental parameters for this specific pathway. The Gibbs free-energy diagram at 250 °C, including the associated transition-state geometries, is shown in Figure 4-4, and the full set of elementary steps is compiled in Table 4-1. The free-energy barrier for β-O-4 C–O bond cleavage is notably low (0.31 eV; Figure 4-4, step 3), whereas hydrogenation of monomeric intermediates constitutes the rate-limiting process. High desorption energies are obtained for phenol and ethylbenzene (Figure 4-4, steps 8 and 9), indicating strong binding of these aromatic products to the Ru surface. In contrast, the corresponding saturated products (following aromatic-ring hydrogenation) desorb more readily (Figure 4-4, steps 12 and 13), suggesting that phenol and ethylbenzene may undergo further hydrogenation prior to desorption. Overall, the computed energetics support Ru as a highly effective catalyst for β-O-4 C–O bond cleavage, characterized by a very low activation barrier.

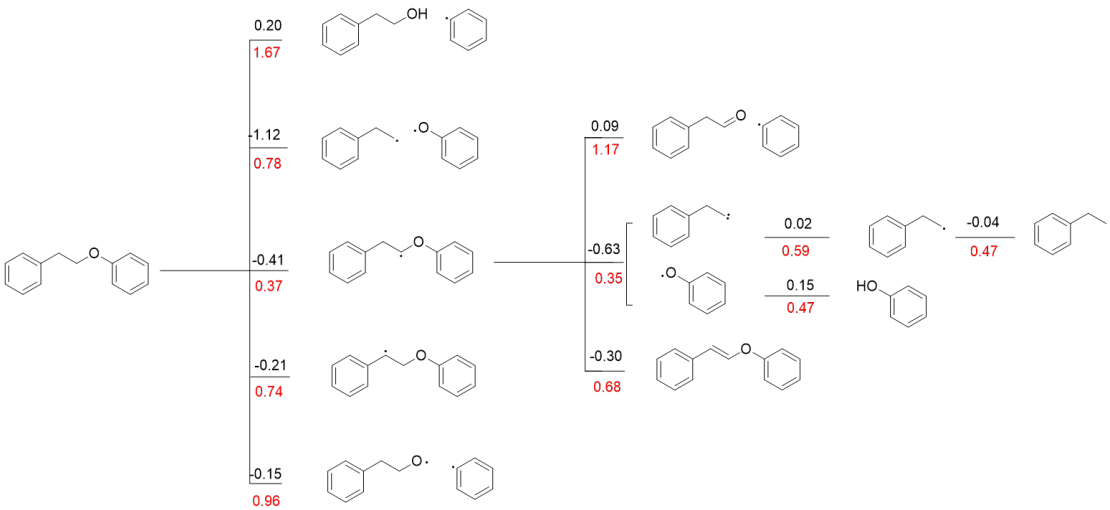

Figure 4-3: Reaction pathways of PPE HDO process, red values are energy barriers, and black values are reaction energy in eV. Source: reprinted from ref. [224] in agreement with the terms of use.

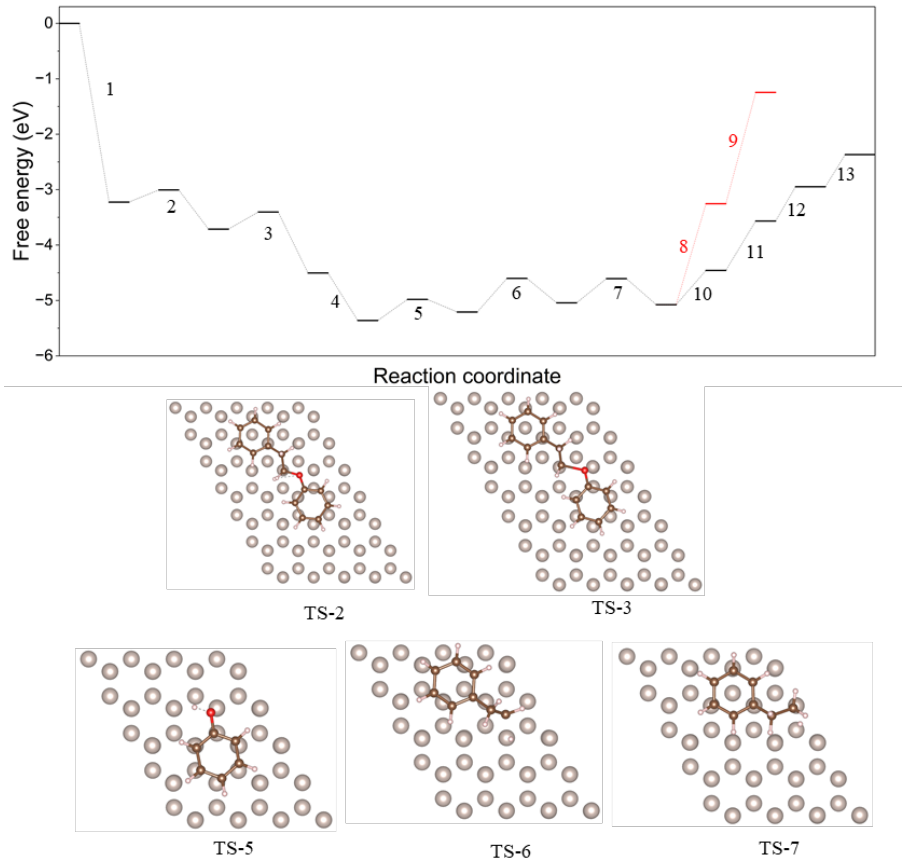

Figure 4-4: Gibbs free energy diagram of PPE HDO process on Ru (0001) surface at a temperature of 250 °C. The black numbers refer to the elemental steps (see also Table 2-1), the 7 optimized transition states (TS) are shown as an inset. Blue values denote

free energy changes during elemental reaction steps while the red values denote reaction free energy barriers. Source: reprinted from ref. [224] in agreement with the terms of use.

Table 4-1: Reaction steps corresponding Figure 4-4. Source: reprinted from ref. [224] in agreement with the terms of use.

	Element steps
1	$C_6H_5CH_2CH_2OC_6H_5$ (g)→ $C_6H_5CH_2CH_2OC_6H_5$*
2	$C_6H_5CH_2CH_2OC_6H_5$* → $C_6H_5CH_2CHOC_6H_5$* + H*
3	$C_6H_5CH_2CHOC_6H_5$* → $C_6H_5CH_2CH$* + *OC_6H_5
4	H_2 (g) → 2H*
5	C_6H_5O* + H* → C_6H_5OH*
6	$C_6H_5CH_2CH$* + H* → $C_6H_5CH_2CH_2$*
7	$C_6H_5CH_2CH_2$* + H*→ $C_6H_5CH_2CH_3$*
8	C_6H_5OH* → C_6H_5OH (g)
9	$C_6H_5CH_2CH_3$* → $C_6H_5CH_2CH_3$ (g)
10	C_6H_5OH* + 6H* → $C_6H_{11}OH$*
11	$C_6H_5CH_2CH_3$* + 6H* → $C_6H_{11}CH_2CH_3$*
12	$C_6H_{11}OH$* → $C_6H_{11}OH$ (g)
13	$C_6H_{11}CH_2CH_3$* → $C_6H_{11}CH_2CH_3$ (g)

4.2.2 Catalyst characterization

To experimentally validate the reaction pathways proposed in Section 4.2.1, a Ru/Nb_2O_5 catalyst was synthesized following the procedure described in Section 3.1.1. The catalyst morphology and elemental distribution are shown in Figure 4-5.[224] The Nb_2O_5 support consists of numerous discrete, block-like particles (Figure 4-5 a,b), whereas the Ru phase appears as star-shaped nanoparticles with characteristic sizes of ca. 100–200 nm. Such particle dimensions are sufficiently large to enable the exposure of extended Ru facets that are representative of Ru (0001)-type surfaces. EDX mapping (Figure 4-5 c-f) confirms a uniform dispersion of Ru across the Nb_2O_5 support. Quantification based on EDX (Table S1) yields a Ru content of 7.28%, exceeding the nominal 5 wt% loading used during preparation, which suggests a surface enrichment of Ru on the support.

The crystalline structure of the catalyst was examined by X-ray diffraction (XRD). As shown in Figure 4-6 a, well-defined reflections attributable to metallic Ru are observed, indicating high crystallinity of the Ru particles. Peaks at 38.383°, 42.183°, 44.017°, 58.340°, 69.413°, and 78.397° are assigned to hexagonal close-packed Ru. For the Nb_2O_5 support, calcination at 380 °C typically induces transformation to the TT phase, which is often associated with weak or poorly resolved diffraction features. Consistent with this behavior, only a broad, low-intensity feature is observed between 20° and 30°, in agreement with the report by Campos Fraga et al.[244] The acidity of Ru/Nb_2O_5 was assessed by NH3-TPD (Figure 4-6 b). Most acid sites are distributed in the low-temperature region (200–350 °C), indicating that weak acid sites dominate; the total acidity is 175.77 μmol g−1. Textural properties were evaluated by N_2 physisorption (Figure 4-6 c and Table S2). After Ru deposition, the specific surface area, pore volume, and average pore size decrease slightly relative to bare Nb_2O_5, consistent with partial pore filling and/or surface coverage by Ru.

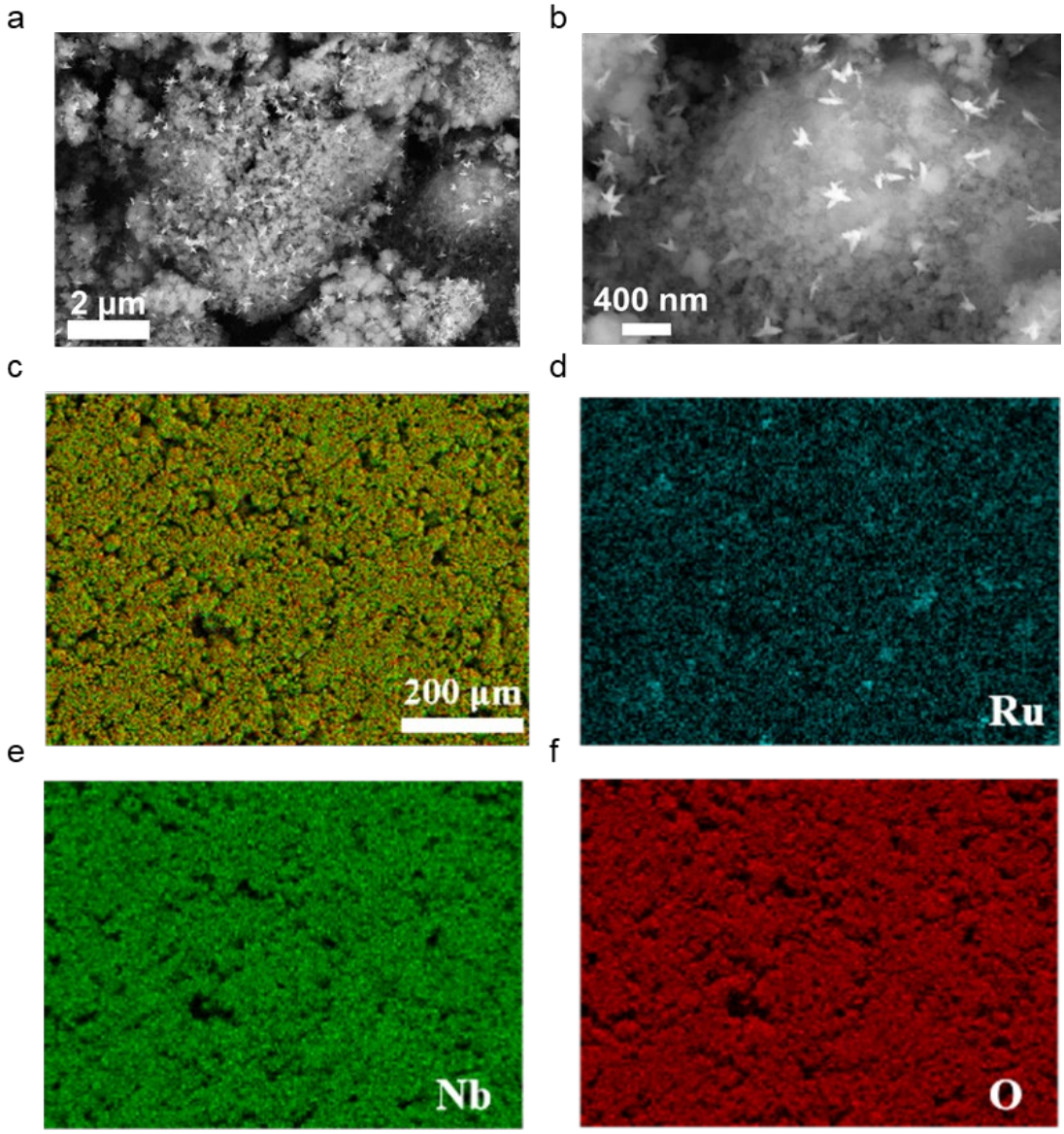

Figure 4-5: a,b. SEM images of fresh Ru/Nb_2O_5; c. EDX elemental mapping of Ru, Nb, O. Source: reprinted from ref. [224] in agreement with the terms of use.

Table 4-2: N_2 physisorption results of Nb_2O_5 and Ru/Nb_2O_5. Source: reprinted from ref. [224] in agreement with the terms of use.

	Surface area (m^2/g_{cat})	Pore volume (cm^3/g_{cat})	Pore diameter (nm)
Nb_2O_5	93.55	0.125	3.567
Ru/Nb_2O_5	87.72	0.118	3.516

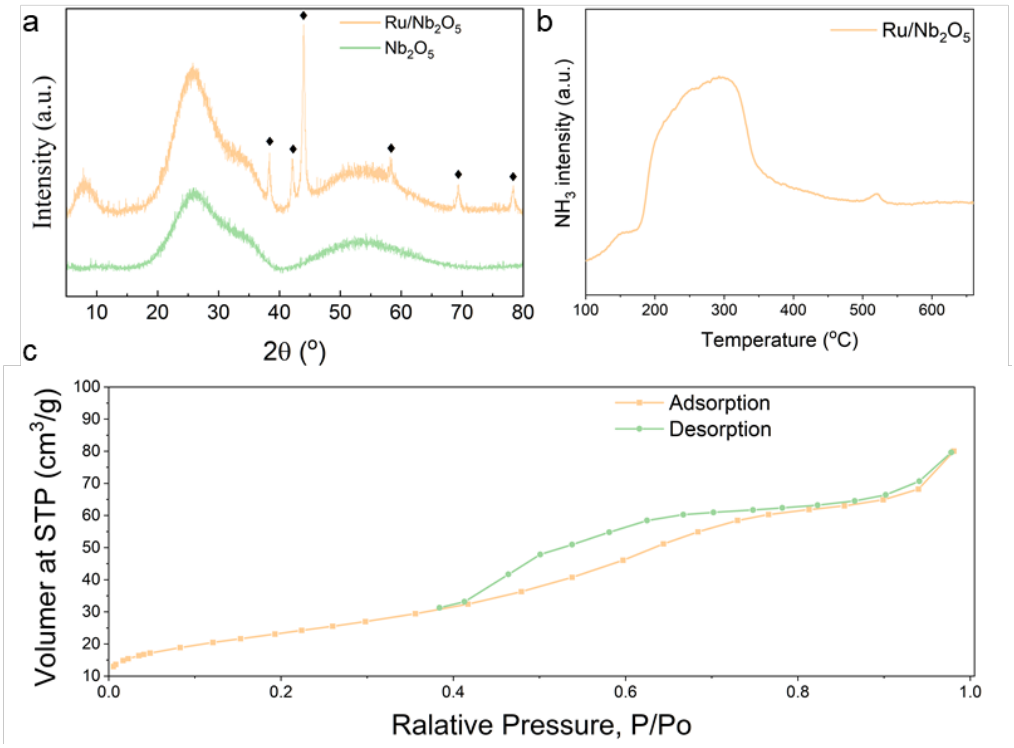

Figure 4-6: a. XRD patterns of Ru/Nb_2O_5; b. NH_3 TPD analysis of Ru/Nb_2O_5; c. N_2 physisorption analysis of Ru/Nb_2O_5. Source: reprinted from ref. [224] in agreement with the terms of use.

4.2.3 HDO catalytic performence

To validate the DFT predictions, hydrodeoxygenation (HDO) experiments were first performed using PPE as a representative model compound. The temperature-dependent performance of PPE HDO over Ru/Nb_2O_5 is summarized in Figure 4-7.[224] Near-quantitative conversion (≈100%) is maintained across the investigated temperature range, indicating that the catalyst is highly active even under relatively mild conditions. This near-complete conversion across all temperatures suggests that temperature primarily governs product selectivity rather than overall activity. At lower temperatures, the product stream is dominated by the hydrogenated dimer, which mainly originates from aromatic-ring hydrogenation while the β-O-4 linkage remains largely intact. This observation indicates that Ru/Nb_2O_5 exhibits strong hydrogenation capability and high efficiency for benzene-ring saturation even at low temperatures.[245] As the temperature increases, the contribution of the hydrogenated dimer steadily decreases. At 250 °C, the products consist predominantly of cyclohexane and ethylcyclohexane, demonstrating that deeper upgrading—i.e., β-O-4 C–O scission followed by extensive

hydrogenation—becomes favored at elevated temperature. The progressive shift from hydrogenated dimer to hydrogenated monomers highlights a transition from ring hydrogenation–dominated chemistry to combined HDO and hydrogenation pathways.

These experimental trends are consistent with the DFT results discussed in Section 3.2, where cyclohexane and ethylcyclohexane were identified as downstream products derived from phenol HDO and subsequent hydrogenation, as well as from hydrogenation of ethylbenzene intermediates. The absence (or low abundance) of arene products such as ethylbenzene in the final product distribution can be rationalized by their strong adsorption on Ru surfaces. Supporting this explanation, the DFT calculations (Figure 4-4) predict high desorption energies for both ethylbenzene and phenol, implying prolonged residence times on the catalyst surface and thus a high likelihood of further hydrogenation to yield cyclohexane and ethylcyclohexane prior to desorption. In this context, strong adsorption not only suppresses early desorption of aromatic intermediates but also promotes sequential hydrogenation, thereby steering the system toward fully saturated products. In addition, variations in reaction time lead to only minor changes in product distribution, indicating that the catalyst maintains sufficient activity to reach steady product selectivity rapidly under the tested conditions.

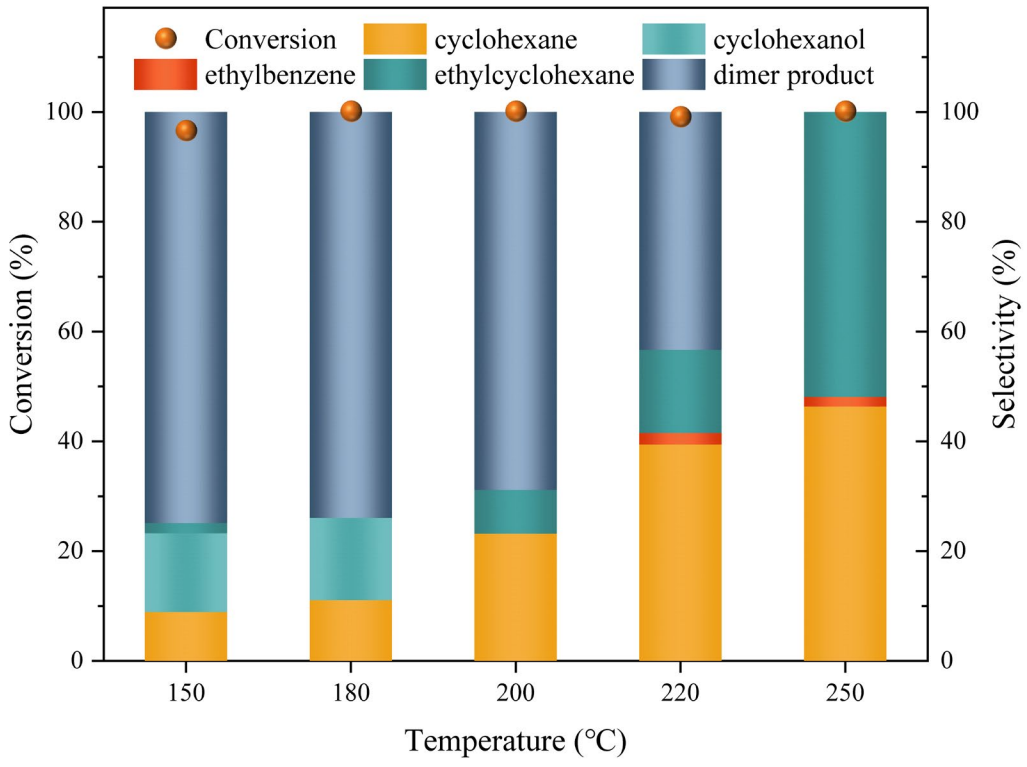

Figure 4-7: Effect of temperature on PPE HDO. Condition: 0.5g PPE, 50g decalin, 0.5g Ru/Nb_2O_5, 5 MPa H_2, 2h. Source: reprinted from ref. [224] in agreement with the terms of use.

To evaluate the catalytic performance toward real feedstocks, BTG light-phase fast pyrolysis oil was employed for HDO over Ru/Nb_2O_5, with experimental details provided in Section 3.3.3. After reaction, gaseous products were collected upon cooling of the reactor and immediately analyzed by gas chromatography. As summarized in Table 2-3, oxygen originating from the bio-oil is predominantly converted into CO_2, with a smaller fraction forming CO, while organic gaseous products are negligible. For example, the CH_4 content is limited to only 0.06%. These results indicate that direct cleavage of carbon-containing moieties into light organic gases is largely suppressed, thereby minimizing carbon loss during the HDO process. Elemental analysis of the upgraded oil phase (Table 2-4) reveals a pronounced decrease in oxygen content, confirming effective deoxygenation. The molecular composition of the liquid products was further characterized by GC–MS, identifying furans, phenols, guaiacols, ketones, carboxylic acids, and esters (Table S2-2). Despite the observed deoxygenation, a substantial fraction of oxygen-containing compounds and unsaturated functionalities remains in the upgraded bio-oil. This behavior is attributed to the direct use of raw bio-oil without solvent addition, which likely leads to insufficient mass transfer and limited adsorption of organic species on the catalyst surface. Moreover, the high intrinsic water content of the raw bio-oil may partially inhibit catalytic activity, while trace inorganic cations (e.g., Na^+ or K^+) could further contribute to catalyst deactivation. Oxygen removed from the bio-oil in the form of H_2O is not accounted for in either the gas-phase analysis (Table 4-3) or the oil-phase composition (Table 4-4) and was therefore not quantified in the present study.

Table 4-3: Composition of the gas phase after the reaction. Source: reprinted from ref. [224] in agreement with the terms of use.

	H_2	CO_2	CO	CH_4	C_2-C_3
Content (w%)	89.19	8.38	0.71	0.06	0.04

Table 4-4: Element content result of crude oil and upgrade oil. Source: reprinted from ref. [224] in agreement with the terms of use.

	Content (%)			
	C	H	N	O
Crude oil	42.76	7.18	2.42	47.65
Upgrade oil	63.25±0.84	6.74±0.09	0.29±0.01	29.72±0.75

4.2 Mild catalytic hydrogenolysis of β-O-4 lignin linkage over a synergistic catalyst of Ni (0) and Ni (II)

4.2.1 Catalyst characterization

The synthesis of the $Ni/NiO/Al_2O_3$ catalyst via a coprecipitation route is described in detail in Section 3.1.2. Briefly, a Ni–Al layered double hydroxide (Ni–Al LDH) intermediate was first obtained by coprecipitation, followed by calcination and reduction to yield the Ni–Al-based catalyst.[225] The morphologies of both the LDH intermediate and the final Ni–Al catalyst were examined by SEM (Figure 4-8). The LDH precursor exhibits a typical nanoflower-like morphology, with relatively uniform "petal" thicknesses of ~10 nm (Figure 4-8 a,b). Such a layered architecture favors homogeneous distribution of Ni and Al species, which is further supported by SEM–EDS mapping (Figure S5, Figure S6). By comparing the morphologies of the Ni–Al catalyst (Figure 4-8 c,d) with those of the parent LDH (Figure 4-8 a,b), it is evident that the nanoflower structure undergoes partial reconstruction during calcination and reduction; nevertheless, a layered framework is largely retained, indicating that the basic scaffold remains intact. Preservation of this layered morphology is advantageous because it mitigates particle agglomeration during thermal treatment.

The surface nanostructure of the catalyst was further investigated by TEM (Figure 4-9).[225] As shown in Figure 4-9 a, bright nanoparticles are embedded within a darker matrix. The bright particles are attributed to Ni and its oxides, whereas the dark matrix corresponds to the Al_2O_3 framework. Particle-size statistics for the bright nanoparticles (Figure 4-9 b) show a relatively narrow distribution, with most particles in the range of 7–11 nm, indicating good size uniformity. TEM–EDS mapping further confirms that the matrix region is dominated by Al and O signals (consistent with Al_2O_3), while the nanoparticle regions display strong Ni and O signals, suggesting a mixture of metallic Ni and NiO.

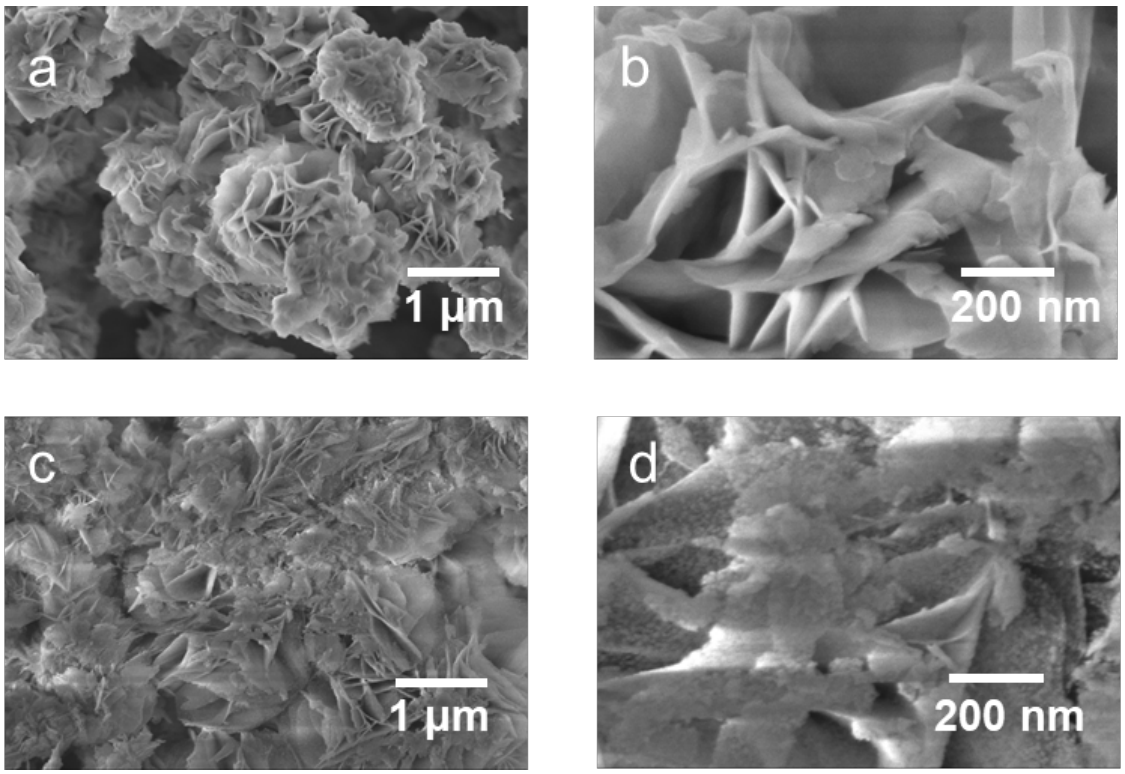

Figure 4-8: a,b, SEM images of Ni Al LDH structure; c,d. SEM images of Ni/Al catalyst. Source: reprinted from ref. [225] in agreement with the terms of use.

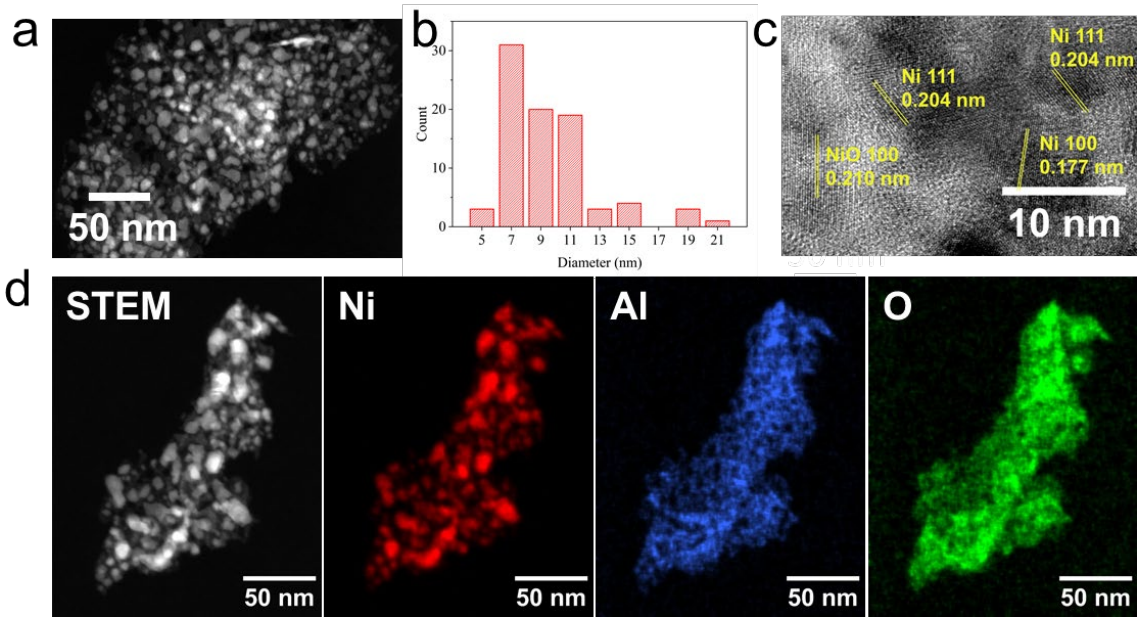

Figure 4-9: a. the TEM image of Ni/Al catalyst; b. Ni/NiO particle size distribution; c. HRTEM image of Ni/Al catalyst; d. EDS-mapping from STEM of Ni/Al catalyst. Source: reprinted from ref. [225] in agreement with the terms of use.

The formation and phase evolution of the Ni–Al catalyst were subsequently examined by XRD (Figure 4-10 a).[225] The dried intermediate after coprecipitation is denoted as Ni–Al LDH; the calcined sample is denoted as NiO/Al_2O_3 LDO; and the reduced material is denoted as $Ni/NiO/Al_2O_3$. After calcination, the precursor is converted predominantly into NiO and Al_2O_3. Notably, after reduction, NiO remains present alongside metallic Ni, indicating incomplete reduction under the applied conditions. Specifically, diffraction peaks at 37.3°, 43.4°, and 63.0° are assigned to NiO, whereas peaks at 44.5° and 51.8° correspond to metallic Ni. Distinct Al_2O_3 reflections are not clearly observed, likely due to its low crystallinity. Owing to the compositional tunability of the LDH approach, catalysts with different Ni loadings were prepared by adjusting the Ni precursor ratio, and the resulting Ni contents were quantified by ICP–OES (Table 4- 5). To elucidate the influence of Ni/Al ratio, XRD (Figure 4-10 b) and Raman spectroscopy (Figure 4-10 d) were further performed for catalysts with different compositions. For the lowest Ni-loading sample (Ni/Al = 0.25), the Ni-related diffraction features are markedly broadened and of lower intensity, indicating smaller crystallite sizes and enhanced dispersion of Ni species. With increasing Ni/Al ratio (from 0.5 to 4), the characteristic Ni-related reflections become progressively sharper and more intense, consistent with larger crystallites and/or higher overall Ni content. The presence of NiO reflections corroborates the coexistence of Ni(0) and Ni(II) species. Notably, NiO diffraction peaks are detected only for samples with Ni/Al > 1, suggesting that higher Ni concentration facilitates the detection of residual NiO after reduction. Raman spectra show a band at ~550 cm^{-1} attributable to NiO, while metallic Ni is Raman-inactive; this observation is consistent with the XRD results and confirms the persistence of NiO.

Ni 2p XPS spectra (Figure 4-10 c) exhibit a complex peak structure, including a distinct feature at ~852 eV, a main peak at ~856 eV, and characteristic shake-up satellites at higher binding energy (~862 eV).[225] Based on literature reference values, the ~852 eV component is assigned to metallic Ni, whereas the ~856 eV peak and the accompanying satellite features are characteristic of Ni(II), providing additional evidence for the presence of NiO species. Collectively, these features indicate that metallic Ni and oxidized Ni species coexist at the catalyst surface, implying partial reduction during synthesis and/or post-treatment rather than complete conversion to the metallic state. Finally, HRTEM (Figure 4-9 c) reveals multiple lattice spacings, indicating the exposure of different crystallographic planes of both Ni and NiO and further supporting the coexistence of metallic and ionic Ni species. In agreement with these observations, H_2-TPR of the Ni/Al-2 catalyst (Figure S7) shows a reduction feature near 700 °C, suggesting that reduction at 500 °C is insufficient to fully convert NiO to Ni. This finding provides additional support for the rational coexistence of Ni(0) and Ni(II) in the catalyst.

The evolution of Ni species under reducing conditions was monitored by in situ XAS during thermal treatment from ambient temperature to 600 °C in a H_2/He atmosphere.[225]

The in situ XANES spectra (Figure 4-10 e) display systematic changes in both the absorption-edge position and the white-line intensity with increasing temperature, consistent with progressive reduction of NiO-like species to metallic Ni. Specifically, the edge position shifts toward that of the Ni-foil reference, indicating a growing fraction of zero-valent Ni. Nevertheless, even at 600 °C the sample spectra do not fully coincide with the Ni-foil standard, implying the persistence of oxidized Ni species; this conclusion is further supported by the still-elevated white-line intensity relative to the metallic reference. Quantification by linear-combination fitting (Table S3) indicates that at 500 °C the sample contains 56.8% Ni(II) and 43.2% Ni(0). Upon heating to 600 °C, the Ni(II) fraction decreases to 20.7%, confirming continued reduction at higher temperature while indicating that complete conversion to metallic Ni is not achieved under the applied conditions. The structural evolution is corroborated by FT k^3-weighted EXAFS (Figure 4-10 f), together with k^2-weighted EXAFS spectra (Figure S8). With increasing reduction temperature, the Ni–O contribution characteristic of NiO (≈1.6 Å, phase-uncorrected) diminishes, whereas the Ni–Ni contribution (≈2.5 Å) intensifies, in line with the transformation of the NiO lattice toward metallic Ni. Importantly, a residual Ni–O feature remains detectable even at the maximum temperature, indicating incomplete reduction. First-shell EXAFS fitting at 600 °C (and after cooling to ambient temperature) yields Ni–O coordination numbers of 1.1–1.3 (out of a maximum of 6), as summarized in Table S4 and Figure S9. This corresponds to an overall reduction degree of approximately 80% and quantitatively confirms the coexistence of metallic and oxidized Ni species.

Overall, the combined in situ XANES and EXAFS analyses demonstrate that metallic Ni is progressively formed with increasing reduction temperature, while a non-negligible fraction of NiO remains stable. These results establish that the catalyst retains a dual-phase composition of Ni(0) and NiO after reduction under the specified conditions.

Table 4- 5: Ni element content test results obtained through ICP-OES. Source: reprinted from ref. [225] in agreement with the terms of use.

	Ni/Al-0.25	Ni/Al-0.5	Ni/Al-1	Ni/Al-2	Ni/Al-4
Ni content (%)	22	33	47	70	73

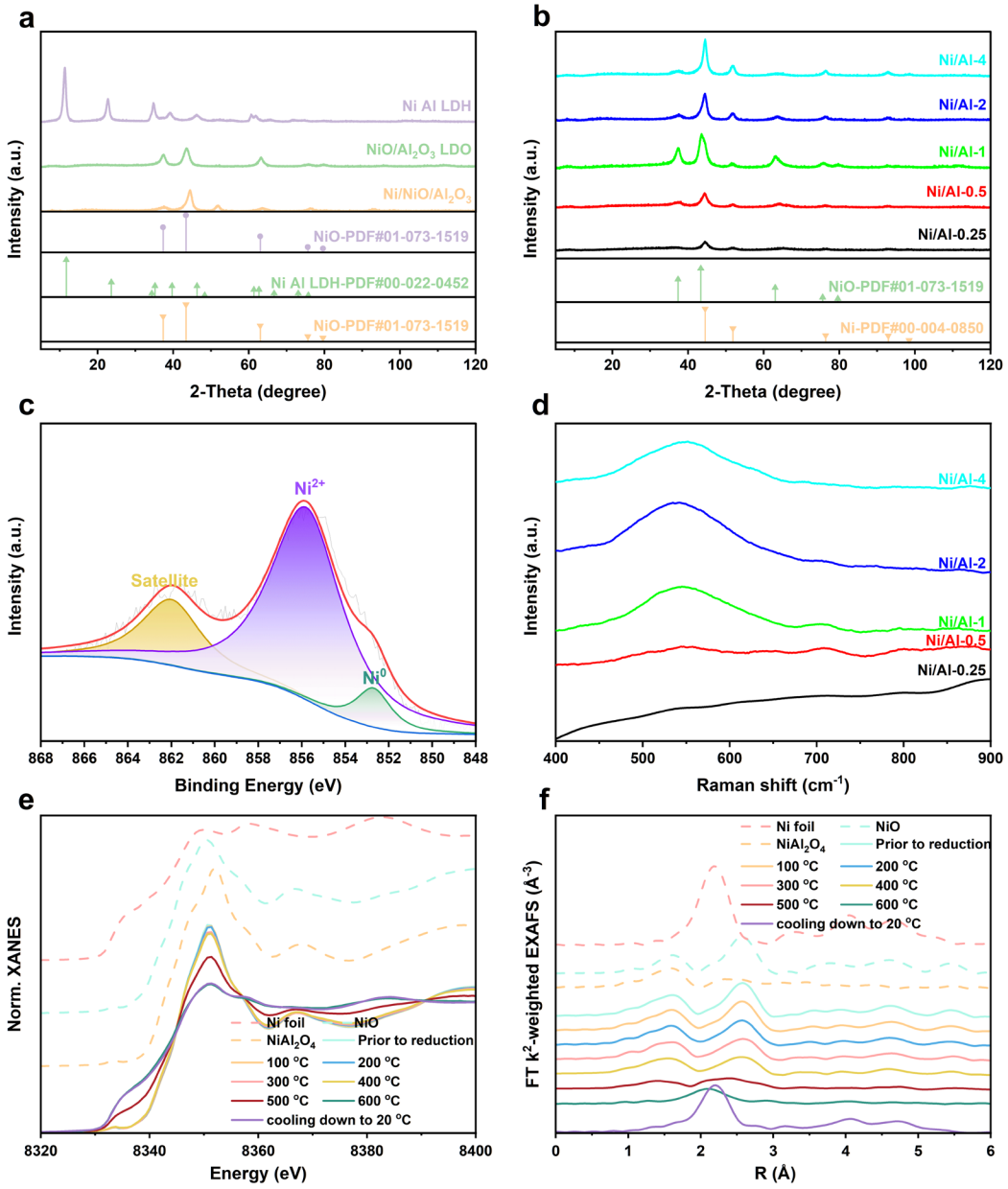

Figure 4-10: a. XRD patterns of Ni-Al LDH, Ni-Al LDO, and Ni/Al-2 catalyst after reduction; b. XRD patterns of different Ni/Al ratio catalysts; c. Ni 2p High resolution XPS spectra for Ni/Al catalyst; d. Raman spectra for different Ni/Al ratio catalysts; e. Normalized Ni K edge XANES spectra of the Ni/Al-2 catalyst and selected Ni reference compounds. Source: reprinted from ref. [225] in agreement with the terms of use.

4.2.2 Hydrogenolysis of PPE

To evaluate the catalytic performance of the catalysts via PPE hydrogenolysis, catalysts prepared by different methods were first examined; the preparation procedures are described in detail in Section 3.1.2. As shown in Figure 4-11 a, the Ni/Al-2 catalyst derived from an LDH precursor exhibits superior activity, achieving the target conversion at only 125 °C.[225] In contrast, catalysts prepared by wet impregnation and conventional coprecipitation require temperatures of at least 180 °C and reach complete conversion only at 220 °C. Although all three catalysts contain Ni–Al components, the Ni species in the impregnated and coprecipitated catalysts are fully reduced to metallic Ni(0) after reduction. This observation suggests that the high activity of the Ni–Al–LDH-derived catalyst under mild conditions is associated with the presence of NiO.

Subsequently, the LDH-derived Ni/Al catalyst was benchmarked against catalysts reported in the literature. (Figure 4-11 b)[242,246–250] For PPE hydrogenolysis, Ru is commonly employed as the active metal, whereas non-noble transition metals such as Ni typically require higher reaction temperatures. In the present study, by tuning the relative proportions of Ni(0) and Ni(II), the LDH-derived Ni/Al catalysts exhibit high catalytic activity under comparatively mild conditions. Detailed experimental conditions for these comparisons are provided in Table 4-6.

The influence of the Ni/Al ratio was then investigated. (Figure 4-11 c) The conversion increases with increasing Ni/Al ratio and reaches 100% when the ratio exceeds 1. This enhancement is likely related to the absence of the NiO phase at low Ni/Al ratios (<0.5). Notably, for PPE hydrogenolysis, the catalyst with a Ni/Al ratio of 2 produces only a negligible amount of dimer byproducts while achieving the highest selectivity toward monomer products. This result indicates that the synergistic interaction between Ni and NiO is optimal at a Ni/Al ratio of 2. Moreover, the products are predominantly fully hydrogenated benzene derivatives, suggesting that aromatic compounds are not stable under the applied hydrogen-rich conditions.

Finally, the catalytic performance of the LDH-derived Ni/Al catalyst (Ni/Al = 2) was evaluated at different temperatures (Figure 4-11d). No catalytic activity is observed at 100 °C; however, once the temperature exceeds 125 °C, complete conversion is achieved. In terms of product selectivity, increasing temperature leads to a higher yield of dimeric byproducts, while the main product shifts from ethylbenzene to the fully hydrogenated product ethylcyclohexane. These results demonstrate that the LDH-derived Ni/Al catalyst exhibits optimal hydrogenolysis performance under relatively mild reaction conditions.

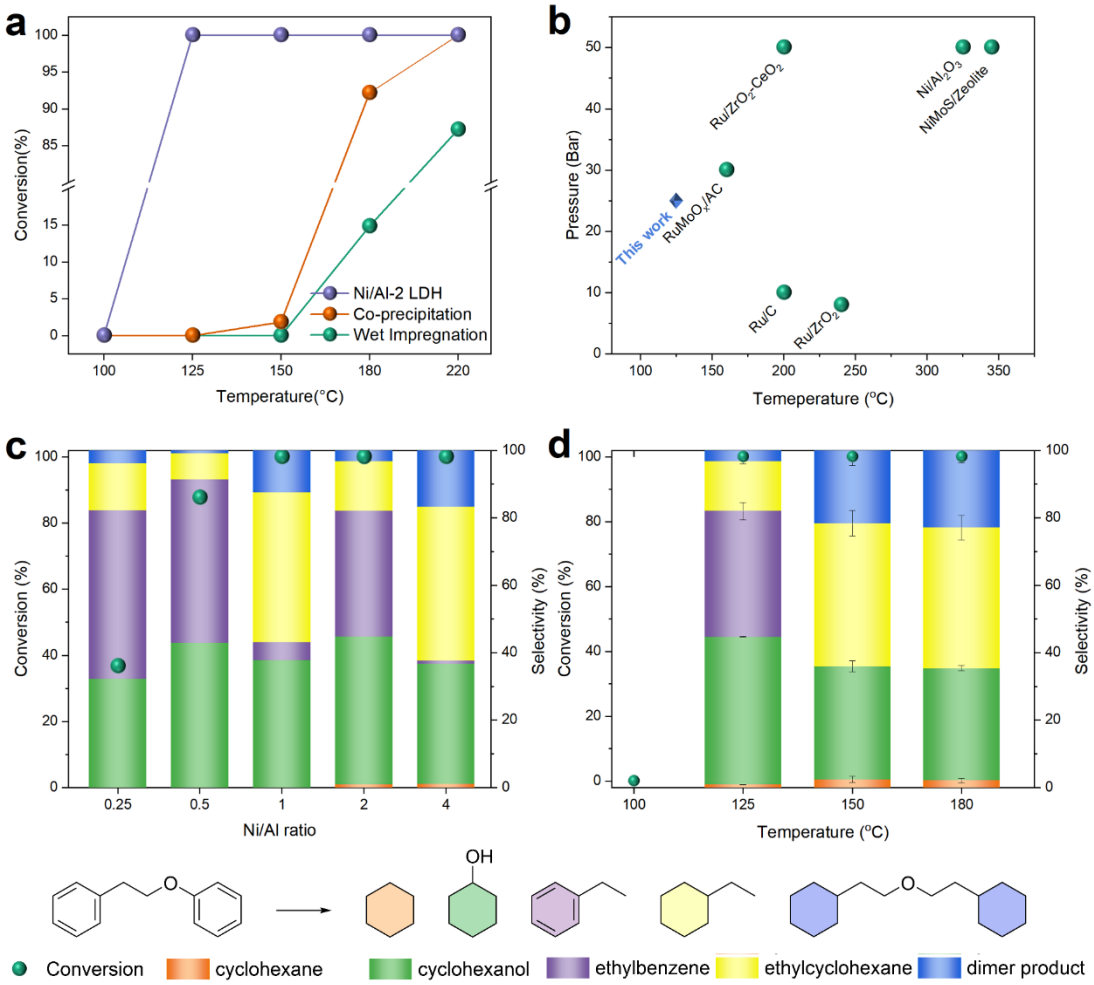

Figure 4-11: a. The conversion of PPE Hydrogenolysis over Ni/Al catalysts prepared by different methods at various temperature. Reaction conditions: 0.2 g PPE, 0.2 g Catalyst, 20 g decalin, 25 bar H_2, 1h; b. Comparison of PPE hydrogenolysis conditions from different literatures; c. The conversion and selectivity of PPE hydrogenolysis over different Ni-Al ratio catalysts. Reaction conditions: 0.2 g PPE, 0.2 g Catalyst, 20 g decalin, 125 °C, 25 bar H_2, 1h; d. The conversion and selectivity of PPE hydrogenolysis over Ni/Al-2 catalyst at various temperature. Reaction conditions: 0.2 g PPE, 0.2 g Catalyst, 20 g decalin, 25 bar H_2, 1h. Source: reprinted from ref. [225] in agreement with the terms of use.

Table 4-6: Comparation of reaction conditions and results of PPE hydrolysis over different catalysts from literatures. Source: reprinted from ref. [225] in agreement with the terms of use.

Catalysts	Conversion (%)	Temperature °C	Pressure Mpa	Time h	Reference
Ru/ZrO_2-CeO_2	100	200	5	2	[246]
Ru/ZrO_2	100	240	0.8	1.5	[247]
$RuMoO_x$/AC	99.3	160	3	3	[248]
Ru/C	91.2	200	1	4	[249]
NiMoS/zeolites	100	345	5	3	[250]
Ni/Al_2O_3	100	325	5	1	[242]
Ni-Al-2-LDH	100	125	2.5	1	our work

4.3.3 DFT calculation

DFT calculations were performed to elucidate the hydrogenolysis mechanism and, in particular, to compare the intrinsic catalytic roles of metallic Ni, NiO, and their interfacial combination.[225] The stable low-index facets Ni (111) and NiO (100) were therefore selected to model metallic Ni and NiO, respectively (Figure S10 and Figure S11). In addition, a Ni/NiO nanowire model was constructed to capture the synergistic interaction between Ni(0) and Ni(II) species at the interface.[251–253] To reduce computational cost while retaining physical fidelity, the influence of NiO slab thickness was first examined. Reactant adsorption energies computed on two-layer and three-layer NiO slabs differ by only ~0.1 eV, indicating that a two-layer slab provides an adequate description. The stability of Ni nanowires adsorbed at different sites on the NiO surface was further evaluated (Figure S12), showing that the most stable configuration involves Ni bonding to surface oxygen atoms. Based on these benchmarks, a composite model consisting of a two-layer NiO (100) slab supporting a three-layer Ni nanowire was adopted (Figure 4-12 a).

Electronic-structure modifications induced by NiO were then analyzed by comparing the density of states (DOS) of Ni (111) with that of the Ni/NiO nanowire model. The partial DOS (PDOS) of Ni 3d states is shown in Figure 4-12 b. Relative to Ni (111), the Ni/NiO system exhibits a noticeable shift in the 3d-state peak near −2 eV, indicating that interaction with the underlying NiO layer perturbs the electronic structure of surface Ni. In addition, the Ni 3d states become more localized in the Ni/NiO system. Because Ni is not purely metallic in this composite environment, redistribution of

orbital occupancy and energy levels leads to a downward shift of the d-band center. Such shifts are known to modulate adsorption strength and surface reactivity, with a d-band center closer to the Fermi level typically associated with higher activation capability.

Next, PPE adsorption was evaluated on Ni (111), NiO (100), and Ni/NiO (Figure S 13 and Figure S14; Table S5-7), and the most stable adsorption configurations are summarized in Figure 4-12 c. Among the three surfaces, NiO (100) exhibits the weakest adsorption, whereas stronger binding is obtained on Ni (111) and Ni/NiO. Because PPE adsorption is dominated by aromatic-ring interactions, and adsorption of monocyclic aromatics on metal surfaces often correlates with the d-band center (a lower d-band center generally leading to stronger adsorption), Ni/NiO would be expected to bind PPE more strongly than Ni (111). However, the calculated adsorption energy on Ni (111) is slightly higher than that on Ni/NiO. This apparent inconsistency can be rationalized by stronger coupling and charge transfer upon adsorption, which increases the occupation of antibonding states and thereby weakens the net adsorption strength on the interfacial model.[254,255] To probe this effect, charge-density difference plots and Bader charge analysis were performed (Figure 4-12 d–f). Pronounced charge redistribution is observed upon PPE adsorption on both Ni (111) and the Ni/NiO nanowire, indicating strong chemisorption, whereas charge transfer on NiO (100) is much weaker, consistent with predominantly physisorptive interactions. Bader analysis quantifies electron transfer of 0.51 e and 0.80 e from the Ni (111) and Ni/NiO surfaces to PPE, respectively, while negligible charge transfer is obtained for NiO.

Finally, reaction pathway diagrams for PPE hydrogenolysis were constructed on Ni (111) and Ni/NiO (Figure 4-12 g).[225] The elementary steps and corresponding energies are summarized in Table 4-7 and Table S8-9, and the relevant transition-state structures are provided in Figure S15 and Figure S16. The overall reaction is exothermic, with a Gibbs free-energy change (ΔG) of -168.85 kJ mol^{-1} at the experimental temperature of 125 °C. Compared with Ni (111), the Ni/NiO system exhibits a smoother free-energy profile along the key hydrogenolysis steps, indicating more favorable thermodynamics. In the product-desorption steps, larger free-energy changes are obtained on Ni/NiO, suggesting stronger binding of monomeric products and, consequently, an increased likelihood of subsequent hydrogenation and aromatic-ring saturation prior to desorption. Notably, the activation barrier for β-O-4 C–O bond cleavage is only 0.35 eV on Ni/NiO, compared with 0.94 eV on Ni (111), demonstrating a substantially lower kinetic barrier at the interface. This result is consistent with experimental observations that catalysts prepared by wet impregnation or conventional coprecipitation, as well as the Ni/Al-0.25 LDH catalyst lacking NiO, fail to activate C–O bond cleavage at 125 °C. Moreover, for hydrogenation of monomeric intermediates after C–O cleavage, Ni/NiO also exhibits lower barriers than Ni (111), indicating faster intermediate conversion and an overall enhancement of reaction rate.

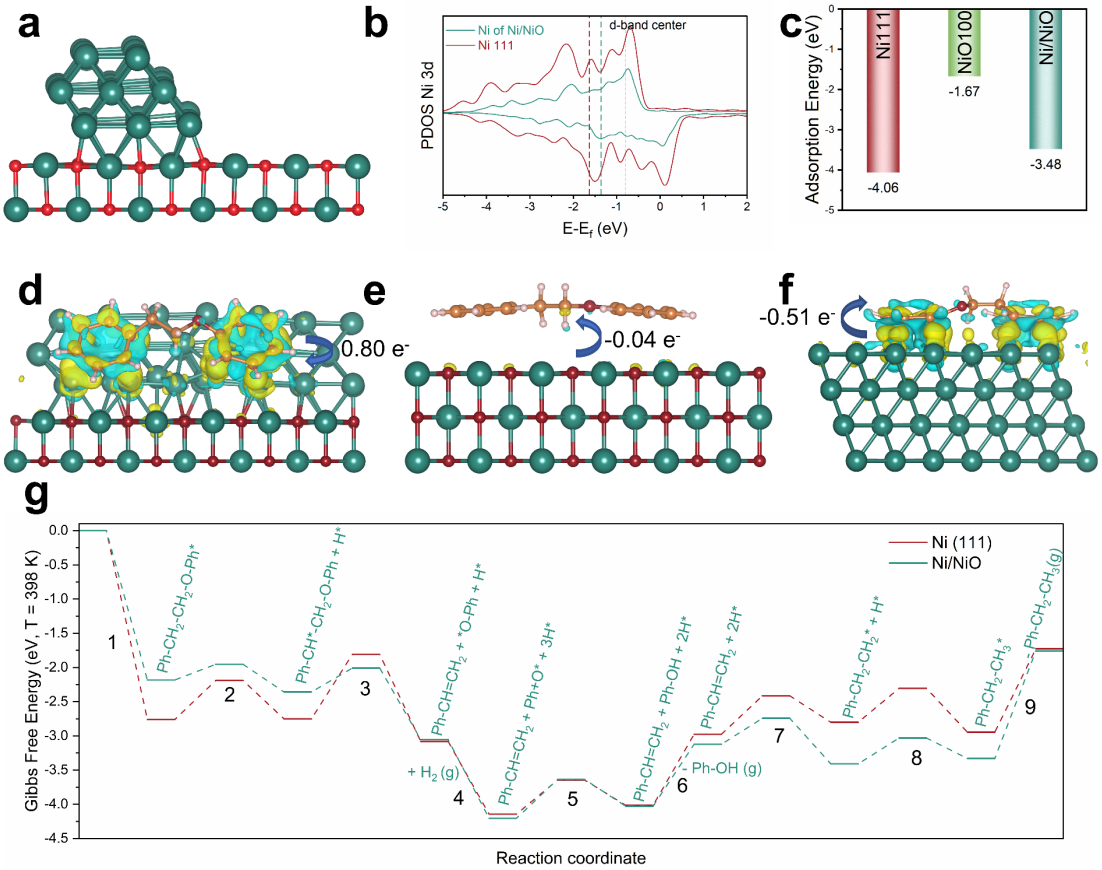

Figure 4-12: a. The Ni/NiO nanowire model; b. PDOS and d-band center of Ni supported on NiO and Ni (111); c. Comparison of adsorption energies over Ni (111), NiO (100), and Ni/NiO; d-f. Charge density difference of Ni/NiO (d), NiO (100) (e), and Ni (111) (f); The blue (yellow) distribution corresponds to charge accumulation (depletion), and the black value represent the number of electron transfers in Bader charges; The Ni, O, C, H atoms are presented as green, red, orange and pink, respectively; g. The Gibbs Free energy diagram of PPE hydrogenolysis over Ni/NiO and Ni (111) under 398 K (125°C), The numbers 1-9 represent the elementary steps listed in Table 4-7. Source: reprinted from ref. [225] in agreement with the terms of use.

Table 4-7: Reaction coordinate steps over Ni (111) and Ni/NiO slab. Source: reprinted from ref. [225] in agreement with the terms of use.

	Element step	
	Ni (111)	Ni/NiO
1	PPE(g) → PPE*	
2	PPE* → Ph-CH_2-CH*-O-Ph + H*	PPE* → Ph-CH*-CH_2-O-Ph + H*
3	Ph-CH_2-CH*-O-Ph → Ph-CH_2-CH* + *O-Ph	Ph-CH*-CH_2-O-Ph → Ph-CH=CH_2* + *O-Ph
4	H_2(g) → 2H*	
5	Ph-O* + H*→ Ph-OH*	
6	Ph-OH* → Phenol (g)	
7	Ph-CH_2-CH* + H* → Ph-CH_2-CH_2*	Ph-CH=CH_2* + H* → Ph-CH_2-CH_2*
8	Ph-CH_2-CH_2* + H* → Ph-CH_2-CH_3*	
9	Ph-CH_2-CH_3* → Ph-CH_2-CH_3(g)	

4.3 Interlayer doping of Mo in Ni/Al_2O_3 catalysts for enhanced hydrodeoxygenation performance of bio-oil

4.3.1 Catalyst characterization

As written in the Methods catalyst preparation section, a series of doped Ni/Al_2O_3 catalysts were synthesized via a co-precipitation approach. Mo was selected as the optimal dopant based on preliminary screening experiments, which revealed its superior catalytic performance in HDO compared to other oxophilic metals (Figure 4-13). During synthesis, the co-precipitation process led to the formation of a LDH precursor, with MoO_x and CO_3^{2-} anions intercalated into the interlayer spaces. This structural feature facilitated the uniform incorporation of Mo within the Ni-Al LDH, leading to the development of a multi-phase metal–oxide system characterized by a high surface area and potential synergistic effects between the components. Subsequently, the precipitate underwent calcination and reduction, forming the morphology illustrated in the schematic. In this process, metal and metal oxide nanoparticles were uniformly dispersed on the Al_2O_3 support, enhancing the interaction between the active metal species and the support material. On a finer scale, as observed in last part of Figure 4-13, a portion of the MoO_x species appears to decorate the Ni surface.

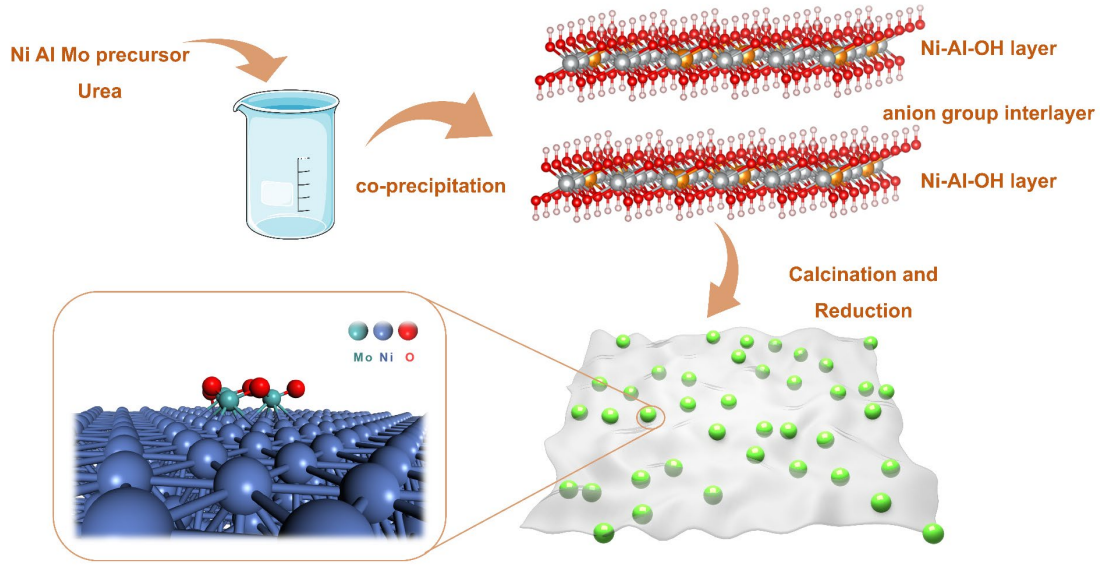

Figure 4-13: Schematic illustration of the synthesis of Mo doped Ni Al catalyst derived from LDH structure.

Firstly, the morphology of the Mo doped Ni/Al_2O_3 catalyst was investigated using SEM, and the results are presented in Figure 4-14 a,b. The catalyst exhibits loose aggregates with distinct flower-like or lamellar structures, a hallmark of LDH-type morphologies consistent with those reported by Joseph and Feng et al. [256,257] The flower-like and lamellar structures significantly enhance the catalyst's porosity and accessibility of active sites, which are critical for achieving high catalytic efficiency in HDO processes. Remarkably, these morphological features persist even after calcination and reduction, suggesting the retention of porous and layered structures. This architecture enables a uniform distribution of active catalyst particles. Results of the N_2 adsorption–desorption (BET) measurements are presented in Figure S 17. The high surface area of the support, derived from the preserved LDH-like features, is particularly advantageous for exposing additional active sites, thereby improving HDO performance. Elemental mapping via energy-dispersive X-ray spectroscopy (EDX), as shown in Figure S18 and Table S10, confirms the uniform spatial distribution of Ni, Mo, Al, and O across the sample. Importantly, no evidence of particle aggregation or element segregation was observed. The efficient integration of Mo within the Ni/Al_2O_3 matrix via impregnation and calcination appears to foster synergies between the Ni and Mo species, likely enhancing the overall catalytic performance. To further elucidate the structural properties of the catalyst, TEM characterization was conducted, and the corresponding results are shown in Figure 4-14 c. The TEM images reveal bright regions corresponding to Ni-rich areas, while the gray domains are primarily attributed to the Al_2O_3 support material. Particle size analysis, performed using ImageJ[258] software and illustrated in Figure 4-14 d, demonstrates that the majority of nanoparticles have diameters ranging between 10 and 15 nm. The narrow particle size distribution and high degree of dispersion contribute significantly to the catalyst's enhanced performance. Specifically, the small particle sizes ensure a greater number of exposed active metal sites, which is crucial for facilitating guaiacol HDO reactions with high efficiency. In summary, the preparation and characterization of Mo doped Ni/Al_2O_3 catalysts demonstrate a well-defined structure with uniformly dispersed nanoparticles and preserved LDH-like morphologies. The combination of SEM and TEM analyses highlights the structural advantages of the catalyst, including high surface area, uniform dispersion, and narrow particle size distribution, all of which are critical for improving catalytic performance in hydrodeoxygenation reactions.

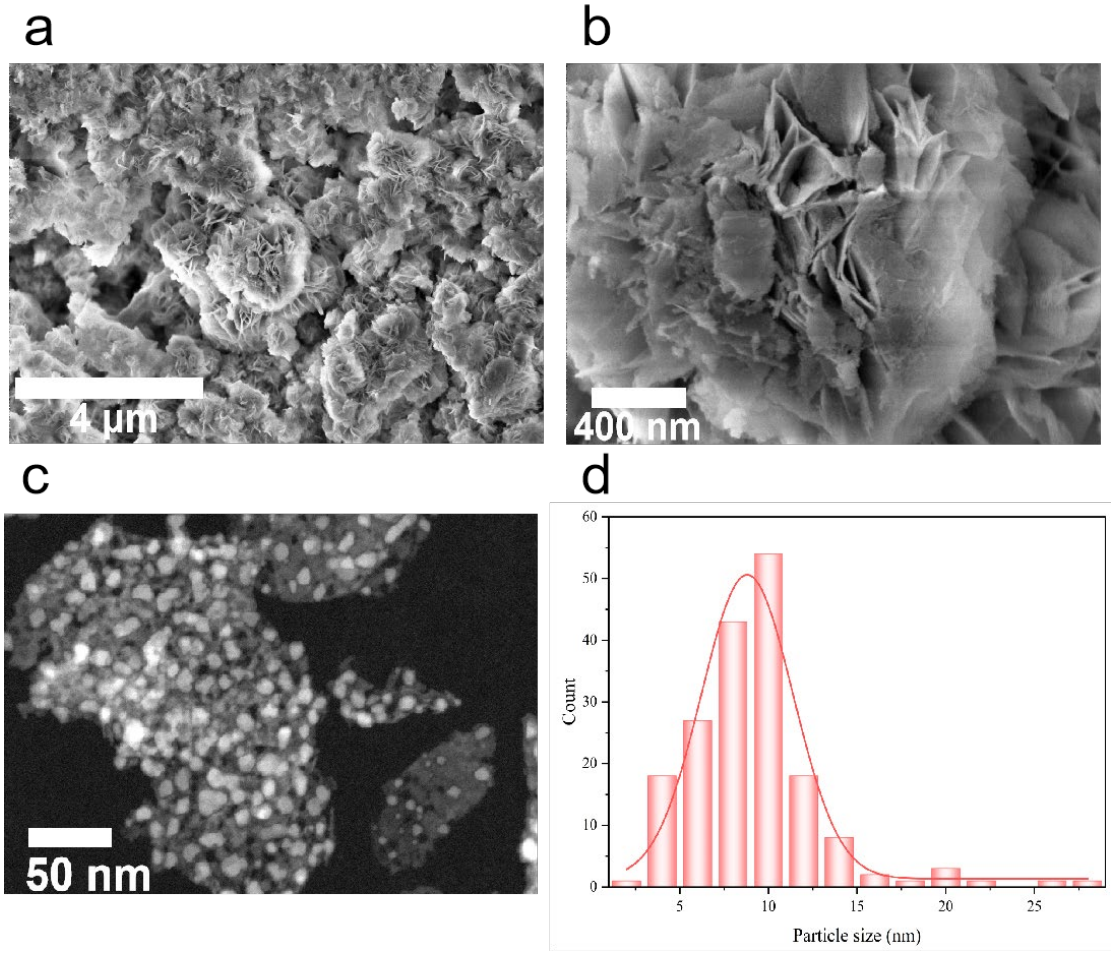

Figure 4-14: a,b. SEM images of Mo doped Ni/Al_2O_3 catalyst; c. TEM image of Mo doped Ni/Al_2O_3 catalyst; d. Particle size distribution from TEM image.

XRD patterns of Ni/Al_2O_3 and doped Ni/Al_2O_3 catalysts (doped with Mo, Nb, Ce, and W) were shown in Figure 4-15. Based on the standard PDF cards, the primary diffraction peaks correspond to metallic Ni and the Al_2O_3 support. For the Al_2O_3 characteristic peaks, their subdued intensity suggests an irregular crystal morphology induced during calcination, which likely increases the number of exposed active sites on the support. Additionally, faint peaks attributed to NiO are observed, indicating that a portion of Ni species remains in an oxidized state post-reduction, as confirmed in our previous studies. A comparison of the XRD patterns shows that the overall phase composition is not significantly affected by the addition of dopants (Mo, Nb, Ce, and W), likely due to the low doping ratio of only 1%, the precise dopant contents determined by ICP-OES are shown in Table S11. The characteristic reflections of Ni and Al_2O_3 remain dominant across all samples. However, slight shifts or changes in peak intensities can be observed, suggesting partial incorporation of dopants or the

formation of small amounts of dopant-containing phases that are either amorphous or below the detection limit of XRD.

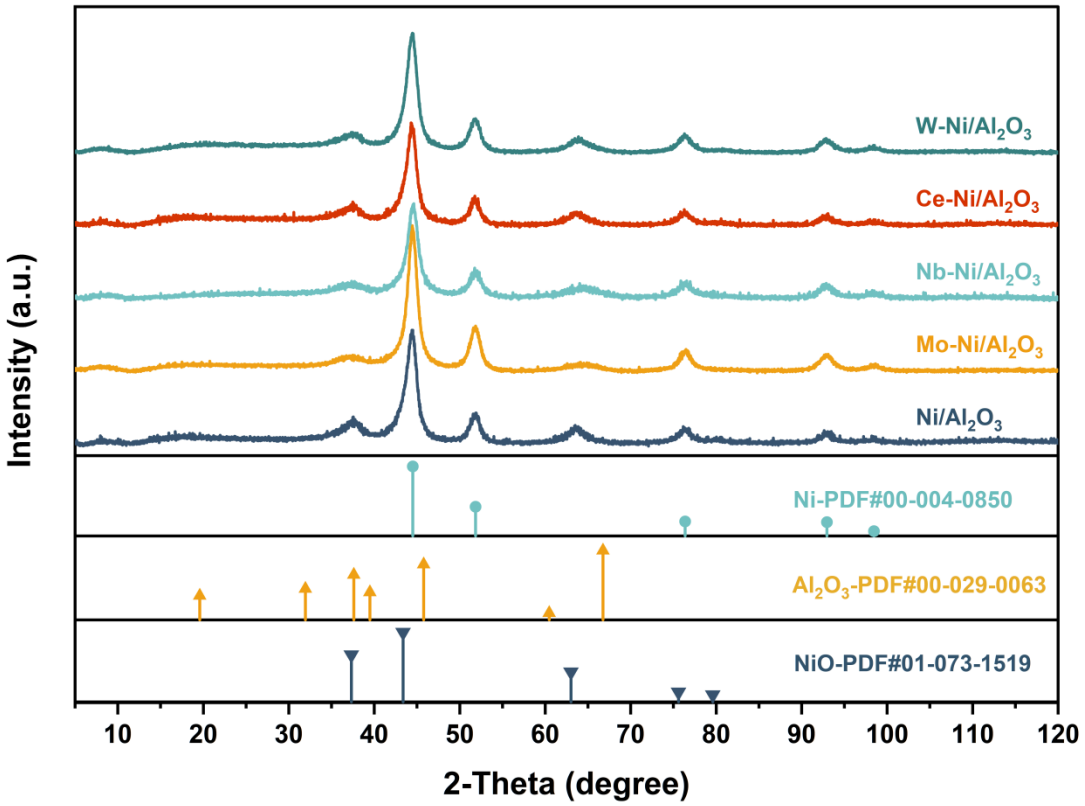

Figure 4-15: XRD patterns of undoped Ni/Al_2O_3 and Ni/Al_2O_3 doped with Mo, Ce, Nb, and W.

High-resolution XPS spectra of the Mo 3d (a) and Ni 2p (b) regions were obtained for the Mo doped Ni/Al_2O_3 catalyst, as shown in Figure 4-16. In the Mo 3d spectrum (Figure 4-16 a), multiple peaks were deconvoluted, revealing Mo(IV) (229.3 eV), Mo(V) (231.0 eV), and Mo(VI) (232.7 eV), in agreement with previous studies.[259–261] The coexistence of these oxidation states indicates that partial reduction occurred during catalyst preparation. Notably, the unsaturated Mo species in Mo(IV) and Mo(V) oxidation states exposed additional acidic sites, which could enhance deoxygenation efficiency in subsequent HDO processes.

In the Ni 2p region (Figure 4-16 b), peaks corresponding to Ni^{2+} (centered around 855.6 eV) and Ni^0 (near 852 eV) were observed, along with a satellite feature at approximately 860 eV, characteristic of Ni-based compounds. The simultaneous presence of Ni^{2+} and Ni^0 suggests that complete reduction was not achieved or that partial re-oxidation occurred, consistent with our previous findings. The elevated Ni^{2+} signal was primarily attributed to the high Ni content (70%) in the Ni/Al_2O_3 catalyst, which rendered it susceptible to oxidation during storage and difficult to fully reduce.

Overall, the XPS results elucidated the intricate surface chemistry of the Mo doped Ni/Al_2O_3 catalyst and highlighted the synergistic effects arising from the unsaturated oxidation states of Mo and Ni in promoting HDO catalytic performance.

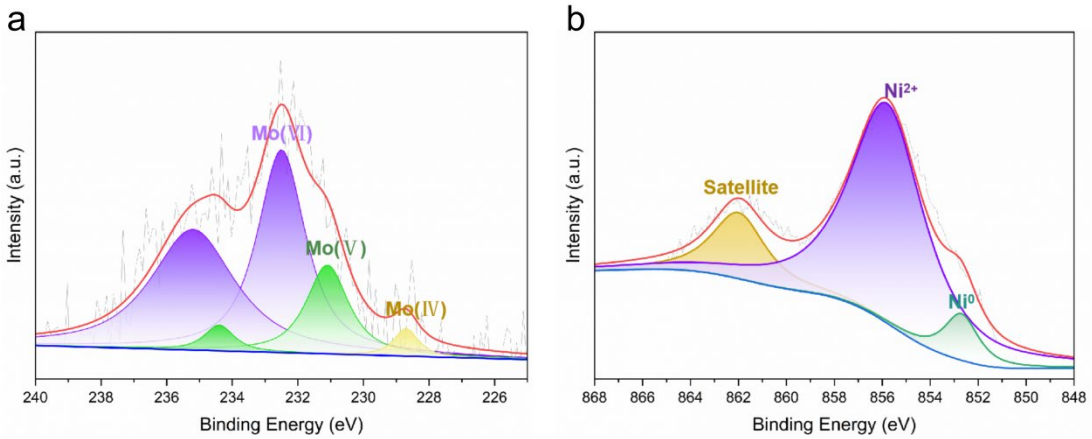

Figure 4-16: Mo 3d and Ni 2p High resolution XPS spectra for Mo doped Ni/Al_2O_3 catalyst.

4.3.2 HDO of guaiacol

The catalytic HDO of guaiacol was conducted using both unmodified Ni/Al_2O_3 and doped Ni/Al_2O_3 catalysts (Mo, Ce, Nb, W), as illustrated in Figure 4-17 a. Notably, complete conversion (100%) was achieved in all catalytic systems, demonstrating that unmodified Ni/Al_2O_3 already possesses sufficient activity for guaiacol transformation. This discussion focuses on the impact of doping on product selectivity. Overall, the product distributions predominantly consisted of cyclohexanol and cyclohexane, with minor byproducts, such as methoxycyclohexanol and 1,2-cyclohexanediol. For the undoped Ni/Al_2O_3 catalyst, approximately 40% of the products comprised cyclohexanol, suggesting limited deoxygenation efficiency under the reaction conditions.

The introduction of dopants significantly influenced selectivity patterns, reflecting differences in active sites and cleavage mechanisms. Among the doped catalysts, W doped Ni/Al_2O_3 produced more oxygenated compounds, indicating that W had adverse effects during the HDO process. Similarly, for Ce and Nb doped Ni/Al_2O_3 catalysts, although the cyclohexanol content decreased, the proportion of other oxygenated compounds increased, suggesting limited improvements in deoxygenation efficiency.

In contrast, the Mo doped Ni/Al_2O_3 catalyst exhibited the best performance, yielding a higher proportion of cyclohexane compared to other doped catalysts. This suggests that

Mo species facilitated partial hydrogenation and promoted complete deoxygenation. Deoxygenation processes are typically associated with acidic sites on metal oxides. XPS analysis revealed abundant unsaturated MoO_x species in Mo doped Ni/Al_2O_3, where these surface exposed sites provided additional acidic centers that directly correlated with the enhanced deoxygenation rate, consistent with previous studies, and the NH_3-TPD result is shown in Figure S19.[262,263] Mechanistic investigations of guaiacol HDO have established that all catalysts in this study effectively drive the demethoxylation of guaiacol, followed by Ni-mediated hydrogenation of the aromatic ring to yield cyclohexanol as the primary intermediate.[264,265] However, for the subsequent dehydroxylation of cyclohexanol to cyclohexane, the activity of Ni is relatively low, while the additional acidic sites introduced by MoO_x play a crucial role.

The influence of reaction temperature on product selectivity was also investigated, as shown in Figure 4-17 b. At lower temperatures (200 and 220 °C), intermediates such as methoxycyclohexanol and 1,2-cyclohexanol dominated the product distribution. As the temperature increased, the selectivity for deoxygenated products such as cyclohexane gradually rose, while the amount of cyclohexanol declined. At 280 °C, the product distribution shifted toward fully deoxygenated products, enhancing the selectivity for cyclohexane. These results demonstrate that higher temperatures facilitate subsequent hydrogenation and deoxygenation steps, favoring cyclohexane formation.

In summary, over Mo doped Ni/Al_2O_3 catalyst, the cyclohexane selectivity reached 89% in 250 °C and 99% in 280 °C. Compared with the reported results in the literatuter, it is better than them as shown in Table 4-8. Furthermore, these findings confirm that the HDO reaction mechanism of guaiacol follows a pathway from guaiacol to cyclohexanol and subsequently to cyclohexane, with the latter representing the key deoxygenation step. Overall, the results underscore the combined effects of catalyst composition and reaction conditions in modulating the HDO performance of guaiacol.

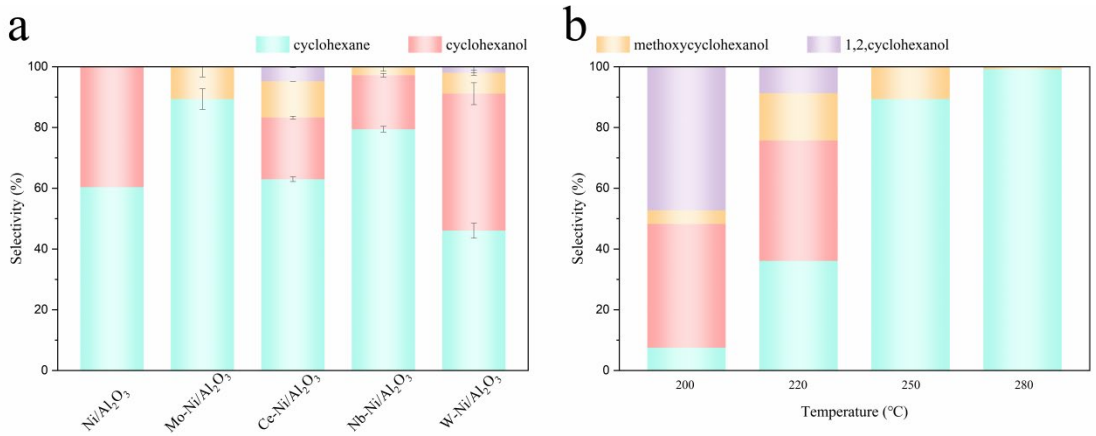

Figure 4-17: a. The product distribution of guaiacol HDO over different catalysts, reaction conditions: 250 °C, 50 bar H_2, 2h. b. the product distribution of guaiacol

HDO over Mo doped Ni/Al_2O_3 catalyst under different temperatures; reaction conditions: 50 bar H_2, 2h.

Table 4-8: Catalytic performance of various catalysts for the hydrodeoxygenation of guaiacol, with cyclohexanol as the primary product.

Catalyst	Selectivity %	Temperature °C	Pressure bar	Time hour	ref
Ni/SiO_2	56	140	30	5	[266]
Co/ZrP	76	200	70	2.5	[267]
Ni/SiO_2-ZrO_2	97	300	50	8	[268]
$NiCu/ZrO_2$-SiO_2	81	300	50	8	[269]
Ni/HZSM-5	79	250	50	4	[270]
Ni/CNT	45	300	40	4	[271]
$NiCo/Al_2O_3$	96	200	50	8	[272]
NiZr-SBA-TS	88	300	50	8	[273]
NiMo/SBA-15	90	250	50	3	[274]
$Ni-Co/Al_2O_3$	54	300	10	4	[275]
$NiFe/Al_2O_3$	88	260	10	1	[276]
FeNi/BN	78	300	30	2	[277]
Ni-Mg/AC	98	300	50	4	[278]

4.3.3 HDO of bio-oil

The composition of the bio-oil before and after upgrading was determined by GC–MS. Semi-quantitative analysis was performed by normalizing total ion chromatogram (TIC) peak areas to 100%. Deoxygenated hydrocarbon products were grouped by carbon number as C_1–C_6, C_7–C_{12}, and C_{13}+. Oxygen-containing species are reported as oxygenated hydrocarbons (oxygenates) in the same carbon-number ranges (C_1–C_6, C_7–C_{12}, C_{13+}). Detailed GC–MS results for the feed bio-oil and for the upgraded oils obtained over Mo–Ni/Al_2O_3 and Ru/C are provided in Table S12 to Table S14.

As illustrated in Figure 4-18, the leftmost bar represents the composition of the bio-oil feedstock, whereas the middle and rightmost bars correspond to the product distributions obtained using the Mo doped Ni/Al_2O_3 catalyst and the commercial Ru/C catalyst, respectively. The feedstock primarily consisted of oxygenated compounds

spanning the C_1–C_6 and C_7–C_{12} ranges, with only minor contributions from deoxygenated hydrocarbons. When the Mo doped Ni/Al_2O_3 catalyst was employed for HDO, a significant reduction in the overall oxygenated species was observed, accompanied by an increased proportion of hydrocarbons—notably within the C_7–C_{12} range. This behavior indicates that Mo doped Ni/Al_2O_3 effectively removed oxygen from the bio-oil under the investigated conditions while largely preserving mid-range carbon structures. The resultant higher degree of deoxygenation suggests that Mo doped Ni/Al_2O_3 facilitated more complete oxygen removal, thereby producing a greater yield of C_7–C_{12} hydrocarbons. In contrast, the commercial Ru/C catalyst produced a noticeable fraction of oxygenated compounds, particularly within the C_7–C_{12} range and extending to higher carbon numbers. This outcome suggests that under identical reaction conditions, Ru/C exhibited a lower extent of deoxygenation, allowing a substantial amount of partially oxygenated species to persist in the product. It is hypothesized that Ru/C may preferentially facilitate partial hydrogenation or inhibit deeper deoxygenation steps, leaving residual oxygen in the upgraded bio-oil.

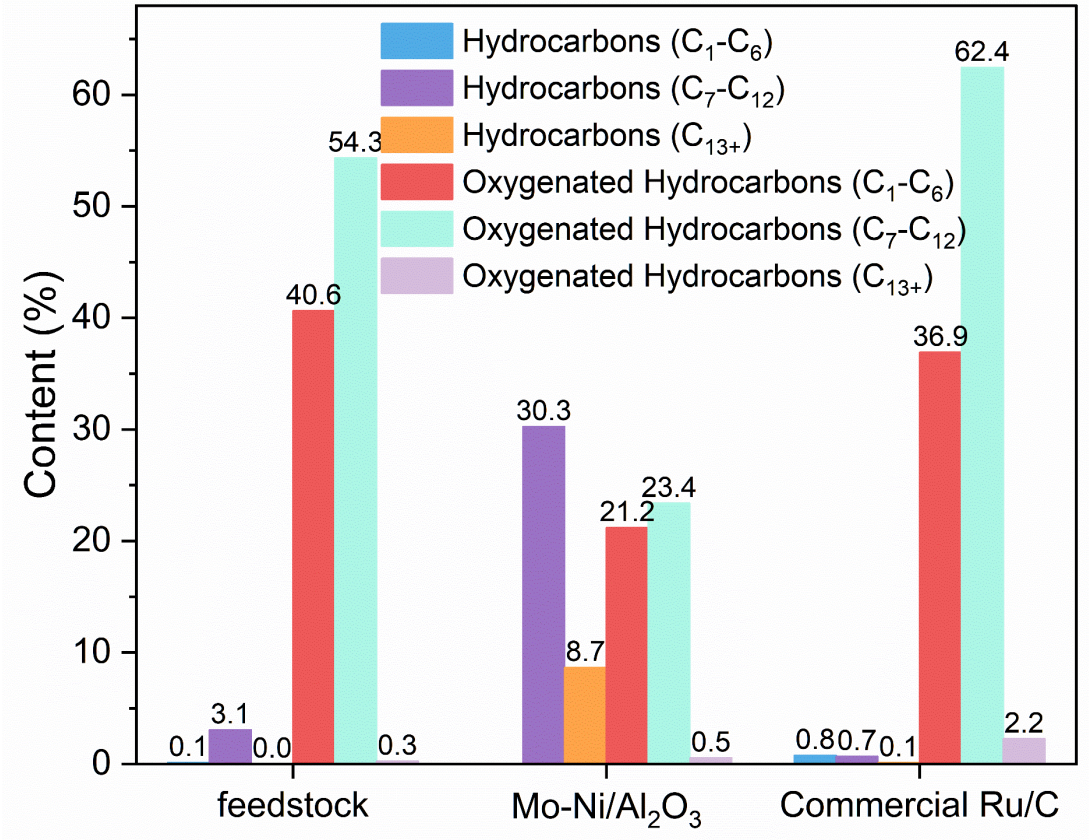

Figure 4-18: The product distribution of bio-oil HDO over Mo doped Ni/Al_2O_3 catalyst. Reaction conditions: 250 °C, 50 bar H_2, 2h.

Product analysis shows that upgrading over Mo–Ni/Al_2O_3 virtually eliminates phenolics, indicating highly efficient dehydroxylation and demethoxylation, and produces a large fraction of newly formed cycloalkanes. In contrast, the commercial Ru/C catalyst performs less effectively, retaining a noticeable amount of phenolic species. For other oxygenates (e.g., ketones and acids), the Mo/Al_2O_3 catalyst likewise exhibits superior activity, converting most of them into alcohols and hydrocarbons. The Ru/C product, however, still contains abundant cyclohexanone and anhydrides, evidencing insufficient deep deoxygenation and a tendency to accumulate highly oxygenated functionalities.

In summary, Mo doped Ni/Al_2O_3 and Ru/C exhibited markedly different catalytic behaviors during bio-oil HDO. Mo doped Ni/Al_2O_3 achieved a higher degree of oxygen removal, resulting in an increased yield of mid-range deoxygenated hydrocarbons. These findings demonstrate that the Mo doped Ni/Al_2O_3 catalyst is not only highly effective in achieving high deoxygenation rates and selectivity in guaiacol model compound HDO but also performs exceptionally well with real complex bio-oil feedstocks.

4.3.4 DFT calculation

To gain a deeper understanding of the HDO catalytic process discussed in the experimental section, DFT calculations were employed. A Ni (111) surface model was initially constructed to investigate the behavior of Ni/Al_2O_3 catalysts. For the case of Mo doping, MoO_x clusters were modeled on the Ni (111) surface. Based on previous studies by Wu et al,[279] which systematically explored the configurations of Mo_3O_x (x=3-9) clusters, Mo_3O_5 was identified as the most stable structure under hydrogen atmosphere. This finding aligns with our XPS results, which revealed the presence of unsaturated Mo species. Consequently, subsequent comparative studies focused on the Ni (111) surface and the Mo_3O_5 cluster on Ni (111).

In the experimental HDO of guaiacol, the introduction of Mo into the Ni/Al_2O_3 catalyst shifted the product distribution from cyclohexanol to cyclohexane as the dominant product. Both Ni/Al_2O_3 and Mo doped Ni/Al_2O_3 catalysts demonstrated excellent activity for the conversion of guaiacol to cyclohexanol. Thus, our DFT investigation primarily targeted the conversion of cyclohexanol. The adsorption of various cyclohexanol configurations on Ni (111) and Mo_3O_5/Ni (111) surfaces was explored, with detailed results presented in Figure S20 and Figure S21. As shown in Figure 4-19, the most stable adsorption geometries of cyclohexanol on the two surfaces, Ni (111) (Figure 4-19 a) and Mo_3O_5/Ni (111) (Figure 4-19 b), were obtained via DFT calculations. The adsorption energies were calculated to be −1.28 eV for Ni (111) and −1.78 eV for Mo_3O_5/Ni (111), indicating that cyclohexanol binds more strongly to the Mo_3O_5 modified Ni surface. The OH group in cyclohexanol exhibited enhanced

interaction with the Mo sites, suggesting that Mo doping increased the surface's affinity for oxygen-containing functional groups.

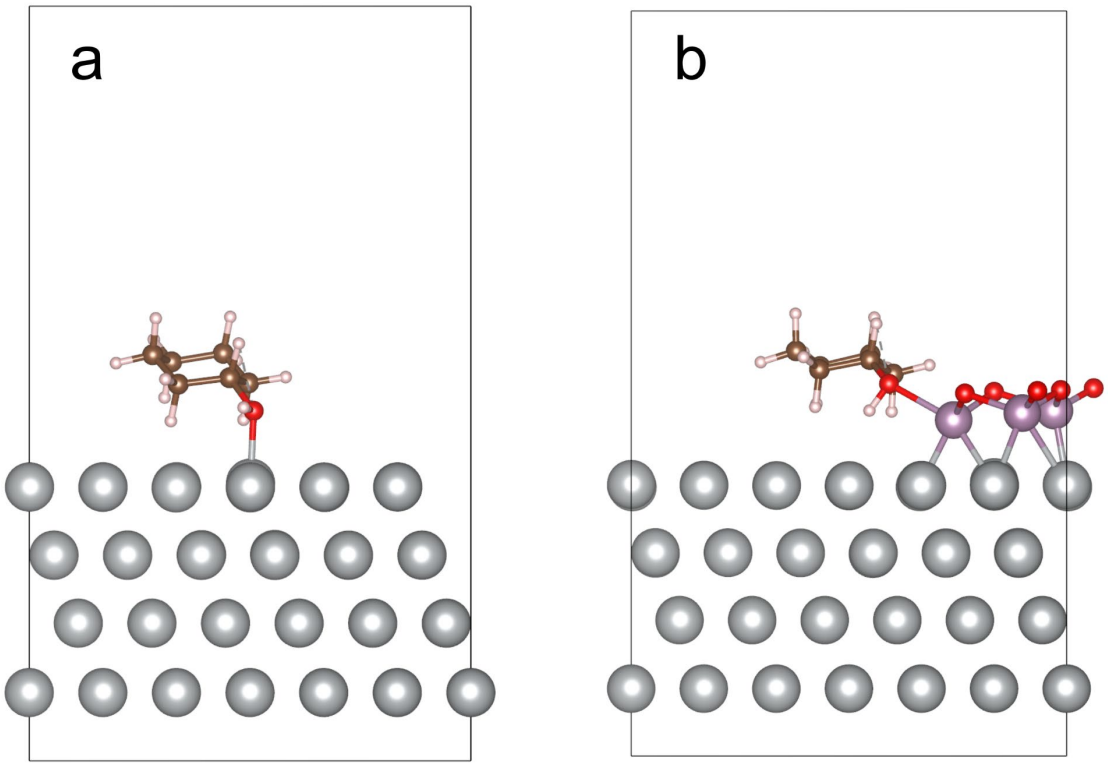

Figure 4-19: DFT models of Ni (111) and Mo_3O_5/Ni (111); The Ni, Mo, O, C, H atoms are presented as grey, purple, red, orange and pink, respectively.

Figure 4-20 presents the charge density difference plots for these adsorption configurations. In these plots, regions of electron accumulation are shown in blue, while regions of electron depletion appear in yellow. On Ni (111) (Figure 4-20 a), moderate electron redistribution near the adsorbed cyclohexanol was observed, consistent with a typical molecular-surface interaction where the OH group donates electron density to the metal site. In contrast, a more pronounced charge redistribution occurred on Mo_3O_5/Ni (111) (Figure 4-20 b). Additional blue regions near the Mo species and the hydroxyl group indicated stronger electronic interactions, aligning with the larger adsorption energy. These observations suggest that partial bonding or coordination between the oxygen atom and Mo atoms contributes to the more stable adsorption state.

Overall, these DFT results demonstrate that introducing Mo_3O_5 onto the Ni (111) surface significantly enhances the adsorption strength of cyclohexanol. This effect is likely beneficial for catalytic reactions involving C–O bond activation, as stronger substrate-molecule interactions often facilitate bond cleavage and promote reactivity.

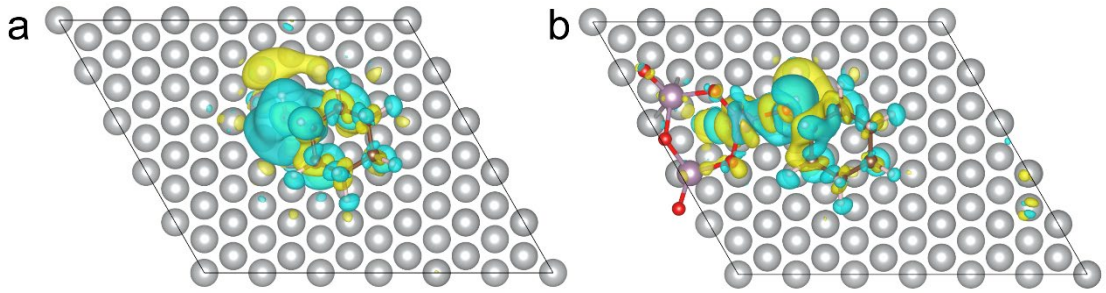

Figure 4-20: Charge density difference of Ni (111) (a), Mo_3O_5/Ni (111) (b); The blue (yellow) distribution corresponds to charge accumulation (depletion)

The energy barrier for cyclohexanol C–O bond cleavage on Ni (111) (bule line) and Mo_3O_5/Ni (111) (orange line) was calculated, as shown in Figure 4-21 to Figure 4-23. A higher TS energy was observed on Ni (111) compared to Mo_3O_5/Ni (111), indicating that the intrinsic barrier for C–O bond cleavage was substantially reduced by the presence of the Mo_3O_5 overlayer. This reduction suggests a more favorable reaction pathway on the Mo containing surface, potentially leading to an enhanced reaction rate under identical reaction conditions. The incorporation of Mo_3O_5 onto Ni (111) lowered the energy barrier for C–O bond cleavage. These energetic advantages were attributed to modifications in the electronic structure and the geometric configuration of active sites introduced by the Mo species. Consequently, the enhanced ability to activate and cleave C–O bonds in cyclohexanol was associated with the strong interaction and favorable energy landscape provided by the Mo_3O_5/Ni (111) system.

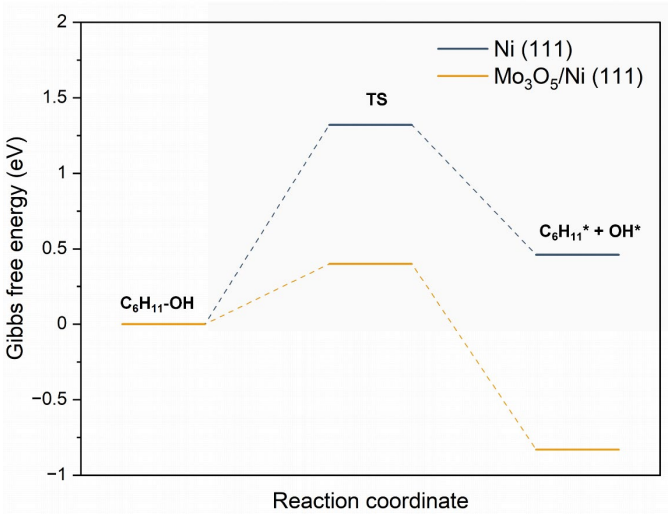

Figure 4-21: The Gibbs Free energy diagram of C-O cleavage on Ni (111) and Mo_3O_5/Ni (111) at a temperature of 250 °C.

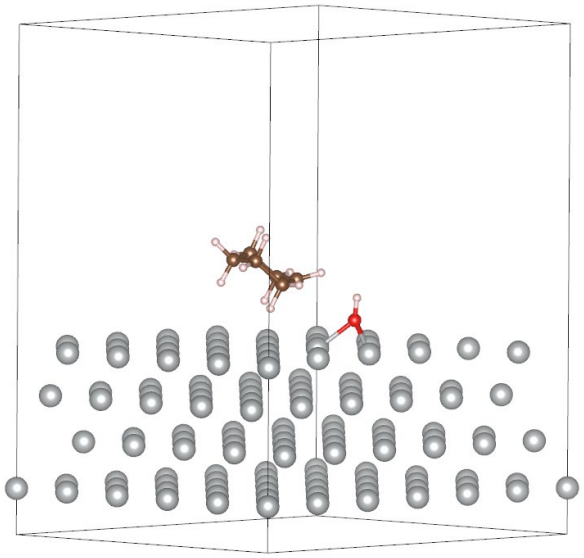

Figure 4-22: Transitation state structures over Ni (111) slab

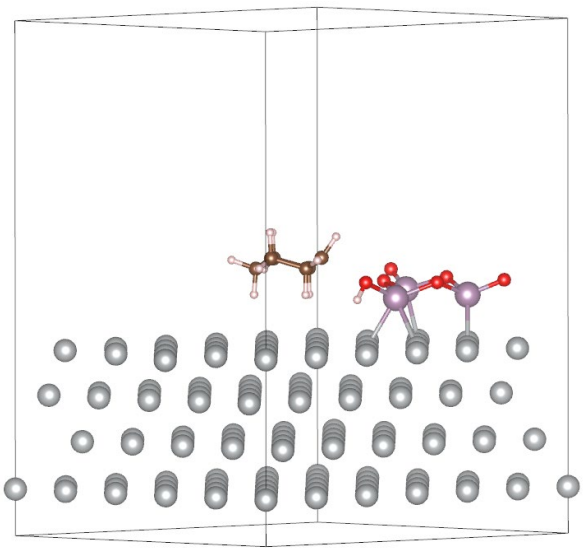

Figure 4-23: Transitation state structures over Mo_3O_5/Ni (111) surface.

4.4 Syngas-promoted catalytic C–C coupling of bio-oil toward longer-chain products

4.4.1 Catalyst characterization

The morphology and elemental distribution of the Ru/β-Zeolite catalyst were investigated using scanning electron microscopy (SEM) coupled with energy-dispersive X-ray spectroscopy (EDX). Figure 4-24 shows SEM images of the β-Zeolite support at different magnifications, illustrating its well-defined crystalline structure and relatively uniform particle (or pore) size distribution. At higher magnification (Figure 4-24 b), Ru nanoparticles are observed as fine, bright spots on the zeolite surface, indicating their successful deposition in the nanometer range. The absence of large agglomerates suggests effective dispersion of Ru—an essential factor for maximizing accessible catalytic active sites.

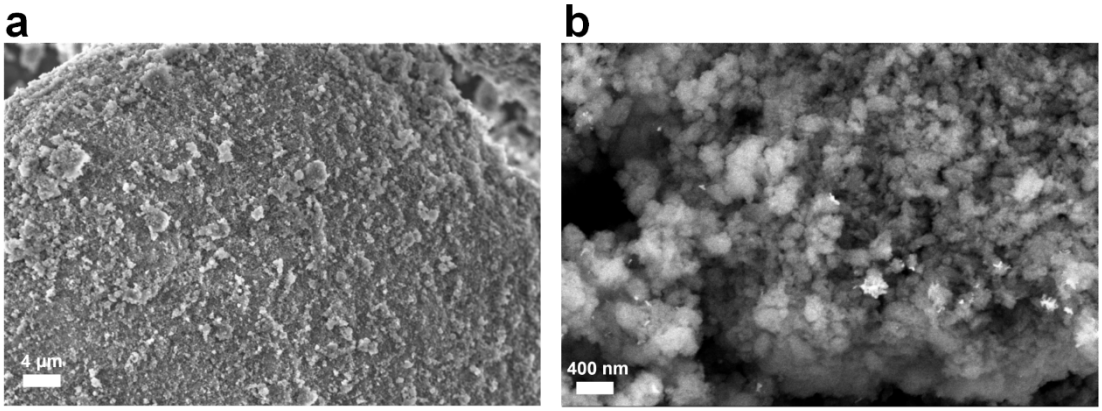

Figure 4-24: SEM images of Ru/β-zeolite catalyst.

To further confirm the presence and distribution of Ru, SEM-EDX elemental mapping was performed (Figure 4-25). The homogeneous spatial distribution of Ru signals overlapping with the zeolite framework points to uniform anchoring of Ru nanoparticles. Such uniformity helps maintain good contact between the active metal sites and the reactants during catalytic processes.

Quantitative EDX analysis (Table 4-9) confirms the targeted Ru loading, measured at 0.43 atomic% (2.14 mass%). This result verifies the successful incorporation of Ru into the β-zeolite support, creating well-dispersed active sites without notable phase segregation. The combination of SEM observations and elemental analysis thus establishes that Ru/β-zeolite was synthesized with uniformly distributed Ru nanoparticles—an advantageous feature for subsequent catalytic applications.

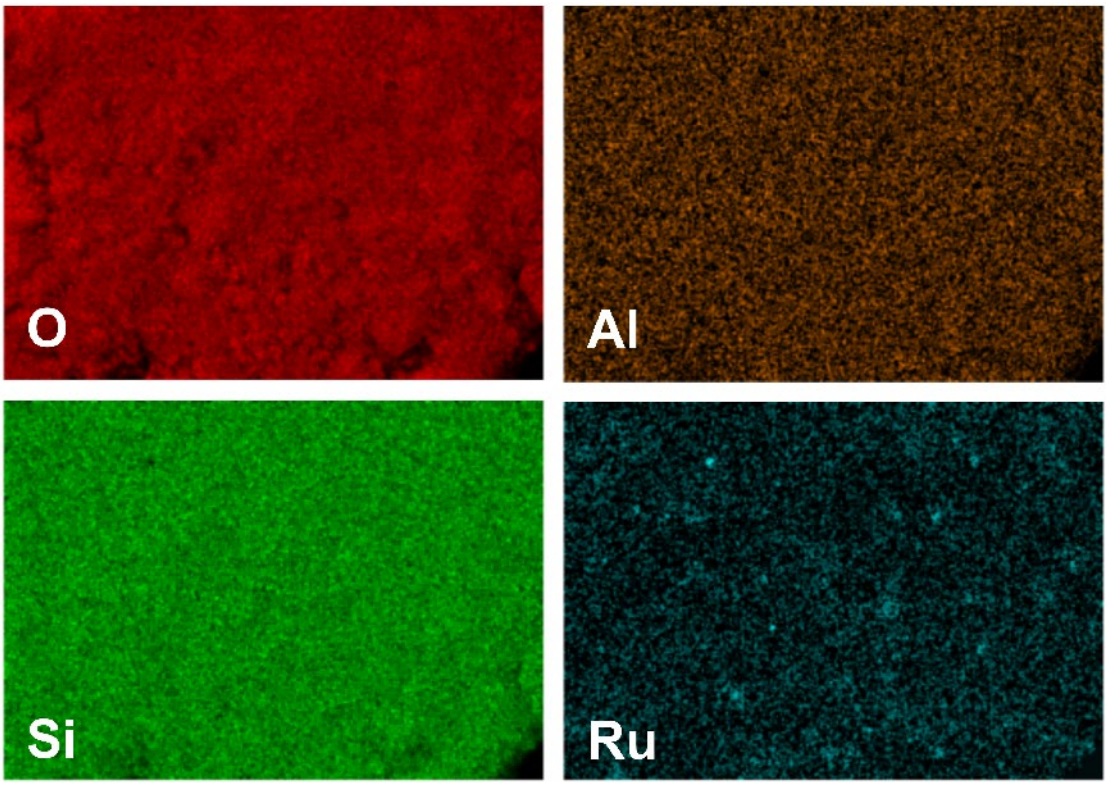

Figure 4-25: SEM-EDX mapping of Ru/β-zeolite catalyst.

Table 4-9: Element content of Ru/β-zeolite catalyst by SEM-EDX.

Element	Mass%	Atom %
O	49.21	63.65
Al	3.46	2.66
Si	45.11	33.24
Ru	2.22	0.46

The XRD patterns of β-zeolite and Ru/β-zeolite samples are presented in the Figure 4-26. The main diffraction peaks of both β-zeolite (gray line) and Ru/β-zeolite (red line) samples appear at similar positions, indicating that the loading of Ru did not alter the crystalline structure of the β-zeolite support. Both samples exhibit characteristic diffraction peaks at 2θ values of 7.7° and 22.5°, which are attributed to the (101) and (302) crystal planes of β-zeolite, respectively.

In the Ru/β-zeolite sample, characteristic diffraction peaks corresponding to metallic Ru are observed at 2θ values of 38.4°, 42.2°, 44.0°, and 58.3°, confirming the successful incorporation of Ru onto the β-zeolite support. However, the relatively low intensity of these Ru peaks suggests poor crystallinity of the Ru phase, which can be attributed to the low loading amount (2%) that inhibited the formation of larger crystallites.

Furthermore, the overall peak profiles and relative intensities of the Ru-loaded sample remain consistent with those of pristine β-zeolite, further confirming that the introduction of Ru did not cause significant structural changes or collapse of the support, thereby preserving the crystallinity and porous architecture of the β-zeolite. In conclusion, the XRD results demonstrate the successful deposition of 2% Ru onto β-zeolite while maintaining the structural integrity of the support, providing a solid foundation for subsequent catalytic performance studies.

The N_2 adsorption–desorption isotherm (Figure 4-27) exhibits a steep initial uptake at low relative pressures ($P/P_0 < 0.05$), followed by a quasi-linear increase and an H3-type hysteresis loop that closes at $P/P_0 \approx 0.45$.[280] This behaviour is characteristic of an IUPAC type IV isotherm, indicating a predominantly mesoporous framework formed by the loose aggregation of plate-like particles.[281] The average pore diameter derived from the Barrett–Joyner–Halenda (BJH) model is 7.4 nm, while a minor low-pressure knee reveals the presence of a small fraction of micropores (< 2 nm).[282] Together with a moderate BET surface area of 158 $m^2 g^{-1}$ and a high total pore volume of 0.624 $cm^3 g^{-1}$, these textural features provide abundant, interconnected mesopore channels that ensure effective dispersion of metal active sites and rapid diffusion of bulky bio-oil molecules.

The NH_3-TPD curve of Ru/β-zeolite (Figure 4-28) displays three successive desorption maxima at ~210, 370, and 500 °C, evidencing a hierarchical acid-strength distribution. The low-temperature peak (210 °C) originates from weak Brønsted sites on external silanol nests, the intermediate peak at 370 °C corresponds to medium-strength framework Brønsted acid sites (Al–OH–Si), and the high-temperature peak at 500 °C reflects a smaller population of strong Lewis centres generated by extra-framework Al species and Ru–O–Al interfacial ensembles.[283,284] Because weak-to-medium sites dominate the total acidity, the catalyst provides sufficient protonation capacity for C–O activation and C–C coupling without promoting extensive cracking, while the limited fraction of strong sites delivers the energy required for cleaving recalcitrant bonds.[285–287] This hierarchically graded acidity, combined with the hydrogenation function of Ru nanoparticles, furnishes an optimal balance for selective hydrodeoxygenation and carbon-retentive upgrading of bio-oil toward SAF-range hydrocarbons.

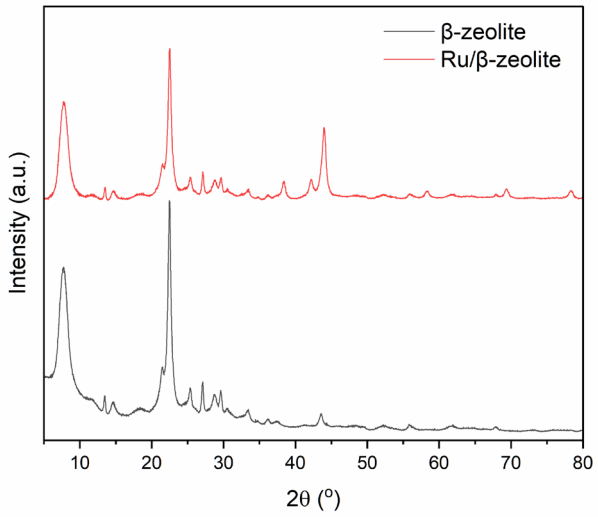

Figure 4-26: XRD patterns of β-zeolite and Ru/β-zeolite catalysts.

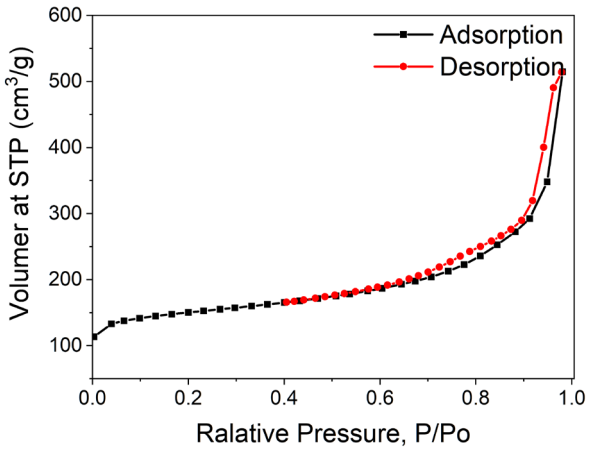

Figure 4-27: N_2 physisorption analysis of Ru/ β-zeolite.

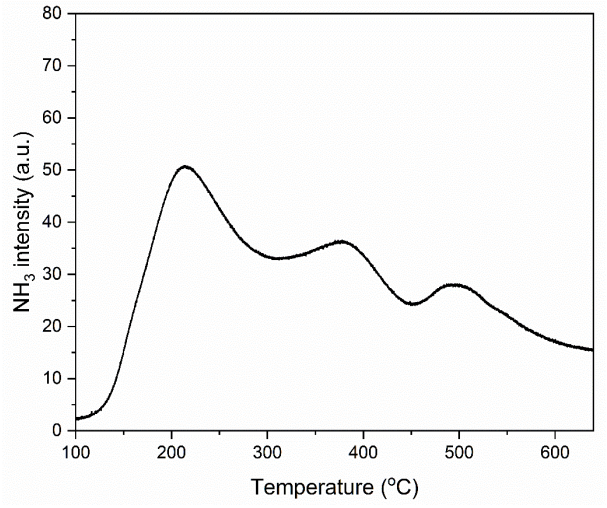

Figure 4-28: NH_3-TPD analysis of Ru/β-zeolite.

4.4.2 C-C coupling of guaiacol

The overall catalytic activity was benchmarked for guaiacol upgrading biomass-derived syngas (CO/H_2) atmosphere over three metal/support combinations (Figure 4-29). Ru/β-zeolite reached a guaiacol conversion of 65.6 %, far surpassing Co/β-zeolite (45.8 %) and Ru/C (17.7 %). The detailed compounds identified by GC-MS are listed in Table S15 to Table S17. The outstanding performance of Ru/β-zeolite is attributed to the bifunctional cooperation between highly active, CO-tolerant Ru sites and the Brønsted/Lewis acid sites of the β-zeolite, which together facilitate C–O bond cleavage, hydrogenation, and subsequent C–C coupling/chain-growth steps.[288–291] When the acidic β-zeolite is replaced by essentially inert activated carbon (Ru/C), conversion drops sharply, underscoring the indispensable role of acid sites in adsorbing and activating guaiacol. Substituting Ru with cobalt on the same β-zeolite support (Co/β-zeolite) recovers part of the activity, confirming that the zeolitic acid function remains beneficial; however, the intrinsic hydrogenation and hydrodeoxygenation activity of Co is lower than that of Ru, leading to the observed intermediate conversion.

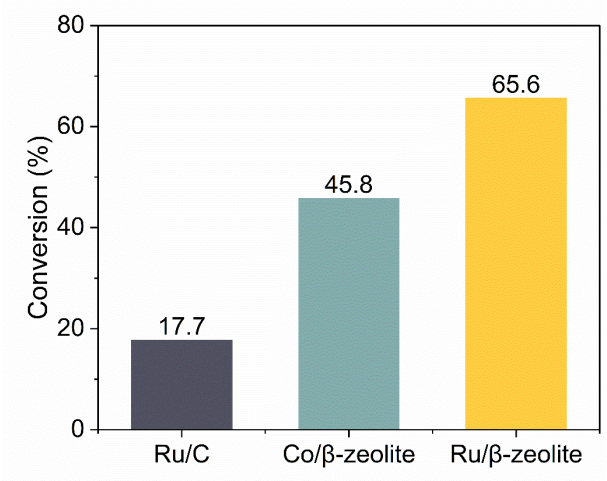

Figure 4-29: Conversion of guaiacol in syngas over different catalysts

Figure 4-30 illustrates the product distribution obtained from the catalytic upgrading of guaiacol (GU) in a biomass-derived syngas (CO/H_2) atmosphere over Ru/β-zeolite catalyst at 250 °C (Table S17) and 300 °C (Table S18). Notably, the products generated under these conditions originate from two distinct reaction pathways occurring simultaneously: (1) reactions of guaiacol with CO and H_2, including direct C–C coupling, hydrogenation, hydrodeoxygenation, and other synergistic reactions (marked as GU), and (2) Fischer–Tropsch (FT) synthesis from syngas alone.

At a lower reaction temperature (250 °C), products derived from guaiacol reactions with CO and H_2 (GU-250) predominantly fall within the desirable aviation-fuel range (C8–C10), displaying around 55% selectivity. Concurrently, FT synthesis at the same temperature (FT-250) primarily yields shorter-chain hydrocarbons ($<C_7$), exhibiting notably less selectivity towards the target SAF-range products. In terms of overall carbon yield, FT-derived species account for only about 14 %, while GU-derived species dominate with 86 %. This clearly indicates that guaiacol undergoes effective carbon-chain elongation, likely accompanied by hydrogenation or other synergistic reactions with CO and H_2, whereas the pure FT route tends to form lighter hydrocarbons under identical conditions.

Upon increasing the reaction temperature to 300 °C, the selectivity toward C_8–C_{10} hydrocarbons derived from guaiacol reactions with CO and H_2 (GU-300) significantly increases to approximately 75%. This result confirms enhanced activity and selectivity for guaiacol upgrading reactions (including C–C coupling, hydrogenation, and hydrodeoxygenation) at elevated temperatures, likely due to improved catalytic activation and increased reaction kinetics. Concomitantly, the share of FT-derived products rises to ~19 % (GU products 81 %), showing that more syngas molecules are diverted into the FT pathway at elevated temperature, even though GU upgrading still dominates. In contrast, FT synthesis products (FT-300) continue to show a broad carbon distribution, although there is a slight shift toward shorter-chain hydrocarbons, likely

due to increased formation of lighter molecules from the FT reaction at higher temperatures.

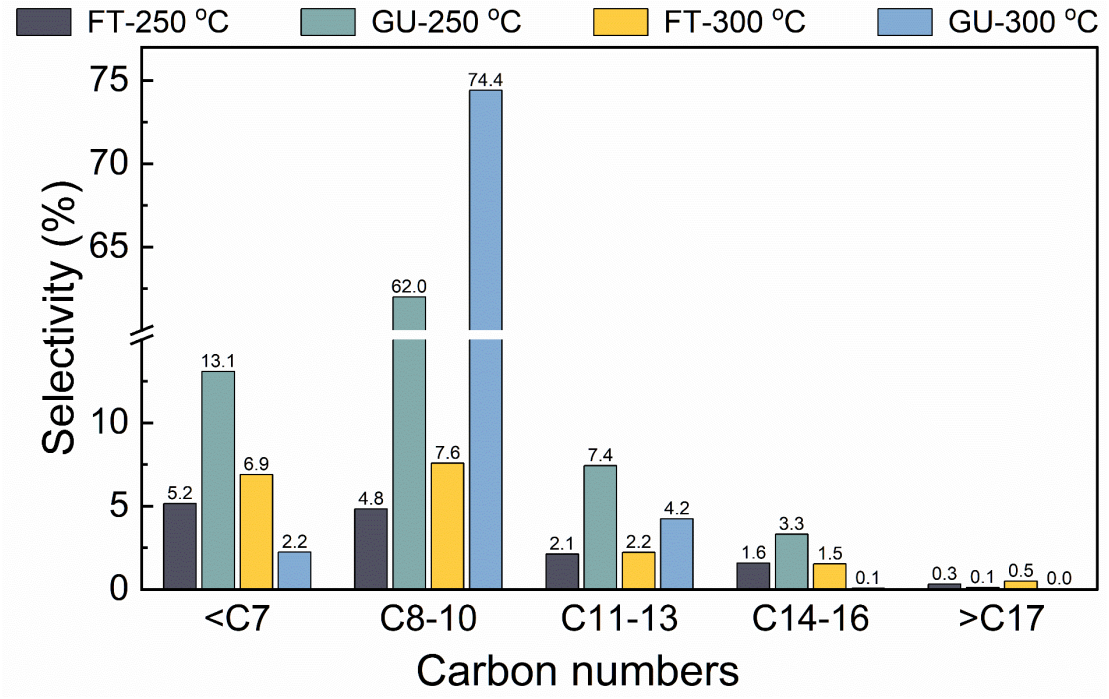

Figure 4-30: Products distribution of syngas upgrading of guaiacol at 250 °C and 300 °C over Ru/β-zeolite catalyst.

4.4.3 C-C coupling of bio-oil

The catalytic upgrading of BTG bio-oil feedstock under the same reaction conditions was further compared (Figure 4-31), and the detailed compositional distribution is presented in Table S19 to Table S21. At 250 °C, a clear shift towards higher-carbon-number products, particularly in the C_8–C_{10} range, is observed, with selectivity significantly increasing from approximately 25% in the feedstock to nearly 65% in the product. This highlights effective carbon-chain elongation reactions occurring during catalytic upgrading.

At 300 °C, although there remains substantial formation of C_8–C_{10} hydrocarbons, a concurrent increase in lighter hydrocarbons (<C_7) is evident. This change can be attributed to enhanced cracking reactions, secondary reactions, and possibly increased Fischer–Tropsch-derived short-chain product formation at elevated temperatures. Nonetheless, the selectivity toward aviation-fuel range hydrocarbons remains significantly higher compared to the original feedstock.

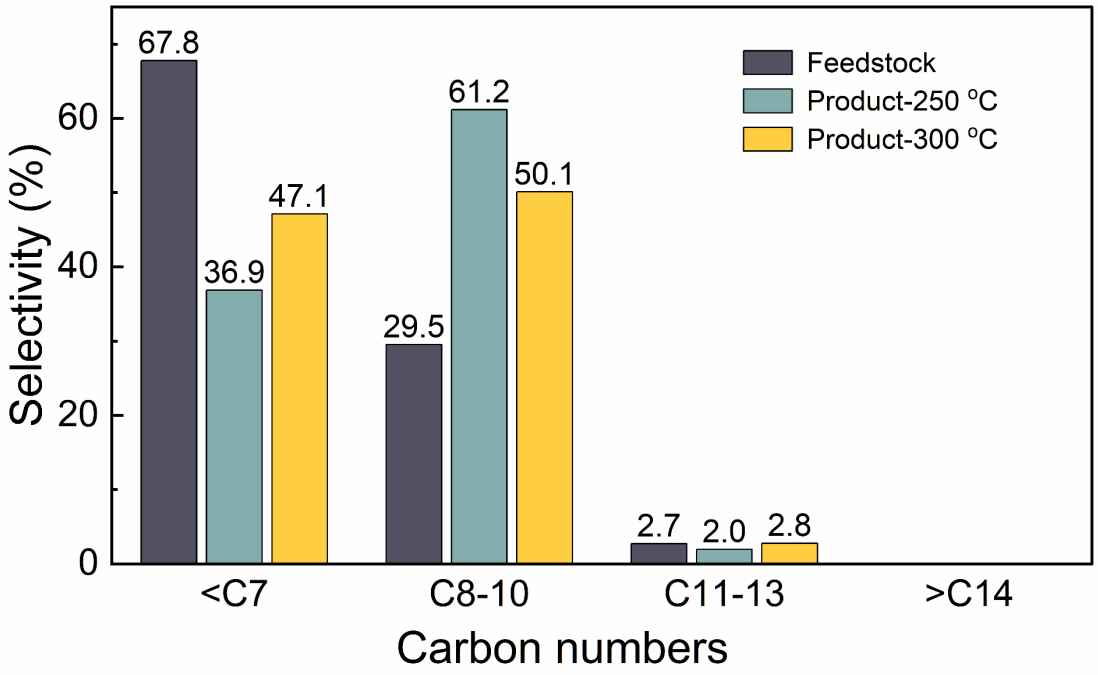

Figure 4-31: Products distribution of syngas upgrading of bio-oil at 250 ºC and 300 ºC.

To assess both the de-oxygenation of phenolic species and the subsequent hydrogenation (ring saturation), the relative amounts of phenolic aromatics and cycloalkanes in the feed and upgraded oils are summarised in Table 4-10. The raw bio-oil is dominated by oxygenated aromatics, whereas cycloalkanes are scarcely present. After upgrading, the cycloalkane fraction rises markedly. This outcome demonstrates that the mixed CO/H_2 atmosphere not only drives carbon-chain extension but also shifts the ring population from highly aromatic toward naphthenic—a decisive step toward producing drop-in sustainable aviation fuel.

Table 4-10: Distribution of aromatics and cycloalkanes in bio-oil feedstock and upgraded products under 250 ºC and 300 ºC.

	Aromatics (%)	Cycloalkanes (%)	Ratio of Aromativs and Cycloalkanes
Feedstock	45.4	7.5	6.0 : 1
Product-250 ºC	50.3	28.9	1.7 : 1
Product-300 ºC	38.7	28.6	1.4 : 1

A comparison of the raw bio-oil with the products obtained after upgrading at 250 °C and 300 °C shows that carbon-chain growth is driven by three principal mechanisms:

Firstly, Fischer–Tropsch-type CO/H_2 homologation – light C_1–C_3 alcohols and acids are converted into C_{7+} branched hydrocarbons. Secondly, self-condensation of native C_2–C_4 carboxylic acids, ketones and aldehydes – these small molecules couple to form higher-molecular-weight acids and ketones. Lastly, side-chain elongation of phenolic species in the presence of CO – phenols undergo alkylation, generating longer-chain substituted phenols.

These findings demonstrate that the Ru/β-zeolite catalyst efficiently upgrades both pure guaiacol and complex bio-oil feedstocks under syngas conditions, significantly enhancing selectivity toward SAF-range hydrocarbons. The observed variations with temperature underline the necessity of optimizing reaction conditions to balance desirable C–C coupling and minimize undesired side reactions for industrial bio-oil upgrading processes.

Chapter 5 Final conclusion and outlook

In conclusion, a three-stage strategy was followed: first, oligomeric bio-oil species (e.g., PPE) were hydrotreated to depolymerize them into oxygenated monomers; second, these monomers were hydrodeoxygenated to small deoxygenated molecules; and finally, syngas-assisted C–C coupling was promoted to generate longer-chain, fuel-range products. By integrating experimental approaches with DFT calculations, several promising catalytic systems were developed and comprehensively evaluated, contributing significantly toward sustainable and economically feasible biomass upgrading technologies.

The initial part of this investigation focused on ruthenium-based catalysts, employing both theoretical and experimental methodologies to elucidate the mechanisms involved in HDO. Computational studies demonstrated that the cleavage of the β-O-4 linkage in biomass-derived dimers occurred with notably low activation energies on the Ru surface, particularly highlighting the catalyst's efficiency in breaking strong chemical bonds prevalent in lignin-derived structures. Experimental validations using a synthesized Ru/Nb_2O_5 catalyst further supported these theoretical findings, showcasing exceptional catalytic performance. The catalyst achieved nearly complete conversion of model compounds under relatively mild reaction conditions (250 °C, 5 MPa), yielding benzene, cyclohexane, and ethylcyclohexane as primary products. Crucially, the catalyst also exhibited robust performance in real bio-oil systems, underscoring its potential applicability to complex, real-world biomass streams. These combined results underscore the promise of Ru/Nb_2O_5 catalysts as effective, scalable solutions for industrial biomass upgrading.

In the second part, the synthesis and characterization of Ni-based catalysts derived from layered double hydroxides (LDH) were systematically explored for biomass oligomer depolymerization. The developed catalysts, notably containing both Ni (0) and Ni (II), demonstrated exceptional catalytic efficacy in facilitating hydrogenolysis reactions under mild reaction conditions (125 °C, 25 bar). Detailed characterization, including advanced techniques such as transmission electron microscopy (TEM) and X-ray photoelectron spectroscopy (XPS), confirmed the co-existence of metallic Ni (0) and oxidized Ni (II), elucidating a clear correlation between catalyst structure and activity. The mechanistic investigation, reinforced by DFT analysis, revealed that the presence of Ni (II) significantly altered the electronic properties of Ni (0), shifting the d-band center and consequently influencing the adsorption behavior and reactivity towards biomass-derived compounds. This synergistic effect was pivotal for efficiently lowering the energy barrier associated with critical bond-cleavage reactions, thereby facilitating more efficient catalytic transformations under mild conditions. These findings highlight the importance of precisely tuning catalyst properties to achieve

optimal performance and provide essential insights into catalytic design and mechanism for biomass conversion processes.

Moreover, the third segment of this research involved the introduction of oxophilic metals, particularly molybdenum (Mo), into Ni/Al_2O_3 catalysts through an innovative interlayer doping method based on LDH structures. This novel doping strategy notably enhanced catalytic performance in HDO processes, as demonstrated by both theoretical insights and experimental validation. Mo-doped Ni-based catalysts showed superior catalytic efficiency in the selective deoxygenation of bio-oil model compounds such as guaiacol, achieving nearly quantitative selectivity towards cyclohexane under optimized reaction conditions. The detailed synergistic mechanism was uncovered through combined experimental and computational investigations, highlighting MoOx species as crucial promoters that effectively reduced activation energy barriers for key C–O bond cleavage steps. This advancement not only provides a viable cost-effective alternative to noble metal catalysts but also offers significant insights into catalyst design strategies for broader biomass upgrading applications.

The final part of the study presented a pioneering approach to longer-chain products via catalytic C–C coupling processes under a syngas (CO and H_2) atmosphere. Among various catalyst candidates, Ru/β-zeolite emerged as the optimal catalyst, demonstrating remarkable efficiency in facilitating C–C bond formation reactions. Utilizing guaiacol and real bio-oil fractions, this catalyst exhibited superior activity and selectivity toward producing hydrocarbons within the desirable SAF carbon chain range. Advanced catalyst characterization techniques confirmed the robust dispersion of Ru nanoparticles on the zeolite support, maintaining structural integrity and ensuring abundant active sites throughout the reaction process. This approach not only demonstrated a successful strategy for bio-oil upgrading but also emphasized its potential for industrial implementation due to its adaptability and compatibility with diverse biomass-derived feedstocks.

For enginerring outlook, future research should focus on further optimizing these catalytic systems to enhance their long-term stability, recyclability, and scalability under continuous industrial conditions. It is essential to investigate catalyst performance and stability comprehensively across various biomass feedstocks, considering differences in chemical composition and complexity. In tandem, deeper exploration of integrated C–C coupling and HDO pathways will be critical for achieving extended carbon chains and minimized oxygen content in the final products, thus maximizing carbon utilization and producing fuels with superior properties. Furthermore, integrating advanced downstream separation techniques, including selective extraction and adsorption methods, will be crucial to further improve the quality of the final upgraded biofuels. Addressing these future challenges will solidify the role of catalytic biomass upgrading technologies in the broader transition toward sustainable energy systems, contributing significantly to global sustainability goals by

reducing carbon emissions and providing economically viable solutions for renewable energy industries.

For DFT outlook, owing to the compositional complexity of bio-oil, future DFT studies should move beyond ideal single-crystal surfaces and single-molecule models. They should simulate more realistic conditions, including water-in-oil systems, complex reaction networks, and dynamic catalyst evolution. This may be enabled by machine-learning force fields, such as Deep Potential. Looking ahead, DFT-derived microscopic parameters (e.g., activation energies) should serve as key inputs. They should be embedded into microkinetic models, mesoscopic finite-element chemical simulations, and macroscale reactor CFD (Computational Fluid Dynamics). This will give the simulation results greater value for guiding industrial practice. Finally, chemistry-specialized generative AI models could identify reaction networks among the complex reactants and products in bio-oil and, combined with existing DFT insights, establish more precise relationships between catalytic upgrading performance and catalyst structure.

Reference

(1) Pakulska, T. The Energy Crisis—Looking at the Renewable Transition. *Energies* **2023**, *16* (15), 5705. https://doi.org/10.3390/en16155705.

(2) Wei, Y.-M.; Chen, K.; Kang, J.-N.; Chen, W.; Wang, X.-Y.; Zhang, X. Policy and Management of Carbon Peaking and Carbon Neutrality: A Literature Review. *Engineering* **2022**, *14*, 52–63. https://doi.org/10.1016/j.eng.2021.12.018.

(3) Smal, T.; Wieprow, J. Energy Security in the Context of Global Energy Crisis: Economic and Financial Conditions. *Energies* **2023**, *16* (4), 1605. https://doi.org/10.3390/en16041605.

(4) Pirnau, C.; Ghiculescu, L. D.; Pirnau, M.; Ghena, M. F. The Dimensions Balance of the Energy Trilemma and the Current Energy Crisis. In *2023 15th International Conference on Electronics, Computers and Artificial Intelligence (ECAI)*; IEEE: Bucharest, Romania, 2023; pp 01–05. https://doi.org/10.1109/ECAI58194.2023.10194098.

(5) Fetting, C. The European Green Deal. *ESDN Rep. Dec.* **2020**, *2* (9), 53.

(6) Bäckstrand, K. Towards a Climate-Neutral Union by 2050? The European Green Deal, Climate Law, and Green Recovery. In *Routes to a Resilient European Union*; Bakardjieva Engelbrekt, A., Ekman, P., Michalski, A., Oxelheim, L., Eds.; Springer International Publishing: Cham, 2022; pp 39–61. https://doi.org/10.1007/978-3-030-93165-0_3.

(7) Silva, W. R.; Santos, T. M.; Carregosa, J. C.; Schmitt, C. C.; Raffelt, K.; Dahmen, N.; Wisniewski, A. Bio-Oil as a Source of Renewable Chemicals: The Chemistry of Pyrolytic Lignin. *Biomass Convers. Biorefinery* **2025**, *15* (4), 5401–5418. https://doi.org/10.1007/s13399-024-05622-1.

(8) Dahmen, N.; Sauer, J. Evaluation of Techno-Economic Studies on the Bioliq® Process for Synthetic Fuels Production from Biomass. *Processes* **2021**, *9* (4), 684. https://doi.org/10.3390/pr9040684.

(9) Li, G.; Wang, R.; Pang, J.; Wang, A.; Li, N.; Zhang, T. Production of Renewable Hydrocarbon Biofuels with Lignocellulose and Its Derivatives over Heterogeneous Catalysts. *Chem. Rev.* **2024**, *124* (6), 2889–2954. https://doi.org/10.1021/acs.chemrev.2c00756.

(10) Maqbool, W.; Hobson, P.; Dunn, K.; Doherty, W. Supercritical Carbon Dioxide Separation of Carboxylic Acids and Phenolics from Bio-Oil of Lignocellulosic Origin: Understanding Bio-Oil Compositions, Compound Solubilities, and Their Fractionation. *Ind. Eng. Chem. Res.* **2017**, *56* (12), 3129–3144. https://doi.org/10.1021/acs.iecr.6b04111.

(11) Lian, X.; Xue, Y.; Zhao, Z.; Xu, G.; Han, S.; Yu, H. Progress on Upgrading Methods of Bio-Oil: A Review: Upgrading Progress of Bio-Oil. *Int. J. Energy Res.* **2017**, *41* (13), 1798–1816. https://doi.org/10.1002/er.3726.

(12) Xiu, S.; Shahbazi, A. Bio-Oil Production and Upgrading Research: A Review. *Renew. Sustain. Energy Rev.* **2012**, *16* (7), 4406–4414. https://doi.org/10.1016/j.rser.2012.04.028.

(13) Qu, L.; Jiang, X.; Zhang, Z.; Zhang, X.; Song, G.; Wang, H.; Yuan, Y.; Chang, Y. A Review of Hydrodeoxygenation of Bio-Oil: Model Compounds, Catalysts, and Equipment. *Green Chem.* **2021**, *23* (23), 9348–9376. https://doi.org/10.1039/D1GC03183J.

(14) Cordero-Lanzac, T.; Rodríguez-Mirasol, J.; Cordero, T.; Bilbao, J. Advances and Challenges in the Valorization of Bio-Oil: Hydrodeoxygenation Using Carbon-Supported Catalysts. *Energy Fuels* **2021**, *35* (21), 17008–17031. https://doi.org/10.1021/acs.energyfuels.1c01700.

(15) Lee, H.; Kim, Y.-M.; Lee, I.-G.; Jeon, J.-K.; Jung, S.-C.; Chung, J. D.; Choi, W. G.; Park, Y.-K. Recent Advances in the Catalytic Hydrodeoxygenation of Bio-Oil. *Korean J. Chem. Eng.* **2016**, *33* (12), 3299–3315. https://doi.org/10.1007/s11814-016-0214-3.

(16) Weih, N.; Niebel, A.; Pfitzer, C.; Funke, A.; Parku, G. K.; Dahmen, N. Operational Experience with Miscanthus Feedstock at the Bioliq® Fast Pyrolysis Plant. *J. Anal. Appl. Pyrolysis* **2024**, *177*, 106338. https://doi.org/10.1016/j.jaap.2023.106338.

(17) Fonseca, F. G.; Funke, A.; Niebel, A.; Soares Dias, A. P.; Dahmen, N. Moisture Content as a Design and Operational Parameter for Fast Pyrolysis. *J. Anal. Appl. Pyrolysis* **2019**, *139*, 73–86. https://doi.org/10.1016/j.jaap.2019.01.012.

(18) El Bari, H.; Fanezoune, C. K.; Dorneanu, B.; Arellano-Garcia, H.; Majozi, T.; Elhenawy, Y.; Bayssi, O.; Hirt, A.; Peixinho, J.; Dhahak, A.; Gadalla, M. A.; Khashaba, N. H.; Ashour, F. H. Catalytic Fast Pyrolysis of Lignocellulosic Biomass: Recent Advances and Comprehensive Overview. *J. Anal. Appl. Pyrolysis* **2024**, *178*, 106390. https://doi.org/10.1016/j.jaap.2024.106390.

(19) Zheng, A.; Wang, Q.; Liu, S.; Huang, Z.; Wei, G.; Zhao, K.; Wang, S.; Zhao, Z.; Li, H. Selective Sequential Fractionation of Biomass for Quantitatively Elucidating the Compositional Factors Affecting Biomass Fast Pyrolysis. *J. Anal. Appl. Pyrolysis* **2021**, *156*, 105106. https://doi.org/10.1016/j.jaap.2021.105106.

(20) Zhang, H.; Wu, J.; Qin, Z.; Luo, Y. The Effect of Bio-Oil on High-Temperature Performance of Bio-Oil Recycled Asphalt Binders. *J. Renew. Mater.* **2022**, *10* (4), 1025–1037. https://doi.org/10.32604/jrm.2022.017483.

(21) Zhuang, X.; Gan, Z.; Chen, D.; Cen, K.; Ba, Y.; Jia, D. An Approach for Upgrading Bio-Oil by Using Heavy Bio-Oil Co-Pyrolyzed with Bamboo Leached with Light Bio-Oil. *Fuel* **2023**, *331*, 125931. https://doi.org/10.1016/j.fuel.2022.125931.

(22) Cen, K.; Zhuang, X.; Gan, Z.; Zhang, H.; Chen, D. Biomass Pyrolysis Polygeneration with Bio-Oil Recycling: Co-Pyrolysis of Heavy Bio-Oil and Pine Wood Leached with Light Bio-Oil for Product Upgradation. *Fuel* **2023**, *335*, 127057. https://doi.org/10.1016/j.fuel.2022.127057.

(23) Lv, S.; Ju, Z.; Peng, X.; Borges Cabrera, M.; Wang, Z.; Yuan, J.; Hu, L. Preparation and Performance of Polyphosphoric Acid/Bio-Oil Composite–Modified Asphalt Containing a High Content Bio-Oil. *J. Mater. Civ. Eng.* **2022**, *34* (3), 04021484. https://doi.org/10.1061/(ASCE)MT.1943-5533.0004124.

(24) Saeed, S. M.; Sutanto, M. H.; Napiah, M.; Usman, A.; Batari, A.; Aman, M. Y.; Aliyu Yaro, N. S. Optimization of Rubber Seed Oil Content as Bio-Oil Rejuvenator and Total Water Content for Cold Recycled Asphalt Mixtures Using Response Surface Methodology. *Case Stud. Constr. Mater.* **2021**, *15*, e00561. https://doi.org/10.1016/j.cscm.2021.e00561.

(25) Chen, H.; Xu, H.; Zhu, H.; Yan, S.; Zhang, S.; Zhang, H.; Guo, X.; Hu, X.; Gao, W. A Review on Bioslurry Fuels Derived from Bio-Oil and Biochar: Preparation, Fuel Properties and Application. *Fuel* **2024**, *355*, 129283. https://doi.org/10.1016/j.fuel.2023.129283.

(26) Xu, J.; Brodu, N.; Abdelouahed, L.; Taouk, B. Investigation of the Combination of Fractional Condensation and Water Extraction for Improving the Storage Stability of Pyrolysis Bio-Oil. *Fuel* **2022**, *314*, 123019. https://doi.org/10.1016/j.fuel.2021.123019.

(27) Demirbas, M. F. Characterization of Bio-Oils from Spruce Wood (*Picea Orientalis* L.) via Pyrolysis. *Energy Sources Part Recovery Util. Environ. Eff.* **2010**, *32* (10), 909–916. https://doi.org/10.1080/15567030903059970.

(28) Deng, W.; Wang, X.; Lam, C. H.; Xiong, Z.; Han, H.; Xu, J.; Jiang, L.; Su, S.; Hu, S.; Wang, Y.; Xiang, J. Evolution of Coke Structures during Electrochemical Upgrading of Bio-Oil. *Fuel Process. Technol.* **2022**, *225*, 107036. https://doi.org/10.1016/j.fuproc.2021.107036.

(29) Leng, E.; He, B.; Chen, J.; Liao, G.; Ma, Y.; Zhang, F.; Liu, S.; E, J. Prediction of Three-Phase Product Distribution and Bio-Oil Heating Value of Biomass Fast Pyrolysis Based on Machine Learning. *Energy* **2021**, *236*, 121401. https://doi.org/10.1016/j.energy.2021.121401.

(30) Mateus, M. M.; Bordado, J. M.; Galhano Dos Santos, R. Estimation of Higher Heating Value (HHV) of Bio-Oils from Thermochemical Liquefaction by Linear Correlation. *Fuel* **2021**, *302*, 121149. https://doi.org/10.1016/j.fuel.2021.121149.

(31) Anh Vo, T.; Kim, J.; Tae Hwang, H.; Kim, S.-S. Fast Pyrolysis of Cashew Nut Shells in a Bubbling Fluidized Bed Reactor for Producing High-Heating Value Bio-Oil Using Dolomite as a Catalyst and Carbon Capture Sorbent. *Fuel* **2024**, *364*, 131024. https://doi.org/10.1016/j.fuel.2024.131024.

(32) Terry, L. M.; Li, C.; Chew, J. J.; Aqsha, A.; How, B. S.; Loy, A. C. M.; Chin, B. L. F.; Khaerudini, D. S.; Hameed, N.; Guan, G.; Sunarso, J. Bio-Oil Production from Pyrolysis of Oil Palm Biomass and the Upgrading Technologies: A Review. *Carbon Resour. Convers.* **2021**, *4*, 239–250. https://doi.org/10.1016/j.crcon.2021.10.002.

(33) Chen, G.; Liang, L.; Li, N.; Lu, X.; Yan, B.; Cheng, Z. Upgrading of Bio-Oil Model Compounds and Bio-Crude into Biofuel by Electrocatalysis: A Review. *ChemSusChem* **2021**, *14* (4), 1037–1052. https://doi.org/10.1002/cssc.202002063.

(34) Chukwuneke, J. L.; Orugba, H. O.; Olisakwe, H. C.; Chikelu, P. O. Pyrolysis of Pig-Hair in a Fixed Bed Reactor: Physico-Chemical Parameters of Bio-Oil. *South Afr. J. Chem. Eng.* **2021**, *38*, 115–120. https://doi.org/10.1016/j.sajce.2021.09.003.

(35) Irfan, M.; Ghalib, S. A.; Waqas, S.; Khan, J. A.; Rahman, S.; Faraj Mursal, S. N.; Ghanim, A. A. J. Response Surface Methodology for the Synthesis and Characterization of Bio-Oil Extracted from Biomass Waste and Upgradation Using the Rice Husk Ash Catalyst. *ACS Omega* **2023**, *8* (20), 17869–17879. https://doi.org/10.1021/acsomega.3c00868.

(36) Wang, H.; Gross, A.; Liu, J. Influence of Methanol Addition on Bio-Oil Thermal Stability and Corrosivity. *Chem. Eng. J.* **2022**, *433*, 133692. https://doi.org/10.1016/j.cej.2021.133692.

(37) Yi, W.; Wang, X.; Zeng, K.; Yang, H.; Shao, J.; Zhang, S.; Chen, H. Improving Bio-Oil Stability by Fractional Condensation and Solvent Addition. *Fuel* **2021**, *290*, 119929. https://doi.org/10.1016/j.fuel.2020.119929.

(38) Forero, J. A. J.; Tran, T. H. T.; Tana, T.; Baker, A.; Beltramini, J.; Doherty, W. O. S.; Moghaddam, L. Hydrothermal Liquefaction of Sugarcane Bagasse to Bio-Oils: Effect of Liquefaction Solvents on Bio-Oil Stability. *Fuel* **2022**, *312*, 122793. https://doi.org/10.1016/j.fuel.2021.122793.

(39) Umar, Y.; Velasco, O.; Abdelaziz, O. Y.; Aboelazayem, O.; Gadalla, M. A.; Hulteberg, C. P.; Saha, B. A Renewable Lignin-Derived Bio-Oil for Boosting the Oxidation Stability of Biodiesel. *Renew. Energy* **2022**, *182*, 867–878. https://doi.org/10.1016/j.renene.2021.10.061.

(40) Bhatnagar, A.; Barthen, R.; Tolvanen, H.; Konttinen, J. Bio-Oil Stability through Stepwise Pyrolysis of Groundnut Shells: Role of Chemical Composition, Alkali and Alkaline Earth Metals, and Storage Conditions. *J. Anal. Appl. Pyrolysis* **2021**, *157*, 105219. https://doi.org/10.1016/j.jaap.2021.105219.

(41) Lachos-Perez, D.; Martins-Vieira, J. C.; Missau, J.; Anshu, K.; Siakpebru, O. K.; Thengane, S. K.; Morais, A. R. C.; Tanabe, E. H.; Bertuol, D. A. Review on Biomass Pyrolysis with a Focus on Bio-Oil Upgrading Techniques. *Analytica* **2023**, *4* (2), 182–205. https://doi.org/10.3390/analytica4020015.

(42) Panwar, N. L.; Paul, A. S. An Overview of Recent Development in Bio-Oil Upgrading and Separation Techniques. *Environ. Eng. Res.* **2020**, *26* (5), 200382–0. https://doi.org/10.4491/eer.2020.382.

(43) Chaihad, N.; Karnjanakom, S.; Abudula, A.; Guan, G. Zeolite-Based Cracking Catalysts for Bio-Oil Upgrading: A Critical Review. *Resour. Chem. Mater.* **2022**, *1* (2), 167–183. https://doi.org/10.1016/j.recm.2022.03.002.

(44) Lahijani, P.; Mohammadi, M.; Mohamed, A. R.; Ismail, F.; Lee, K. T.; Amini, G. Upgrading Biomass-Derived Pyrolysis Bio-Oil to Bio-Jet Fuel through Catalytic Cracking and Hydrodeoxygenation: A Review of Recent Progress. *Energy Convers. Manag.* **2022**, *268*, 115956. https://doi.org/10.1016/j.enconman.2022.115956.

(45) Shahbeik, H.; Shafizadeh, A.; Gupta, V. K.; Lam, S. S.; Rastegari, H.; Peng, W.; Pan, J.; Tabatabaei, M.; Aghbashlo, M. Using Nanocatalysts to Upgrade Pyrolysis Bio-Oil: A Critical Review. *J. Clean. Prod.* **2023**, *413*, 137473. https://doi.org/10.1016/j.jclepro.2023.137473.

(46) Zhang, M. Y.; Hu, Y. L.; Wang, H. Y.; Li, H. Y.; Han, X.; Zeng, Y. M.; Xu, C. C. A Review of Bio-Oil Upgrading by Catalytic Hydrotreatment: Advances, Challenges, and Prospects. *Mol. Catal.* **2021**, *504*. https://doi.org/10.1016/j.mcat.2021.111438.

(47) Kumar, R.; Strezov, V. Thermochemical Production of Bio-Oil: A Review of Downstream Processing Technologies for Bio-Oil Upgrading, Production of Hydrogen and High Value-Added Products. *Renew. Sustain. Energy Rev.* **2021**, *135*. https://doi.org/10.1016/j.rser.2020.110152.

(48) Grams, J.; Jankowska, A.; Goscianska, J. Advances in Design of Heterogeneous Catalysts for Pyrolysis of Lignocellulosic Biomass and Bio-Oil Upgrading. *Microporous Mesoporous Mater.* **2023**, *362*, 112761. https://doi.org/10.1016/j.micromeso.2023.112761.

(49) Onwudili, J.; Scaldaferri, C. Catalytic Upgrading of Intermediate Pyrolysis Bio-Oil to Hydrocarbon-Rich Liquid Biofuel via a Novel Two-Stage Solvent-Assisted Process. *FUEL* **2023**, *352*. https://doi.org/10.1016/j.fuel.2023.129015.

(50) Wang, H.; Liu, S.; Dai, Y.; Kim, C. S.; Smith, K. J. Two-Step Bio-Oil Upgrading Using Carbon-Supported Mo2C Catalysts. *Energy Fuels* **2024**, *38* (1), 647–658. https://doi.org/10.1021/acs.energyfuels.3c03279.

(51) Page, J. R.; Manfredi, Z.; Bliznakov, S.; Valla, J. A. Recent Progress in Electrochemical Upgrading of Bio-Oil Model Compounds and Bio-Oils to Renewable Fuels and Platform Chemicals. *Materials* **2023**, *16* (1), 394. https://doi.org/10.3390/ma16010394.

(52) Yuan, X.; Sun, M.; Wang, C.; Zhu, X. Full Temperature Range Study of Rice Husk Bio-Oil Distillation: Distillation Characteristics and Product Distribution. *Sep. Purif. Technol.* **2021**, *263*, 118382. https://doi.org/10.1016/j.seppur.2021.118382.

(53) Li, K.; Nan, D.; Li, Z.; Xie, J.; Ma, S.; Huang, Y.; Lu, Q. Preparation and Optimization of Nitrogen-Doped Porous Carbon Derived from Bio-Oil Distillation Residue for High-Performance Supercapacitors. *J. Energy Storage* **2023**, *57*, 106219. https://doi.org/10.1016/j.est.2022.106219.

(54) Diao, R.; Lu, H.; Yang, Y.; Bai, J.; Zhu, X. Strategic Valorization of Bio-Oil Distillation Sludge via Gasification: A Comparative Study for Reactivities, Kinetics, Prediction and Ash Deposition. *Chem. Eng. J.* **2022**, *433*, 134334. https://doi.org/10.1016/j.cej.2021.134334.

(55) Krutof, A.; Hawboldt, K. A. Thermodynamic Model of Fast Pyrolysis Bio-Oil Advanced Distillation Curves. *Fuel* **2020**, *261*, 116446. https://doi.org/10.1016/j.fuel.2019.116446.

(56) Wang, S. High-Efficiency Separation of Bio-Oil. In *Biomass Now - Sustainable Growth and Use*; Matovic, M. D., Ed.; InTech, 2013. https://doi.org/10.5772/51423.

(57) Shao, S.; Liu, L.; Li, X. Production of Solid Fuel in the Vacuum Distillation of Bio-Oil. *Fuel Process. Technol.* **2023**, *242*, 107618. https://doi.org/10.1016/j.fuproc.2022.107618.

(58) Shao, S.; Luo, M.; Xia, X.; Li, X.; Wu, S. Study on Preparation of New Solid Fuel and Its Combustion Performance from Bio-Oil and Waste Cooking Oil Mixture via Vacuum Distillation. *Biomass Bioenergy* **2025**, *193*, 107562. https://doi.org/10.1016/j.biombioe.2024.107562.

(59) Ma, Y.; Yuan, X.; Luo, Z.; Zhu, X. Influence of Vacuum Degrees in Rectification System on Distillation Characteristics of Bio-Oil Model Compounds. *J. Fuel Chem. Technol.* **2022**, *50* (2), 160–165. https://doi.org/10.1016/S1872-5813(21)60140-8.

(60) Zhang, F.; Wang, B.; Wang, F.; Liu, S.-S.; Fan, Y.-C.; Duan, P.-G. Catalytic Hydrotreating of Crude Bio-Oil from Straw and Its Distillates Obtained by Molecular Distillation: A Comparative Study. *J. Anal. Appl. Pyrolysis* **2023**, *176*, 106253. https://doi.org/10.1016/j.jaap.2023.106253.

(61) Drugkar, K.; Rathod, W.; Sharma, T.; Sharma, A.; Joshi, J.; Pareek, V. K.; Ledwani, L.; Diwekar, U. Advanced Separation Strategies for Up-Gradation of Bio-Oil into Value-Added Chemicals: A Comprehensive Review. *Sep. Purif. Technol.* **2022**, *283*, 120149. https://doi.org/10.1016/j.seppur.2021.120149.

(62) Jiang, L.; Zhang, X.; Liu, J.; Zhang, J.; Shao, J.; Zhang, S.; Yang, H.; Chen, H. Simple Distillation to Obtain Bio-Pitch from Bio-Oil for Carbon Anode

Production. *J. Anal. Appl. Pyrolysis* **2025**, *186*, 106933. https://doi.org/10.1016/j.jaap.2024.106933.

(63) Wang, H.; Gunawan, R.; Wang, Z.; Zhang, L.; Liu, Y.; Wang, S.; Hasan, M. D. M.; Li, C.-Z. High-Pressure Reactive Distillation of Bio-Oil for Reduced Polymerisation. *Fuel Process. Technol.* **2021**, *211*, 106590. https://doi.org/10.1016/j.fuproc.2020.106590.

(64) Kiss, A. A.; Muthia, R.; Pazmiño-Mayorga, I.; Harmsen, J.; Jobson, M.; Gao, X. Conceptual Methods for Synthesis of Reactive Distillation Processes: Recent Developments and Perspectives. *J. Chem. Technol. Biotechnol.* **2024**, *99* (6), 1263–1290. https://doi.org/10.1002/jctb.7633.

(65) Rasmussen, J. B.; Mansouri, S. S.; Zhang, X.; Abildskov, J.; Kjøbsted Huusom, J. Analysing Separation and Reaction Stage Performance in a Reactive Cyclic Distillation Process. *Chem. Eng. Process. - Process Intensif.* **2021**, *167*, 108515. https://doi.org/10.1016/j.cep.2021.108515.

(66) Ding, Q.; Geng, X.; Li, H.; Gao, X. Unraveling the Matching of Reaction and Separation for Reactive Distillation Process Based on Reaction Equilibrium Degree (RED). *Chem. Eng. Sci.* **2023**, *275*, 118719. https://doi.org/10.1016/j.ces.2023.118719.

(67) Kiss, A. A.; Jobson, M.; Gao, X. Reactive Distillation: Stepping Up to the Next Level of Process Intensification. *Ind. Eng. Chem. Res.* **2019**, *58* (15), 5909–5918. https://doi.org/10.1021/acs.iecr.8b05450.

(68) Leng, L.; Li, H.; Yuan, X.; Zhou, W.; Huang, H. Bio-Oil Upgrading by Emulsification/Microemulsification: A Review. *Energy* **2018**, *161*, 214–232. https://doi.org/10.1016/j.energy.2018.07.117.

(69) Lin, B.-J.; Chen, W.-H.; Budzianowski, W. M.; Hsieh, C.-T.; Lin, P.-H. Emulsification Analysis of Bio-Oil and Diesel under Various Combinations of Emulsifiers. *Appl. Energy* **2016**, *178*, 746–757. https://doi.org/10.1016/j.apenergy.2016.06.104.

(70) Liu, K.; Zhao, W.; Guo, T.; Lei, Q.; Guan, Y.; Wang, D.; Cui, M.; Fu, S.; Zhao, J.; Zong, Z.; Wei, X. Emulsification and Performance Measurement of Bio-Oil with Diesel. *Waste Biomass Valorization* **2021**, *12* (6), 2933–2944. https://doi.org/10.1007/s12649-019-00917-1.

(71) Ma, Z.; Wang, H.; Li, Y.; Yang, X.; Leng, Z. Optimized Bio-Oil Emulsification for Sustainable Asphalt Production: A Step towards a Low-Carbon Pavement. *Constr. Build. Mater.* **2024**, *419*, 135218. https://doi.org/10.1016/j.conbuildmat.2024.135218.

(72) He, R.; Ye, X. P.; Harte, F.; English, B. Effects of High-Pressure Homogenization on Physicochemical Properties and Storage Stability of Switchgrass Bio-Oil. *Fuel*

Process. Technol. **2009**, *90* (3), 415–421. https://doi.org/10.1016/j.fuproc.2008.11.003.

(73) Yadykova, A. Y.; Ilyin, S. O. Compatibility and Rheology of Bio-Oil Blends with Light and Heavy Crude Oils. *Fuel* **2022**, *314*, 122761. https://doi.org/10.1016/j.fuel.2021.122761.

(74) Chong, J. W.; Chemmangattuvalappil, N. G.; Muthoosamy, K.; Thangalazhy-Gopakumar, S. Stable Diesel and Bio-Oil Emulsion through Solvent Extraction and Ultrasonic Aided Emulsification. *Process Saf. Environ. Prot.* **2024**, *190*, 616–624. https://doi.org/10.1016/j.psep.2024.07.038.

(75) Li, Y.; Wang, T.; Liang, W.; Wu, C.; Ma, L.; Zhang, Q.; Zhang, X.; Jiang, T. Ultrasonic Preparation of Emulsions Derived from Aqueous Bio-Oil Fraction and 0# Diesel and Combustion Characteristics in Diesel Generator. *Energy Fuels* **2010**, *24* (3), 1987–1995. https://doi.org/10.1021/ef9010934.

(76) Wang, W.; Li, B.-Y.; Zhang, M.-J.; Su, Y.-Y.; Pan, D.-W.; Liu, Z.; Ju, X.-J.; Xie, R.; Faraj, Y.; Chu, L.-Y. Microfluidic Emulsification Techniques for Controllable Emulsion Production and Functional Microparticle Synthesis. *Chem. Eng. J.* **2023**, *452*, 139277. https://doi.org/10.1016/j.cej.2022.139277.

(77) Wang, H.; Wei, B.; Sun, Z.; Du, Q.; Hou, J. Microfluidic Study of Heavy Oil Emulsification on Solid Surface. *Chem. Eng. Sci.* **2021**, *246*, 117009. https://doi.org/10.1016/j.ces.2021.117009.

(78) Jiang, X.; Ellis, N. Upgrading Bio-Oil through Emulsification with Biodiesel: Mixture Production. *Energy Fuels* **2010**, *24* (2), 1358–1364. https://doi.org/10.1021/ef9010669.

(79) Zhang, M.; Wu, H. Separation of Bio-Oil by Hydrophilic Surfactants. *Energy Fuels* **2018**, *32* (3), 3559–3565. https://doi.org/10.1021/acs.energyfuels.7b04007.

(80) Yuan, X.; Ding, X.; Leng, L.; Li, H.; Shao, J.; Qian, Y.; Huang, H.; Chen, X.; Zeng, G. Applications of Bio-Oil-Based Emulsions in a DI Diesel Engine: The Effects of Bio-Oil Compositions on Engine Performance and Emissions. *Energy* **2018**, *154*, 110–118. https://doi.org/10.1016/j.energy.2018.04.118.

(81) Farooq, A.; Shafaghat, H.; Jae, J.; Jung, S.-C.; Park, Y.-K. Enhanced Stability of Bio-Oil and Diesel Fuel Emulsion Using Span 80 and Tween 60 Emulsifiers. *J. Environ. Manage.* **2019**, *231*, 694–700. https://doi.org/10.1016/j.jenvman.2018.10.098.

(82) Zhou, H.; Brown, R. C.; Wen, Z. Anaerobic Digestion of Aqueous Phase from Pyrolysis of Biomass: Reducing Toxicity and Improving Microbial Tolerance. *Bioresour. Technol.* **2019**, *292*, 121976. https://doi.org/10.1016/j.biortech.2019.121976.

(83) Hu, M. Z.; Engtrakul, C.; Bischoff, B. L.; Jang, G. G.; Theiss, T. J.; Davis, M. F. Superhydrophobic and Superhydrophilic Surface-Enhanced Separation Performance of Porous Inorganic Membranes for Biomass-to-Biofuel Conversion Applications. *Sep. Sci. Technol.* **2017**, *52* (3), 528–543. https://doi.org/10.1080/01496395.2016.1260144.

(84) Ikura, M.; Stanciulescu, M.; Hogan, E. Emulsification of Pyrolysis Derived Bio-Oil in Diesel Fuel. *Biomass Bioenergy* **2003**, *24* (3), 221–232. https://doi.org/10.1016/S0961-9534(02)00131-9.

(85) Wang, H.; Liu, J. Emulsification and Corrosivity Study of Bio-Oil and Vacuum Gas Oil Mixtures with a Novel Surfactant System. *Fuel* **2023**, *333*, 126460. https://doi.org/10.1016/j.fuel.2022.126460.

(86) Tuisku, A. Emulsion-Based Synthesis and Characterization of Bio-Oil Upgrading Catalyst CoMoS. *Aalto Univ.* **2023**, *Finland*.

(87) Liu, R.; Lu, Y.; Pu, W.; Lian, K.; Sun, L.; Du, D.; Song, Y.; Sheng, J. J. Low-Energy Emulsification of Oil-in-Water Emulsions with Self-Regulating Mobility via a Nanoparticle Surfactant. *Ind. Eng. Chem. Res.* **2020**, *59* (41), 18396–18411. https://doi.org/10.1021/acs.iecr.0c03153.

(88) Suota, M. J.; Simionatto, E. L.; Scharf, D. R.; Meier, H. F.; Wiggers, V. R. Esterification, Distillation, and Chemical Characterization of Bio-Oil and Its Fractions. *Energy Fuels* **2019**, *33* (10), 9886–9894. https://doi.org/10.1021/acs.energyfuels.9b01971.

(89) Prasertpong, P.; Jaroenkhasemmeesuk, C.; Regalbuto, J. R.; Lipp, J.; Tippayawong, N. Optimization of Process Variables for Esterification of Bio-Oil Model Compounds by a Heteropolyacid Catalyst. *Energy Rep.* **2020**, *6*, 1–9. https://doi.org/10.1016/j.egyr.2019.11.026.

(90) Mei, D.; Guo, D.; Wang, C.; Dai, P.; Du, J.; Wang, J. Evaluation of Esterified Pyrolysis Bio-Oil as a Diesel Alternative. *J. Energy Inst.* **2020**, *93* (4), 1382–1389. https://doi.org/10.1016/j.joei.2019.12.008.

(91) Yu, S.; Wu, S.; Li, L.; Ge, X. Upgrading Bio-Oil from Waste Cooking Oil by Esterification Using SO_4^{2-}/ZrO_2 as Catalyst. *Fuel* **2020**, *276*, 118019. https://doi.org/10.1016/j.fuel.2020.118019.

(92) Osatiashtiani, A.; Puértolas, B.; Oliveira, C. C. S.; Manayil, J. C.; Barbero, B.; Isaacs, M.; Michailof, C.; Heracleous, E.; Pérez-Ramírez, J.; Lee, A. F.; Wilson, K. On the Influence of Si:Al Ratio and Hierarchical Porosity of FAU Zeolites in Solid Acid Catalysed Esterification Pretreatment of Bio-Oil. *Biomass Convers. Biorefinery* **2017**, *7* (3), 331–342. https://doi.org/10.1007/s13399-017-0254-x.

(93) Prasertpong, P.; Tippayawong, N. Upgrading of Biomass Pyrolysis Oil Model Compound via Esterification: Kinetic Study Using Heteropoly Acid. *Energy Procedia* **2019**, *160*, 253–259. https://doi.org/10.1016/j.egypro.2019.02.144.

(94) Sondakh, R. C.; Hambali, E.; Indrasti, N. S. Improving Characteristic of Bio-Oil by Esterification Method. *IOP Conf. Ser. Earth Environ. Sci.* **2019**, *230* (1), 012071. https://doi.org/10.1088/1755-1315/230/1/012071.

(95) Lu, J.; Guo, S.; Fu, Y.; Chang, J. Catalytic Upgrading of Bio-Oil by Simultaneous Esterification and Alkylation with Azeotropic Water Removal. *Fuel Process. Technol.* **2017**, *161*, 193–198. https://doi.org/10.1016/j.fuproc.2016.10.020.

(96) Omar, S.; Yang, Y.; Wang, J. A Review on Catalytic & Non-Catalytic Bio-Oil Upgrading in Supercritical Fluids. *Front. Chem. Sci. Eng.* **2021**, *15* (1), 4–17. https://doi.org/10.1007/s11705-020-1933-x.

(97) Park, Y.-K.; Ha, J.-M.; Oh, S.; Lee, J. Bio-Oil Upgrading through Hydrogen Transfer Reactions in Supercritical Solvents. *Chem. Eng. J.* **2021**, *404*, 126527. https://doi.org/10.1016/j.cej.2020.126527.

(98) Gouda, N.; Singh, R. K.; Meher, S. N.; Panda, A. K. Production and Characterization of Bio Oil and Bio Char from Flax Seed Residue Obtained from Supercritical Fluid Extraction Industry. *J. Energy Inst.* **2017**, *90* (2), 265–275. https://doi.org/10.1016/j.joei.2016.01.003.

(99) Remón, J.; Arcelus-Arrillaga, P.; García, L.; Arauzo, J. Simultaneous Production of Gaseous and Liquid Biofuels from the Synergetic Co-Valorisation of Bio-Oil and Crude Glycerol in Supercritical Water. *Appl. Energy* **2018**, *228*, 2275–2287. https://doi.org/10.1016/j.apenergy.2018.07.093.

(100) Yan, S.; Xia, D.; Mao, R.; Liu, X. A Conceptual Biomass Liquefaction System with Supercritical Water for Bio-Oil, Power and Heating Trigeneration: Thermodynamic and Environmental Analysis. *Energy Convers. Manag.* **2021**, *244*, 114474. https://doi.org/10.1016/j.enconman.2021.114474.

(101) Feng, Y.; Meier, D. Supercritical Carbon Dioxide Extraction of Fast Pyrolysis Oil from Softwood. *J. Supercrit. Fluids* **2017**, *128*, 6–17. https://doi.org/10.1016/j.supflu.2017.04.010.

(102) Qiu, B.; Yang, C.; Shao, Q.; Liu, Y.; Chu, H. Recent Advances on Industrial Solid Waste Catalysts for Improving the Quality of Bio-Oil from Biomass Catalytic Cracking: A Review. *Fuel* **2022**, *315*, 123218. https://doi.org/10.1016/j.fuel.2022.123218.

(103) Zhang, H.; Yang, C.; Tao, Y.; Chen, M.; Xiao, R. Catalytic Cracking of Model Compounds of Bio-Oil: Characteristics and Mechanism Research on Guaiacol and Acetic Acid. *Fuel Process. Technol.* **2022**, *238*, 107512. https://doi.org/10.1016/j.fuproc.2022.107512.

(104) Ibarra, Á.; Hita, I.; Azkoiti, M. J.; Arandes, J. M.; Bilbao, J. Catalytic Cracking of Raw Bio-Oil under FCC Unit Conditions over Different Zeolite-Based Catalysts. *J. Ind. Eng. Chem.* **2019**, *78*, 372–382. https://doi.org/10.1016/j.jiec.2019.05.032.

(105) Hita, I.; Cordero-Lanzac, T.; Kekalainen, T.; Okafor, O.; Rodriguez-Mirasol, J.; Cordero, T.; Bilbao, J.; Janis, J.; Castano, P. In-Depth Analysis of Raw Bio-Oil and Its Hydrodeoxygenated Products for a Comprehensive Catalyst Performance Evaluation. *Acs Sustain. Chem. Eng.* **2020**, *8* (50), 18433–18445. https://doi.org/10.1021/acssuschemeng.0c05533.

(106) Nanda, S.; Pattnaik, F.; Borugadda, V. B.; Dalai, A. K.; Kozinski, J. A.; Naik, S. Catalytic and Noncatalytic Upgrading of Bio-Oil to Synthetic Fuels: An Introductory Review. In *Catalytic and Noncatalytic Upgrading of Oils*; ACS Symposium Series; American Chemical Society, 2021; Vol. 1379, pp 1–28. https://doi.org/10.1021/bk-2021-1379.ch001.

(107) García-Gómez, N.; Valecillos, J.; Valle, B.; Remiro, A.; Bilbao, J.; Gayubo, A. G. Combined Effect of Bio-Oil Composition and Temperature on the Stability of Ni Spinel Derived Catalyst for Hydrogen Production by Steam Reforming. *Fuel* **2022**, *326*, 124966. https://doi.org/10.1016/j.fuel.2022.124966.

(108) Guvenc, C.; Alan, E.; Degirmencioglu, P.; Celik Ozcan, M.; Pekmezci Karaman, B.; Oktar, N. Catalytic Upgrading of Bio-Oil Model Mixtures in the Presence of Microporous HZSM-5 and γ-Al2O3 Based Ni, Ta and Zr Catalysts. *Fuel* **2023**, *350*, 128870. https://doi.org/10.1016/j.fuel.2023.128870.

(109) Gong, F.; Yang, Z.; Hong, C.; Huang, W.; Ning, S.; Zhang, Z.; Xu, Y.; Li, Q. Selective Conversion of Bio-Oil to Light Olefins: Controlling Catalytic Cracking for Maximum Olefins. *Bioresour. Technol.* **2011**, *102* (19), 9247–9254. https://doi.org/10.1016/j.biortech.2011.07.009.

(110) Shemfe, M.; Gu, S.; Fidalgo, B. Techno-Economic Analysis of Biofuel Production *via* Bio-Oil Zeolite Upgrading: An Evaluation of Two Catalyst Regeneration Systems. *Biomass Bioenergy* **2017**, *98*, 182–193. https://doi.org/10.1016/j.biombioe.2017.01.020.

(111)Hita, I.; Arandes, J. M.; Bilbao, J. Upgrading of Bio-Oil via Fluid Catalytic Cracking. In *Chemical Catalysts for Biomass Upgrading*; John Wiley & Sons, Ltd, 2020; pp 61–96. https://doi.org/10.1002/9783527814794.ch3.

(112) Kotsur, M. An Evaluation of Catalyst Applications in Bio-Oil Upgrading and Biomass Pyrolysis. *J. Enterp. Bus. Intell.* **2022**, 235–246. https://doi.org/10.53759/5181/JEBI202202023.

(113) Chen, G.; Zhang, R.; Ma, W.; Liu, B.; Li, X.; Yan, B.; Cheng, Z.; Wang, T. Catalytic Cracking of Model Compounds of Bio-Oil over HZSM-5 and the Catalyst Deactivation. *Sci. Total Environ.* **2018**, *631–632*, 1611–1622. https://doi.org/10.1016/j.scitotenv.2018.03.147.

(114) *Kinetic study of catalytic cracking of bio-oil over silica-alumina catalyst :: BioResources*. https://bioresources.cnr.ncsu.edu/ (accessed 2025-10-29).

(115) Qin, L.; Li, J.; Zhang, S.; Liu, Z.; Li, S.; Luo, L. Catalytic Performance of Ni–Co/HZSM-5 Catalysts for Aromatic Compound Promotion in Simulated Bio-Oil Upgrading. *RSC Adv.* **2023**, *13* (11), 7694–7702. https://doi.org/10.1039/D2RA07706J.

(116) Valle, B.; Gayubo, A. G.; Aguayo, A. T.; Olazar, M.; Bilbao, J. Selective Production of Aromatics by Crude Bio-Oil Valorization with a Nickel-Modified HZSM-5 Zeolite Catalyst. *Energy Fuels* **2010**, *24* (3), 2060–2070. https://doi.org/10.1021/ef901231j.

(117) Bertero, M.; Sedran, U. Conversion of Pine Sawdust Bio-Oil (Raw and Thermally Processed) over Equilibrium FCC Catalysts. *Bioresour. Technol.* **2013**, *135*, 644–651. https://doi.org/10.1016/j.biortech.2012.11.070.

(118) García, J. R.; Bertero, M.; Falco, M.; Sedran, U. Catalytic Cracking of Bio-Oils Improved by the Formation of Mesopores by Means of Y Zeolite Desilication. *Appl. Catal. Gen.* **2015**, *503*, 1–8. https://doi.org/10.1016/j.apcata.2014.11.005.

(119) Wang, S.; Chen, J.; Cai, Q.; Zhang, F.; Wang, Y.; Ru, B.; Wang, Q. The Effect of Mild Hydrogenation on the Catalytic Cracking of Bio-Oil for Aromatic Hydrocarbon Production. *Int. J. Hydrog. Energy* **2016**, *41* (37), 16385–16393. https://doi.org/10.1016/j.ijhydene.2015.12.024.

(120) Kar, Y. Catalytic Cracking of Pyrolytic Oil by Using Bentonite Clay for Green Liquid Hydrocarbon Fuels Production. *Biomass Bioenergy* **2018**, *119*, 473–479. https://doi.org/10.1016/j.biombioe.2018.10.014.

(121) Gollakota, A. R. K.; Shu, C.-M.; Sarangi, P. K.; Shadangi, K. P.; Rakshit, S.; Kennedy, J. F.; Gupta, V. K.; Sharma, M. Catalytic Hydrodeoxygenation of Bio-Oil and Model Compounds - Choice of Catalysts, and Mechanisms. *Renew. Sustain. Energy Rev.* **2023**, *187*, 113700. https://doi.org/10.1016/j.rser.2023.113700.

(122) Cordero-Lanzac, T.; Palos, R.; Arandes, J. M.; Castaño, P.; Rodríguez-Mirasol, J.; Cordero, T.; Bilbao, J. Stability of an Acid Activated Carbon Based Bifunctional Catalyst for the Raw Bio-Oil Hydrodeoxygenation. *Appl. Catal. B Environ.* **2017**, *203*, 389–399. https://doi.org/10.1016/j.apcatb.2016.10.018.

(123) Li, X.; Chen, G.; Liu, C.; Ma, W.; Yan, B.; Zhang, J. Hydrodeoxygenation of Lignin-Derived Bio-Oil Using Molecular Sieves Supported Metal Catalysts: A Critical Review. *Renew. Sustain. Energy Rev.* **2017**, *71*, 296–308. https://doi.org/10.1016/j.rser.2016.12.057.

(124) Pourzolfaghar, H.; Abnisa, F.; Daud, W.; Aroua, M. K. Atmospheric Hydrodeoxygenation of Bio-Oil Oxygenated Model Compounds: A Review. *J. Anal. Appl. Pyrolysis* **2018**, *133*, 117–127. https://doi.org/10.1016/j.jaap.2018.04.013.

(125) He, C.; Ruan, T.; Ouyang, X.; Ma, Y.; Qian, Y.; Qiu, X. Selective Hydrodeoxygenation of Monophenolics from Lignin Bio-Oil for Preparing Cyclohexanol and Its Derivatives over Ni-Co/Al2O3-MgO Catalyst. *Ind. Crops Prod.* **2023**, *202*, 117045. https://doi.org/10.1016/j.indcrop.2023.117045.

(126) Oh, S.; Seok Choi, H.; Choi, I.-G.; Weon Choi, J. Evaluation of Hydrodeoxygenation Reactivity of Pyrolysis Bio-Oil with Various Ni-Based Catalysts for Improvement of Fuel Properties. *RSC Adv.* **2017**, *7* (25), 15116–15126. https://doi.org/10.1039/C7RA01166K.

(127) Kong, X.; Liu, C.; Wang, B.; Xu, W.; Fan, Y.; Li, M.; Xiao, R. Boosted Hydrodeoxygenation of Lignin-Derived Phenolics to Cycloalkanes with a Complex Copper Acid Catalyst. *ACS Appl. Energy Mater.* **2021**, *4* (10), 11215–11224. https://doi.org/10.1021/acsaem.1c02061.

(128) Hunns, J. A.; Durndell, L. J.; Zhang, X.; Konarova, M.; Lee, A. F.; Wilson, K. Tuning Acid-Metal Synergy in *m* -Cresol Hydrodeoxygenation over Bifunctional Pt/Aluminosilicate Catalysts. *ACS Catal.* **2024**, *14* (9), 7052–7061. https://doi.org/10.1021/acscatal.4c00402.

(129) Deng, W.; Xu, K.; Xiong, Z.; Chaiwat, W.; Wang, X.; Su, S.; Hu, S.; Qiu, J.; Wang, Y.; Xiang, J. Evolution of Aromatic Structures during the Low-Temperature Electrochemical Upgrading of Bio-Oil. *Energy Fuels* **2019**, *33* (11), 11292–11301. https://doi.org/10.1021/acs.energyfuels.9b03099.

(130) Lam, C. H.; Deng, W.; Lang, L.; Jin, X.; Hu, X.; Wang, Y. Minireview on Bio-Oil Upgrading via Electrocatalytic Hydrogenation: Connecting Biofuel Production with Renewable Power. *Energy Fuels* **2020**, *34* (7), 7915–7928. https://doi.org/10.1021/acs.energyfuels.0c01380.

(131) Bu, Q.; Lei, H.; Zacher, A. H.; Wang, L.; Ren, S.; Liang, J.; Wei, Y.; Liu, Y.; Tang, J.; Zhang, Q.; Ruan, R. A Review of Catalytic Hydrodeoxygenation of Lignin-Derived Phenols from Biomass Pyrolysis. *Bioresour. Technol.* **2012**, *124*, 470–477. https://doi.org/10.1016/j.biortech.2012.08.089.

(132) Mäki-Arvela, P.; Murzin, D. Y. Hydrodeoxygenation of Lignin-Derived Phenols: From Fundamental Studies towards Industrial Applications. *Catalysts* **2017**, *7* (9), 265. https://doi.org/10.3390/catal7090265.

(133) Gil, A.; Sancho-Sanz, I.; Korili, S. A. Progress and Perspectives in the Catalytic Hydrotreatment of Bio-Oils: Effect of the Nature of the Metal Catalyst. *Ind. Eng. Chem. Res.* **2024**, *63* (27), 11759–11775. https://doi.org/10.1021/acs.iecr.4c00747.

(134) Mudi, I.; Hart, A.; Ingram, A.; Wood, J. A Kinetic Model of Furfural Hydrogenation to 2-Methylfuran on Nanoparticles of Nickel Supported on Sulfuric Acid-Modified Biochar Catalyst. *Catalysts* **2024**, *14* (1), 54. https://doi.org/10.3390/catal14010054.

(135) Popova, M.; Trendafilova, I.; Oykova, M.; Mitrev, Y.; Shestakova, P.; Mihályi, M. R.; Szegedi, Á. Hydrodeoxygenation of Levulinic Acid to γ-Valerolactone over Mesoporous Silica-Supported Cu-Ni Composite Catalysts. *Molecules* **2022**, *27* (17), 5383. https://doi.org/10.3390/molecules27175383.

(136) Lin, B. Q.; Li, R. X.; Shu, R. Y.; Wang, C.; Yuan, Z. Q.; Liu, Y.; Chen, Y. Synergistic Effect of Highly Dispersed Ru and Moderate Acid Site on the Hydrodeoxygenation of Phenolic Compounds and Raw Bio-Oil. *J. Energy Inst.* **2020**, *93* (3), 847–856. https://doi.org/10.1016/j.joei.2019.07.009.

(137) Cheng, S. Y.; Wei, L.; Alsowij, M. R.; Corbin, F.; Julson, J.; Boakye, E.; Raynie, D. In Situ Hydrodeoxygenation Upgrading of Pine Sawdust Bio-Oil to Hydrocarbon Biofuel Using Pd/C Catalyst. *J. Energy Inst.* **2018**, *91* (2), 163–171. https://doi.org/10.1016/j.joei.2017.01.004.

(138) Shu, R. Y.; Lin, B. Q.; Wang, C.; Zhang, J. T.; Cheng, Z. D.; Chen, Y. Upgrading Phenolic Compounds and Bio-Oil through Hydrodeoxygenation Using Highly Dispersed Pt/TiO2 Catalyst. *Fuel* **2019**, *239*, 1083–1090. https://doi.org/10.1016/j.fuel.2018.11.107.

(139) Horáček, J.; Kubička, D. Bio-Oil Hydrotreating over Conventional CoMo & NiMo Catalysts: The Role of Reaction Conditions and Additives. *Fuel* **2017**, *198*, 49–57. https://doi.org/10.1016/j.fuel.2016.10.003.

(140) Stummann, M. Z.; Hoj, M.; Hansen, A. B.; Beato, P.; Wiwel, P.; Gabrielsen, J.; Jensen, P. A.; Jensen, A. D. Deactivation of a CoMo Catalyst during Catalytic Hydropyrolysis of Biomass. Part 1. Product Distribution and Composition. *Energy Fuels* **2019**, *33* (12), 12374–12386. https://doi.org/10.1021/acs.energyfuels.9b02523.

(141) Muangsuwan, C.; Kriprasertkul, W.; Ratchahat, S.; Liu, C.-G.; Posoknistakul, P.; Laosiripojana, N.; Sakdaronnarong, C. Upgrading of Light Bio-Oil from Solvothermolysis Liquefaction of an Oil Palm Empty Fruit Bunch in Glycerol by Catalytic Hydrodeoxygenation Using NiMo/Al2O3 or CoMo/Al2O3 Catalysts. *ACS Omega* **2021**, *6* (4), 2999–3016. https://doi.org/10.1021/acsomega.0c05387.

(142) Abdus Salam, M.; Creaser, D.; Arora, P.; Tamm, S.; Lind Grennfelt, E.; Olsson, L. Influence of Bio-Oil Phospholipid on the Hydrodeoxygenation Activity of NiMoS/Al2O3 Catalyst. *Catalysts* **2018**, *8* (10), 418. https://doi.org/10.3390/catal8100418.

(143) Aiamsiri, P.; Tumnantong, D.; Yoosuk, B.; Ngamcharussrivichai, C.; Prasassarakich, P. Biohydrogenated Diesel from Palm Oil Deoxygenation over Unsupported and γ-Al2O3 Supported Ni–Mo Catalysts. *Energy Fuels* **2021**, *35* (18), 14793–14804. https://doi.org/10.1021/acs.energyfuels.1c02083.

(144) Mortensen, P. M.; Gardini, D.; Damsgaard, C. D.; Grunwaldt, J.-D.; Jensen, P. A.; Wagner, J. B.; Jensen, A. D. Deactivation of Ni-MoS2 by Bio-Oil Impurities

during Hydrodeoxygenation of Phenol and Octanol. *Appl. Catal. Gen.* **2016**, *523*, 159–170. https://doi.org/10.1016/j.apcata.2016.06.002.

(145) Sihombing, J. L.; Herlinawati, H.; Pulungan, A. N.; Simatupang, L.; Rahayu, R.; Wibowo, A. A. Effective Hydrodeoxygenation Bio-Oil via Natural Zeolite Supported Transition Metal Oxide Catalyst. *Arab. J. Chem.* **2023**, *16* (6), 104707. https://doi.org/10.1016/j.arabjc.2023.104707.

(146) Cheng, S.; Wei, L.; Julson, J.; Rabnawaz, M. Upgrading Pyrolysis Bio-Oil through Hydrodeoxygenation (HDO) Using Non-Sulfided Fe-Co/SiO2 Catalyst. *Energy Convers. Manag.* **2017**, *150*, 331–342. https://doi.org/10.1016/j.enconman.2017.08.024.

(147) Yang, Y.; Xu, X.; He, H.; Huo, D.; Li, X.; Dai, L.; Si, C. The Catalytic Hydrodeoxygenation of Bio-Oil for Upgradation from Lignocellulosic Biomass. *Int. J. Biol. Macromol.* **2023**, *242*, 124773. https://doi.org/10.1016/j.ijbiomac.2023.124773.

(148) Cheng, S.; Wei, L.; Julson, J.; Muthukumarappan, K.; Kharel, P. R.; Boakye, E. Hydrocarbon Bio-Oil Production from Pyrolysis Bio-Oil Using Non-Sulfide Ni-Zn/Al2O3 Catalyst. *Fuel Process. Technol.* **2017**, *162*, 78–86. https://doi.org/10.1016/j.fuproc.2017.04.001.

(149) Shi, Y.; Xing, E.; Wu, K.; Wang, J.; Yang, M.; Wu, Y. Recent Progress on Upgrading of Bio-Oil to Hydrocarbons over Metal/Zeolite Bifunctional Catalysts. *Catal. Sci. Technol.* **2017**, *7* (12), 2385–2415. https://doi.org/10.1039/C7CY00574A.

(150) Oh, S.; Lee, J. H.; Choi, I. G.; Choi, J. W. Enhancement of Bio-Oil Hydrodeoxygenation Activity over Ni-Based Bimetallic Catalysts Supported on SBA-15. *Renew. Energy* **2020**, *149*, 1–10. https://doi.org/10.1016/j.renene.2019.12.027.

(151) Bharath, G.; Rambabu, K.; Hai, A.; Banat, F.; Taher, H.; Schmidt, J. E.; Show, P. L. Catalytic Hydrodeoxygenation of Biomass-Derived Pyrolysis Oil over Alloyed Bimetallic Ni3Fe Nanocatalyst for High-Grade Biofuel Production. *Energy Convers. Manag.* **2020**, *213*. https://doi.org/10.1016/j.enconman.2020.112859.

(152) Wu, Y. J.; Sun, Y.; Liang, K. L.; Yang, Z. G.; Tu, R.; Fan, X. D.; Cheng, S. C.; Yu, H. P.; Jiang, E. C.; Xu, X. W. Enhancing Hydrodeoxygenation of Bio-Oil via Bimetallic Ni-V Catalysts Modified by Cross-Surface Migrated-Carbon from Biochar. *Acs Appl. Mater. Interfaces* **2021**, *13* (18), 21482–21498. https://doi.org/10.1021/acsami.1c05350.

(153) Raikwar, D.; Majumdar, S.; Shee, D. Synergistic Effect of Ni-Co Alloying on Hydrodeoxygenation of Guaiacol over Ni-Co/Al2O3 Catalysts. *Mol. Catal.* **2021**, *499*, 111290. https://doi.org/10.1016/j.mcat.2020.111290.

(154) Jiang, J.; Ding, W.; Zhang, W.; Li, H. Defect-Rich ZrO2 Anchored Pd Nanoparticles for Selective Hydrodeoxygenation of Bio-Models at Room Temperature. *Fuel* **2022**, *318*, 123529. https://doi.org/10.1016/j.fuel.2022.123529.

(155) Al-Ali, L. I.; Elmutasim, O.; Al Ali, K.; Singh, N.; Polychronopoulou, K. Transition Metal Phosphides (TMP) as a Versatile Class of Catalysts for the Hydrodeoxygenation Reaction (HDO) of Oil-Derived Compounds. *Nanomaterials* **2022**, *12* (9), 1435. https://doi.org/10.3390/nano12091435.

(156) Fan, L.; Zhang, Y.; Liu, S.; Zhou, N.; Chen, P.; Cheng, Y.; Addy, M.; Lu, Q.; Omar, M. M.; Liu, Y.; Wang, Y.; Dai, L.; Anderson, E.; Peng, P.; Lei, H.; Ruan, R. Bio-Oil from Fast Pyrolysis of Lignin: Effects of Process and Upgrading Parameters. *Bioresour. Technol.* **2017**, *241*, 1118–1126. https://doi.org/10.1016/j.biortech.2017.05.129.

(157) Srifa, A.; Chaiwat, W.; Pitakjakpipop, P.; Anutrasakda, W.; Faungnawakij, K. Chapter 6 - Advances in Bio-Oil Production and Upgrading Technologies. In *Sustainable Bioenergy*; Rai, M., Ingle, A. P., Eds.; Elsevier, 2019; pp 167–198. https://doi.org/10.1016/B978-0-12-817654-2.00006-X.

(158) Oh, S.; Seok Choi, H.; Choi, I.-G.; Weon Choi, J. Evaluation of Hydrodeoxygenation Reactivity of Pyrolysis Bio-Oil with Various Ni-Based Catalysts for Improvement of Fuel Properties. *RSC Adv.* **2017**, *7* (25), 15116–15126. https://doi.org/10.1039/C7RA01166K.

(159) Dabros, T. M. H.; Stummann, M. Z.; Høj, M.; Jensen, P. A.; Grunwaldt, J.-D.; Gabrielsen, J.; Mortensen, P. M.; Jensen, A. D. Transportation Fuels from Biomass Fast Pyrolysis, Catalytic Hydrodeoxygenation, and Catalytic Fast Hydropyrolysis. *Prog. Energy Combust. Sci.* **2018**, *68*, 268–309. https://doi.org/10.1016/j.pecs.2018.05.002.

(160) Gil, A.; Sancho-Sanz, I.; Korili, S. A. Progress and Perspectives in the Catalytic Hydrotreatment of Bio-Oils: Effect of the Nature of the Metal Catalyst. *Ind. Eng. Chem. Res.* **2024**, *63* (27), 11759–11775. https://doi.org/10.1021/acs.iecr.4c00747.

(161) Wu, L.; Wang, Y.; Zheng, L.; Shi, M.; Li, J. Design and Optimization of Bio-Oil Co-Processing with Vacuum Gas Oil in a Refinery. *Energy Convers. Manag.* **2019**, *195*, 620–629. https://doi.org/10.1016/j.enconman.2019.05.041.

(162) Bagnato, G.; Sanna, A. Process and Techno-Economic Analysis for Fuel and Chemical Production by Hydrodeoxygenation of Bio-Oil. *Catalysts* **2019**, *9* (12), 1021. https://doi.org/10.3390/catal9121021.

(163) Liu, D.; Li, Z.; Wu, C.; Song, L.; Wu, P.; Li, M.; Wang, C.; Men, Z.; Yan, Z.; Gates, I. D. Exploration of In-Situ Formed MoSx Catalyst for Co-Hydrodeoxygenation of Sawdust and Vacuum Gas Oil in Pilot-Scale Plant. *Appl.*

Catal. B Environ. **2021**, *297*, 120499. https://doi.org/10.1016/j.apcatb.2021.120499.

(164) Verdier, S.; D. Mante, O.; B. Hansen, A.; G. Poulsen, K.; H. Christensen, J.; Ammtizboll, N.; Gabrielsen, J.; C. Dayton, D. Pilot-Scale Hydrotreating of Catalytic Fast Pyrolysis Biocrudes: Process Performance and Product Analysis. *Sustain. Energy Fuels* **2021**, *5* (18), 4668–4679. https://doi.org/10.1039/D1SE00540E.

(165) Liu, Y.; Chen, L.; Chen, Y.; Zhang, X.; Liu, J.; Liu, Q.; Li, Y.; Wang, C.; Zhang, Q.; Ma, L. Pilot Study on Production of Aviation Fuel from Catalytic Conversion of Corn Stover. *Bioresour. Technol.* **2023**, *372*, 128653. https://doi.org/10.1016/j.biortech.2023.128653.

(166) Zheng, Y.; Wang, J.; Li, D.; Liu, C.; Lu, Y.; Lin, X.; Zheng, Z. Highly Efficient Catalytic Pyrolysis of Biomass Vapors Upgraded into Jet Fuel Range Hydrocarbon-Rich Bio-Oil over a Bimetallic Pt–Ni/γ-Al2O3 Catalyst. *Int. J. Hydrog. Energy* **2021**, *46* (55), 27922–27940. https://doi.org/10.1016/j.ijhydene.2021.06.082.

(167) Shu, R. Y.; Li, R. X.; Liu, Y.; Wang, C.; Liu, P. F.; Chen, Y. Enhanced Adsorption Properties of Bimetallic RuCo Catalyst for the Hydrodeoxygenation of Phenolic Compounds and Raw Lignin-Oil. *Chem. Eng. Sci.* **2020**, *227*. https://doi.org/10.1016/j.ces.2020.115920.

(168) Ou, X.; Wu, C.; Shi, K.; Hardacre, C.; Zhang, J.; Jiao, Y.; Fan, X. Structured ZSM-5/SiC Foam Catalysts for Bio-Oils Upgrading. *Appl. Catal. Gen.* **2020**, *599*, 117626. https://doi.org/10.1016/j.apcata.2020.117626.

(169) *CaSH research project demonstrated novel path for bio-oils valorisation | VTT*. https://www.vttresearch.com/en/project_news/cash-research-project-demonstrated-novel-path-bio-oils-valorisation (accessed 2025-10-31).

(170) *Honeywell And Preem Conduct Commercial Co-Processing Trial to Produce Renewable Fuel*. https://uop.honeywell.com/content/uop/en/us/home/news-events/2021/september/honeywell-and-preem-conduct-commercial-co-processing-trial-to-produce-renewable-fuel.html (accessed 2025-10-31).

(171) Shu, R. Y.; Lin, B. Q.; Zhang, J. T.; Wang, C.; Yang, Z.; Chen, Y. Efficient Catalytic Hydrodeoxygenation of Phenolic Compounds and Bio-Oil over Highly Dispersed Ru/TiO2. *Fuel Process. Technol.* **2019**, *184*, 12–18. https://doi.org/10.1016/j.fuproc.2018.11.004.

(172) Wang, J. D.; Jabbour, M.; Abdelouahed, L.; Mezghich, S.; Estel, L.; Thomas, K.; Taouk, B. Catalytic Upgrading of Bio-Oil: Hydrodeoxygenation Study of Acetone as Molecule Model of Ketones. *Can. J. Chem. Eng.* **2021**, *99* (5), 1082–1093. https://doi.org/10.1002/cjce.23909.

(173) Li, Z. Y.; Jiang, E. C.; Xu, X. W.; Sun, Y.; Tu, R. Hydrodeoxygenation of Phenols, Acids, and Ketones as Model Bio-Oil for Hydrocarbon Fuel over Ni-Based Catalysts Modified by Al, La and Ga. *Renew. Energy* **2020**, *146*, 1991–2007. https://doi.org/10.1016/j.renene.2019.08.012.

(174) Fermoso, J.; Pizarro, P.; Coronado, J. M.; Serrano, D. P. Advanced Biofuels Production by Upgrading of Pyrolysis Bio-Oil. *Wiley Interdiscip. Rev.-Energy Environ.* **2017**, *6* (4), 1–18. https://doi.org/10.1002/wene.245.

(175) Wang, S.; Liu, Y.; Zhang, M.; Li, F.; Chen, Y.; Song, H. Construction of Highly Active and Water-Resistant Ni-Based Catalyst for HDO Reaction of Phenol. *Sustain. Energy Fuels* **2022**, 10.1039.D2SE00918H. https://doi.org/10.1039/D2SE00918H.

(176) Robinson, A. M.; Hensley, J. E.; Medlin, J. W. Bifunctional Catalysts for Upgrading of Biomass-Derived Oxygenates: A Review. *ACS Catal.* **2016**, *6* (8), 5026–5043. https://doi.org/10.1021/acscatal.6b00923.

(177) Luo, X.; Su, S.; Zeng, Q.; Peng, H.; Yang, X. A High-Performance Porous Carbon Coated CoxP Dual Functional Catalyst for Upgrading of Furfuryl Alcohol. *Appl. Surf. Sci.* **2025**, *679*, 161290. https://doi.org/10.1016/j.apsusc.2024.161290.

(178) Gil, A.; Sancho-Sanz, I.; Korili, S. A. Progress and Perspectives in the Catalytic Hydrotreatment of Bio-Oils: Effect of the Nature of the Metal Catalyst. *Ind. Eng. Chem. Res.* **2024**, *63* (27), 11759–11775. https://doi.org/10.1021/acs.iecr.4c00747.

(179) He, Y. F.; Bie, Y. W.; Lehtonen, J.; Liu, R. H.; Cai, J. M. Hydrodeoxygenation of Guaiacol as a Model Compound of Lignin-Derived Pyrolysis Bio-Oil over Zirconia-Supported Rh Catalyst: Process Optimization and Reaction Kinetics. *Fuel* **2019**, *239*, 1015–1027. https://doi.org/10.1016/j.fuel.2018.11.103.

(180) Cordero-Lanzac, T.; Hita, I.; Garcia-Mateos, F. J.; Castano, P.; Rodriguez-Mirasol, J.; Cordero, T.; Bilbao, J. Adaptable Kinetic Model for the Transient and Pseudo-Steady States in the Hydrodeoxygenation of Raw Bio-Oil. *Chem. Eng. J.* **2020**, *400*, 124679. https://doi.org/10.1016/j.cej.2020.124679.

(181) Kay Lup, A. N.; Abnisa, F.; Daud, W. M. A. W.; Aroua, M. K. A Review on Reaction Mechanisms of Metal-Catalyzed Deoxygenation Process in Bio-Oil Model Compounds. *Appl. Catal. Gen.* **2017**, *541*, 87–106. https://doi.org/10.1016/j.apcata.2017.05.002.

(182) Yang, T. H.; Shi, L. P.; Li, R. D.; Li, B. S.; Kai, X. P. Hydrodeoxygenation of Crude Bio-Oil in Situ in the Bio-Oil Aqueous Phase with Addition of Zero-Valent Aluminum. *Fuel Process. Technol.* **2019**, *184*, 65–72. https://doi.org/10.1016/j.fuproc.2018.10.025.

(183) Li, Z. Y.; Xu, X. W.; Jiang, E. C.; Han, P.; Sun, Y.; Zhou, L.; Zhong, P. D.; Fan, X. D. Alkane from Hydrodeoxygenation (HDO) Combined with in-Situ

Multistage Condensation of Biomass Continuous Pyrolysis Bio-Oil via Mixed Supports Catalyst Ni/HZSM-5-Gamma-Al2O3. *Renew. Energy* **2020**, *149*, 535–548. https://doi.org/10.1016/j.renene.2019.10.035.

(184) Zhao, B.; Hu, Y.; Gao, J.; Zhao, G.; Ray, M. B.; Xu, C. C. Recent Advances in Hydroliquefaction of Biomass for Bio-Oil Production Using In Situ Hydrogen Donors. *Ind. Eng. Chem. Res.* **2020**, *59* (39), 16987–17007. https://doi.org/10.1021/acs.iecr.0c01649.

(185) Nørskov, J. K.; Studt, F.; Abild-Pedersen, F.; Bligaard, T. *Fundamental Concepts in Heterogeneous Catalysis*, 1st ed.; Wiley, 2014. https://doi.org/10.1002/9781118892114.

(186) Islam, N.; Kaya, S. *Conceptual Density Functional Theory and Its Application in the Chemical Domain*, 1st ed.; CRC Press, 2018.

(187) Sholl, D. S.; Steckel, J. A. *Density Functional Theory: A Practical Introduction*, 1st ed.; John Wiley & Sons, 2009.

(188) Martin, R. M. *Electronic Structure: Basic Theory and Practical Methods*, 2nd ed.; Cambridge University Press, 2020.

(189) Moreno, J. R.; Carleo, G.; Georges, A. Deep Learning the Hohenberg-Kohn Maps of Density Functional Theory. *Phys. Rev. Lett.* **2020**, *125* (7), 076402. https://doi.org/10.1103/PhysRevLett.125.076402.

(190) Görling, A. Density-Functional Theory beyond the Hohenberg-Kohn Theorem. *Phys. Rev. A* **1999**, *59* (5), 3359–3374. https://doi.org/10.1103/PhysRevA.59.3359.

(191) Sahni, V. *Quantal Density Functional Theory*, 1st ed.; Springer: Berlin, Heidelberg, 2004.

(192) Scuseria, G. E.; Staroverov, V. N. *Theory and Applications of Computational Chemistry*, 1st ed.; Elsevier: Amsterdam, 2005.

(193) Ernzerhof, M.; Scuseria, G. E. Assessment of the Perdew–Burke–Ernzerhof Exchange-Correlation Functional. *J. Chem. Phys.* **1999**, *110* (11), 5029–5036. https://doi.org/10.1063/1.478401.

(194) Marini, A.; Onida, G.; Del Sole, R. Plane-Wave DFT-LDA Calculation of the Electronic Structure and Absorption Spectrum of Copper. *Phys. Rev. B* **2001**, *64* (19), 195125. https://doi.org/10.1103/PhysRevB.64.195125.

(195) Stampfl, C.; Mannstadt, W.; Asahi, R.; Freeman, A. J. Electronic Structure and Physical Properties of Early Transition Metal Mononitrides: Density-Functional Theory LDA, GGA, and Screened-Exchange LDA FLAPW Calculations. *Phys. Rev. B* **2001**, *63* (15), 155106. https://doi.org/10.1103/PhysRevB.63.155106.

(196) Christensen, R.; A. Hansen, H.; Vegge, T. Identifying Systematic DFT Errors in Catalytic Reactions. *Catal. Sci. Technol.* **2015**, *5* (11), 4946–4949. https://doi.org/10.1039/C5CY01332A.

(197) Perdew, J. P.; Burke, K.; Ernzerhof, M. Generalized Gradient Approximation Made Simple. *Phys. Rev. Lett.* **1996**, *77* (18), 3865–3868. https://doi.org/10.1103/PhysRevLett.77.3865.

(198) Becke, A. D. Density-Functional Thermochemistry. III. The Role of Exact Exchange. *J. Chem. Phys.* **1993**, *98* (7), 5648–5652. https://doi.org/10.1063/1.464913.

(199) Lee, C.; Yang, W.; Parr, R. G. Development of the Colle-Salvetti Correlation-Energy Formula into a Functional of the Electron Density. *Phys. Rev. B* **1988**, *37* (2), 785–789. https://doi.org/10.1103/PhysRevB.37.785.

(200) Zhao, Y.; Truhlar, D. G. The M06 Suite of Density Functionals for Main Group Thermochemistry, Thermochemical Kinetics, Noncovalent Interactions, Excited States, and Transition Elements: Two New Functionals and Systematic Testing of Four M06-Class Functionals and 12 Other Functionals. *Theor. Chem. Acc.* **2008**, *120* (1–3), 215–241. https://doi.org/10.1007/s00214-007-0310-x.

(201) Grimme, S.; Antony, J.; Ehrlich, S.; Krieg, H. A Consistent and Accurate *Ab Initio* Parametrization of Density Functional Dispersion Correction (DFT-D) for the 94 Elements H-Pu. *J. Chem. Phys.* **2010**, *132* (15), 154104. https://doi.org/10.1063/1.3382344.

(202) Grimme, S. Semiempirical GGA-type density functional constructed with a long-range dispersion correction. *J. Comput. Chem.* **2006**, *27* (15), 1787–1799. https://doi.org/10.1002/jcc.20495.

(203) Dion, M.; Rydberg, H.; Schröder, E.; Langreth, D. C.; Lundqvist, B. I. Van Der Waals Density Functional for General Geometries. *Phys. Rev. Lett.* **2004**, *92* (24), 246401. https://doi.org/10.1103/PhysRevLett.92.246401.

(204) Zhou, T.; Ma, S.; Peng, Q.; Liu, H.; Dou, T.; Jiang, X. Selective Direct Deoxygenation of M-Cresol on Heusler Alloy Catalysts via Precise Control of Electronic Structure: An Integrated Density Function Theory and Microkinetic Modeling Study. *Energy* **2024**, *312*, 133532. https://doi.org/10.1016/j.energy.2024.133532.

(205) Jia, X.; An, W.; Wang, Z.; Zhou, J. Effect of Doped Metals on Hydrodeoxygenation of Phenol over Pt-Based Bimetallic Alloys: C_{aryl}–OH Versus $C_{aliphatic}$H–OH Bond Scission. *J. Phys. Chem. C* **2019**, *123* (27), 16873–16882. https://doi.org/10.1021/acs.jpcc.9b04457.

(206) Jiang, S. N.; Ji, N.; Diao, X. Y.; Li, H. Y.; Rong, Y.; Lei, Y. X.; Yu, Z. H. Vacancy Engineering in Transition Metal Sulfide and Oxide Catalysts for Hydrodeoxygenation of Lignin-Derived Oxygenates. *Chemsuschem* **2021**, *14* (20), 4377–4396. https://doi.org/10.1002/cssc.202101362.

(207) Xiao, X.; Bergstrom, H.; Saenger, R.; Johnson, B.; Sun, R.; Peterson, A. The Role of Oxygen Vacancies in Biomass Deoxygenation by Reducible Zinc/Zinc

Oxide Catalysts. *Catal. Sci. Technol.* **2018**, *8* (7), 1819–1827. https://doi.org/10.1039/C7CY02535A.

(208) Deo, S.; Janik, M. J. Predicting an Optimal Oxide/Metal Catalytic Interface for Hydrodeoxygenation Chemistry of Biomass Derivatives. *Catal. Sci. Technol.* **2021**, *11* (16), 5606–5618. https://doi.org/10.1039/d1cy00707f.

(209) Deo, S.; Medlin, W.; Nikolla, E.; Janik, M. J. Reaction Paths for Hydrodeoxygenation of Furfuryl Alcohol at TiO2/Pd Interfaces. *J. Catal.* **2019**, *377*, 28–40. https://doi.org/10.1016/j.jcat.2019.07.012.

(210) Liu, X. Y.; An, W.; Turner, C. H.; Resasco, D. E. Hydrodeoxygenation of M-Cresol over Bimetallic NiFe Alloys: Kinetics and Thermodynamics Insight into Reaction Mechanism. *J. Catal.* **2018**, *359*, 272–286. https://doi.org/10.1016/j.jcat.2018.01.006.

(211) Zhang, Y.; Wang, W.; Fan, G.; Yang, L.; Li, F. Defect-Decorated NiFe Bimetallic Nanocatalysts for the Enhanced Hydrodeoxygenation of Guaiacol. *ChemCatChem* **2022**, *14* (19), e202200585. https://doi.org/10.1002/cctc.202200585.

(212) Chen, N.; Ren, Y.; Qian, E. W. Elucidation of the Active Phase in PtSn/SAPO-11 for Hydrodeoxygenation of Methyl Palmitate. *J. Catal.* **2016**, *334*, 79–88. https://doi.org/10.1016/j.jcat.2015.11.001.

(213) Xie, J.; Falcone, D. D.; Davis, R. J. Restructuring of Supported PtSn Bimetallic Catalysts during Aqueous Phase Oxidation of 1,6-Hexanediol. *J. Catal.* **2015**, *332*, 38–50. https://doi.org/10.1016/j.jcat.2015.09.011.

(214) Chiu, C.; Genest, A.; Borgna, A.; Rösch, N. Hydrodeoxygenation of Guaiacol over Ru(0001): A DFT Study. *ACS Catal.* **2014**, *4* (11), 4178–4188. https://doi.org/10.1021/cs500911j.

(215) Taylor, M. J.; Jiang, L.; Reichert, J.; Papageorgiou, A. C.; Beaumont, S. K.; Wilson, K.; Lee, A. F.; Barth, J. V.; Kyriakou, G. Catalytic Hydrogenation and Hydrodeoxygenation of Furfural over Pt(111): A Model System for the Rational Design and Operation of Practical Biomass Conversion Catalysts. *J. Phys. Chem. C* **2017**, *121* (15), 8490–8497. https://doi.org/10.1021/acs.jpcc.7b01744.

(216) You, K.-E.; Ammal, S. C.; Lin, Z.; Wan, W.; Chen, J. G.; Heyden, A. Understanding the Effect of Mo2C Support on the Activity of Cu for the Hydrodeoxygenation of Glycerol. *J. Catal.* **2020**, *388*, 141–153. https://doi.org/10.1016/j.jcat.2020.05.007.

(217) Zhang, J. J.; Fidalgo, B.; Shen, D. K.; Zhang, X. L.; Gu, S. Mechanism of Hydrodeoxygenation (HDO) in Anisole Decomposition over Metal Loaded Bronsted Acid Sites: Density Functional Theory (DFT) Study. *Mol. Catal.* **2018**, *454*, 30–37. https://doi.org/10.1016/j.mcat.2018.05.015.

(218) Badawi, M.; Cristol, S.; Paul, J. F.; Payen, E. DFT Study of Furan Adsorption over Stable Molybdenum Sulfide Catalyst under HDO Conditions. *Comptes Rendus Chim.* **2009**, *12* (6–7), 754–761. https://doi.org/10.1016/j.crci.2008.10.023.

(219) Banerjee, A.; Mushrif, S. H. Reaction Pathways for the Deoxygenation of Biomass-Pyrolysis-Derived Bio-Oil on Ru: A DFT Study Using Furfural as a Model Compound. *Chemcatchem* **2017**, *9* (14), 2828–2838. https://doi.org/10.1002/cctc.201700036.

(220) Dupont, C.; Lemeur, R.; Daudin, A.; Raybaud, P. Hydrodeoxygenation Pathways Catalyzed by MoS2 and NiMoS Active Phases: A DFT Study. *J. Catal.* **2011**, *279* (2), 276–286. https://doi.org/10.1016/j.jcat.2011.01.025.

(221) Yang, W.; Abdelfatah, K. E.; Kundu, S. K.; Rajbanshi, B.; Terejanu, G. A.; Heyden, A. Machine Learning Accelerated First-Principles Study of the Hydrodeoxygenation of Propanoic Acid. *ACS Catal.* **2024**, *14* (13), 10148–10163. https://doi.org/10.1021/acscatal.4c01419.

(222) Lyu, H.; Liu, J.; Chen, Y.; Li, G.; Jiang, H.; Zhang, M. Effect of Surface Oxygen Vacancy Sites on Ethanol Synthesis from Acetic Acid Hydrogenation on a Defective In 2 O 3 (110) Surface. *Phys. Chem. Chem. Phys.* **2018**, *20* (10), 7156–7166. https://doi.org/10.1039/C7CP07568E.

(223) Cheng, C.; Bian, F.; Lu, C.; Wang, Q.; Shen, D.; Jiang, X. DFT Investigation of Hydrodeoxygenation of Guaiacol on Fe-Decorated Ni (111). *J. Energy Inst.* **2024**, *112*, 101460. https://doi.org/10.1016/j.joei.2023.101460.

(224) Wen, Y.; Zormpa, F.; Sharapa, D. I.; Studt, F.; Raffelt, K.; Dahmen, N. Exploring the Hydrodeoxygenation of Lignin β-O-4 Dimer Model Compound and Bio-Oil by DFT and Experimental Studies. *Mol. Catal.* **2025**, *580*, 115134. https://doi.org/10.1016/j.mcat.2025.115134.

(225) Wen, Y.; Li, W.; Sharapa, D. I.; Zevaco, T. A.; Schild, D.; Studt, F.; Raffelt, K.; Dahmen, N. Engineering Ni(0)/Ni(II) Interfaces in LDH-Derived Ni–Al Catalysts for Mild Lignin Depolymerization. *Bioresour. Technol.* **2026**, *442*, 133697. https://doi.org/10.1016/j.biortech.2025.133697.

(226) Chen, Y.; Bao, Y.; Yang, G.; Yu, Z. Study on Structure and Photoluminescence of Tb-Doped ZnAl–NO3 Layered Double Hydroxides Prepared by Co-Precipitation. *Mater. Chem. Phys.* **2016**, *176*, 24–31. https://doi.org/10.1016/j.matchemphys.2016.03.012.

(227) Janani, F. Z.; Taoufik, N.; Khiar, H.; Elhalil, A.; Qourzal, S.; Sadiq, M.; Barka, N. Effect of Ag Doping on Photocatalytic Activity of ZnO-Al2O3 Derived from LDH Structure: Synthesis, Characterization and Experimental Study. *Appl. Surf. Sci. Adv.* **2023**, *16*, 100430. https://doi.org/10.1016/j.apsadv.2023.100430.

(228) Pavel, O. D.; Zăvoianu, R.; Bîrjega, R.; Angelescu, E.; Pârvulescu, V. I. Mechanochemical versus Co-Precipitated Synthesized Lanthanum-Doped Layered Materials for Olefin Oxidation. *Appl. Catal. Gen.* **2017**, *542*, 10–20. https://doi.org/10.1016/j.apcata.2017.05.012.

(229) Ravel, B.; Newville, M. ATHENA, ARTEMIS, HEPHAESTUS: Data Analysis for X-Ray Absorption Spectroscopy Using IFEFFIT. *J. Synchrotron Radiat.* **2005**, *12* (4), 537–541. https://doi.org/10.1107/S0909049505012719.

(230) Ravel, B.; Newville, M. *ATHENA* , *ARTEMIS* , *HEPHAESTUS* : Data Analysis for X-Ray Absorption Spectroscopy Using *IFEFFIT*. *J. Synchrotron Radiat.* **2005**, *12* (4), 537–541. https://doi.org/10.1107/S0909049505012719.

(231) Kresse, G.; Furthmüller, J. Efficiency of Ab-Initio Total Energy Calculations for Metals and Semiconductors Using a Plane-Wave Basis Set. *Comput. Mater. Sci.* **1996**, *6* (1), 15–50. https://doi.org/10.1016/0927-0256(96)00008-0.

(232) Kresse, G.; Furthmüller, J. Efficient Iterative Schemes for Ab Initio Total-Energy Calculations Using a Plane-Wave Basis Set. *Phys. Rev. B* **1996**, *54* (16), 11169–11186. https://doi.org/10.1103/PhysRevB.54.11169.

(233) Bahn, S. R.; Jacobsen, K. W. An Object-Oriented Scripting Interface to a Legacy Electronic Structure Code. *Comput. Sci. Eng.* **2002**, *4* (3), 56–66. https://doi.org/10.1109/5992.998641.

(234) Blöchl, P. E. Projector Augmented-Wave Method. *Phys. Rev. B* **1994**, *50* (24), 17953–17979. https://doi.org/10.1103/PhysRevB.50.17953.

(235) Kresse, G.; Joubert, D. From Ultrasoft Pseudopotentials to the Projector Augmented-Wave Method. *Phys. Rev. B* **1999**, *59* (3), 1758–1775. https://doi.org/10.1103/PhysRevB.59.1758.

(236) Henkelman, G.; Uberuaga, B. P.; Jónsson, H. A Climbing Image Nudged Elastic Band Method for Finding Saddle Points and Minimum Energy Paths. *J. Chem. Phys.* **2000**, *113* (22), 9901–9904. https://doi.org/10.1063/1.1329672.

(237) Wang, V.; Xu, N.; Liu, J.-C.; Tang, G.; Geng, W.-T. VASPKIT: A User-Friendly Interface Facilitating High-Throughput Computing and Analysis Using VASP Code. *Comput. Phys. Commun.* **2021**, *267*, 108033. https://doi.org/10.1016/j.cpc.2021.108033.

(238) Chiu, C. C.; Genest, A.; Borgna, A.; Rosch, N. Hydrodeoxygenation of Guaiacol over Ru(0001): A DFT Study. *Acs Catal.* **2014**, *4* (11), 4178–4188. https://doi.org/10.1021/cs500911j.

(239) Fan, C.; Zhu, Y.-A.; Zhou, X.-G.; Liu, Z.-P. Catalytic Hydrogenation of Benzene to Cyclohexene on Ru(0001) from Density Functional Theory

Investigations☆. *Catal. Today* **2011**, *160* (1), 234–241. https://doi.org/10.1016/j.cattod.2010.03.075.

(240) Xia, Y.; Fan, C.; Zhou, Z.-L.; Zhu, Y.-A.; Zhou, X.-G. Effect of Zn on the Selectivity of Ru in Benzene Partial Hydrogenation from Density Functional Theory Investigations. *J. Mol. Catal. Chem.* **2013**, *370*, 44–49. https://doi.org/10.1016/j.molcata.2012.12.014.

(241) Ab Initio DFT Studies of Adsorption Characteristics of Benzene on Close-Packed Surfaces of Transition Metals. *Comput. Mater. Sci.* **2017**, *137*, 10–19. https://doi.org/10.1016/j.commatsci.2017.05.019.

(242) Bjelic, A.; Likozar, B.; Grilc, M. Scaling of Lignin Monomer Hydrogenation, Hydrodeoxygenation and Hydrocracking Reaction Micro-Kinetics over Solid Metal/Acid Catalysts to Aromatic Oligomers. *Chem. Eng. J.* **2020**, *399*. https://doi.org/10.1016/j.cej.2020.125712.

(243) Gao, H.-B.; Qiu, L.-L.; Wu, F.-P.; Xiao, J.; Zhao, Y.-P.; Liang, J.; Bai, Y.-H.; Liu, F.-J.; Cao, J.-P. Highly Efficient Catalytic Hydrogenolysis of Lignin Model Compounds over Hydrotalcite-Derived Ni/Al2O3 Catalysts. *Fuel* **2023**, *337*, 127196. https://doi.org/10.1016/j.fuel.2022.127196.

(244) Campos Fraga, M. M.; Vogt, J.; Lacerda de Oliveira Campos, B.; Schmitt, C. C.; Raffelt, K.; Dahmen, N. Investigation of Nb2O5 and Its Polymorphs as Catalyst Supports for Pyrolysis Oil Upgrading through Hydrodeoxygenation. *Energy Fuels* **2023**, *37* (14), 10474–10492. https://doi.org/10.1021/acs.energyfuels.3c01152.

(245) Jiang, L.; Dong, Y.; Zhou, G.; Li, R.; He, D. Promoting the Performances of TiO2 Submicrosphere-Embedded Ru Nanoparticles in Benzene Selective Hydrogenation by Morphology Manipulation. *Ind. Eng. Chem. Res.* **2020**, *59* (3), 1083–1092. https://doi.org/10.1021/acs.iecr.9b05215.

(246) Luo, Z.; Wang, Y.; He, M.; Zhao, C. Precise Oxygen Scission of Lignin Derived Aryl Ethers to Quantitatively Produce Aromatic Hydrocarbons in Water. *Green Chem.* **2016**, *18* (2), 433–441. https://doi.org/10.1039/C5GC01790D.

(247) Zhang, X.; Yan, H.; Zhu, L. J.; Li, T.; Wang, S. R. Hydrodeoxygenation of Lignin-Derived Monomers and Dimers over a Ru Supported Solid Super Acid Catalyst for Cycloalkane Production. *Adv. Sustain. Syst.* **2020**, *4* (10). https://doi.org/10.1002/adsu.201900136.

(248) Lv, W.; Hu, X.; Zhu, Y.; Xu, Y.; Liu, S.; Chen, P.; Wang, C.; Ma, L. Molybdenum Oxide Decorated Ru Catalyst for Enhancement of Lignin Oil Hydrodeoxygenation to Hydrocarbons. *Renew. Energy* **2022**, *188*, 195–210. https://doi.org/10.1016/j.renene.2021.12.148.

(249) Yang, Z.; Luo, B.; Shu, R.; Zhong, Z.; Tian, Z.; Wang, C.; Chen, Y. Synergistic Effect of Active Metal–Acid Sites on Hydrodeoxygenation of Lignin-Derived Phenolic Compounds under Mild Conditions Using Ru/C-HPW Catalyst. *Fuel* **2022**, *319*, 123617. https://doi.org/10.1016/j.fuel.2022.123617.

(250) Salam, M. A.; Cheah, Y. W.; Ho, P. H.; Olsson, L.; Creaser, D. Hydrotreatment of Lignin Dimers over NiMoS-USY: Effect of Silica/Alumina Ratio. *Sustain. Energy Fuels* **2021**, *5* (13), 3445–3457. https://doi.org/10.1039/D1SE00412C.

(251) Zhao, Z.-J.; Li, Z.; Cui, Y.; Zhu, H.; Schneider, W. F.; Delgass, W. N.; Ribeiro, F.; Greeley, J. Importance of Metal-Oxide Interfaces in Heterogeneous Catalysis: A Combined DFT, Microkinetic, and Experimental Study of Water-Gas Shift on Au/MgO. *J. Catal.* **2017**, *345*, 157–169. https://doi.org/10.1016/j.jcat.2016.11.008.

(252) Whittaker, T.; Kumar, K. B. S.; Peterson, C.; Pollock, M. N.; Grabow, L. C.; Chandler, B. D. H2 Oxidation over Supported Au Nanoparticle Catalysts: Evidence for Heterolytic H2 Activation at the Metal–Support Interface. *J. Am. Chem. Soc.* **2018**, *140* (48), 16469–16487. https://doi.org/10.1021/jacs.8b04991.

(253) Polierer, S.; Jelic, J.; Pitter, S.; Studt, F. On the Reactivity of the Cu/ZrO2 System for the Hydrogenation of CO2 to Methanol: A Density Functional Theory Study. *J. Phys. Chem. C* **2019**, *123* (44), 26904–26911. https://doi.org/10.1021/acs.jpcc.9b06500.

(254) Hammer, B.; Nørskov, J. K. Theoretical Surface Science and Catalysis—Calculations and Concepts. In *Advances in Catalysis*; Elsevier, 2000; Vol. 45, pp 71–129. https://doi.org/10.1016/S0360-0564(02)45013-4.

(255) Toyoda, K.; Nakano, Y.; Hamada, I.; Lee, K.; Yanagisawa, S.; Morikawa, Y. First-Principles Study of Benzene on Noble Metal Surfaces: Adsorption States and Vacuum Level Shifts. *Surf. Sci.* **2009**, *603* (18), 2912–2922. https://doi.org/10.1016/j.susc.2009.07.039.

(256) Joseph, X. B.; Baby, J. N.; Wang, S.-F.; Sriram, B.; George, M. Interfacial Superassembly of Mo_2 C@NiMn-LDH Frameworks for Electrochemical Monitoring of Carbendazim Fungicide. *ACS Sustain. Chem. Eng.* **2021**, *9* (44), 14900–14910. https://doi.org/10.1021/acssuschemeng.1c05056.

(257) Feng, Q.; Zhang, H.; Guo, Z.; Liu, Y.; Shi, N.; Zhang, J.; Wang, S.; Xie, L. Three-Dimensional Porous Flower-like NiCo-MOF@Ni-LDH Composite Electrode for High-Performance Supercapacitors. *ACS Appl. Energy Mater.* **2024**, *7* (15), 6267–6277. https://doi.org/10.1021/acsaem.4c00919.

(258) Schneider, C. A.; Rasband, W. S.; Eliceiri, K. W. NIH Image to ImageJ: 25 Years of Image Analysis. *Nat. Methods* **2012**, *9* (7), 671–675. https://doi.org/10.1038/nmeth.2089.

(259) Poovan, F.; Chandrashekhar, V. G.; Natte, K.; Jagadeesh, R. V. Synergy between Homogeneous and Heterogeneous Catalysis. *Catal. Sci. Technol.* **2022**, *12* (22), 6623–6649. https://doi.org/10.1039/D2CY00232A.

(260) Lahive, C. W.; Kamer, P. C. J.; Lancefield, C. S.; Deuss, P. J. An Introduction to Model Compounds of Lignin Linking Motifs; Synthesis and Selection Considerations for Reactivity Studies. *ChemSusChem* **2020**, *13* (17), 4238–4265. https://doi.org/10.1002/cssc.202000989.

(261) Bordet, A.; El Sayed, S.; Sanger, M.; Boniface, K. J.; Kalsi, D.; Luska, K. L.; Jessop, P. G.; Leitner, W. Selectivity Control in Hydrogenation through Adaptive Catalysis Using Ruthenium Nanoparticles on a CO2-Responsive Support. *Nat. Chem.* **2021**, *13* (9), 916–922. https://doi.org/10.1038/s41557-021-00735-w.

(262) Cao, X.; Long, F.; Zhai, Q.; Liu, P.; Xu, J.; Jiang, J. Enhancement of Fatty Acids Hydrodeoxygenation Selectivity to Diesel-Range Alkanes over the Supported Ni-MoOx Catalyst and Elucidation of the Active Phase. *Renew. Energy* **2020**, *162*, 2113–2125. https://doi.org/10.1016/j.renene.2020.10.052.

(263) Qiu, S.; Huang, Z.; Sang, X.; Liu, Y.; Zhang, Q.; Chen, Q.; Meng, Q.; Wang, T. Regulating Isomerization of Gasoline-Alkanes in Aqueous-Phase Hydrodeoxygenation of Sorbitol Using Regenerable Ni@MoOx Catalysts. *Fuel Process. Technol.* **2023**, *242*, 107647. https://doi.org/10.1016/j.fuproc.2022.107647.

(264) Lu, J.; Behtash, S.; Mamun, O.; Heyden, A. Theoretical Investigation of the Reaction Mechanism of the Guaiacol Hydrogenation over a Pt(111) Catalyst. *ACS Catal.* **2015**, *5* (4), 2423–2435. https://doi.org/10.1021/cs5016244.

(265) Lee, K.; Gu, G. H.; Mullen, C. A.; Boateng, A. A.; Vlachos, D. G. Guaiacol Hydrodeoxygenation Mechanism on Pt(111): Insights from Density Functional Theory and Linear Free Energy Relations. *Chemsuschem* **2015**, *8* (2), 315–322. https://doi.org/10.1002/cssc.201402940.

(266) Wang, X.; Zhu, S.; Wang, S.; He, Y.; Liu, Y.; Wang, J.; Fan, W.; Lv, Y. Low Temperature Hydrodeoxygenation of Guaiacol into Cyclohexane over Ni/SiO_2 Catalyst Combined with Hβ Zeolite. *RSC Adv.* **2019**, *9* (7), 3868–3876. https://doi.org/10.1039/c8ra09972c.

(267) Han, G.-H.; Lee, M. W.; Park, S.; Kim, H. J.; Ahn, J.-P.; Seo, M.; Lee, K.-Y. Revealing the Factors Determining the Selectivity of Guaiacol HDO Reaction Pathways Using ZrP-Supported Co and Ni Catalysts. *J. Catal.* **2019**, *377*, 343–357. https://doi.org/10.1016/j.jcat.2019.07.034.

(268) Zhang, X.; Zhang, Q.; Chen, L.; Xu, Y.; Wang, T.; Ma, L. Effect of Calcination Temperature of Ni/SiO2-ZrO2 Catalyst on Its Hydrodeoxygenation of Guaiacol. *Chin. J. Catal.* **2014**, *35* (3), 302–309. https://doi.org/10.1016/s1872-2067(12)60733-5.

(269) Zhang, X.; Wang, T.; Ma, L.; Zhang, Q.; Yu, Y.; Liu, Q. Characterization and Catalytic Properties of Ni and NiCu Catalysts Supported on ZrO2–SiO2 for Guaiacol Hydrodeoxygenation. *Catal. Commun.* **2013**, *33*, 15–19. https://doi.org/10.1016/j.catcom.2012.12.011.

(270) Barton, R. R.; Carrier, M.; Segura, C.; Fierro, J. L. G.; Park, S.; Lamb, H. H.; Escalona, N.; Peretti, S. W. Ni/HZSM-5 Catalyst Preparation by Deposition-Precipitation. Part 2. Catalytic Hydrodeoxygenation Reactions of Lignin Model Compounds in Organic and Aqueous Systems. *Appl. Catal. Gen.* **2018**, *562*, 294–309. https://doi.org/10.1016/j.apcata.2018.06.012.

(271) Dongil, A. B.; Ghampson, I. T.; García, R.; Fierro, J. L. G.; Escalona, N. Hydrodeoxygenation of Guaiacol over Ni/Carbon Catalysts: Effect of the Support and Ni Loading. *RSC Adv.* **2016**, *6* (4), 2611–2623. https://doi.org/10.1039/c5ra22540j.

(272) Zhou, M.; Ye, J.; Liu, P.; Xu, J.; Jiang, J. Water-Assisted Selective Hydrodeoxygenation of Guaiacol to Cyclohexanol over Supported Ni and Co Bimetallic Catalysts. *ACS Sustain. Chem. Eng.* **2017**, *5* (10), 8824–8835. https://doi.org/10.1021/acssuschemeng.7b01615.

(273) López, M.; Palacio, R.; Mamede, A.-S.; Fernández, J. J.; Royer, S. Hydrodeoxygenation of Guaiacol into Cyclohexane over Mesoporous Silica Supported Ni–ZrO2 Catalyst. *Microporous Mesoporous Mater.* **2020**, *309*, 110452. https://doi.org/10.1016/j.micromeso.2020.110452.

(274) Phan, B. M. Q.; Ha, Q. L. M.; Le, N. P.; Ngo, P. T.; Nguyen, T. H.; Dang, T. T.; Nguyen, L. H.; Nguyen, D. A.; Luu, L. C. Influences of Various Supports, γ-Al2O3, CeO2, and SBA-15 on HDO Performance of NiMo Catalyst. *Catal. Lett.* **2015**, *145* (2), 662–667. https://doi.org/10.1007/s10562-014-1412-4.

(275) Raikwar, D.; Majumdar, S.; Shee, D. Synergistic Effect of Ni-Co Alloying on Hydrodeoxygenation of Guaiacol over Ni-Co/Al2O3 Catalysts. *Mol. Catal.* **2021**, *499*, 111290. https://doi.org/10.1016/j.mcat.2020.111290.

(276) Zhang, Y.; Wang, W.; Fan, G.; Yang, L.; Li, F. Defect-Decorated NiFe Bimetallic Nanocatalysts for the Enhanced Hydrodeoxygenation of Guaiacol. *ChemCatChem* **2022**, *14* (19). https://doi.org/10.1002/cctc.202200585.

(277) Zhang, H.; Yang, T.; Tong, Y.; Li, B.; Wang, J.; Li, R. FeNi/Hexagonal Boron Nitride for Catalytic Hydrodeoxygenation of Guaiacol Derived from Lignin to Cycloalkanes. *Fuel* **2024**, *368*, 131620. https://doi.org/10.1016/j.fuel.2024.131620.

(278) Matos, J.; Samudio-González, D.; Blanco, E.; Poon, P. S.; Escalona, N. Alkali-Driven Selectivity of Products on Carbon-Supported Ni-Based Catalysts during the HDO of Guaiacol. *Fuel* **2024**, *374*, 132442. https://doi.org/10.1016/j.fuel.2024.132442.

(279) Wu, B.; Li, L.; Wang, H.; Han, J.; Zhu, X.; Ge, Q. Role of MoO_x/Ni(111) Interfacial Sites in Direct Deoxygenation of Phenol toward Benzene. *Catal. Sci. Technol.* **2023**, *13* (7), 2201–2211. https://doi.org/10.1039/D2CY01529C.

(280) Thommes, M.; Kaneko, K.; Neimark, A. V.; Olivier, J. P.; Rodriguez-Reinoso, F.; Rouquerol, J.; Sing, K. S. W. Physisorption of Gases, with Special Reference to the Evaluation of Surface Area and Pore Size Distribution (IUPAC Technical Report). *Pure Appl. Chem.* **2015**, *87* (9–10), 1051–1069. https://doi.org/10.1515/pac-2014-1117.

(281) Schlumberger, C.; Thommes, M. Characterization of Hierarchically Ordered Porous Materials by Physisorption and Mercury Porosimetry—A Tutorial Review. *Adv. Mater. Interfaces* **2021**, *8* (4), 2002181. https://doi.org/10.1002/admi.202002181.

(282) *From Micropores to Macropores: Investigating Pore Characteristics of Longmaxi Shale in the Sichuan Basin | Energy & Fuels*. https://pubs.acs.org/doi/10.1021/acs.energyfuels.3c04516?utm_source=chatgpt.com (accessed 2025-07-27).

(283) Hernando, H.; Moreno, I.; Fermoso, J.; Ochoa-Hernández, C.; Pizarro, P.; Coronado, J. M.; Čejka, J.; Serrano, D. P. Biomass Catalytic Fast Pyrolysis over Hierarchical ZSM-5 and Beta Zeolites Modified with Mg and Zn Oxides. *Biomass Convers. Biorefinery* **2017**, *7* (3), 289–304. https://doi.org/10.1007/s13399-017-0266-6.

(284) Yao, J.; He, Y.; Zeng, Y.; Feng, X.; Fan, J.; Komiyama, S.; Yong, X.; Zhang, W.; Zhao, T.; Guo, Z.; Peng, X.; Yang, G.; Tsubaki, N. Ammonia Pools in Zeolites for Direct Fabrication of Catalytic Centers. *Nat. Commun.* **2022**, *13* (1), 935. https://doi.org/10.1038/s41467-022-28606-z.

(285) Suárez-Méndez, A.; Mendoza-Cruz, R.; Martínez-Klimov, M. E.; Wärnå, J.; Albuquerque, J. S.; Murzin, D. Yu.; Klimova, T. E. NiPt Supported on Zeolite Y and SBA-15 Composites as Efficient Catalysts for the Hydrodeoxygenation of Anisole under Mild Conditions. *Fuel* **2025**, *400*, 135793. https://doi.org/10.1016/j.fuel.2025.135793.

(286) Petcuta, O.; Guzo, N.; Bordeiasu, M.; Nicolaev, A.; Parvulescu, V. I.; Coman, S. Ru/Beta Zeolite Catalysts for Levulinic Acid Hydrogenation: The Importance of Catalyst Synthesis Methodology. *Catalysts* **2025**, *15*, 80. https://doi.org/10.3390/catal15010080.

(287) Valle, B.; Palos, R.; Bilbao, J.; Gayubo, A. G. Role of Zeolite Properties in Bio-Oil Deoxygenation and Hydrocarbons Production by Catalytic Cracking. *Fuel Process. Technol.* **2022**, *227*, 107130. https://doi.org/10.1016/j.fuproc.2021.107130.

(288) Wang, Z.; Dong, C.; Tang, X.; Qin, X.; Liu, X.; Peng, M.; Xu, Y.; Song, C.; Zhang, J.; Liang, X.; Dai, S.; Ma, D. CO-Tolerant RuNi/TiO2 Catalyst for the Storage and Purification of Crude Hydrogen. *Nat. Commun.* **2022**, *13* (1), 4404. https://doi.org/10.1038/s41467-022-32100-x.

(289) Xie, Y.; Lian, B.; Deng, S.; Lin, Q.; Wang, K.; Zheng, Y.; Zhuang, Z.; Liu, Y.; Sun, K.; Yan, W.; Zhang, J. Advanced Ru/Ti4O7 Catalyst for Tolerating CO and H2S Poisoning to Hydrogen Oxidation Reaction. *Int. J. Hydrog. Energy* **2024**, *65*, 205–214. https://doi.org/10.1016/j.ijhydene.2024.04.031.

(290) He, P.; Yi, Q.; Geng, H.; Shao, Y.; Liu, M.; Wu, Z.; Luo, W.; Liu, Y.; Valtchev, V. Boosting the Catalytic Activity and Stability of Ru Metal Clusters in Hydrodeoxygenation of Guaiacol through MWW Zeolite Pore Constraints. *ACS Catal.* **2022**, *12* (23), 14717–14726. https://doi.org/10.1021/acscatal.2c04597.

(291) L. Weber, J.; Hernández Mejía, C.; Jong, K. P. de; Jongh, P. E. de. Recent Advances in Bifunctional Synthesis Gas Conversion to Chemicals and Fuels with a Comparison to Monofunctional Processes. *Catal. Sci. Technol.* **2024**, *14* (17), 4799–4842. https://doi.org/10.1039/D4CY00437J.

Supporting Information

Figure S1 to S4 and Table S1 to S2. Source: reprinted from ref. [224] in agreement with the terms of use.
Figure S5 to S19 and Table S3 to S9. Source: reprinted from ref. [225] in agreement with the terms of use.

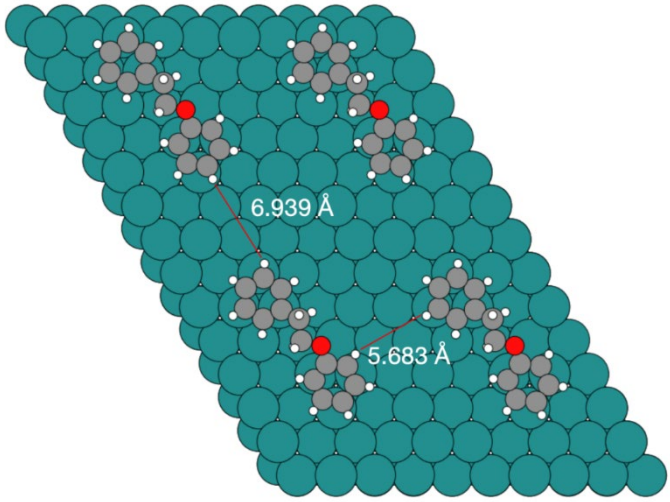

Figure S1: The atomic distance between adjacent mirrored molecules.

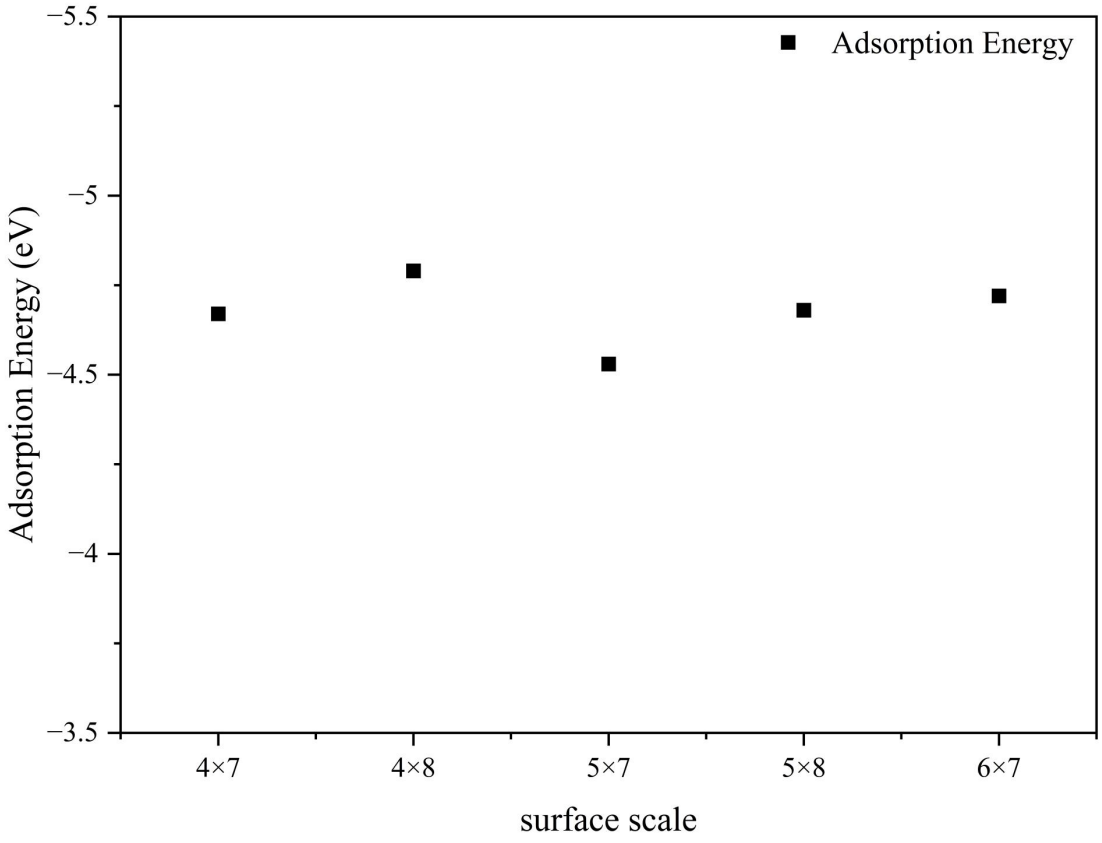

Figure S2: Convergence testing of adsorption energy at different surface scales.

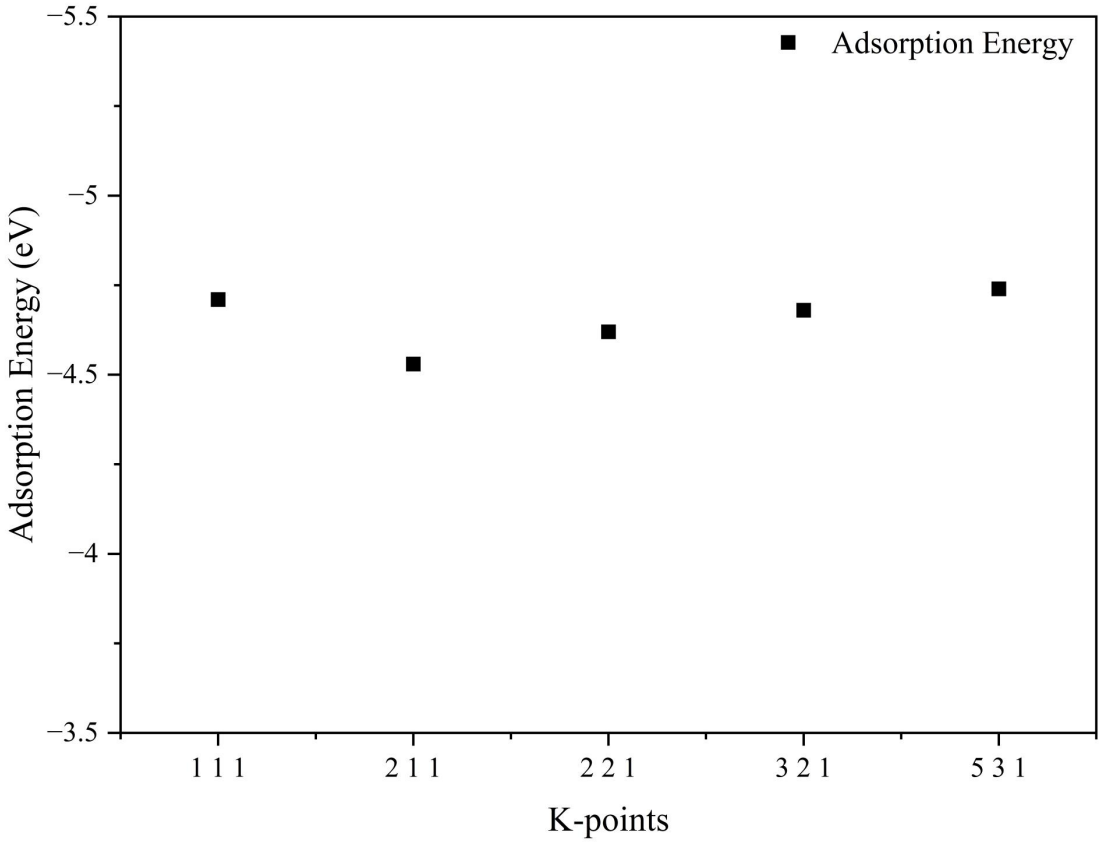

Figure S 3: Convergence testing of adsorption energy at different K-points.

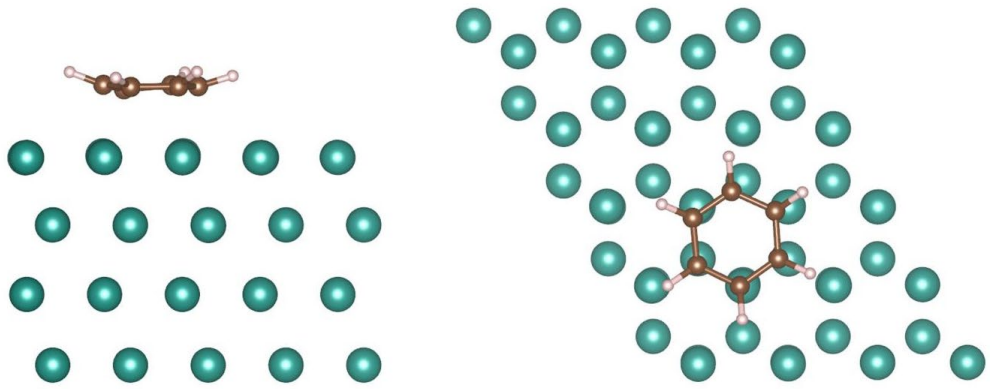

Figure S4: Adsorption structure of benzene on Ru (0001) surface.

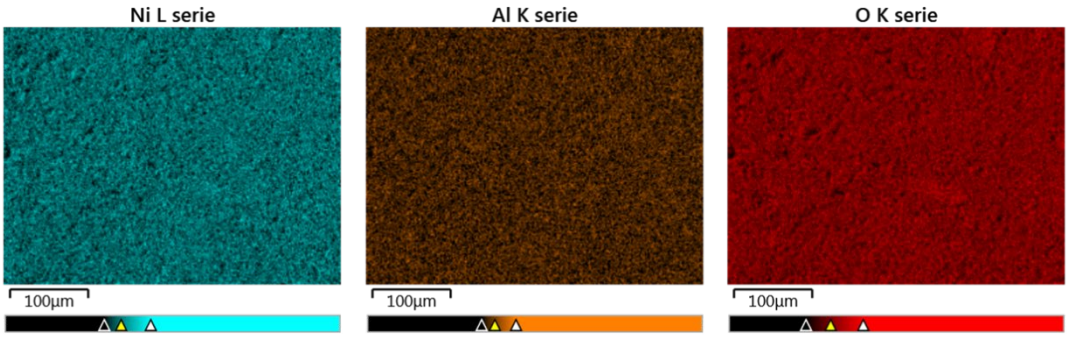

Figure S5: SEM-EDX Mapping of Ni/Al-2 LDH structure.

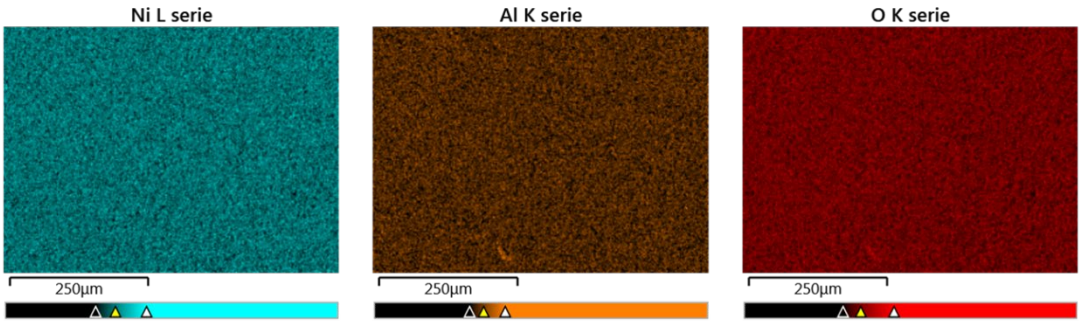

Figure S6: SEM-EDX Mapping of reduced Ni/Al-2 catalyst.

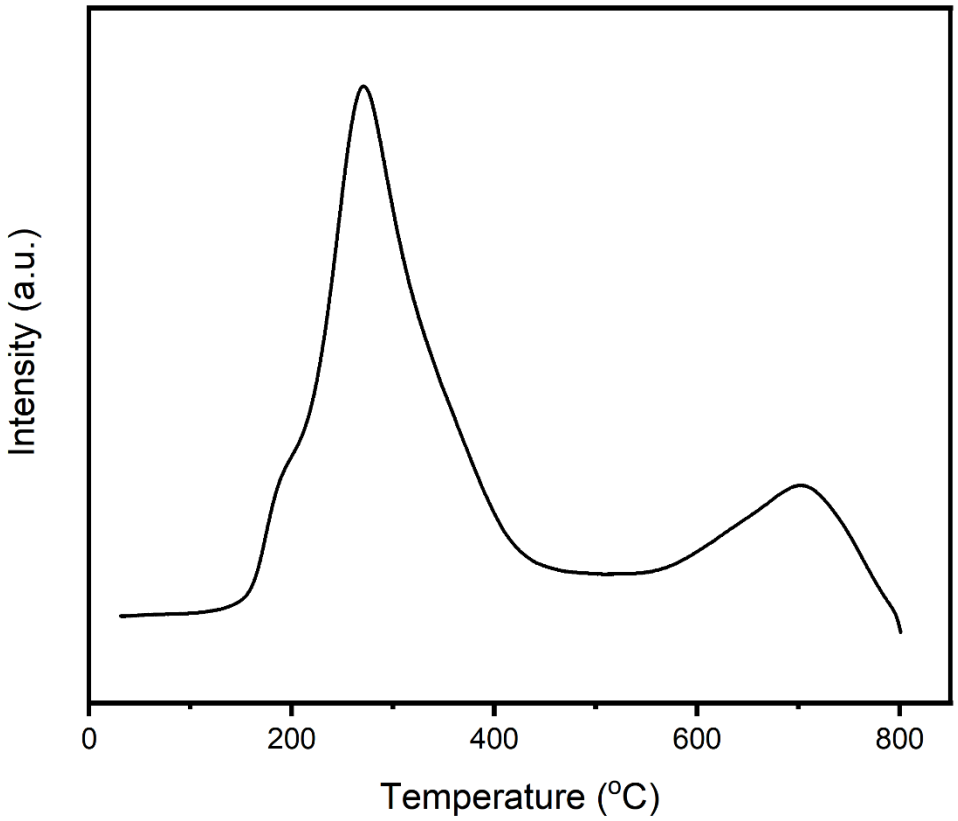

Figure S7: H_2-TPR analysis of Ni/Al-2 catalyst.

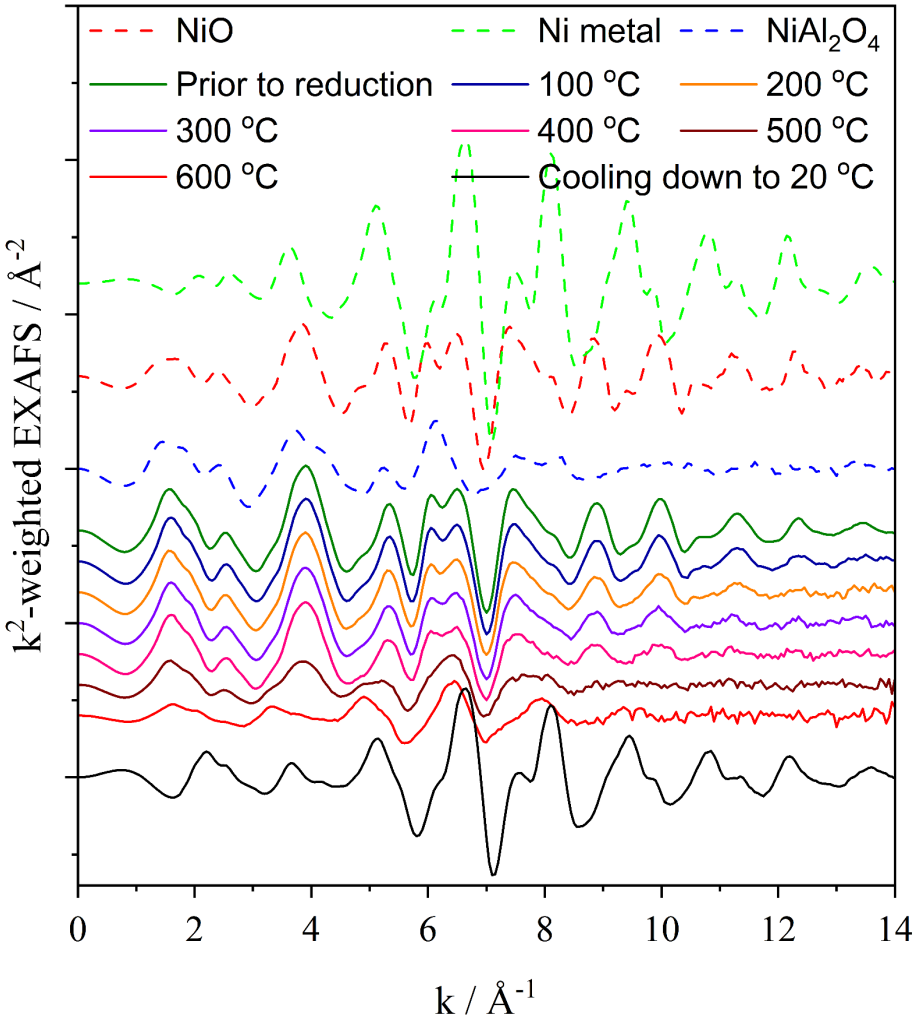

Figure S8: k^2-weighted EXAFS spectra of the Ni/NiO catalyst and selected Ni reference compounds.

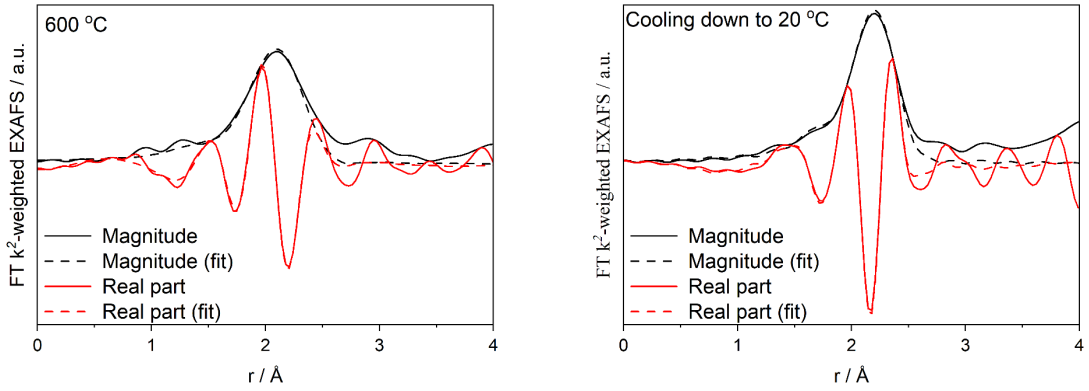

Figure S9: First shell fits of the Ni K edge FT EXAFS spectra.

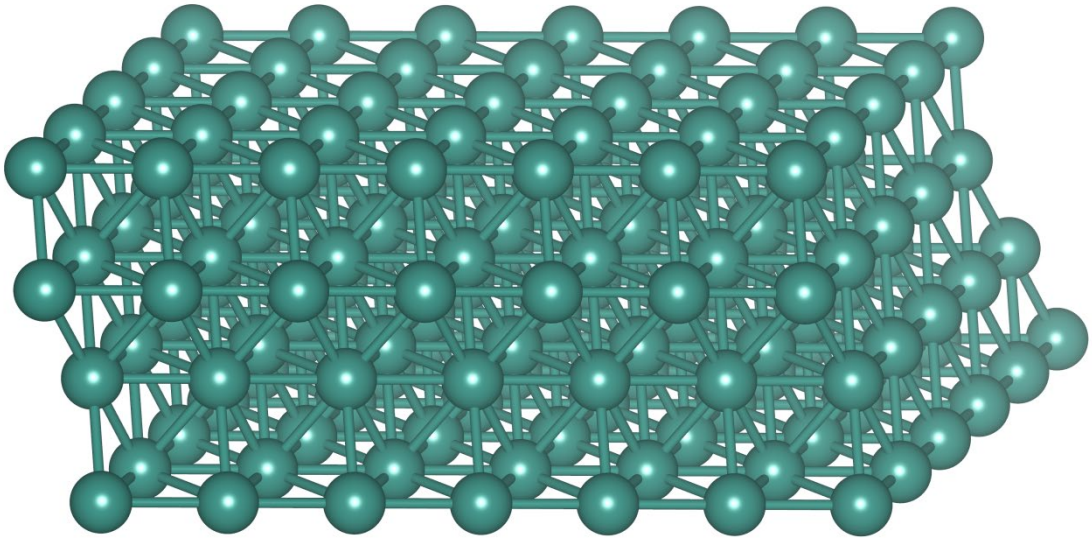

Figure S10: Ni (111) model

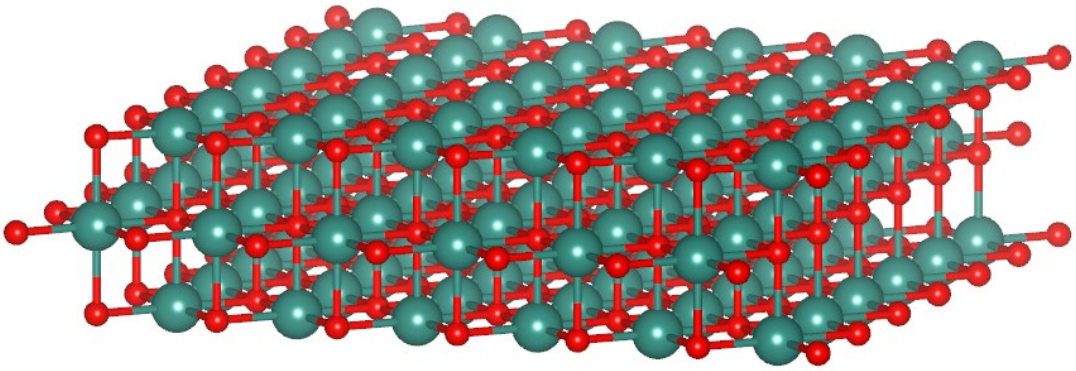

Figure S11: Ni (100) model

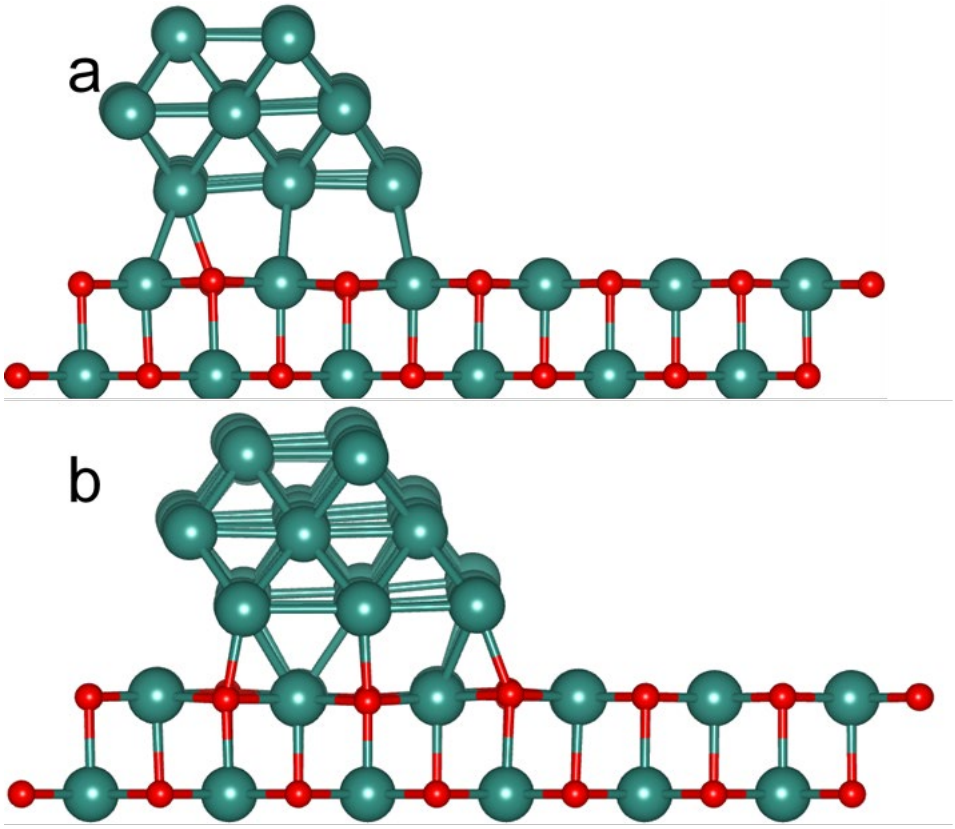

Figure S12: Ni/NiO model

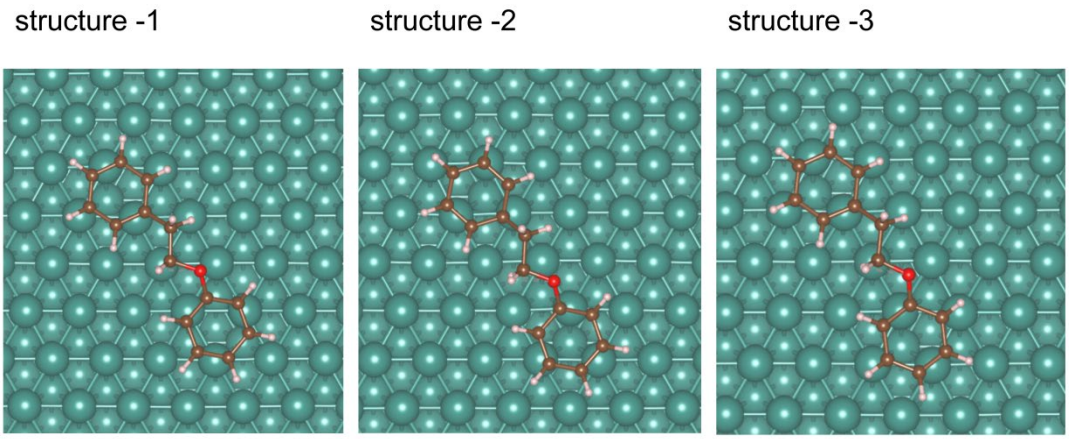

Figure S 13: Different adsorption structure of PPE on Ni (111) slab

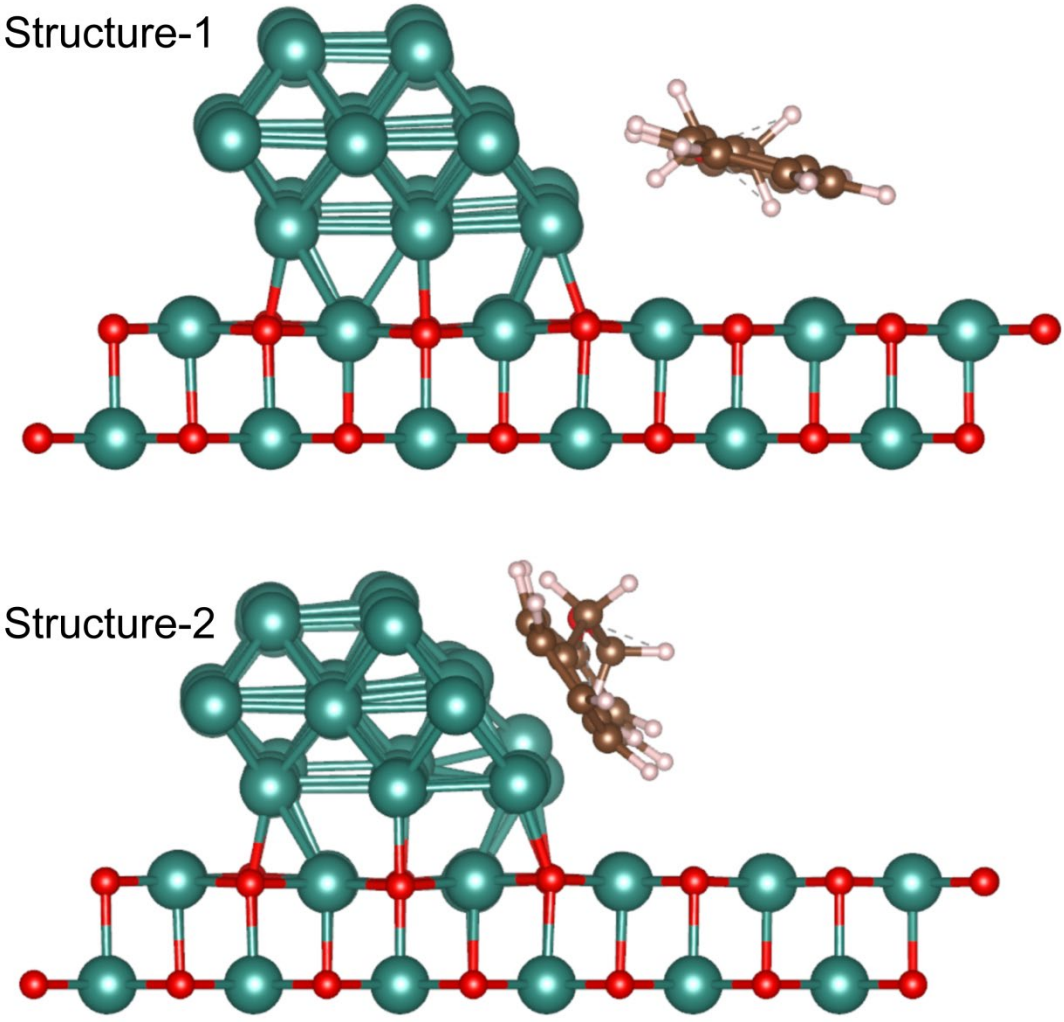

Figure S14: Different adsorption structure of PPE on Ni/NiO slab.

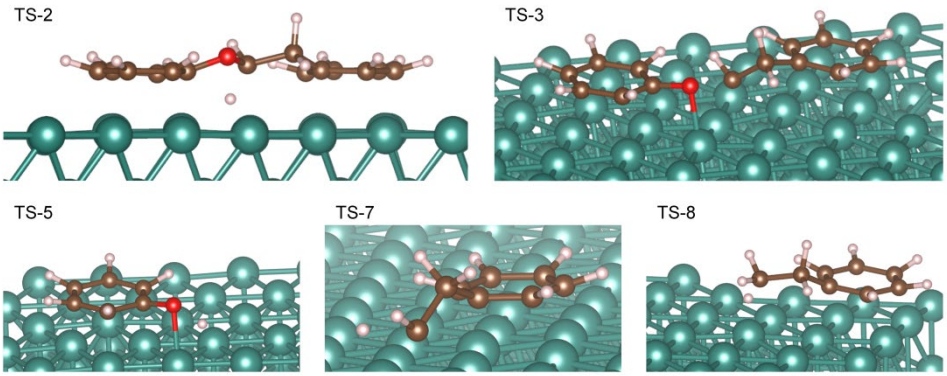

Figure S15: Transitation state structures over Ni (111) slab

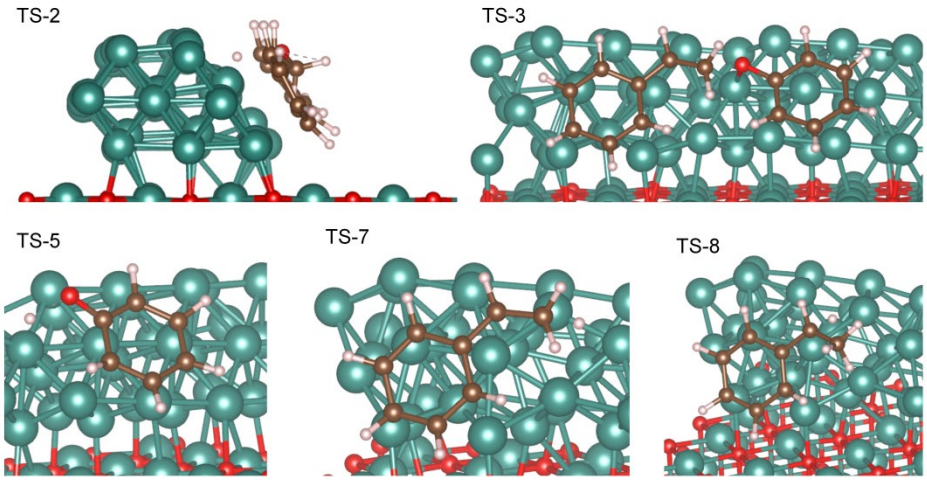

Figure S16: Transitation state structures over Ni/NiO slab

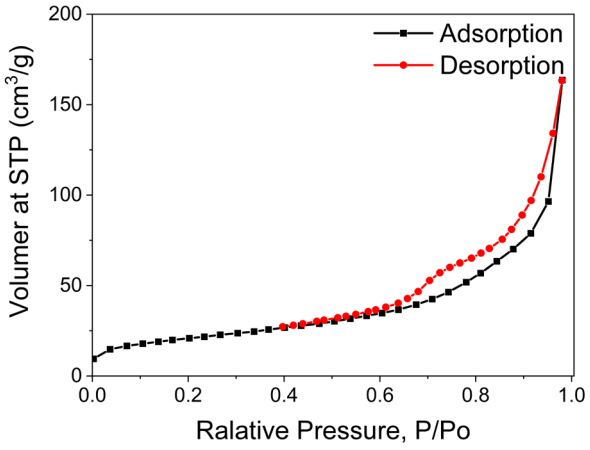

Figure S 17: N_2 physisorption analysis of Mo doped Ni/Al_2O_3 catalyst

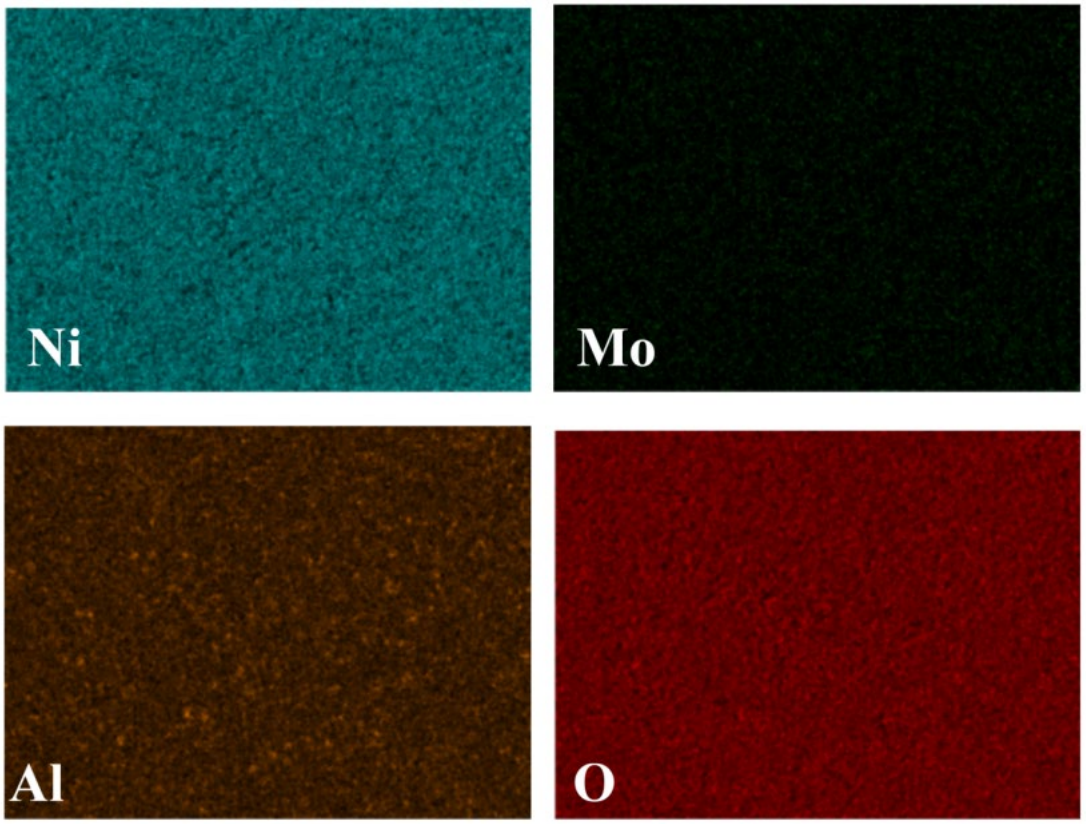

Figure S18: SEM-EDX mapping of Mo doped Ni/Al_2O_3 catalyst

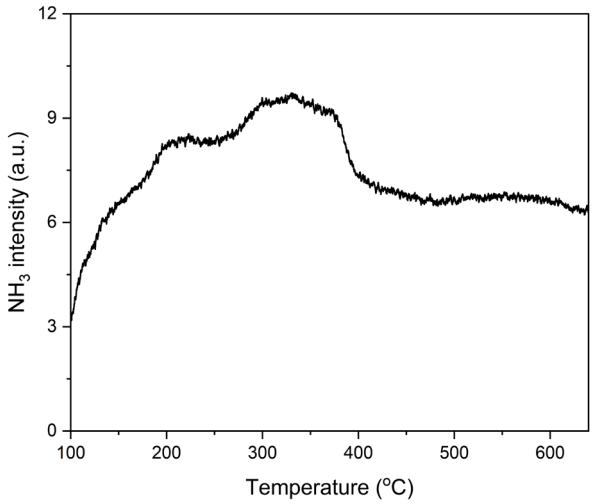

Figure S19: NH_3-TPD analysis of Mo doped Ni/Al_2O_3 catalyst

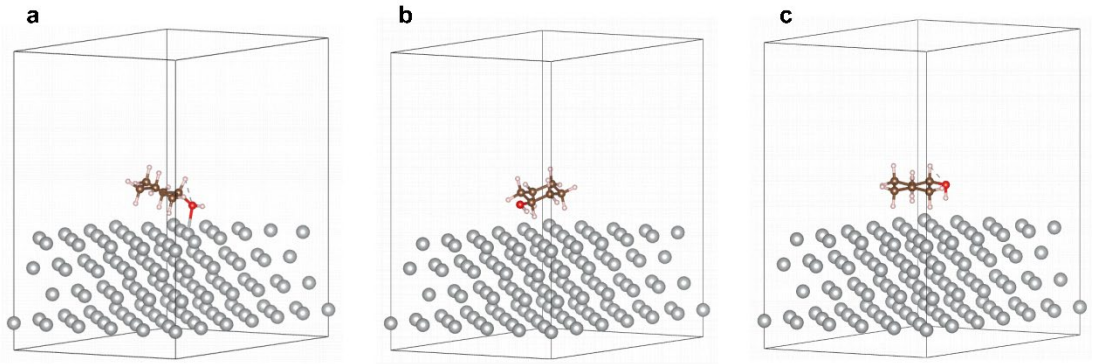

Figure S20: Different adsorption structures of cyclohexanol on Ni (111) surface.

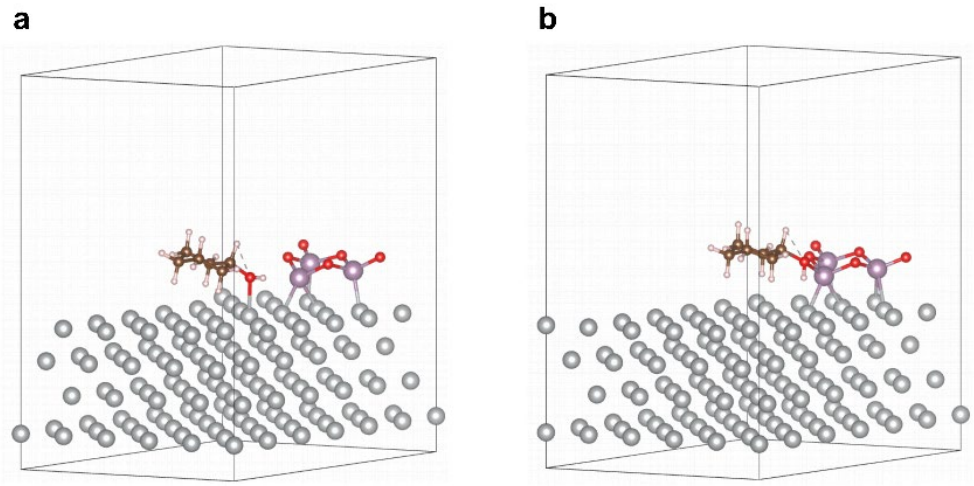

Figure S21: Different adsorption structures of cyclohexanol on Mo_3O_5/Ni (111) surface.

Table S1: Ru content of Ru/Nb_2O_5 catalyst from EDX.

	Ru content (%)
theory	5.0
fresh catalyst	7.3
used catalyst	6.2

Table S2: Compounds identified by GC-MS in the oil-phase after the reaction.

Component RT[1]	Compound name	Component RT	Compound name
3.1635	Acetic acid, methyl ester	15.9483	3-Methyl-5-nonylpyrrolizidine
6.2342	Furan, 2-methoxy-	15.9518	Phenol, 2-methoxy-
8.2165	Cyclopentanone	16.416	l-Alanine, N-(2-furoyl)-, butyl ester
8.5427	Propanoic acid	17.2114	Phenol, 3,4-dimethyl-
9.7412	Oxetane, 3-(1-methylethyl)-	18.0593	4-Methylpyridazine
9.7416	Cyclohexanone	18.0664	2-Methoxy-5-methylphenol
11.2763	Propane, 1-acetoxy-2-isocyano-	18.0712	1,2-Benzenediol,

			mono(methylcarbamate)
11.2968	Ethanol, 2-[2-(2-propenyloxy)ethoxy]-	19.6646	Phenol, 4-ethyl-2-methoxy-
11.569	2-Cyclopenten-1-one, 2-methyl-	19.833	1,2-Benzenediol, 4-methyl-
12.5023	L-Pyroglutamic acid	21.2325	Phenol, 2-methoxy-4-propyl-
12.736	Cyclopentane, methyl-	23.2184	Ethanone, 1-(3-hydroxy-4-methoxyphenyl)-
12.7361	Cyclohexanone, 2-methyl-	23.5273	Butylated Hydroxytoluene
13.5019	2-Vinylfuran	23.535	Phenylethyne
14.8246	Furan, 2,3,5-trimethyl-	23.8489	Propan-2-one, 1-(4-isopropoxy-3-methoxyphenyl)-
15.4432	Bicyclo[3.1.0]hexan-3-one	25.6514	Homovanillic acid

1 RT denotes retention time

Table S3: Results of the linear combination analysis of XANES (fit in the range -10 eV – +40 eV relative to E_0) with the Ni metal spectra as references of Ni/Al-2.

Temperature (scan at 7 min after it was reached)	Ni^{2+} (molar fraction)	Ni^0 metal (molar fraction)	ρ (%)
100 °C	0.991±0.002	0.009±0.002	0.004
200 °C	0.975±0.002	0.025±0.002	0.003
300 °C	0.937±0.003	0.063±0.003	0.01
400 °C	0.912±0.005	0.088±0.005	0.02
500 °C	0.568±0.007	0.432±0.007	0.04
600 °C	0.207±0.009	0.793±0.009	0.08
Cooling down to 20 °C	0.213±0.007	0.787±0.007	0.17

Table S4: Results of EXAFS fits at the highest degree of reduction.

Spectrum	600 °C	Cooling down to 20 °C
Ni-O distance (Å)	2.02±0.03	2.02±0.04
CN (O)	1.3±0.7	1.1±0.6
σ^2 O (10^{-3} Å^2)	8.6±10.7	3.0±7.9
Ni-Ni (metal) distance (Å)	2.46±0.01	2.48±0.01
CN (Ni)	6.4±1.4	8.1±1.1
σ^2 Ni (10^{-3} Å^2)	14.5±2.6	6.7±1.1
δE_0 (eV)	-3.9±1.5	6.4±1.2
ρ (%)	2.1	0.9

Table S5: The adsorption energy (eV) of different structures of PPE on Ni (111) slab.

	Adsorption energy	Slab+molecule	Slab	molecule
Structure-1	-4.02	-947.32	−758. 89	−184. 42
Structure-2	-4.06	-947.36	−758. 89	−184. 42
Structure-3	-3.74	-947.04	−758. 89	−184. 42

Table S6: The adsorption energy of different structures of PPE on Ni/NiO slab.

	Adsorption Energy	Slab+molecule	Slab	molecule
Structure-1	-2.42	-1168.97	-982.13	-184.34
Structure-2	-3.48	-1169.97	-982.13	-184.34

Table S7: The adsorption energy of PPE on NiO (110) slab.

	Adsorption Energy	Slab+molecule	Slab	molecule
Structure-1	-1.67	-1267.10	-1081.09	-184.34

Table S8: The energies of intermediates on Ni (111).

Name	Energy (eV)	Entropy (eV/K)	Zero point energy (eV)	Gibbs free energy (eV, T = 398 K)
IS-1	-943.306	6.57E-03	6.420	-938.852
FS-1	-947.362	2.94E-03	6.268	-941.613
IS-2	-947.362	2.94E-03	6.268	-941.613
TS-2	-946.632	2.91E-03	6.100	-941.042
FS-2	-947.277	2.84E-03	6.159	-941.604
IS-3	-943.509	2.80E-03	5.948	-938.044
TS-3	-942.436	2.92E-03	5.853	-937.101
FS-3	-943.686	3.02E-03	5.849	-938.372
IS-4	-765.623	5.02E-04	0.296	-765.431
FS-4	-766.850	7.50E-05	0.362	-766.495
IS-5	-518.852	1.47E-03	2.593	-516.527
TS-5	-518.283	1.01E-03	2.505	-516.030
FS-5	-518.820	1.54E-03	2.707	-516.398
IS-6	-518.820	1.54E-03	2.707	-516.398
FS-6	-516.761	4.20E-03	2.772	-515.360
IS-7	-541.451	1.67E-03	3.637	-538.106
TS-7	-540.867	1.67E-03	3.616	-537.544
FS-7	-541.340	1.78E-03	3.735	-537.930
IS-8	-545.282	1.78E-03	3.933	-541.667
TS-8	-544.788	1.73E-03	3.921	-541.170
FS-8	-545.510	1.99E-03	4.078	-541.812
IS-9	-545.510	1.99E-03	4.078	-541.812
FS-9	-543.234	4.76E-03	4.150	-540.594

- IS, TS, and FS in the names of intermediates represent the initial state, transition state, and final state, respectively, while the numbers indicate the elementary reaction step sequence (Figure S15).

Table S9: The energies of intermediates on Ni/NiO.

Name	Energy (eV)	Entropies (eV/K)	Zero point energy (eV)	Gibbs free energy (eV, T = 398 K)
IS-1	-1166.469	6.57E-03	6.420	-1162.015
FS-1	-1169.9719	2.91E-03	6.286	-1164.198
IS-2	-1169.9719	2.91E-03	6.286	-1164.198
TS-2	-1169.6128	2.82E-03	6.129	-1163.970
FS-2	-1170.04	2.88E-03	6.168	-1164.374
IS-3	-1166.6192	2.84E-03	5.983	-1161.134
TS-3	-1166.1196	2.88E-03	5.890	-1160.784
FS-3	-1167.1504	3.15E-03	5.895	-1161.829
IS-4	-989.03558	6.97E-04	0.309	-988.881
FS-4	-990.36736	1.20E-04	0.349	-990.032
IS-5	-1067.1555	1.47E-03	2.565	-1161.829
TS-5	-1066.5094	1.50E-03	2.496	-1161.829
FS-5	-1067.0883	1.55E-03	2.698	-1161.829
IS-6	-1067.0883	1.55E-03	2.698	-1161.829
FS-6	-1065.175	4.20E-03	2.772	-1063.773
IS-7	-1089.9745	1.90E-03	3.661	-1161.829
TS-7	-1089.5043	1.52E-03	3.482	-1161.829
FS-7	-1090.4253	1.79E-03	3.798	-1161.829
IS-8	-1094.2659	1.86E-03	3.980	-1161.829
TS-8	-1093.8751	1.79E-03	3.948	-1161.829
FS-8	-1094.2745	1.95E-03	4.098	-1161.829
IS-9	-1094.2745	1.95E-03	4.098	-1161.829
FS-9	-1091.446	4.73E-03	4.153	-1088.976

- IS, TS, and FS in the names of intermediates represent the initial state, transition state, and final state, respectively, while the numbers indicate the elementary reaction step sequence (Figure S16).

Table S10: Element analysis of Mo-Ni/Al_2O_3 catalyst from SEM-EDX

Element	Content (wt%)
C	8.52
O	45.77
Al	16.54
Ni	37.11
Mo	0.58

Table S11: Element analysis of different doped Ni/Al_2O_3 catalyst from ICP-OES.

Catalyst	Dopant (wt%)
Mo-Ni/Al_2O_3	Mo 0.87 ± 0.01
Ce-Ni/Al_2O_3	Ce 1.92 ± 0.03
Nb-Ni/Al_2O_3	Nb 1.18 ± 0.05
W-Ni/Al_2O_3	W 0.15

Table S12: Compounds identified by GC-MS of bio-oil feedstock.

Compound name	Formula	Relative intensity
1,3,5-Trioxane	$C_3H_6O_3$	20612.5
(S)-(+)-1,2-Propanediol	$C_3H_8O_2$	10305.3
Glycerin	$C_3H_8O_3$	63521.2
2(5H)-Furanone	$C_4H_4O_2$	197083.3
1,4-Dioxin, 2,3-dihydro-	$C_4H_6O_2$	17215.4
Succindialdehyde	$C_4H_6O_2$	245798.2
Butyrolactone	$C_4H_6O_2$	133816.3
2-Hydroxy-gamma-butyrolactone	$C_4H_6O_3$	28891.2

2-Butanone	C_4H_8O	65330.1
Cyclopropyl carbinol	C_4H_8O	72625.4
1-Hydroxy-2-butanone	$C_4H_8O_2$	149109.2
1,2-Ethanediol, monoacetate	$C_4H_8O_3$	337208.8
1,2-Ethanediol, monoacetate	$C_4H_8O_3$	99760.4
1,3-Dioxolane-2-methanol	$C_4H_8O_3$	77837
Pentanoic acid	$C_5H_{10}O_2$	14148.1
Neopentane	C_5H_{12}	14915.6
Furfural	$C_5H_4O_2$	20494.7
Furfural	$C_5H_4O_2$	422712.9
2,5-Furandione, dihydro-3-methylene-	$C_5H_4O_3$	13291.3
2-Cyclopenten-1-one	C_5H_6O	161866.4
2(5H)-Furanone, 5-methyl-	$C_5H_6O_2$	45420.7
2(5H)-Furanone, 3-methyl-	$C_5H_6O_2$	75556.2
Cyclopentanone	C_5H_8O	40373.1
2-Propanone, 1-(acetyloxy)-	$C_5H_8O_3$	141607.3
5-(Hydroxymethyl)dihydrofuran-2(3H)-one	$C_5H_8O_3$	94572.5
1-Propanone, 1-cyclopropyl-	$C_6H_{10}O$	87248.3
2,5-Hexanedione	$C_6H_{10}O_2$	13834.6
2,2'-Bi-1,3-dioxolane	$C_6H_{10}O_4$	24351.2
2,2'-Bi-1,3-dioxolane	$C_6H_{10}O_4$	10547.7
.beta.-D-Glucopyranose, 1,6-anhydro-	$C_6H_{10}O_5$	180837.4
1,6-Anhydro-.beta.-D-glucofuranose	$C_6H_{10}O_5$	62755.1
Butanal, 2-ethyl-	$C_6H_{12}O$	83455.6
2-Butanone, 3-methoxy-3-methyl-	$C_6H_{12}O_2$	25736.7
1,3-Dioxolane, 2-propyl-	$C_6H_{12}O_2$	13211.5
1-Butanol, 2,2-dimethyl-	$C_6H_{14}O$	50096
2,5-Furandicarboxaldehyde	$C_6H_4O_3$	24869.3
Phenol	C_6H_6O	108968.3
Ethanone, 1-(2-furanyl)-	$C_6H_6O_2$	33333.9

2-Furancarboxaldehyde, 5-methyl-	$C_6H_6O_2$	62073
Ethanone, 1-(2-furanyl)-	$C_6H_6O_2$	15212.2
Catechol	$C_6H_6O_2$	502486.9
3-Furancarboxylic acid, methyl ester	$C_6H_6O_3$	15701.9
Maltol	$C_6H_6O_3$	20615.1
2-Cyclopenten-1-one, 2-methyl-	C_6H_8O	76913.7
4-Methyl-2H-pyran	C_6H_8O	74606.3
2-Cyclopenten-1-one, 2-hydroxy-3-methyl-	$C_6H_8O_2$	570070.6
1,4:3,6-Dianhydro-.alpha.-d-glucopyranose	$C_6H_8O_4$	96137
2,3-Anhydro-d-mannosan	$C_6H_8O_4$	190721.5
Furan, 2,3,5-trimethyl-	$C_7H_{10}O$	44556
2-Cyclopenten-1-one, 2-hydroxy-3,4-dimethyl-	$C_7H_{10}O_2$	50458.2
2-Cyclopenten-1-one, 3-ethyl-2-hydroxy-	$C_7H_{10}O_2$	43945.5
5-Oxotetrahydrofuran-2-carboxylic acid, ethyl ester	$C_7H_{10}O_4$	62714.8
Propanoic acid, 2-methyl-, 2-propenyl ester	$C_7H_{12}O_2$	22459.1
Cyclohexane, methyl-	C_7H_{14}	78788.3
2-Methyl-5-hexen-3-ol	$C_7H_{14}O$	30457.6
1,3-Dioxolane, 2-butyl-	$C_7H_{14}O_2$	129744
Phenol, 2-methyl-	C_7H_8O	96748.6
p-Cresol	C_7H_8O	192752.7
Phenol, 2-methoxy-	$C_7H_8O_2$	780236.9
1,2-Benzenediol, 3-methyl-	$C_7H_8O_2$	161111.9
1,2-Benzenediol, 4-methyl-	$C_7H_8O_2$	309594.3
Phenol, 3,4-dimethyl-	$C_8H_{10}O$	84386.3
Benzene, 1,4-dimethoxy-	$C_8H_{10}O_2$	22574.1
Creosol	$C_8H_{10}O_2$	937549.6
1,3-Benzenediol, 4,5-dimethyl-	$C_8H_{10}O_2$	12639.4
1,3-Benzenediol, 4-ethyl-	$C_8H_{10}O_2$	104978.3
2,3-Dimethoxyphenol	$C_8H_{10}O_3$	36861.2
2-Octen-4-one	$C_8H_{14}O$	12751.6

Ethanol, 2,2'-oxybis-, diacetate	$C_8H_{14}O_5$	34060
Cyclohexane, ethyl-	C_8H_{16}	25950.4
Octane	C_8H_{18}	41296.8
2,2,4-Trimethyl-3-pentanol	$C_8H_{18}O$	41238.8
Benzaldehyde, 3-hydroxy-4-methoxy-	$C_8H_8O_3$	424790.3
Phenol, 5-ethenyl-2-methoxy-	$C_9H_{10}O_2$	55338.2
Ethanone, 1-(3-hydroxy-4-methoxyphenyl)-	$C_9H_{10}O_3$	260704.8
Homovanillic acid	$C_9H_{10}O_4$	191309
3,4-Dimethoxytoluene	$C_9H_{12}O_2$	13595.7
Phenol, 4-ethyl-2-methoxy-	$C_9H_{12}O_2$	363475.6
5-Octen-4-one, 7-methyl-	$C_9H_{16}O$	61714.7
Coniferyl aldehyde	$C_{10}H_{10}O_3$	365251.1
Eugenol	$C_{10}H_{12}O_2$	289133.1
Phenol, 2-methoxy-4-(1-propenyl)-	$C_{10}H_{12}O_2$	189033.4
Phenol, 2-methoxy-4-(1-propenyl)-	$C_{10}H_{12}O_2$	255475.6
2-Propanone, 1-(4-hydroxy-3-methoxyphenyl)-	$C_{10}H_{12}O_3$	156384.3
4-(1-Hydroxyallyl)-2-methoxyphenol	$C_{10}H_{12}O_3$	81856.2
1-Propanone, 1-(4-hydroxy-3-methoxyphenyl)-	$C_{10}H_{12}O_3$	59349.6
Phenol, 2-methoxy-4-propyl-	$C_{10}H_{14}O_2$	83595.3
Phenol, 2-methoxy-4-propyl-	$C_{10}H_{14}O_2$	73604.9
Naphthalene, decahydro-	$C_{10}H_{18}$	183639.8
2-Ethylhexanal ethylene glycol acetal	$C_{10}H_{20}O_2$	172944.6
Heptane, 2,3,5-trimethyl-	$C_{10}H_{22}$	39189.6
(2S,6R,7S,8E)-(+)-2,7-Epoxy-4,8-megastigmadiene	$C_{13}H_{20}O$	28563.1

Table S13: Compounds identified by GC-MS in the oil phase after HDO upgrading at 250 °C over Mo-Ni/Al_2O_3 catalyst.

Compound name	Formula	Relative intensity
1,3-Propanediol	$C_3H_8O_2$	24490.7

Cyclopentanol	$C_5H_{10}O$	312992.8
Ethyl-1-propenyl ether	$C_5H_{10}O$	36426.3
3-Pentanone	$C_5H_{10}O$	165365.5
n-Propyl acetate	$C_5H_{10}O_2$	15758.1
1-Butanol, 2-methyl-	$C_5H_{12}O$	104075.7
Propanoic acid, ethenyl ester	$C_5H_8O_2$	208408.2
Cyclopentanone, 2-methyl-	$C_6H_{10}O$	71671
Furan, tetrahydro-2,5-dimethyl-, trans-(.+/-.)-	$C_6H_{12}O$	72746.2
Furan, tetrahydro-2,4-dimethyl-, trans-	$C_6H_{12}O$	72031.1
2H-Pyran, tetrahydro-2-methyl-	$C_6H_{12}O$	610899.1
Furan, tetrahydro-2,5-dimethyl-, trans-(.+/-.)-	$C_6H_{12}O$	58147.8
2-Ethyltetrahydrofuran	$C_6H_{12}O$	519674.9
2H-Pyran, tetrahydro-3-methyl-	$C_6H_{12}O$	97534.2
Methyl Isobutyl Ketone	$C_6H_{12}O$	47027.7
Furan, tetrahydro-3,4-dimethyl-, cis-	$C_6H_{12}O$	46694.7
Cyclopentanol, 2-methyl-, cis-	$C_6H_{12}O$	538193.5
Cyclohexanol	$C_6H_{12}O$	1199496
2H-Pyran-2-methanol, tetrahydro-	$C_6H_{12}O_2$	58415.2
Propanoic acid, propyl ester	$C_6H_{12}O_2$	53110.2
Acetic acid, butyl ester	$C_6H_{12}O_2$	51122.1
Butane, 1-methoxy-3-methyl-	$C_6H_{14}O$	20607.9
3-Hexanol	$C_6H_{14}O$	201662.4
2-Hexanol	$C_6H_{14}O$	205214.7
Furan, 2-ethyl-5-methyl-	$C_7H_{10}O$	13882.9
Acetyl valeryl	$C_7H_{12}O_2$	31404.2
2-Furanmethanol, tetrahydro-, acetate	$C_7H_{12}O_3$	23889
Methyl oxane-2-carboxylate	$C_7H_{12}O_3$	121164.3
Cyclohexane, methyl-	C_7H_{14}	1457125
Cyclopentane, ethyl-	C_7H_{14}	351954.7
4-Heptanone	$C_7H_{14}O$	82704.5

2,4-Dimethylcyclopentanol	$C_7H_{14}O$	60157.2
Cyclohexanol, 2-methyl-, cis-	$C_7H_{14}O$	169789
Cyclohexanol, 4-methyl-, trans-	$C_7H_{14}O$	465746.3
Butanoic acid, propyl ester	$C_7H_{14}O_2$	211002.9
Propanoic acid, butyl ester	$C_7H_{14}O_2$	216114.4
Butane, 1-propoxy-	$C_7H_{16}O$	533286.2
1-Propanone, 1-(2-furanyl)-	$C_7H_8O_2$	20566.6
Pentalene, octahydro-	C_8H_{14}	77070.3
2-Pentene, 2,4,4-trimethyl-	C_8H_{16}	88926.3
Cyclohexane, ethyl-	C_8H_{16}	93487.9
Cyclohexane, ethyl-	C_8H_{16}	77883.6
2-Pentene, 2,4,4-trimethyl-	C_8H_{16}	51314.3
3-Hexene, 2,2-dimethyl-, (E)-	C_8H_{16}	44595.1
Cyclopentane, propyl-	C_8H_{16}	139639.1
Cyclohexane, ethyl-	C_8H_{16}	1514221
1-Hexene, 3,3-dimethyl-	C_8H_{16}	37748.3
Cyclohexanol, 2,3-dimethyl-	$C_8H_{16}O$	162580.2
4-Ethylcyclohexanol	$C_8H_{16}O$	431843.7
Butanoic acid, butyl ester	$C_8H_{16}O_2$	581756.4
Heptane, 3-methyl-	C_8H_{18}	38416.9
Octane	C_8H_{18}	169070.7
Hexane, 3,3-dimethyl-	C_8H_{18}	12315.9
n-Butyl ether	$C_8H_{18}O$	62709.3
1-Pentanone, 1-(2-furanyl)-	$C_9H_{12}O_2$	13885.4
1H-Indene, octahydro-, cis-	C_9H_{16}	24443.4
1H-Indene, octahydro-, cis-	C_9H_{16}	214071.8
Cyclohexane, 2-propenyl-	C_9H_{16}	79311
Ethanone, 1-(1-methylcyclohexyl)-	$C_9H_{16}O$	56192.5
Bicyclo[2.2.2]octan-1-ol, 2-methyl-	$C_9H_{16}O$	167177.6
3-Hexen-1-ol, propanoate, (Z)-	$C_9H_{16}O_2$	38543.2

1-Ethyl-3-methylcyclohexane (c,t)	C_9H_{18}	81365.2
1-Ethyl-4-methylcyclohexane	C_9H_{18}	79421
Cyclohexane, propyl-	C_9H_{18}	50502
Cyclohexane, propyl-	C_9H_{18}	1214836
Cyclohexane, (1-methylethyl)-	C_9H_{18}	27423.1
Cyclohexane, 1-ethyl-1-methyl-	C_9H_{18}	20294.1
Cyclohexane, 1-ethyl-1-methyl-	C_9H_{18}	39290.6
2-Propylcyclohexanol	$C_9H_{18}O$	96639.8
2-Propylcyclohexanol	$C_9H_{18}O$	413238.3
Cyclohexanol, 4-(1-methylethyl)-	$C_9H_{18}O$	359596.1
3,5-O-Furylidene-d-xylofuranose	$C_{10}H_{12}O_6$	23533.5
Cyclobutanecarboxylic acid, 3-methylbut-2-enyl ester	$C_{10}H_{16}O_2$	30352.7
Cyclohexene, 1-butyl-	$C_{10}H_{18}$	94798.6
Cyclohexane, butyl-	$C_{10}H_{20}$	35988.5
Cyclohexane, butyl-	$C_{10}H_{20}$	217945
Cyclohexane, 1,1,3,5-tetramethyl-, cis-	$C_{10}H_{20}$	17961.9
Benzene, 1-(1,1-dimethylethyl)-4-methoxy-	$C_{11}H_{16}O$	37005.7
(Z)-(Z)-Hex-3-en-1-yl 2-methylbut-2-enoate	$C_{11}H_{18}O_2$	27181.4
Cyclohexene, 1-pentyl-	$C_{11}H_{20}$	28586.7
Cyclopentylcyclohexane	$C_{11}H_{20}$	79994.6
Butanoic acid, 2-methylcyclohexyl ester, cis-	$C_{11}H_{20}O_2$	680698.9
Cyclohexane, pentyl-	$C_{11}H_{22}$	156152.1
trans-3-tert-butylcycloheptanol	$C_{11}H_{22}O$	13016.4
Oxalic acid, cyclohexyl isobutyl ester	$C_{12}H_{20}O_4$	28218.1
1,1'-Bicyclohexyl	$C_{12}H_{22}$	42654.2
1,1'-Bicyclohexyl	$C_{12}H_{22}$	36273.8
1,1'-Bicyclohexyl	$C_{12}H_{22}$	83393.1
Cyclohexane, hexyl-	$C_{12}H_{24}$	57459.2
1-Isopropyl-1,4,5-trimethylcyclohexane	$C_{12}H_{24}$	113448.5

Cyclohexane, 1,1'-methylenebis-	$C_{13}H_{24}$	57582.2
Cyclohexane, 1,1'-methylenebis-	$C_{13}H_{24}$	48213.7
Cyclohexane, 1,1'-methylenebis-	$C_{13}H_{24}$	42716.8
Decane, 2,3,8-trimethyl-	$C_{13}H_{28}$	17379
1,2-Di-but-2-enyl-cyclohexane	$C_{14}H_{24}$	164262.5
1,3-Benzenediol, o-cyclopropanecarbonyl-o'-(3-methylbut-2-enoyl)-	$C_{15}H_{16}O_4$	20938
Cyclohexane, 1,1'-(1,3-propanediyl)bis-	$C_{15}H_{28}$	85019.5
1-Cyclohexyl-1-(4-methylcyclohexyl)ethane	$C_{15}H_{28}$	147449.9
Cyclohexane, 1,1'-(1,3-propanediyl)bis-	$C_{15}H_{28}$	113134.8
Cyclohexane, 1,1'-(1-methylethylidene)bis-	$C_{15}H_{28}$	35857.3
Fumaric acid, di(cis-hex-3-enyl) ester	$C_{16}H_{24}O_4$	34076.3
Fumaric acid, di(trans-hex-3-enyl) ester	$C_{16}H_{24}O_4$	48693
1,1'-Bicyclooctyl	$C_{16}H_{30}$	22851.5
1-Cyclohexyl-1-(4-ethylcyclohexyl)ethane	$C_{16}H_{30}$	89054.3
Cyclohexane, 1,1'-(1,4-butanediyl)bis-	$C_{16}H_{30}$	55931.7
Decane, 2-cyclohexyl-	$C_{16}H_{32}$	20712.4
Cyclohexane, 1,1'-(1,5-pentanediyl)bis-	$C_{17}H_{32}$	77049.8
Heptadecane	$C_{17}H_{36}$	159177.7
4b,8-Dimethyl-2-isopropylphenanthrene, 4b,5,6,7,8,8a,9,10-octahydro-	$C_{19}H_{28}$	59741.4
4b,8-Dimethyl-2-isopropylphenanthrene, 4b,5,6,7,8,8a,9,10-octahydro-	$C_{19}H_{28}$	196193.9
4b,8-Dimethyl-2-isopropylphenanthrene, 4b,5,6,7,8,8a,9,10-octahydro-	$C_{19}H_{28}$	461870.7
Phenanthrene, 1,2,3,4,4a,9,10,10a-octahydro-1,1,4a-trimethyl-7-(1-methylethyl)-, (4aS-trans)-	$C_{20}H_{30}$	105972.7
Phthalic acid, di(2-ethylcyclohexyl) ester	$C_{24}H_{34}O_4$	16648.5

Table S14: Compounds identified by GC-MS in the oil phase after HDO upgrading at 250 °C over Ru/C catalyst.

Compound name	Formula	Relative intensity
Trimethylene oxide	C_3H_6O	16120
Acetic acid, methyl ester	$C_3H_6O_2$	20556.8
Propylene Glycol	$C_3H_8O_2$	881813.9
Methylal	$C_3H_8O_2$	48987.2
Propane, 2-methoxy-	$C_4H_{10}O$	274874.5
2,3-Butanediol, [S-(R*,R*)]-	$C_4H_{10}O_2$	45350.7
1,2-Butanediol	$C_4H_{10}O_2$	200611.1
Ethoxyacetylene	C_4H_6O	61567.2
Butyrolactone	$C_4H_6O_2$	410859.9
2,2'-Bioxirane	$C_4H_6O_2$	12008.6
1-Hydroxy-2-butanone	$C_4H_8O_2$	504325.7
Butanoic acid	$C_4H_8O_2$	440339
1,2-Ethanediol, monoacetate	$C_4H_8O_3$	696096.9
1,3-Dioxolane-2-methanol	$C_4H_8O_3$	74735.2
2-Methyl-1-butene	C_5H_{10}	188340
Propanoic acid, ethyl ester	$C_5H_{10}O_2$	23198.8
Butanoic acid, methyl ester	$C_5H_{10}O_2$	17252.3
2-Hydroxy-3-pentanone	$C_5H_{10}O_2$	218803.4
2-Furanmethanol, tetrahydro-	$C_5H_{10}O_2$	21542.8
1,2-Propanediol, 1-acetate	$C_5H_{10}O_3$	104514.4
Propanoic acid, 2-hydroxyethyl ester	$C_5H_{10}O_3$	56210.2
4-Methyl-5H-furan-2-one	$C_5H_6O_2$	69680
Cyclopentanone	C_5H_8O	591816.7
Propanoic acid, ethenyl ester	$C_5H_8O_2$	96705.9
3(2H)-Furanone, dihydro-2-methyl-	$C_5H_8O_2$	446997.1
2(3H)-Furanone, dihydro-3-methyl-	$C_5H_8O_2$	29809.9
2(3H)-Furanone, dihydro-5-methyl-	$C_5H_8O_2$	104131.4
2(3H)-Furanone, dihydro-4-methyl-	$C_5H_8O_2$	56506

2,3-Pentanedione	$C_5H_8O_2$	41782.7
2H-Pyran-2-one, tetrahydro-	$C_5H_8O_2$	98807.5
2-Propanone, 1-(acetyloxy)-	$C_5H_8O_3$	114083.4
5-(Hydroxymethyl)dihydrofuran-2(3H)-one	$C_5H_8O_3$	228328.8
Cyclopentanone, 2-methyl-	$C_6H_{10}O$	888972.5
Cyclohexanone	$C_6H_{10}O$	515870.9
1-Penten-3-one, 2-methyl-	$C_6H_{10}O$	178226.3
1-Penten-3-one, 2-methyl-	$C_6H_{10}O$	43293.5
Butanal, 3,3-dimethyl-2-oxo-, hemihydrate	$C_6H_{10}O_2$	155410.8
Cyclohexanone, 2-hydroxy-	$C_6H_{10}O_2$	76243.8
Propanoic acid, anhydride	$C_6H_{10}O_3$	40402.7
2-Butanone, 1-(acetyloxy)-	$C_6H_{10}O_3$	51027
1,1-Ethanediol, diacetate	$C_6H_{10}O_4$	16653.3
Dianhydromannitol	$C_6H_{10}O_4$	30029
Cyclopropane, propyl-	C_6H_{12}	39061.4
3-Hexanone	$C_6H_{12}O$	147884.7
2-Hexanone	$C_6H_{12}O$	57268.7
Acetic acid, butyl ester	$C_6H_{12}O_2$	31711.5
4-Hydroxy-3-hexanone	$C_6H_{12}O_2$	426511
4-Hydroxy-3-hexanone	$C_6H_{12}O_2$	87284.6
2H-Pyran-2-methanol, tetrahydro-	$C_6H_{12}O_2$	123816.3
2,5-Furandicarboxaldehyde	$C_6H_4O_3$	21148.1
Phenol	C_6H_6O	214353.1
Ethanone, 1-(2-furanyl)-	$C_6H_6O_2$	95189.8
Catechol	$C_6H_6O_2$	697318.1
Isomaltol	$C_6H_6O_3$	24139.7
2,3-dimethylfuran	C_6H_8O	218682.6
Furan, 2-ethyl-	C_6H_8O	18174.7
2-Cyclopenten-1-one, 2-methyl-	C_6H_8O	546640.7
2-Cyclopenten-1-one, 3-methyl-	C_6H_8O	120849.9

2(3H)-Furanone, 5-acetyldihydro-	$C_6H_8O_3$	14604.3
Furan, 2-ethyl-5-methyl-	$C_7H_{10}O$	47520.9
Furan, 2-ethyl-5-methyl-	$C_7H_{10}O$	18693.4
Furan, 2,3,5-trimethyl-	$C_7H_{10}O$	100016
2-Cyclopenten-1-one, 3-ethyl-	$C_7H_{10}O$	145982.1
2-Cyclopenten-1-one, 3,4-dimethyl-	$C_7H_{10}O$	56587.6
Furan, 2-ethyl-5-methyl-	$C_7H_{10}O$	105772.1
2-Cyclopenten-1-one, 2,3-dimethyl-	$C_7H_{10}O$	163435.9
2-Cyclopenten-1-one, 2,3-dimethyl-	$C_7H_{10}O$	129936.8
4-Ethyl-2-hydroxycyclopent-2-en-1-one	$C_7H_{10}O_2$	62395.4
4-Hexen-3-one, 5-methyl-	$C_7H_{12}O$	15109.2
trans-3,4-Dimethylcyclopentanone	$C_7H_{12}O$	32552.8
4-Hexen-3-one, 5-methyl-	$C_7H_{12}O$	20992.4
Cyclopentanone, 2-ethyl-	$C_7H_{12}O$	138297.3
1-Hepten-3-one	$C_7H_{12}O$	13672.7
4-Hexen-3-one, 5-methyl-	$C_7H_{12}O$	53811.3
4-Hexen-3-one, 5-methyl-	$C_7H_{12}O$	22478.1
3,6-Heptanedione	$C_7H_{12}O_2$	16267.1
Cyclohexane, methyl-	C_7H_{14}	84151.9
4-Heptanol	$C_7H_{16}O$	17812.4
1-Hexanol, 4-methyl-	$C_7H_{16}O$	55699.5
Toluene	C_7H_8	52411.8
Phenol, 2-methyl-	C_7H_8O	195108.3
p-Cresol	C_7H_8O	366954.6
1-Propanone, 1-(2-furanyl)-	$C_7H_8O_2$	51970.4
1-Propanone, 1-(2-furanyl)-	$C_7H_8O_2$	24315.3
Phenol, 2-methoxy-	$C_7H_8O_2$	1596023.6
5-Ethyl-2-furaldehyde	$C_7H_8O_2$	48318.3
1,2-Benzenediol, 3-methyl-	$C_7H_8O_2$	229928
1,2-Benzenediol, 3-methyl-	$C_7H_8O_2$	491537.3

1,2-Benzenediol, 4-methyl-	$C_7H_8O_2$	489910.9
Benzene, 1,3-dimethyl-	C_8H_{10}	13769.4
Phenol, 2-ethyl-	$C_8H_{10}O$	23194.4
Phenol, 2,4-dimethyl-	$C_8H_{10}O$	197716.3
Phenol, 4-ethyl-	$C_8H_{10}O$	85424.2
Phenol, 4-methoxy-3-methyl-	$C_8H_{10}O_2$	23190.5
Phenol, 4-methoxy-3-methyl-	$C_8H_{10}O_2$	65407
2-Methoxy-5-methylphenol	$C_8H_{10}O_2$	2396625.9
Benzeneethanol, 4-hydroxy-	$C_8H_{10}O_2$	12515.8
Ethyl p-hydroxybenzoate	$C_8H_{10}O_2$	369383.8
Phenol, 2,6-dimethoxy-	$C_8H_{10}O_3$	82505
2-Acetonylcyclopentanone	$C_8H_{12}O_2$	35338.1
4-Methyl-6-hepten-4-olide	$C_8H_{12}O_2$	12959.6
4-Methyl-6-hepten-4-olide	$C_8H_{12}O_2$	27690.6
Propanoic acid, 2-methyl-, anhydride	$C_8H_{14}O_3$	28167.8
Propanoic acid, 2-methyl-, anhydride	$C_8H_{14}O_3$	139967.9
Butanoic acid, anhydride	$C_8H_{14}O_3$	331178.8
Propanoic acid, 2-methyl-, anhydride	$C_8H_{14}O_3$	155794.1
Propanoic acid, 2-methyl-, anhydride	$C_8H_{14}O_3$	17622.6
Propanoic acid, 2-methyl-, anhydride	$C_8H_{14}O_3$	26541.3
n-Butyric acid tetrahydrofurfuryl ester	$C_8H_{14}O_3$	25849.9
Ethane-1,1-diol dipropanoate	$C_8H_{14}O_4$	27444
1-Butanol, 2-methyl-, propanoate	$C_8H_{16}O_2$	27224.4
Ethanone, 1-(2,5-dihydroxyphenyl)-	$C_8H_8O_3$	28037.2
3',5'-Dihydroxyacetophenone	$C_8H_8O_3$	12188
Resorcinol, 2-acetyl-	$C_8H_8O_3$	23426.3
3-Hydroxy-4-methoxybenzoic acid	$C_8H_8O_4$	203524.9
Ethanone, 1-(2-hydroxy-4-methoxyphenyl)-	$C_9H_{10}O_3$	35083.7
Apocynin	$C_9H_{10}O_3$	378953.3
2,5-Dihydroxy-4-methoxyacetophenone	$C_9H_{10}O_4$	69267

2,5-Dimethylanisole	$C_9H_{12}O$	36125.4
Phenol, 2,3,5-trimethyl-	$C_9H_{12}O$	26385.4
Phenol, 4-ethyl-2-methyl-	$C_9H_{12}O$	26167.9
Phenol, 4-ethyl-2-methyl-	$C_9H_{12}O$	77970.2
Phenol, 4-ethyl-2-methyl-	$C_9H_{12}O$	16850.6
Phenol, 4-propyl-	$C_9H_{12}O$	186663.7
Benzene, 1-ethyl-4-methoxy-	$C_9H_{12}O$	21042.3
Phenol, 4-ethyl-2-methyl-	$C_9H_{12}O$	21699.2
Phenol, 4-ethyl-2-methoxy-	$C_9H_{12}O_2$	36243.4
Phenol, 4-ethyl-2-methoxy-	$C_9H_{12}O_2$	1766770.8
Phenol, 4-ethyl-2-methoxy-	$C_9H_{12}O_2$	32688.9
1,3-Benzenediol, 4-propyl-	$C_9H_{12}O_2$	332680.5
3,5-Dimethoxy-4-hydroxytoluene	$C_9H_{12}O_3$	122022.7
Homovanillyl alcohol	$C_9H_{12}O_3$	127223.4
2,2-Dimethyl-3-heptanone	$C_9H_{18}O$	56768.6
Heptane, 2,4-dimethyl-	C_9H_{20}	131658.4
1-Heptanol, 2,4-dimethyl-,	$C_9H_{20}O$	102570.3
2,6-Dimethyl-4H-furo[3,2-c]pyran-4-one	$C_9H_8O_3$	34861.8
1(2H)-Naphthalenone, 3,4-dihydro-	$C_{10}H_{10}O$	14176.6
Eugenol	$C_{10}H_{12}O_2$	110374.3
benzoic acid, 4-hydroxy-3-propyl-	$C_{10}H_{12}O_3$	55908.9
2-Propanone, 1-(4-hydroxy-3-methoxyphenyl)-	$C_{10}H_{12}O_3$	237423.6
1-Propanone, 1-(4-hydroxy-3-methoxyphenyl)-	$C_{10}H_{12}O_3$	99890.9
Homosyringaldehyde	$C_{10}H_{12}O_4$	154739.4
2-Propanone, 1-hydroxy-3-(4-hydroxy-3-methoxyphenyl)-	$C_{10}H_{12}O_4$	101387.3
Benzeneacetic acid, 4-hydroxy-3-methoxy-, methyl ester	$C_{10}H_{12}O_4$	21748.3
Thymol	$C_{10}H_{14}O$	14002.1
Benzene, 1-methoxy-4-propyl-	$C_{10}H_{14}O$	124248.7
Phenol, 2-methoxy-4-propyl-	$C_{10}H_{14}O_2$	3145972.5

Benzenepropanol, 4-hydroxy-3-methoxy-	$C_{10}H_{14}O_3$	925615.5
2-Ethylhexanal ethylene glycol acetal	$C_{10}H_{20}O_2$	13658.7
2-Ethylhexanal ethylene glycol acetal	$C_{10}H_{20}O_2$	31385.9
Benzofuran, 2-ethenyl-	$C_{10}H_8O$	12379.7
Phenol, 2-(1,1-dimethylethyl)-4-methyl-	$C_{11}H_{16}O$	409187
Guaiacol, 4-butyl-	$C_{11}H_{16}O_2$	118245.6
2,7-Nonadien-5-one, 4,6-dimethyl-	$C_{11}H_{18}O$	41313.6
3,7-Decadiene, 2,9-dimethyl-	$C_{12}H_{22}$	47963.6
Propan-2-one, 1-(4-isopropoxy-3-methoxyphenyl)-	$C_{13}H_{18}O_3$	28244
(2S,6R,7S,8E)-(+)-2,7-Epoxy-4,8-megastigmadiene	$C_{13}H_{20}O$	27947.4
2-[(2-Methyl-endo-2-norbornyl)oxy]-tetrahydropyran	$C_{13}H_{22}O_2$	15042.3

Table S15: Compounds identified by GC-MS in the oil phase after guaiacol syngas C–C coupling upgrading at 250 °C over Ru/C catalyst.

Compound name	Formula	Relative intensity	
Isobutyl acetate	$C_6H_{12}O_2$	18814.1	FT
Butane, 1,4-dimethoxy-	$C_6H_{14}O_2$	15911.9	FT
3-Methyl-1-penten-4-yn-3-ol	C_6H_8O	717595.6	FT
4-Hexen-3-one, 5-methyl-	$C_7H_{12}O$	20318.9	FT
Propanoic acid, 2-methyl-, anhydride	$C_8H_{14}O_3$	15623.8	FT
Octane	C_8H_{18}	44530.6	FT
1,5-Heptadiene, 2,6-dimethyl-	C_9H_{16}	721544.9	FT
Cyclohexane, methyl-	C_7H_{14}	106512	GU
Benzene, 1,2-dimethoxy-	$C_8H_{10}O_2$	105991.5	GU
Butanoic acid, anhydride	$C_8H_{14}O_3$	17438.5	GU

Benzeneacetic acid, methyl ester	$C_9H_{10}O_2$	11727.4	GU
Phenol, 2-(1,1-dimethylethyl)-5-methyl-	$C_{11}H_{16}O$	124488.2	GU
1,4-Benzenediol, 2,5-bis(1,1-dimethylethyl)-	$C_{14}H_{22}O_2$	284701.5	GU
Isophthalic acid, butyl phenyl ester	$C_{18}H_{18}O_4$	8370578.9	GU

- FT denotes the products of Fischer–Tropsch synthesis, GU denotes the products obtained after guaiacol upgrading.

Table S16: Compounds identified by GC-MS in the oil phase after guaiacol syngas C–C coupling upgrading at 250 °C over Co/β-zeolite catalyst.

Compound name	Formula	Relative intensity	
Cyclopropane, [(1-propenyloxy)methyl]-	$C_7H_{12}O$	3397.3	FT
Isobutyl acrylate	$C_7H_{12}O_2$	3755	FT
Propanoic acid, 2-methyl-, anhydride	$C_8H_{14}O_3$	18575.3	FT
Propanoic acid, 2-methyl-, anhydride	$C_8H_{14}O_3$	24429.5	FT
6-Hepten-1-ol, 5-methyl-	$C_8H_{16}O$	50424.2	FT
3-Methyl-2-butenoic acid, cyclobutyl ester	$C_9H_{14}O_2$	7056.5	FT
But-3-enyl (E)-2-methylbut-2-enoate	$C_9H_{14}O_2$	6274.4	FT
3,4-Hexanedione, 2,2,5-trimethyl-	$C_9H_{16}O_2$	12784.2	FT
3,4-Hexanedione, 2,2,5-trimethyl-	$C_9H_{16}O_2$	9346	FT
3,4-Hexanedione, 2,2,5-trimethyl-	$C_9H_{16}O_2$	9544	FT
3,4-Hexanedione, 2,2,5-trimethyl-	$C_9H_{16}O_2$	8400.6	FT
3,4-Hexanedione, 2,2,5-trimethyl-	$C_9H_{16}O_2$	6591.1	FT
3,4-Hexanedione, 2,2,5-trimethyl-	$C_9H_{16}O_2$	9326.8	FT
1,5-Heptadien-4-one, 3,3,6-trimethyl-	$C_{10}H_{16}O$	8659.8	FT
1,5-Heptadien-4-one, 3,3,6-trimethyl-	$C_{10}H_{16}O$	20910.5	FT
Octane, 2,7-dimethyl-	$C_{10}H_{22}$	5173.5	FT
4H-Pyran-4-one, 5-hydroxy-2-(hydroxymethyl)-	$C_6H_6O_4$	12858.3	GU
Pentalene, octahydro-	C_8H_{14}	220789.3	GU
1-Propylcyclopentene	C_8H_{14}	16484.3	GU
Cyclohexene, 1-ethyl-	C_8H_{14}	16502.1	GU

6-Methylisoeugenol	$C_{11}H_{14}O_2$	93728.5	GU
5'-Hydroxy-2',3',4'-trimethylacetophenone	$C_{11}H_{14}O_2$	19847.8	GU
Guaiacol, 4-butyl-	$C_{11}H_{16}O_2$	19093.9	GU
Oxalic acid, cyclohexyl propyl ester	$C_{11}H_{18}O_4$	2194.4	GU
6-Methoxyfuro[2,3-h]chromen-2-one	$C_{12}H_8O_4$	53331.6	GU
6-Methoxyfuro[2,3-h]chromen-2-one	$C_{12}H_8O_4$	12464.3	GU
4,6-Dimethoxy-1-naphthaldehyde	$C_{13}H_{12}O_3$	34280.9	GU
Indan, 1,1,6,7-tetramethyl-	$C_{13}H_{18}$	8595.1	GU
Propan-2-one, 1-(4-isopropoxy-3-methoxyphenyl)-	$C_{13}H_{18}O_3$	13149.4	GU
Propan-2-one, 1-(4-isopropoxy-3-methoxyphenyl)-	$C_{13}H_{18}O_3$	34066.5	GU
Trioxsalen	$C_{14}H_{12}O_3$	34728.1	GU
Phenol, 2,5-bis(1-methylethyl)-, acetate	$C_{14}H_{20}O_2$	20224	GU
9H-Fluorene, 2-ethyl-	$C_{15}H_{14}$	7991.3	GU
Ethanone, 1-[2,3-dihydro-1,1,2,6-tetramethyl-3-(1-methylethyl)-1H-inden-5-yl]-	$C_{18}H_{26}O$	136901.9	GU
2-Butyl-4-phenoxy-1-naphthalenol	$C_{20}H_{20}O_2$	1560.6	GU
Cyclobutane, 1R,3E-bis(4-methoxy-2-oxo-2H-pyran-6-yl)-2Z,4E-bis(4-ethylphenyl)-	$C_{32}H_{32}O_6$	51274.1	GU

- FT denotes the products of Fischer–Tropsch synthesis, GU denotes the products obtained after guaiacol upgrading.

Table S17: Compounds identified by GC-MS in the oil phase after guaiacol syngas C–C coupling upgrading at 250 °C over Ru/β-zeolite catalyst.

Compound name	Formula	Relative intensity	
Propene	C_3H_6	4398.7	FT
Butane	C_4H_{10}	51806.2	FT
3-Buten-2-ol	C_4H_8O	6927.7	FT
Butane, 2-methyl-	C_5H_{12}	16821.7	FT
Pentane	C_5H_{12}	95666.5	FT
3-Hexen-2-one	$C_6H_{10}O$	4197.2	FT
3-Hexanone	$C_6H_{12}O$	3221.7	FT
Pentane, 2-methyl-	C_6H_{14}	15661.6	FT
n-Hexane	C_6H_{14}	93176	FT
Hexane, 2-methyl-	C_7H_{16}	27377.6	FT
Heptane	C_7H_{16}	110494.6	FT
Heptane, 2-methyl-	C_8H_{18}	16912.2	FT
Heptane, 3-methyl-	C_8H_{18}	7120.6	FT
Octane	C_8H_{18}	110422.3	FT
Hexane, 3,3-dimethyl-	C_8H_{18}	17929	FT
Hexane, 3,3-dimethyl-	C_8H_{18}	12694.7	FT
Hexane, 3,3-dimethyl-	C_8H_{18}	18270.2	FT
Hexane, 3,3-dimethyl-	C_8H_{18}	14168.1	FT
Hexane, 3,3-dimethyl-	C_8H_{18}	5352.2	FT
Hexane, 2,3,5-trimethyl-	C_9H_{20}	10932.5	FT
Nonane	C_9H_{20}	99678.8	FT
Hexane, 2,4,4-trimethyl-	C_9H_{20}	4637.2	FT
Decane	$C_{10}H_{22}$	84639.8	FT
1,11-Dodecadiene	$C_{12}H_{22}$	81824.4	FT
Dodecane	$C_{12}H_{26}$	78959	FT
Undecane, 3-ethyl-	$C_{13}H_{28}$	16207.7	FT
7-Ethyl-4-dodecen-6-one	$C_{14}H_{26}O$	13153.4	FT
7-Ethyl-4-dodecen-6-one	$C_{14}H_{26}O$	14353.4	FT

Tetradecane	$C_{14}H_{30}$	59075.7	FT
Hexadecane	$C_{16}H_{34}$	45050.6	FT
Heptadecane	$C_{17}H_{36}$	27396	FT
2-Butanone, 4-(4-hydroxy-3-methoxyphenyl)-	$C_{11}H_{14}O_3$	22083.7	GU
Guaiacol, 4-butyl-	$C_{11}H_{16}O_2$	38234.9	GU
Guaiacol, 4-butyl-	$C_{11}H_{16}O_2$	29863.6	GU
4'-Hydroxy-3'-methoxyacetophenone, propyl ether	$C_{12}H_{16}O_3$	88156.2	GU
4'-Hydroxy-3'-methoxyacetophenone, propyl ether	$C_{12}H_{16}O_3$	47021.8	GU
4'-Hydroxy-3'-methoxyacetophenone, propyl ether	$C_{12}H_{16}O_3$	51991	GU
Benzene, 4-butyl-1,2-dimethoxy-	$C_{12}H_{18}O_2$	128625.8	GU
Benzene, 4-butyl-1,2-dimethoxy-	$C_{12}H_{18}O_2$	73958.4	GU
Benzene, 4-butyl-1,2-dimethoxy-	$C_{12}H_{18}O_2$	92655.1	GU
Propan-2-one, 1-(4-isopropoxy-3-methoxyphenyl)-	$C_{13}H_{18}O_3$	14688.8	GU
Propan-2-one, 1-(4-isopropoxy-3-methoxyphenyl)-	$C_{13}H_{18}O_3$	13008	GU
Acetoisovanillone, trimethylacetate	$C_{14}H_{18}O_4$	19284.6	GU
p-Methoxyheptanophenone	$C_{14}H_{20}O_2$	8339.2	GU
4'-Hydroxy-3'-methoxyacetophenone, pentyl ether	$C_{14}H_{20}O_3$	3390.1	GU
p-tert-Octylresorcinol	$C_{14}H_{22}O_2$	135268.2	GU
p-tert-Octylresorcinol	$C_{14}H_{22}O_2$	33024.4	GU
p-tert-Octylresorcinol	$C_{14}H_{22}O_2$	22026.6	GU
p-tert-Octylresorcinol	$C_{14}H_{22}O_2$	23354.5	GU
p-tert-Octylresorcinol	$C_{14}H_{22}O_2$	14280.3	GU
Cyclohexane, octyl-	$C_{14}H_{28}$	17176.4	GU
Orcinyl di-angelate	$C_{17}H_{20}O_4$	10208.6	GU
Catechol	$C_6H_6O_2$	894170.7	GU

1,2-Benzenediol, 3-methyl-	$C_7H_8O_2$	100285.1	GU
1,2-Benzenediol, 3-methyl-	$C_7H_8O_2$	96387.3	GU
Phenol, 4-methoxy-3-methyl-	$C_8H_{10}O_2$	88110.9	GU
Benzene, 1,2-dimethoxy-	$C_8H_{10}O_2$	787586.5	GU
Phenol, 2-ethoxy-	$C_8H_{10}O_2$	88163.2	GU
2-Methoxy-5-methylphenol	$C_8H_{10}O_2$	955792.8	GU
Creosol	$C_8H_{10}O_2$	519799.3	GU
Creosol	$C_8H_{10}O_2$	517985.2	GU
1,3-Benzenediol, 4-ethyl-	$C_8H_{10}O_2$	15702.7	GU
Benzene, 1,4-dimethoxy-	$C_8H_{10}O_2$	67391.6	GU
Ethanone, 1-(2,5-dihydroxyphenyl)-	$C_8H_8O_3$	39604.1	GU
Ethanone, 1-(2,4-dihydroxyphenyl)-	$C_8H_8O_3$	189352	GU
Benzaldehyde, 2,4-dihydroxy-6-methyl-	$C_8H_8O_3$	51922	GU
Ethanone, 1-(2-hydroxy-5-methoxyphenyl)-	$C_9H_{10}O_3$	10580.4	GU
Ethanone, 1-(2-hydroxy-4-methoxyphenyl)-	$C_9H_{10}O_3$	155541.7	GU
2',4'-Dihydroxypropiophenone	$C_9H_{10}O_3$	32972.5	GU
3,4-Dimethoxytoluene	$C_9H_{12}O_2$	18828.1	GU
Phenol, 4-ethyl-2-methoxy-	$C_9H_{12}O_2$	144110.5	GU
Phenol, 4-ethyl-2-methoxy-	$C_9H_{12}O_2$	261368.4	GU
Phenol, 4-ethyl-2-methoxy-	$C_9H_{12}O_2$	240305	GU
Phenol, 4-ethyl-2-methoxy-	$C_9H_{12}O_2$	61176.3	GU
Phenol, 4-ethyl-2-methoxy-	$C_9H_{12}O_2$	61205	GU
2-Cyclohexen-1-one, 4,4,6-trimethyl-	$C_9H_{14}O$	10805.9	GU

- FT denotes the products of Fischer–Tropsch synthesis, GU denotes the products obtained after guaiacol upgrading.

Table S18: Compounds identified by GC-MS in the oil phase after guaiacol syngas C–C coupling upgrading at 300 °C.

Compound name	Formula	Relative intensity	
Isobutane	C_4H_{10}	107782.5	FT
Butane	C_4H_{10}	221037.6	FT
Butane, 2-methyl-	C_5H_{12}	278440.9	FT
Pentane	C_5H_{12}	210476.2	FT
Pentane, 2-methyl-	C_6H_{14}	280274.9	FT
Pentane, 3-methyl-	C_6H_{14}	79116.5	FT
n-Hexane	C_6H_{14}	235223.5	FT
Hexane, 2-methyl-	C_7H_{16}	327929.5	FT
Hexane, 2,2,5-trimethyl-	C_9H_{20}	20857.3	FT
Hexane, 3-methyl-	C_7H_{16}	98224.9	FT
Heptane	C_7H_{16}	232104.5	FT
Hexane, 2,5-dimethyl-	C_8H_{18}	59817.8	FT
Pentane, 3-ethyl-	C_7H_{16}	7114.8	FT
Toluene	C_7H_8	21936.3	FT
Heptane, 2-methyl-	C_8H_{18}	174409.2	FT
Heptane, 3-methyl-	C_8H_{18}	82649	FT
3,3-Diethoxy-1-propyne	$C_7H_{12}O_2$	9272.4	FT
Octane	C_8H_{18}	206281.8	FT
Heptane, 2,6-dimethyl-	C_9H_{20}	30682.6	FT
Heptane, 2,5-dimethyl-	C_9H_{20}	31947.4	FT
(E)-2,6-Dimethylocta-3,7-diene-2,6-diol	$C_{10}H_{18}O_2$	35831.5	FT
Octane, 2-methyl-	C_9H_{20}	119184.4	FT
Octane, 3-methyl-	C_9H_{20}	56967.8	FT
Hexane, 2,4,4-trimethyl-	C_9H_{20}	11481.9	FT
3,6-Heptanedione	$C_7H_{12}O_2$	15788.1	FT
Undecane, 6,6-dimethyl-	$C_{13}H_{28}$	22971.3	FT

2,4-Heptadienal, 2,4-dimethyl-	$C_9H_{14}O$	1204297	FT
Nonane, 2-methyl-	$C_{10}H_{22}$	71473.5	FT
Undecane, 6,6-dimethyl-	$C_{13}H_{28}$	99495.6	FT
Decane	$C_{10}H_{22}$	226340.6	FT
Decane, 6-ethyl-2-methyl-	$C_{13}H_{28}$	82809.6	FT
Undecane, 3-methyl-	$C_{12}H_{26}$	32708.1	FT
Dodecane	$C_{12}H_{26}$	262059.2	FT
Undecane, 3-methyl-	$C_{12}H_{26}$	35259.7	FT
Dodecane, 3-methyl-	$C_{13}H_{28}$	28546.9	FT
Undecane, 2,6-dimethyl-	$C_{13}H_{28}$	24809.7	FT
Undecane, 3-ethyl-	$C_{13}H_{28}$	42369.9	FT
Tridecane, 3-methyl-	$C_{14}H_{30}$	29135.3	FT
Tetradecane	$C_{14}H_{30}$	182650.7	FT
Hexadecane	$C_{16}H_{34}$	111617.7	FT
Heptadecane	$C_{17}H_{36}$	86632.3	FT
Octadecane	$C_{18}H_{38}$	68520.4	FT
Undecane, 3,8-dimethyl-	$C_{13}H_{28}$	55013.5	FT
Dodecane, 2,6,11-trimethyl-	$C_{15}H_{32}$	146303	FT
Cyclohexane, methyl-	C_7H_{14}	318050.3	GU
Cyclohexane, 1,3-dimethyl-, cis-	C_8H_{16}	36386.6	GU
Cyclohexane, 1,3-dimethyl-, cis-	C_8H_{16}	58663.6	GU
Cyclohexane, pentyl-	$C_{11}H_{22}$	20294.3	GU
Orcinyl di-tiglate	$C_{17}H_{20}O_4$	10832.3	GU
Cyclohexane, 1,4-dimethyl-	C_8H_{16}	112059.1	GU
Cyclohexane, ethyl-	C_8H_{16}	38322	GU
Anisole	C_7H_8O	23140.5	GU
Cyclohexene,3-propyl-	C_9H_{16}	136063.5	GU
Cyclohexane, butylidene-	$C_{10}H_{18}$	320502.9	GU
Cyclohexane, propyl-	C_9H_{18}	17290.4	GU
Cyclohexene, 1-butyl-	$C_{10}H_{18}$	267564.5	GU

Phenol, 4-propyl-	$C_9H_{12}O$	83719.6	GU
Cyclopentane, (2-methylbutylidene)-	$C_{10}H_{18}$	233565.4	GU
Cyclohexene, 1-butyl-	$C_{10}H_{18}$	185358.4	GU
Phenol, 4-propyl-	$C_9H_{12}O$	45578.2	GU
Phenol, 4-propyl-	$C_9H_{12}O$	43506.5	GU
Cyclohexene, 1-pentyl-	$C_{11}H_{20}$	45668.5	GU
Cyclohexane, 1-methyl-3-propyl-	$C_{10}H_{20}$	17611.7	GU
Cyclohexene,3-(1-methylpropyl)-	$C_{10}H_{18}$	157758.2	GU
Cyclohexene, 3-methyl-6-(1-methylethyl)-	$C_{10}H_{18}$	98699.9	GU
Cyclohexene, 1-ethyl-6-ethylidene-	$C_{10}H_{16}$	46516.1	GU
Cyclohexene, 1-ethyl-6-ethylidene-	$C_{10}H_{16}$	43211.7	GU
2-Cyclohexen-1-one, 4,4-dimethyl-	$C_8H_{12}O$	35131.8	GU
Cyclohexane, (2-methyl-1-propenyl)-	$C_{10}H_{18}$	545355.8	GU
Cyclohexane, 1-ethyl-2,4-dimethyl-	$C_{10}H_{20}$	123107.9	GU
Cyclohexene, 1-ethyl-6-ethylidene-	$C_{10}H_{16}$	84384.9	GU
Benzene, 1,3-dimethoxy-	$C_8H_{10}O_2$	244360.6	GU
Cyclohexene, 1-butyl-	$C_{10}H_{18}$	1205998	GU
Cyclohexene,3-butyl-	$C_{10}H_{18}$	1599452	GU
Cyclohexane, butylidene-	$C_{10}H_{18}$	242870.6	GU
Phenol	C_6H_6O	63264.8	GU
Cyclohexene,3-butyl-	$C_{10}H_{18}$	887013.8	GU
Carbonic acid, propargyl cyclohexylmethyl ester	$C_{11}H_{16}O_3$	616780.7	GU
Cyclohexene, 1-butyl-	$C_{10}H_{18}$	1650157	GU
Cyclohexene, 4-methyl-1-(1-methylethyl)-	$C_{10}H_{18}$	708380.4	GU
Cyclohexane, butylidene-	$C_{10}H_{18}$	980484.1	GU
Cyclohexane, butylidene-	$C_{10}H_{18}$	919636	GU
Cyclohexene, 1-ethyl-6-ethylidene-	$C_{10}H_{16}$	537744.2	GU
Cyclohexene, 4-methyl-1-(1-methylethyl)-	$C_{10}H_{18}$	3127686	GU

Cyclohexene, 3-methyl-6-(1-methylethyl)-	$C_{10}H_{18}$	3110975	GU
Acetic acid, 4-methylphenyl ester	$C_9H_{10}O_2$	9155	GU
2-Acetoxyacetophenone	$C_{10}H_{10}O_3$	21622.1	GU
Phenol, 4-ethyl-2-methyl-	$C_9H_{12}O$	156006.5	GU
Cyclohexene, 1-butyl-	$C_{10}H_{18}$	824652.5	GU
Cyclohexene, 1-butyl-	$C_{10}H_{18}$	143699.8	GU
p-Cresol	C_7H_8O	146738.9	GU
p-Toluic acid, pentyl ester	$C_{13}H_{18}O_2$	19853	GU
Benzene, 4-ethenyl-1,2-dimethyl-	$C_{10}H_{12}$	53943.8	GU
o-Menth-8-ene	$C_{10}H_{18}$	394501.6	GU
Benzene, 4-ethenyl-1,2-dimethyl-	$C_{10}H_{12}$	94270.7	GU
1,3-Cyclohexadiene, 1-methyl-4-(1-methylethyl)-	$C_{10}H_{16}$	66780.6	GU
2-Ethylbutyric acid, 5-methyl-2-methoxyphenyl ester	$C_{14}H_{20}O_3$	17359.5	GU
Benzene, 4-ethenyl-1,2-dimethyl-	$C_{10}H_{12}$	132826.7	GU
Benzene, 4-ethenyl-1,2-dimethyl-	$C_{10}H_{12}$	184277.1	GU
Phenol, 3,4-dimethyl-	$C_8H_{10}O$	61974.7	GU
Phenol, 3,4-dimethyl-	$C_8H_{10}O$	54210.1	GU
2-Cyclohexen-1-one, 4-ethyl-3,4-dimethyl-	$C_{10}H_{16}O$	70453.1	GU
2-Methoxy-5-methylphenol	$C_8H_{10}O_2$	506931.9	GU
Phenol, 2,3,5,6-tetramethyl-	$C_{10}H_{14}O$	19493.1	GU
2-Methoxy-5-methylphenol	$C_8H_{10}O_2$	136072.3	GU
1H-Indene, 2,3-dihydro-1,1-dimethyl-	$C_{11}H_{14}$	49188.3	GU
2-Methoxy-5-methylphenol	$C_8H_{10}O_2$	170422.3	GU
1,2-Diethoxybenzene	$C_{10}H_{14}O_2$	177803.3	GU
1H-Indene, 2,3-dihydro-4,7-dimethyl-	$C_{11}H_{14}$	32452.5	GU
Phenol, 2-(1-methylethyl)-	$C_9H_{12}O$	12553.3	GU
Phenol, 2-(1-methylethyl)-	$C_9H_{12}O$	14533.1	GU
Resorcinol, 2-acetyl-	$C_8H_8O_3$	7381.8	GU

Phenol, 2-(1-methylethyl)-	$C_9H_{12}O$	53776.7	GU
Phenol, 2,3,6-trimethyl-	$C_9H_{12}O$	242587.1	GU
Phenol, 3,4,5-trimethyl-	$C_9H_{12}O$	89229.8	GU
Phenol, 2,3,5-trimethyl-	$C_9H_{12}O$	15040.3	GU
1H-Indene, 2,3-dihydro-4,7-dimethyl-	$C_{11}H_{14}$	26543.1	GU
1,2-Benzenediol, 3-methyl-	$C_7H_8O_2$	139035.7	GU
Phenol, 4-ethyl-2-methoxy-	$C_9H_{12}O_2$	52795.5	GU
Ethanone, 1-(2,3-dihydro-1H-inden-5-yl)-	$C_{11}H_{12}O$	27834.2	GU
Phenol, 2,3,5-trimethyl-	$C_9H_{12}O$	74497.3	GU
Phenol, 2,3,5-trimethyl-	$C_9H_{12}O$	27693.2	GU
Phenol, 4-ethyl-2-methoxy-	$C_9H_{12}O_2$	203613.9	GU
Resorcinol, 2-acetyl-	$C_8H_8O_3$	30058.8	GU
1,3-Benzenediol, 5-pentyl-	$C_{11}H_{16}O_2$	178751.6	GU
1H-Indene, 2,3-dihydro-4-propyl-	$C_{12}H_{16}$	65204.2	GU
3',5'-Dihydroxyacetophenone	$C_8H_8O_3$	51760.6	GU
Phenol, 3,4,5-trimethyl-	$C_9H_{12}O$	46745.3	GU
1,3-Benzenediol, 4,5-dimethyl-	$C_8H_{10}O_2$	46395.6	GU
2-Hydroxy-5-methoxybenzaldehyde, acetate	$C_{10}H_{10}O_4$	55374	GU
Phenol, 2-(1-methylpropyl)-	$C_{10}H_{14}O$	25147.3	GU
Ethanone, 1-(2-hydroxy-6-methoxyphenyl)-	$C_9H_{10}O_3$	92895.4	GU
2',6'-Dihydroxy-3'-methylacetophenone	$C_9H_{10}O_3$	40219.4	GU
Guaiacol, 4-butyl-	$C_{11}H_{16}O_2$	46699.5	GU
1,3-Benzenediol, 4-ethyl-	$C_8H_{10}O_2$	19014.5	GU
2',6'-Dihydroxy-3'-methylacetophenone	$C_9H_{10}O_3$	59807.5	GU
1,3-Benzenediol, 4,5-dimethyl-	$C_8H_{10}O_2$	74952.2	GU
Ethanone, 1-(2-hydroxy-5-methoxyphenyl)-	$C_9H_{10}O_3$	10186.6	GU

2'-Hydroxy-4'-methoxyacetophenone, acetate	$C_{11}H_{12}O_4$	72450.1	GU
Phenol, 2,3,5,6-tetramethyl-	$C_{10}H_{14}O$	147040.4	GU
1,3-Benzenediol, 4,5-dimethyl-	$C_8H_{10}O_2$	51080.8	GU
Phenol, 4-ethyl-2-methoxy-	$C_9H_{12}O_2$	23790.7	GU
Benzene, 1-pentyl-4-vinyl-	$C_{13}H_{18}$	16346	GU
4-Propoxybenzaldehyde	$C_{10}H_{12}O_2$	8974.2	GU
benzoic acid, 4-hydroxy-3-propyl-	$C_{10}H_{12}O_3$	49262.6	GU
5-Acetyl-2-methoxyphenyl acetate	$C_{11}H_{12}O_4$	119410.2	GU
1-(2,3-Dihydroxyphenyl)ethanone	$C_8H_8O_3$	51108.9	GU
Benzene, 4-butyl-1,2-dimethoxy-	$C_{12}H_{18}O_2$	21177.4	GU
2',4'-Dihydroxy-3'-methylbutyrophenone	$C_{11}H_{14}O_3$	15122.6	GU
2-tert-Butyl-6-methyl-phenol, acetate	$C_{13}H_{18}O_2$	16392.9	GU

Table S19: Compounds identified by GC-MS in oil phase.

Compound name	Formula	Relative intensity
2-Propanone, 1-hydroxy-	$C_3H_6O_2$	65904.3
(S)-(+)-1,2-Propanediol	$C_3H_8O_2$	11199.6
1,4-Butanediol	$C_4H_{10}O_2$	54207.5
Furan	C_4H_4O	16884.5
2(5H)-Furanone	$C_4H_4O_2$	215715.5
Succindialdehyde	$C_4H_6O_2$	230288.8
2-Butanone	C_4H_8O	68079.5
1-Hydroxy-2-butanone	$C_4H_8O_2$	136557
1,2-Ethanediol, monoacetate	$C_4H_8O_3$	83229.3
1,3-Dioxolane-2-methanol	$C_4H_8O_3$	59168
1,2-Ethanediol, monoacetate	$C_4H_8O_3$	322755

Butanoic acid, 4-hydroxy-	$C_4H_8O_3$	105980.2
Pentanoic acid	$C_5H_{10}O_2$	16213.7
Furfural	$C_5H_4O_2$	30339.6
3-Furaldehyde	$C_5H_4O_2$	528061.2
2-Cyclopenten-1-one	C_5H_6O	186151.9
2(5H)-Furanone, 5-methyl-	$C_5H_6O_2$	49919.3
2(5H)-Furanone, 3-methyl-	$C_5H_6O_2$	92057.5
4-Methyl-5H-furan-2-one	$C_5H_6O_2$	90438.3
Cyclopentanone	C_5H_8O	32367.9
2-Propanone, 1-(acetyloxy)-	$C_5H_8O_3$	158309.7
2,2'-Bi-1,3-dioxolane	$C_6H_{10}O_4$	25556.1
.beta.-D-Glucopyranose, 1,6-anhydro-	$C_6H_{10}O_5$	99542.7
.beta.-D-Glucopyranose, 1,6-anhydro-	$C_6H_{10}O_5$	3745329
.beta.-D-Glucopyranose, 1,6-anhydro-	$C_6H_{10}O_5$	564126
2-Butanone, 3-methoxy-3-methyl-	$C_6H_{12}O_2$	32012.6
1,3-Dioxolane, 2-propyl-	$C_6H_{12}O_2$	43885.4
Phenol	C_6H_6O	133596.8
Catechol	$C_6H_6O_2$	432192.1
2-Cyclopenten-1-one, 2-methyl-	C_6H_8O	112615.8
2-Cyclopenten-1-one, 2-hydroxy-3-methyl-	$C_6H_8O_2$	562530.8
2-Furanone, 2,5-dihydro-3,5-dimethyl	$C_6H_8O_2$	71945.4
Vinyl crotonate	$C_6H_8O_2$	16260.8
1,4:3,6-Dianhydro-.alpha.-d-glucopyranose	$C_6H_8O_4$	83064.3
2-Cyclopenten-1-one, 3-ethyl-2-hydroxy-	$C_7H_{10}O_2$	63603.9
2-Cyclopenten-1-one, 2-hydroxy-3,4-dimethyl-	$C_7H_{10}O_2$	46079.9

5-Oxotetrahydrofuran-2-carboxylic acid, ethyl ester	$C_7H_{10}O_4$	59259.2
3,3-Dimethyl-2,4-pentane dione	$C_7H_{12}O_2$	33273.5
Cyclohexane, methyl-	C_7H_{14}	70859.9
Phenol, 2-methyl-	C_7H_8O	129948.5
p-Cresol	C_7H_8O	293706.2
1,2-Benzenediol, 3-methyl-	$C_7H_8O_2$	159036.5
1,2-Benzenediol, 3-methyl-	$C_7H_8O_2$	27351.4
1,2-Benzenediol, 4-methyl-	$C_7H_8O_2$	50091.5
Phenol, 2-methoxy-	$C_7H_8O_2$	977452.5
Phenol, 3,4-dimethyl-	$C_8H_{10}O$	123382.4
2-Methoxy-5-methylphenol	$C_8H_{10}O_2$	1273503
Ethanol, 2,2'-oxybis-, diacetate	$C_8H_{14}O_5$	28969.2
Benzaldehyde, 3-hydroxy-4-methoxy-	$C_8H_8O_3$	498602.2
Ethanone, 1-(2-hydroxy-5-methylphenyl)-	$C_9H_{10}O_2$	67486
Ethanone, 1-(3-hydroxy-4-methoxyphenyl)-	$C_9H_{10}O_3$	322998.8
Homovanillic acid	$C_9H_{10}O_4$	194836.7
Phenol, 4-ethyl-2-methoxy-	$C_9H_{12}O_2$	501064.9
Hexane, 2,3,4-trimethyl-	C_9H_{20}	45489.6
Coniferyl aldehyde	$C_{10}H_{10}O_3$	473345.3
Phenol, 2-methoxy-4-(1-propenyl)-	$C_{10}H_{12}O_2$	281532.5
Eugenol	$C_{10}H_{12}O_2$	444225.7
2-Propanone, 1-(4-hydroxy-3-methoxyphenyl)-	$C_{10}H_{12}O_3$	193759.7
Cyclohexene, 1-butyl-	$C_{10}H_{18}$	78493.9
Phenol, 2-methoxy-4-(2-propenyl)-, acetate	$C_{12}H_{14}O_3$	385560.9

Decane, 3,3,4-trimethyl-	$C_{13}H_{28}$	29582.9

Table S20: Compounds identified by GC-MS in the oil phase after bio-oil syngas C–C coupling upgrading at 250 °C.

Compound name	Formula	Relative intensity
DL-2,3-Butanediol	$C_4H_{10}O_2$	26921.9
Butanoic acid	$C_4H_8O_2$	234689
1-Hydroxy-2-butanone	$C_4H_8O_2$	127534.3
2-Hydroxy-3-pentanone	$C_5H_{10}O_2$	85955.7
2-Methoxytetrahydrofuran	$C_5H_{10}O_2$	59474.6
3-Pentanol	$C_5H_{12}O$	96723.8
1-Butanol, 4-methoxy-	$C_5H_{12}O_2$	174762.5
Furfural	$C_5H_4O_2$	78651.4
1,3-Dioxolan-2-one, 4,5-bis(methylene)-	$C_5H_4O_3$	156203.1
Cyclopentanone	C_5H_8O	263899.7
2(3H)-Furanone, dihydro-4-methyl-	$C_5H_8O_2$	50862.6
2-Propanone, 1-(acetyloxy)-	$C_5H_8O_3$	116962.1
Cyclobutanone, 2,3-dimethyl-, cis-	$C_6H_{10}O$	37759.2
(R)-(+)-3-Methylcyclopentanone	$C_6H_{10}O$	65259.9
Cyclohexanone	$C_6H_{10}O$	231992.3
Cyclopentanone, 2-methyl-	$C_6H_{10}O$	232043.5
2,5-Hexanedione	$C_6H_{10}O_2$	79170.7
Furan, tetrahydro-3,4-dimethyl-, cis-	$C_6H_{12}O$	92797.8
3-Hexanone	$C_6H_{12}O$	26775.1
2H-Pyran-2-methanol, tetrahydro-	$C_6H_{12}O_2$	50275.7
Acetic acid, butyl ester	$C_6H_{12}O_2$	59898.4
1,3-Dioxolane, 2-propyl-	$C_6H_{12}O_2$	40105.5
Phenol	C_6H_6O	143645

Ethanone, 1-(2-furanyl)-	$C_6H_6O_2$	138059.3
Furan, 2-ethyl-	C_6H_8O	22309.2
2-Cyclopenten-1-one, 2-methyl-	C_6H_8O	744844.2
2-Cyclopenten-1-one, 3-methyl-	C_6H_8O	299537.8
Furan, 2,3,5-trimethyl-	$C_7H_{10}O$	28520.3
trans,trans-3,5-Heptadien-2-one	$C_7H_{10}O$	105475.3
Furan, 2-ethyl-5-methyl-	$C_7H_{10}O$	90026.7
Cyclopentanone, 2-ethyl-	$C_7H_{12}O$	37846.5
Hexanoic acid, 2-oxo-, methyl ester	$C_7H_{12}O_3$	19365.3
Cyclohexane, methyl-	C_7H_{14}	95411.8
3-Heptanone	$C_7H_{14}O$	46988.6
Toluene	C_7H_8	55230
p-Cresol	C_7H_8O	266938.7
Phenol, 2-methyl-	C_7H_8O	145176.8
Phenol, 2-methoxy-	$C_7H_8O_2$	1389423
1,2-Benzenediol, 4-methyl-	$C_7H_8O_2$	207324.4
1,2-Benzenediol, 3-methyl-	$C_7H_8O_2$	106489.6
Ethylbenzene	C_8H_{10}	43330.9
Phenol, 3,4-dimethyl-	$C_8H_{10}O$	150094.2
Phenol, 4-ethyl-	$C_8H_{10}O$	81397.4
2-Methoxy-5-methylphenol	$C_8H_{10}O_2$	1630612
2,3'-Bifuran, octahydro-	$C_8H_{14}O_2$	1051380
2,3'-Bifuran, octahydro-	$C_8H_{14}O_2$	1665701
Propanoic acid, 2-methyl-, anhydride	$C_8H_{14}O_3$	19463.7
Propanoic acid, 2-methyl-, anhydride	$C_8H_{14}O_3$	23542.3
Propanoic acid, 2-methyl-, anhydride	$C_8H_{14}O_3$	36609.8
Propanoic acid, 2-methyl-, anhydride	$C_8H_{14}O_3$	31975.9
1,4-Butanediol, diacetate	$C_8H_{14}O_4$	335662.6
3-Heptene, 4-methyl-	C_8H_{16}	26742
4-Octene, (E)-	C_8H_{16}	27083.1

Octane	C_8H_{18}	138767.4
Resorcinol, 2-acetyl-	$C_8H_8O_3$	23662.1
Apocynin	$C_9H_{10}O_3$	328760.7
Homovanillic acid	$C_9H_{10}O_4$	225217.4
Phenol, 2,3,5-trimethyl-	$C_9H_{12}O$	17558.4
Phenol, 4-ethyl-2-methyl-	$C_9H_{12}O$	82194.4
Phenol, 4-propyl-	$C_9H_{12}O$	112152.5
Phenol, 3,4,5-trimethyl-	$C_9H_{12}O$	159528.1
1H-Inden-1-one, 2,3,4,5,6,7-hexahydro-	$C_9H_{12}O$	42789.3
Bicyclo[3.2.2]non-6-en-3-one	$C_9H_{12}O$	31325.1
2,4-Dimethylanisole	$C_9H_{12}O$	19644.8
Phenol, 4-ethyl-2-methoxy-	$C_9H_{12}O_2$	1031981
1-Pentanone, 1-(2-furanyl)-	$C_9H_{12}O_2$	40439.1
2H-Indene, 3,3a,4,5,6,7-hexahydro-	C_9H_{14}	16289
1,6-Heptadiene, 3,3-dimethyl-	C_9H_{16}	233832
2-Butanol, 3-(2,2-dimethylpropoxy)-	$C_9H_{20}O_2$	22487.1
2-Propanone, 1-(4-hydroxy-3-methoxyphenyl)-	$C_{10}H_{12}O_3$	224606.4
Benzene, 1-methoxy-4-propyl-	$C_{10}H_{14}O$	63782.5
Phenol, 2-methoxy-4-propyl-	$C_{10}H_{14}O_2$	2113181
2-Methylbutanoic anhydride	$C_{10}H_{18}O_3$	51483.2
3-Isopropyl-5-methylhexan-2-one	$C_{10}H_{20}O$	21190.5
Octane, 2,7-dimethyl-	$C_{10}H_{22}$	36260.4
1,10-Decanediol	$C_{10}H_{22}O_2$	342237.3
2-Butylbenzofuran	$C_{12}H_{14}O$	18361.7
Phenol, 2-methoxy-4-(1-propenyl)-, acetate	$C_{12}H_{14}O_3$	161158.8
Furan, 2,5-dibutyl-	$C_{12}H_{20}O$	51024
2,4-Dimethylpentan-3-yl (E)-2-methylbut-2-enoate	$C_{12}H_{22}O_2$	21474.4

3-Methyl-2-butenoic acid, oct-3-en-2-yl ester	$C_{13}H_{22}O_2$	84322.3

Table S21: Compounds identified by GC-MS in the oil phase after bio-oil syngas C–C coupling upgrading at 300 °C.

Compound name	Formula	Relative intensity
2(5H)-Furanone	$C_4H_4O_2$	120403
Butyrolactone	$C_4H_6O_2$	460185.4
1-Hydroxy-2-butanone	$C_4H_8O_2$	102938.7
Formic acid, propyl ester	$C_4H_8O_2$	131763.4
1,2-Ethanediol, monoacetate	$C_4H_8O_3$	141215.3
2-Hydroxy-3-pentanone	$C_5H_{10}O_2$	66328.9
1-Butanol, 4-methoxy-	$C_5H_{12}O_2$	371851.9
3-Furaldehyde	$C_5H_4O_2$	52354.1
Cyclopentanone	C_5H_8O	412469.2
1-Penten-3-one, 2-methyl-	$C_6H_{10}O$	88255.2
Cyclopentanone, 2-methyl-	$C_6H_{10}O$	367475.2
Cyclopentanone, 3-methyl-	$C_6H_{10}O$	84508.4
Cyclohexanone	$C_6H_{10}O$	201665.8
2-Vinylethyl acetate	$C_6H_{10}O_2$	89662.1
2,5-Hexanedione	$C_6H_{10}O_2$	354576.3
1,1-Ethanediol, diacetate	$C_6H_{10}O_4$	52350.3
2-Butanone, 3,3-dimethyl-	$C_6H_{12}O$	55921.3
Furan, tetrahydro-3,4-dimethyl-, cis-	$C_6H_{12}O$	155193
2-Hexanone	$C_6H_{12}O$	110927.6
2-Ethyltetrahydrofuran	$C_6H_{12}O$	89543.1
2H-Pyran, tetrahydro-2-methyl-	$C_6H_{12}O$	95465.7
Acetic acid, butyl ester	$C_6H_{12}O_2$	291762
2-Ethoxytetrahydrofuran	$C_6H_{12}O_2$	67038

1,3-Dioxolane, 2-propyl-	$C_6H_{12}O_2$	66812.7
1-Hexanol	$C_6H_{14}O$	15007.9
Ethanol, 2-butoxy-	$C_6H_{14}O_2$	76543.5
1-Butanol, 4-ethoxy-	$C_6H_{14}O_2$	731658.4
Phenol	C_6H_6O	166855.2
Ethanone, 1-(2-furanyl)-	$C_6H_6O_2$	198466.8
2-Cyclopenten-1-one, 3-methyl-	C_6H_8O	292319.3
2-Cyclopenten-1-one, 2-methyl-	C_6H_8O	785706
4-Methyl-2H-pyran	C_6H_8O	23048.8
Vinyl crotonate	$C_6H_8O_2$	67954.6
2(3H)-Furanone, 5-acetyldihydro-	$C_6H_8O_3$	17099.7
2-Cyclopenten-1-one, 3,4-dimethyl-	$C_7H_{10}O$	71419.4
Furan, 2,3,5-trimethyl-	$C_7H_{10}O$	48008.7
Furan, 2-ethyl-5-methyl-	$C_7H_{10}O$	155465.6
2,2-Dimethylglutaric anhydride	$C_7H_{10}O_3$	39741.6
1-Ethylcyclopentene	C_7H_{12}	92708.7
Cyclohexene, 1-methyl-	C_7H_{12}	201663.7
Cyclohexene, 4-methyl-	C_7H_{12}	79338.5
4-Hexen-3-one, 5-methyl-	$C_7H_{12}O$	24122.2
Cyclohexane, methyl-	C_7H_{14}	183167.3
Isopropylcyclobutane	C_7H_{14}	52673.2
1-Pentene, 3,3-dimethyl-	C_7H_{14}	36406.1
2-Heptene, (E)-	C_7H_{14}	83028.8
C2H5C(CH3)2COCH3	$C_7H_{14}O$	247687.6
3-Heptanone	$C_7H_{14}O$	89562.9
Toluene	C_7H_8	111699
Phenol, 2-methyl-	C_7H_8O	166273.9
p-Cresol	C_7H_8O	251503.4
1,2-Benzenediol, 3-methyl-	$C_7H_8O_2$	85909.7
Phenol, 2-methoxy-	$C_7H_8O_2$	1315218

Ethylbenzene	C_8H_{10}	267993.7
Phenol, 3,4-dimethyl-	$C_8H_{10}O$	149206.3
Benzenemethanol, .alpha.-methyl-	$C_8H_{10}O$	20501.8
2-Methoxy-5-methylphenol	$C_8H_{10}O_2$	1442557
Bicyclo[4.1.0]heptane, 7-methylene-	C_8H_{12}	19720
2-Cyclopenten-1-one, 3,4,4-trimethyl-	$C_8H_{12}O$	22073.3
2-Cyclopenten-1-one, 2,3,4-trimethyl-	$C_8H_{12}O$	22073.3
Cyclohexene, 1-ethyl-	C_8H_{14}	318124.9
Cyclohexene, 1,2-dimethyl-	C_8H_{14}	40805.7
Cyclohexene, 1-ethyl-	C_8H_{14}	78268.2
9-Oxabicyclo[6.1.0]nonane, cis-	$C_8H_{14}O$	397759
2,3'-Bifuran, octahydro-	$C_8H_{14}O_2$	893922.8
2,3'-Bifuran, octahydro-	$C_8H_{14}O_2$	532406.2
Propanoic acid, 2-methyl-, anhydride	$C_8H_{14}O_3$	13173.6
Propanoic acid, 2-methyl-, anhydride	$C_8H_{14}O_3$	71040.3
Propanoic acid, 2-methyl-, anhydride	$C_8H_{14}O_3$	62699.3
Butanoic acid, anhydride	$C_8H_{14}O_3$	66296.2
1,4-Butanediol, diacetate	$C_8H_{14}O_4$	352495.4
3-Hexene, 2,3-dimethyl-	C_8H_{16}	33969.7
Cyclohexane, 1,2-dimethyl-, cis-	C_8H_{16}	104837.2
Heptane, 3-methyl-	C_8H_{18}	21917.9
Octane	C_8H_{18}	235826.2
1-Butanol, 4-butoxy-	$C_8H_{18}O_2$	180892.3
Butane, 1,4-diethoxy-	$C_8H_{18}O_2$	90932.5
Ethanone, 1-(3-hydroxy-4-methoxyphenyl)-	$C_9H_{10}O_3$	150930.6
Homovanillic acid	$C_9H_{10}O_4$	67443.5
1H-Inden-1-one, 2,3,4,5,6,7-hexahydro-	$C_9H_{12}O$	67492.2
Phenol, 3,4,5-trimethyl-	$C_9H_{12}O$	174773.4
Phenol, 4-propyl-	$C_9H_{12}O$	88220.2

4,5,6,7-Tetrahydro-3-methylbenzofuran	$C_9H_{12}O$	222440.6
Phenol, 4-ethyl-2-methoxy-	$C_9H_{12}O_2$	877787
2H-Indene, 3,3a,4,5,6,7-hexahydro-	C_9H_{14}	56469.1
2-Cyclopenten-1-one, 2,3,4,5-tetramethyl-	$C_9H_{14}O$	260333.3
2,3-Dimethyl-3-heptene	C_9H_{18}	234908.1
Nonane	C_9H_{20}	129882.1
trans-Isoeugenol	$C_{10}H_{12}O_2$	227195.9
Benzene, 1-methoxy-4-propyl-	$C_{10}H_{14}O$	60526.2
Phenol, 2-methoxy-4-propyl-	$C_{10}H_{14}O_2$	1875867
3-Octene, 2,6-dimethyl-	$C_{10}H_{20}$	77627.8
1-Octene, 3,4-dimethyl-	$C_{10}H_{20}$	199110.8
Nonane, 2-methyl-	$C_{10}H_{22}$	151574.4
Phenol, 2-(1,1-dimethylethyl)-5-methyl-	$C_{11}H_{16}O$	339313.6
Octane, 2,6,6-trimethyl-	$C_{11}H_{24}$	67308.5
Oxalic acid, cyclohexyl butyl ester	$C_{12}H_{20}O_4$	44966.8
1-Undecene, 9-methyl-	$C_{12}H_{24}$	63470.3
5-Undecene, 6-methyl-	$C_{12}H_{24}$	28625.4
1-Heptene, 2-pentyl-	$C_{12}H_{24}$	31953.2

List of Figures

Figure 1-1: Classification of bio-oil upgrading techniques 6

Figure 1-2: Related reactions during the HDO upgrade process, taking guaiacol as an example 13

Figure 4-1: The PPE on Ru (0001) adsorption structure. Source: reprinted from ref. [224] in agreement with the terms of use. 32

Figure 4-2: The charge difference density plots for PPE adsorption, the blue (yellow) distribution corresponds to charge accumulation (depletion). Source: reprinted from ref. [224] in agreement with the terms of use.....33

Figure 4-3: Reaction pathways of PPE HDO process, red values are energy barriers, and black values are reaction energy in eV. Source: reprinted from ref. [224] in agreement with the terms of use. 34

Figure 4-4: Gibbs free energy diagram of PPE HDO process on Ru (0001) surface at a temperature of 250 °C. The black numbers refer to the elemental steps (see also Table 2-1), the 7 optimized transition states (TS) are shown as an inset. Blue values denote free energy changes during elemental reaction steps while the red values denote reaction free energy barriers. Source: reprinted from ref. [224] in agreement with the terms of use. 34

Figure 4-5: a,b. SEM images of fresh Ru/Nb_2O_5; c. EDX elemental mapping of Ru, Nb, O. Source: reprinted from ref. [224] in agreement with the terms of use. 37

Figure 4-6: a. XRD patterns of Ru/Nb_2O_5; b. NH_3 TPD analysis of Ru/Nb_2O_5; c. N_2 physisorption analysis of Ru/Nb_2O_5. Source: reprinted from ref. [224] in agreement with the terms of use. 38

Figure 4-7: Effect of temperature on PPE HDO. Condition: 0.5g PPE, 50g decalin, 0.5g Ru/Nb_2O_5, 5 MPa H_2, 2h. Source: reprinted from ref. [224] in agreement with the terms of use. 39

Figure 4-8: a,b, SEM images of Ni Al LDH structure; c,d. SEM images of Ni/Al catalyst. Source: reprinted from ref. [225] in agreement with the terms of use. 42

Figure 4-9: a. the TEM image of Ni/Al catalyst; b. Ni/NiO particle size distribution; c. HRTEM image of Ni/Al catalyst; d. EDS-mapping from STEM of Ni/Al catalyst. Source: reprinted from ref. [225] in agreement with the terms of use. 42

Figure 4-10: a. XRD patterns of Ni-Al LDH, Ni-Al LDO, and Ni/Al-2 catalyst after reduction; b. XRD patterns of different Ni/Al ratio catalysts; c. Ni 2p High resolution XPS spectra for Ni/Al catalyst; d. Raman spectra for different Ni/Al ratio catalysts; e. Normalized Ni K edge XANES spectra of the Ni/Al-2 catalyst and selected Ni reference compounds. Source: reprinted from ref. [225] in agreement with the terms of use.....45

Figure 4-11: a. The conversion of PPE Hydrogenolysis over Ni/Al catalysts prepared by different methods at various temperature. Reaction conditions: 0.2 g PPE, 0.2 g Catalyst, 20 g decalin, 25 bar H_2, 1h; b. Comparison of PPE hydrogenolysis conditions from different literatures; c. The conversion and selectivity of PPE hydrogenolysis over different Ni-Al ratio catalysts. Reaction conditions: 0.2 g PPE, 0.2 g Catalyst, 20 g decalin, 125 ℃, 25 bar H_2, 1h; d. The conversion and selectivity of PPE hydrogenolysis over Ni/Al-2 catalyst at various temperature. Reaction conditions: 0.2 g PPE, 0.2 g Catalyst, 20 g decalin, 25 bar H_2, 1h. Source: reprinted from ref. [225] in agreement with the terms of use. 47

Figure 4-12: a. The Ni/NiO nanowire model; b. PDOS and d-band center of Ni supported on NiO and Ni (111); c. Comparison of adsorption energies over Ni (111), NiO (100), and Ni/NiO; d-f. Charge density difference of Ni/NiO (d), NiO (100) (e), and Ni (111) (f); The blue (yellow) distribution corresponds to charge accumulation (depletion), and the black value represent the number of electron transfers in Bader charges; The Ni, O, C, H atoms are presented as green, red, orange and pink, respectively; g. The Gibbs Free energy diagram of PPE hydrogenolysis over Ni/NiO and Ni (111) under 398 K (125℃), The numbers 1-9 represent the elementary steps listed in Table 4-7. Source: reprinted from ref. [225] in agreement with the terms of use. 50

Figure 4-13: Schematic illustration of the synthesis of Mo doped Ni Al catalyst derived from LDH structure.....52

Figure 4-14: a,b. SEM images of Mo doped Ni/Al_2O_3 catalyst; c. TEM image of Mo doped Ni/Al_2O_3 catalyst; d. Particle size distribution from TEM image. 54

Figure 4-15: XRD patterns of undoped Ni/Al_2O_3 and Ni/Al_2O_3 doped with Mo, Ce, Nb, and W.....55

Figure 4-16: Mo 3d and Ni 2p High resolution XPS spectra for Mo doped Ni/Al_2O_3 catalyst. 56

Figure 4-17: a. The product distribution of guaiacol HDO over different catalysts, reaction conditions: 250 °C, 50 bar H_2, 2h. b. the product distribution of guaiacol HDO over Mo doped Ni/Al_2O_3 catalyst under different temperatures; reaction conditions: 50 bar H_2, 2h.....57

Figure 4-18: The product distribution of bio-oil HDO over Mo doped Ni/Al_2O_3 catalyst. Reaction conditions: 250 °C, 50 bar H_2, 2h. 59

Figure 4-19: DFT models of Ni (111) and Mo_3O_5/Ni (111); The Ni, Mo, O, C, H atoms are presented as grey, purple, red, orange and pink, respectively. 61

Figure 4-20: Charge density difference of Ni (111) (a), Mo_3O_5/Ni (111) (b); The blue (yellow) distribution corresponds to charge accumulation (depletion) 62

Figure 4-21: The Gibbs Free energy diagram of C-O cleavage on Ni (111) and Mo_3O_5/Ni (111) at a temperature of 250 °C. 62

Figure 4-22: Transitation state structures over Ni (111) slab 63

Figure 4-23: Transitation state structures over Mo_3O_5/Ni (111) surface. 63

Figure 4-24: SEM images of Ru/β-zeolite catalyst. 64

Figure 4-25: SEM-EDX mapping of Ru/β-zeolite catalyst 65

Figure 4-26: XRD patterns of β-zeolite and Ru/β-zeolite catalysts. 67

Figure 4-27: N_2 physisorption analysis of Ru/ β-zeolite 67

Figure 4-28: NH_3-TPD analysis of Ru/β-zeolite 68

Figure 4-29: Conversion of guaiacol in syngas over different catalysts 69

Figure 4-30: Products distribution of syngas upgrading of guaiacol at 250 ºC and 300 ºC over Ru/β-zeolite catalyst. 70

Figure 4-31: Products distribution of syngas upgrading of bio-oil at 250 ºC and 300 ºC 71

Figure S1: The atomic distance between adjacent mirrored molecules. 105

Figure S2: Convergence testing of adsorption energy at different surface scales. 106

Figure S 3: Convergence testing of adsorption energy at different K-points. ... 107

Figure S4: Adsorption structure of benzene on Ru (0001) surface. 107

Figure S5: SEM-EDX Mapping of Ni/Al-2 LDH structure 108

Figure S6: SEM-EDX Mapping of reduced Ni/Al-2 catalyst. 108

Figure S7: H_2-TPR analysis of Ni/Al-2 catalyst. 109

Figure S8: k^2-weighted EXAFS spectra of the Ni/NiO catalyst and selected Ni reference compounds. 110

Figure S9: First shell fits of the Ni K edge FT EXAFS spectra. 111

Figure S10: Ni (111) model 111

Figure S11: Ni (100) model 112
Figure S12: Ni/NiO model 112
Figure S 13: Different adsorption structure of PPE on Ni (111) slab 113
Figure S14: Different adsorption structure of PPE on Ni/NiO slab 113
Figure S15: Transitation state structures over Ni (111) slab 114
Figure S16: Transitation state structures over Ni/NiO slab 114
Figure S 17: N_2 physisorption analysis of Mo doped Ni/Al_2O_3 catalyst 115
Figure S18: SEM-EDX mapping of Mo doped Ni/Al_2O_3 catalyst 115
Figure S19: NH_3-TPD analysis of Mo doped Ni/Al_2O_3 catalyst 116
Figure S20: Different adsorption structures of cyclohexanol on Ni (111) surface. 116
Figure S21: Different adsorption structures of cyclohexanol on Mo_3O_5/Ni (111) surface. 117

List of Tables

Table 1-1: Catalysts and reaction conditions for catalytic cracking 11

Table 4-1: Reaction steps corresponding Figure 4-4. Source: reprinted from ref. [224] in agreement with the terms of use..... 35

Table 4-2: N_2 physisorption results of Nb_2O_5 and Ru/Nb_2O_5. Source: reprinted from ref. [224] in agreement with the terms of use. 37

Table 4-3: Composition of the gas phase after the reaction. Source: reprinted from ref. [224] in agreement with the terms of use. 40

Table 4-4: Element content result of crude oil and upgrade oil. Source: reprinted from ref. [224] in agreement with the terms of use. 40

Table 4- 5: Ni element content test results obtained through ICP-OES. Source: reprinted from ref. [225] in agreement with the terms of use. 44

Table 4-6: Comparation of reaction conditions and results of PPE hydrolysis over different catalysts from literatures. Source: reprinted from ref. [225] in agreement with the terms of use. 48

Table 4-7: Reaction coordinate steps over Ni (111) and Ni/NiO slab. Source: reprinted from ref. [225] in agreement with the terms of use. 51

Table 4-8: Catalytic performance of various catalysts for the hydrodeoxygenation of guaiacol, with cyclohexanol as the primary product. 58

Table 4-9: Element content of Ru/β-zeolite catalyst by SEM-EDX. 65

Table 4-10: Distribution of aromatics and cycloalkanes in bio-oil feedstock and upgraded products under 250 ºC and 300 ºC. 71

Table S1: Ru content of Ru/Nb_2O_5 catalyst from EDX. 117

Table S2: Compounds identified by GC-MS in the oil-phase after the reaction. 117

Table S3: Results of the linear combination analysis of XANES (fit in the range -10 eV – +40 eV relative to E_0) with the Ni metal spectra as references of Ni/Al-2. 118

Table S4: Results of EXAFS fits at the highest degree of reduction. 119

Table S5: The adsorption energy (eV) of different structures of PPE on Ni (111) slab. 120

Table S6: The adsorption energy of different structures of PPE on Ni/NiO slab. 120
Table S7: The adsorption energy of PPE on NiO (110) slab. 120
Table S8: The energies of intermediates on Ni (111). 121
Table S9: The energies of intermediates on Ni/NiO. 122
Table S10: Element analysis of Mo-Ni/Al_2O_3 catalyst from SEM-EDX 123
Table S11: Element analysis of different doped Ni/Al_2O_3 catalyst from ICP-OES. 123
Table S12: Compounds identified by GC-MS of bio-oil feedstock. 123
Table S13: Compounds identified by GC-MS in the oil phase after HDO upgrading at 250 °C over Mo-Ni/Al_2O_3 catalyst. 126
Table S14: Compounds identified by GC-MS in the oil phase after HDO upgrading at 250 °C over Ru/C catalyst. 130
Table S15: Compounds identified by GC-MS in the oil phase after guaiacol syngas C–C coupling upgrading at 250 °C over Ru/C catalyst. 136
Table S16: Compounds identified by GC-MS in the oil phase after guaiacol syngas C–C coupling upgrading at 250 °C over Co/β-zeolite catalyst. 137
Table S17: Compounds identified by GC-MS in the oil phase after guaiacol syngas C–C coupling upgrading at 250 °C over Ru/β-zeolite catalyst. 139
Table S18: Compounds identified by GC-MS in the oil phase after guaiacol syngas C–C coupling upgrading at 300 °C. 142
Table S19: Compounds identified by GC-MS in oil phase. 147
Table S20: Compounds identified by GC-MS in the oil phase after bio-oil syngas C–C coupling upgrading at 250 °C. 150
Table S21: Compounds identified by GC-MS in the oil phase after bio-oil syngas C–C coupling upgrading at 300 °C. 153